NORTHWESTERN UNIVERSITY

Thermodynamic And Electrochemical Models For Predicting Aqueous Materials Formation

A DISSERTATION

SUBMITTED TO THE GRADUATE SCHOOL

IN PARTIAL FULFILLMENT OF THE REQUIREMENTS

for the degree

DOCTOR OF PHILOSOPHY

Field of Materials Science and Engineering

By

Lauren N. Walters

EVANSTON, ILLINOIS

December 2022

Abstract

A fundamental materials science question is "why and how will this material form?" The experimental, computation, and time resources necessary to answer this question consume significant resources due to the predominantly trial-and-error based approaches common in materials research. This dissertation reintroduces a number of fundamental thermodynamics-based tools for the study of contemporary materials stability and formation. Primary modeling types include (multi-element) Pourbaix diagrams, stability diagrams, yield diagrams, convex hulls, ensemble (probability diagrams), and driving force parameters. First, we create (nonstandard state) Pourbaix and driving force diagrams sourced from density functional theory (DFT) calculations to model copper speciation in aqueous, electrochemical environments. We determine hybrid functionals as necessary for free energy of formation modelling to create accurate Pourbaix diagrams, and further develop methods for the efficient calculation of phase diagrams from less computationally-intensive functionals. At elevated temperatures, we report decreased passivation regions, particularly for $CuO_{(s)}$, and pressure dependent aqueous ion predominance. We also establish boundary conditions for thermodynamically driven lead corrosion for nonstandard states, phosophate solutions, and carbonate solutions. Multiple element Pourbaix and stability diagrams, created from DFT-sourced free energies of formation with spin-orbit coupling and van der Waals corrections included, demonstrate that the stability of hydroxylpyromorphite has been overestimated. This work suggests there may be alternative formation routes for lead orthophosphates, such as from early calcium apatite precursors. Our model underscores the need for future research on lead scale identity and stability. Next, we apply predominance diagrams to rationalize the hydrothermal synthesis design of a family of thermoelectric, layered, heteroanionic bismuth oxychalcogenide (BiMOQ) compounds. The stability regions of the targeted oxychalcogenides in initial Pourbaix diagrams indicate hydrothermal synthesizability. Analysis of optimized reaction conditions and potential byproduct creation is completed through extending thermodynamic tools such as probability diagrams, calculated from the canonical ensemble

of chemical potentials, and stability-yield diagrams. We further explore chemical trends for successful synthesis of products, and find copper target phase domains to be larger than silver ones, selenium target domains are larger than sulfur domains, and heteroanionic material domains typically stabilized at moderate pHs. Finally, we introduce two new, quantitative aqueous materials formation descriptors for the development of future corrosion resistant systems: (*i*) the maximum driving force (MDF) to characterize initial surface formation of scales and (*ii*) the effective chemical potential to predict subsurface, compositionally constrained phase formation. We apply these thermodynamic analysis tools to understand nickel thin film evolution in variable pH and potentials. Moreover, we leverage the MDF to intuitively describe the aqueous stability of single element speciation including noble $4d$ metals (*e.g.*, silver, gold) and soluble solid oxides. Finally, we report initial work in developing these parameters for future comparative studies on quantitative elemental- and composition-based corrosion. We conclude by discussing future work, and the important note that compound formation verified by experimentation is imperative for model validation. Successive projects to develop rational synthesis design strategies and corrosion resistance will accelerate materials discovery, enabling new energy, health, and electronics solutions.

Acknowledgments

When I was 14 in my first year of high school, I wrote a to-do list of the 100 things I want to do in my life. These included going to all the continents on our Earth, running the New York City marathon, and getting a PhD in engineering. Neither of my parents have graduate degrees, nor do any of my close relatives, so it must have been the science talks and University of Washington open houses that my dad took me to that made the later a goal of mine. Since then, I've learned to be strong, confident, and also realize how little I really know. I'm proud to have finally made it to the latter goal at nearly double the age I was when I first wrote it down.

I will always have my family to thank this degree. Without their thorough support, from financial and resource support to their emotional support and love, I truly wouldn't be where I am today. My dad gave me a role model and always pushed me to not assume no's but instead at least try. My mom always was there taking care of me, has helped me move across the country multiple times, and was always there with muffins on the best or worst days. Thank you to my brother, Devon, for having so much talent that it always made me want to race ahead for fear of being passed. I will always say the love I have unconditionally and overwhelming gotten from my immediate family is the single best gift I received in my life, and one that I will always work my best to be deserving of.

Thank you to Marc, for whom I would not be who I am today without, and for his unwavering faith in my ability.

Thank you to those who have supported me personally throughout this program: Richard, Raymond, Jaye, Daniel, Nick, Yongjin, Jaye, Jennie, Alanna, Milli, Vivianne, Jackson, Brandon, and Grant. My Case group including Kristen, Jacob, Tom, and Eric really made coming here not feel so different from college. I appreciated how you all made this new place feel like home. In particular, I must thank the brunch bunch, Kate, Kristen, and Julia, for being steadfast rocks of friendship in this sometimes lonely academic world.

You three are all so special to me, and I know that I would not have been able to successful navigate classes or living in a new city without you all. Kate, thank you for always inspiring me with your constant forward motion and love of finding food and traveling. Julia, your support at key times has been crucial: from being on committees and student clubs together and even waking up at 4:30 am to walk me to the marathon, you are always there, really there, when it counts. And Kristen, you will always have been my best roommate ever, I'm pretty sure of it. Thank you for your support, your sass, your wise words when I needed them, helping me learn how to edit my figures, the late night discussions that were always so meaningful, and always being down to hang out with me each night, even if Phyllis was around.

I have benefited from having incredible professional research mentors along the way. My undergraduate research mentors Michael Hore (undergraduate research, Case Western Reserve University), David Schiraldi (undergraduate research, Case Western Reserve University), Robert Riggleman (REU, University of Pennsylvania), and Miguel Sanchez-Soto (summer research internship, Universitat Politécnica de Catalunya, Terrassa Spain) facilitated interesting and fundamental research projects, and advice for which I will always be grateful. In particular, Professor Schiraldi lead a great recruitment session at Case for my dad and I during our visit to see if the school would be a good fit. Without that warm and informative welcome, I probably wouldn't have gone to Case or been a polymers major. Moreover, both Professors Schiraldi and and Hore each helped me find summer research positions after working in their labs, and these research positions lead to so much personal and professional growth, and other mentor relationships. Their help truly helped move my career as a researcher forward. Finally, thank you to Derek and Lee Fallen, for providing me my first (and only) internship while in high school. It was my first taste at what a materials scientist actually does, and that support and opportunity has propelled me forward since.

I really want to thank some of the summer graduate research mentors I had as an undergraduate which prepared me to a successful graduate researcher. Thank you to Tobias Abt for being my first real research mentor, letting me see how great an international dissertation could be and giving me something to strive for, and giving me a worldly but down to earth perspective on both science and living abroad. Thank you to Marianna Sofman for teaching me how to make friends when moving to a new city, how to look for resources, and how to present yourself professional in a charismatic way. You are still one of the best scientific

communicators I know! Most especially I want to thank my REU mentor Emily Lin, with whose advice I would not have been able to choose such a good fit for future professional opportunities. Your wisdom has allowed me to set myself up for success, but your friendship and belief in me made me was one of the first true sources of inclusion I felt in academic research.

Thank you to those who provided many professional development opportunities for me, including those who worked at the SEARLE center to organize the teaching certificate program (TCP). Thank to Professor Ian McCue for allowing me to help be part of the formation of a new class, and being a great teaching and research mentor as part of TCP.

Thank you to all who have been part of different outreach over my years in graduate school. I have always admired the commitment to diversity, inclusion, equity, outreach, and support that so many at Northwestern promote in their opinions, interaction, and efforts. Those in NURPH, GradSWE, MSSA, MSUS, JSC, LPS, and Coding Club have truly helped me and so many others at this school feel valued and valuable. I want to extend a particular thank you to those volunteers who were part of Coding Club its first two years and Blanca Sandoval for believing in my leadership and our shared mission.

I was honored during my time as a graduate student to mentor four undergraduate students: Nathan Szymanski, Alex Tai, Allison Park, and Emily Wang. Each of you made substantial progress in your research, your careers as scientists, and your professional goals. I learned a lot from each of you, and am proud of the initiative you took on your projects and what you have accomplished since.

Thank you to my advisor, Professor James Rondinelli, for providing a work environment in which I could thrive. Your steadfast support of my research projects, both funded and ones that I was personally interested in, will always be appreciated. The opportunities I got while in this group surpass what I expected of graduate school. Furthermore, thank you to the whole of the Materials theory and Design group, including: Nick Wagner, Jaye Harada, Nathan Koocher, Yongjin Shin, Daniel Hickox-Young, Richard Saballos, Raymond Wang, Kyle Miller, Kathleen Mullin, Sean Koyama, Siddhartha Nathan, Graham Pritchard, Danilo Puggioni, Liang-Feng Huang, Mingqiang (Kurt) Gu, Michael Waters, Alexandru Georgescu, and John Cavin. Each of you have provided help, academic support, and laughs. I feel thankful to have been tied into a network with such hardworking and brilliant individuals.

Thank you to those who have contributed to my growth in research and professionally throughout graduate school. Thank you to my committee members who have contributed significant time towards mentorship and evaluation of my degree: Professor Kenneth R. Poeppelmeier, Professor John R. Scully, and Professor Ian McCue, as well as Professor Peter W. Voorhees for contributing to my qualifier evaluation. Your attention, comments, revisions, and questions about my work have greatly helped shape its progress, and allowed me to produce more thoughtful and relevant research. Moreover, I would like to extend significant acknowledgements to key collaborators I have worked with during my time in graduate school. This includes investigations on predicting lead release with Professor John Scully and Professor RJ Santucci; and synthesis prediction studies with Professor Kenneth Poeppelemeier, Professor Vinayak Dravid, and Dr. Chi Zhang. I have greatly appreciated the conversations, help, time, and energy each of you dedicated towards producing impactful and interesting scientific works.

This work was enabled by numerous financial supports and high performance computing (HPC) resources. This includes the Northwestern University Materials Science and Engineering department for financial support through the first year department fellowship, and for the Weertman fellowship. Scholarships and awards through the Materials Research Society (MRS), The Minerals, Metals & Materials Society (TMS), ASM International, PPG, American Physical Society, and The Graduate School (TGS) at Northwestern provided opportunities for professional and academic development. Financial support as a graduate fellow within the Brady program at Northwestern also provided personal and professional development, as well as supplemental financial assistance during three years of my PhD. This work was supported by a number of different agencies, including by the Office of Naval Research (ONR) under MURI Grant No. N000014-16-12280, and by the National Science Foundation's (NSF) MRSEC program (DMR-1720139) at the Materials Research Center of Northwestern University. Computational efforts were supported through the computational resources and staff contributions provided for the Quest high performance computing facility at Northwestern University which is jointly supported by the Office of the Provost, the Office for Research, and Northwestern University Information Technology. This work used the Extreme Science and Engineering Discovery Environment (XSEDE), which is supported by National Science Foundation grant number ACI-1548562. Use of the Center

for Nanoscale Materials, an Office of Science user facility, was supported by the U.S. Department of Energy, Office of Science, Office of Basic Energy Sciences, under Contract No. DE-AC02-06CH11357.

Contents

List of Figures

List of Tables

CHAPTER 1

Introduction

1.1. Motivation

Water, necessary to sustain life, is also fundamental to the formation of many important materials in our world. Water contributes oxygen and hydrogen to many inorganic ceramics. Furthermore, as a solubilizing medium, hydrothermal water-based synthesis methods make available materials that might otherwise be hard to form. On the other hand, metal or alloy contact with water can lead to harmful degradation via corrosive processes. Strategies to prevent corrosion often rely on fostering the formation of stable oxide barriers; thus, limiting degradation requires creating new materials. While aqueous formation of passive oxides is of upmost importance, due to water's complexity, it is not very well understood. Significant work to understand and predict aqueous materials formation is therefore paramount to advancing the field of materials chemistry.

Much of modern thermodynamics was developed by Josiah Willard Gibbs in "On the Equilibrium of Heterogeneous Substances" in 1873 and 1875 [33]. In his foundational works, he develops the concepts of free energy and entropy to describe equilibria and materials stability within simple and isotropic systems. He also furthers geometric representations of chemical systems, creating visualization tools for materials stability across variables like temperature and composition. The creation of these phase diagrams are foundational towards predicting which phases and species is most likely to occur in a given system. These important concepts of energies, entropy, and geometric phase diagrams have allowed researchers in subsequent centuries to develop models for materials formation in different environments, including within aqueous systems.

One such important model of water based materials formation is the Pourbaix diagram, developed by Marcel Pourbaix in 1974 [1]. Pourbaix diagrams are aqueous, electrochemical, pH-potential diagrams which utilize normalized, environmentally dependent formation energies to outline conditions at which different materials phases will be stable. Within "Atlas of Electrochemical Equilibria in Aqueous Solutions", standard state diagrams are reported for nearly all elements stable in water. Since its original publication, other

studies have further developed reported diagrams, including through: (*i*) increased accuracy with better $\Delta_f G$ sourcing, (*ii*) varying parameter studies, such as reporting concentration-pH diagrams, (*iii*) calculating diagrams at nonstandard state and nonstandard corrosion limits, and (*iv*) including phases from multiple different elements.

Within general materials stability, a uniting tool is the convex hull. C. Wolverton *et al.* [34] in 1991 and D.D. Lee *et al.* in 1992 [35] were some of the first works to introduce a materials science "convex hull" describing composition versus energy space. These diagrams show thermodyanmically stable phases connected on a hull line. Meta and unstable materials, sometimes visualized lying above the hull, will generally be harder to synthesize, and at an infinite amount of time should decompose into materials compositionally close to them which are on the hull. Convex hulls can be created with experimental free energies of formation, or enthalpies calculated from DFT-sourced electronic energies. The later strategy is leveraged by computational materials science groups to report extensive multiple element convex hulls in online databases such as Materials Project [36] and the Open Quantum Materials Database [22, 23]. Owing to their prominence and general system applicability, convex hulls have become the field standard first step towards understanding solid materials stability and synthesizability. However, particular to water based materials formation, the competing soluble ions within aqueous systems, where soluble ions compete with solid phases, renders free energies of formation alone as ineffective.

A couple decades ago, some of the first papers by J.M.R. Génin *et al.* [37] and R.M. Nyffenegger *et al.* [38] reported on Pourbaix diagrams repurposed for hydrothermal synthesis. Since then, and particularly within the last 5 years, renewed interested has led to increased reporting of aqueous predominance diagrams focused on understanding materials formation. In 2019, W. Sun *et al.* synthesized metastable manganese oxides in part by utilizing Pourbaix diagrams to identify the pH, potential, and crystallization pathways target phases needed to occur [39]. L. Liu *et al.* in 2018 selected processing conditions for Co(III) catalysts from generated Pourbaix diagrams [40]. Pourbaix diagrams have further been repurposed from bulk materials to include the effects of size, surface orientation, and surface oxidation state [40-43]. However, most of these papers focus on binary compound synthesis, and are not developed for more complex, multielement aqueous materials formation.

The following chapters describe my work focused on thermodynamic models for materials formation. Within this context, we leverage thermodynamic phase diagrams to model the multiple influencing factors on materials formation in aqueous systems. Computer programs and new methods were developed as needed to drive efficient model creation. Models were applied to a variety of predominantly aqueous systems, including for understanding corrosion and hydrothermal synthesis, as depicted in Figure 1.1.

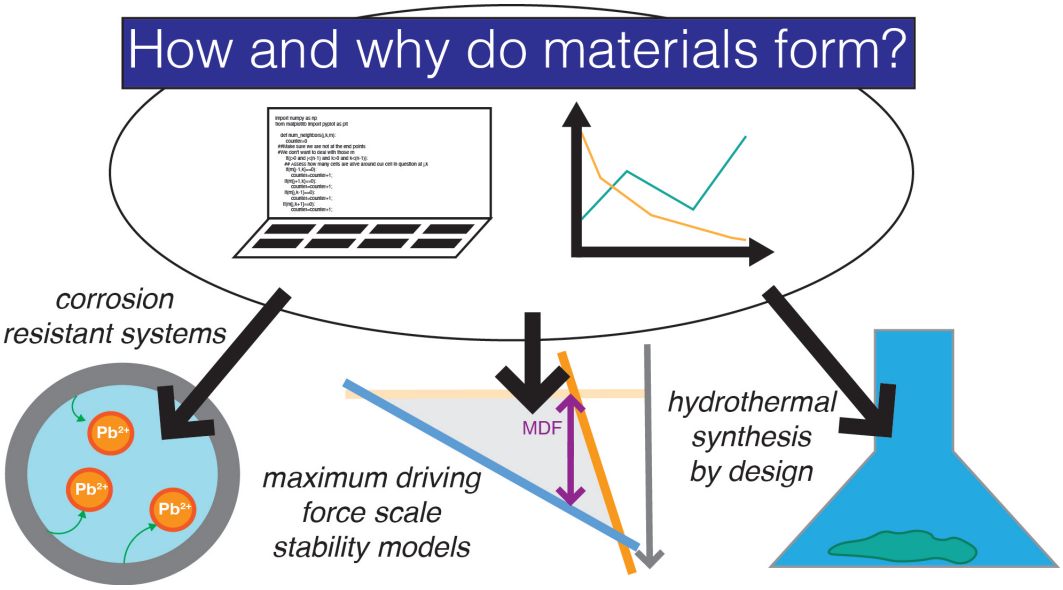

Figure 1.1. Schematic depicting research thrusts relating to why and how materials form. DFT and in house Python libraries (see Section 3.3 and Section 8.12) are utilized to calculate $\Delta_f G$s for thermodynamic phase diagram creation (center). Predominance diagrams model key degradation and formation environments, including for building corrosion resistant systems, creation of maximum driving force models of stable scale formation, and the rational design of hydrothermal syntheses.

The projects presented in this dissertation include: (*i*) understanding (non)standard state copper corrosion behavior, (*ii*) the prediction of stable lead scales in various environments to prevent corrosion in lead pipes, (*iii*) the design and verification of the synthesis techniques for a thermoelectric family of copper or silver containing bismuth oxychalcogenides (i.e., BiMOQ) by leveraging computationally sourced, multi-element Pourbaix and stability diagrams to identify conditions that favored target phase formation, (*iv*) the application of Ellingham diagrams to verify the formation of thin films via high temperature oxidation or 2D synthesis, and (*v*) the development of a model to predict stable scale formation utilizing maximum driving forces (MDF). Each of these projects rely on having accurate $\Delta_f G$ databases from density functional theory (DFT), as

demonstrated in Figure 1.1. Collaborative experimental works, imperative to substantiate computational models and which has increased the impact of each work, are briefly highlighted in subsequent chapters where relevant. Proposed projects, discussed in more detail in the future work section, include the evaluation of the corrosion behavior of copper-aluminum and copper-tin for predicting selective corrosion products for nanoporous materials synthesis, the inclusion of further scales for stability evaluation in aqueous lead systems, and hydrothermal synthesis design for other heteroanionic systems. The broader goal of this dissertation is to normalize and diversify thermodynamically sourced diagrams to predict stable phases, and provide analysis to accelerate future synthesis and corrosion resistance design.

1.2. Research Objectives and Statements

The foundation of this dissertation lies in the advancement of predicting when new materials will form for synthesis and corrosion sciences. We leverage computational tools, including DFT and phase diagrams, to understand materials degradation and design strategies for novel synthesis routes. Better design rules guiding materials stability will accelerate the discovery of new materials, thereby giving materials scientists a larger materials phase space to study and utilize. In pursuit of that goal, the following objectives were identified:

(1) *Evaluate* the differences between experimentally and computationally predicted diagrams
(2) *Establish* refined DFT $\Delta_f G$s as appropriate for describing the energetic landscape of a system of solids for phase diagram creation
(3) *Expand* the synthesis systems described and predicted by computation, including novel formation of complex layered, heteroanionic compounds
(4) *Develop* novel methodologies to apply computational tools and diagrams to corrosion systems, including systems of multiple elements and varying compositions
(5) *Increase* the adoption of new workflow for understanding materials formation in aqueous systems

The pursuit of these objectives was facilitated by uniting computational methods, analysis, and results with experimental collaboration in peer-reviewed publications. The main questions addressed in this dissertation are as follows:

- What benchmarking is necessary to establish a level of DFT that can create accurate Pourbaix diagrams? Are there methods we can develop to improve the accuracy and efficiency of Pourbaix diagram creation? Are there further analytical tools that we can develop, beyond the Pourbaix diagram, using DFT-calculated free energies of formation?
- Do calculated lead predominance diagrams match what we know about lead release, particularly in legacy water systems? Can we learn anything new about limiting Pb corrosion by studying the thermodynamic contributions to lead solubilization?
- Can we effectively utilize predominance diagrams to understand and optimize hydrothermal synthesis methods for multiple element products? Are there ways that we can bridge the gap between traditional thermodynamic and kinetic modeling of materials formation?
- Are there further models or descriptors we could develop to provide quantitative information for aqueous materials formation? How do we ground this descriptor in physical observation and experiment?

1.3. Organization

This thesis is organized to mirror the research objectives as follows:

- Chapter 2 outlines key background and history for understanding the foundational methods and previously published literature leading to this work.
- Chapter 3 provides details on the different methods necessary for developing the projects in this dissertation.
- Chapter 4 utilizes Pourbaix and driving force diagrams, sourced from free energies of formation calculated with first principles methods, to model copper corrosion in various environments.
- Chapter 5 explores how lead solubilization changes with varying environmental conditions through calculation of predominance diagrams with DFT sourced free energies of formation.
- Chapter 6 develops thermodynamic models and predominance diagrams for understanding and optimizing hydrothermal synthesis of heteroanionic bismuth oxychalcogenides.

- Chapter 7 establishes new quantitative descriptors of aqueous materials formation, the MDF and effective chemical potential. These parameters are then applied to interpret experimental Ni thin film data, calculate trends within possible corrosion behavior of a broad set of periodic table elements, and understand cantor alloy scale behavior.
- Chapter 8 summarizes the most important findings within this dissertation and discusses future directions for this work.

CHAPTER 2

Background

Predicting when and how materials form is at the cornerstone of new materials discovery and the efficient design of materials systems. New materials synthesis is challenging. Development usually progresses through trial-and-error approaches, leading to resource and time waste. Furthermore, the lifetime of a material is limited by degradation; often degradation processes involve redox reactions whose products dictate usability and application lifetime. Generally, it is challenging and time consuming to understand how the multitude of experimentally tunable variables (*e.g.*, time, temperature, pressure, solution chemistry) affect potential product, ion, or solid surface oxidation (scale) formation. Much work has been completed to develop and apply models to predict materials creation. Here, we review approaches for understanding aqueous materials formation, though recognize that our limited focus is by no means extensive.

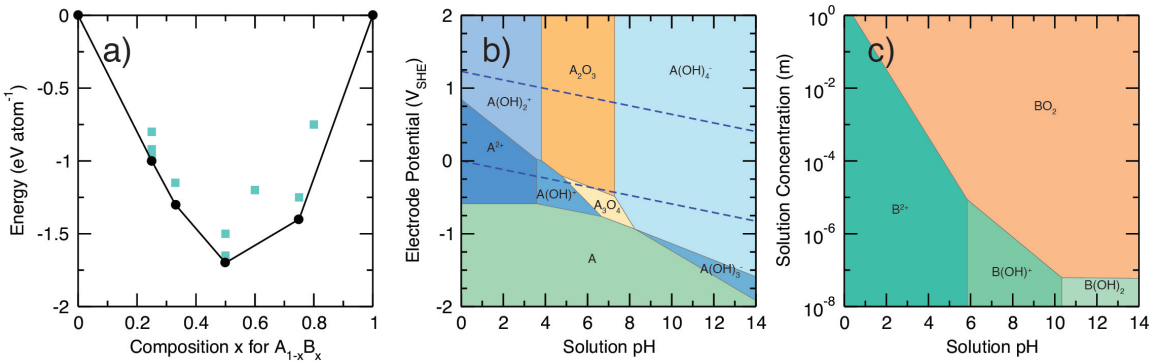

Figure 2.1. Thermodynamic models for A-B materials stability. (a) A composition-energy convex hull for the A-B composition family. Stable compositions are shown by black circles connected by the solid black hull line (at 0%, 25%, 33%, 50%, 75%, and 100% B). Meta and unstable phases appear as teal squares. (b) Pourbaix diagram of element A. Regions for electrochemically stable aqueous ions (blues), elemental A (green), and solid oxides (oranges) are shown within and outside the dotted water stability lines at varying pHs and electrode potentials. (c) Aqueous ion concentration-solution pH stability diagram of element B. The diagram is dominated by a large BO_2 stability region (salmon), with B(II) species appearing at very low ion concentrations and more prominently at acidic pHs (teals).

The core of each dissertation project presented herein lies in utilizing thermodynamic models sourced from density functional theory (DFT) calculation outputs to understand materials formation in aqueous environments. At the outset of these works, the consideration of free energies of formation ($\Delta_f G$) calculated from DFT was found to yield highly physical results [4, 27, 44]. Furthermore, DFT-sourced $\Delta_f G$ sets allow us to form consistent and predictive models with energies for materials not yet synthesized or whose thermodynamic data have not been reported. Previously, thermodynamic phase diagrams had already found some success in predicting materials formation as found in key publications, including for magnesium oxide and delafossite $CaGaO_2$ [37, 45-50]. In fact, past work in our group has established the use of Pourbaix diagrams to accurately predict scale-dependent aqueous thin film formation for nickle (hydr-)oxides [21, 27]. We focus on numerous aspects of utilizing thermodynamic and electrochemical models, including system complexity, diagram creation efficiency, and energetic sourcing.

2.1. Energy Sourcing

The accuracy of general thermodynamic phase diagrams relies on careful sourcing of the Gibbs free energies of formation ($\Delta_f G$) to calculate reaction chemical potentials. However, challenges in thermodynamic data sourcing have historically limited the creation of phase diagrams. Traditional techniques to find the $\Delta_f G$ values of solids include combustion calorimetry, which has been associated with significant errors [1, 3, 4, 6, 27]. Previous studies have found that materials or compounds that are prone to sample defects, such as NiO, often lack precise experimentally determined free energies of formation [27]. In other cases, the DFT formation energies are preferred to create an accurate version of shallow convex hulls or when there is a lack of experimental data across a composition or material family [27, 44]. In comparison, these studies also found success using $\Delta_f G$ values generated from bulk first-principles calculations, which allow for ideal sample analysis and meticulous control over simulation quality [4, 27, 44]. We note that thermodynamic modeling literature largely relies on experimentally-sourced free energies of formation aqueous ions, as the $\Delta_f G$ values of aqueous ions are computationally intensive to calculate. Moreover, experimental techniques for aqueous ions are associated with much smaller errors than solid state formation energy methods [4]. Herein, we chose to utilize solid $\Delta_f G$s sourced from DFT to further benchmark their use for thermodynamic models, and out of necessity in the case of synthesis projects where target phase free energies of formation are not reported.

A key consideration when creating thermodynamic data sets from DFT calculations is the level of theory necessary to sufficiently describe the energetics of the materials family. In order to benchmark this, scientists will often examine how well described other known properties of the phase are, including lattice constants, formula unit volume, dynamic stability, and electronic behavior. Input parameters in DFT and density functional approximations control how precisely the model can replicate the system. In other words, scientists may choose to include more accurate functionals, spin orbit coupling, van der Waals effects, and U additional on site electron-electron interactions in the model. Proper choice of DFT inputs and convergence criteria often yields relatively accurate energies for reasonable resource and time costs.

2.2. Convex Hull

Convex hulls are a field standard within computational materials science work to understand stability, ground state compositions, and potential decomposition phases. Convex hulls were originally introduced to broad materials science literature in the 1990s for structure selection and stability [34, 35]. Since, they have been utilized in high throughput DFT databases and countless works have implemented them to describe ground state phases for a given composition range. Moreover, convex hulls are used to describe how metastable a material may be, *i.e.*, how energetically far a material is above the hull. Figure 2.1a shows a convex hull for an A-B element system. Ground state phases, displayed as black circles, include A, A_3B, A_2B, AB, AB_3, and B. Included metastable and unstable phases, teal squares, are any phases above the solid black hull line. Metastable phases at the same composition as a ground state phase represent a material which might occur through a phase transition from the ground state to another structure. Convex hulls can be used to as a metric for synthesizability by reporting if the material is on or near the hull [51, 52]. Moreover, DFT-sourced free energy of formation data sets can be benchmarked against others with different calculations inputs, and against experimental sets, through visualizing the convex hulls.

2.3. Pourbaix Diagrams

A commonly constructed model for aqueous materials formation is the electrochemical pH-potential phase diagram (Pourbaix diagram) depicting phase stability under varying solution pH and electrode potential [1]. In other words, Pourbaix diagrams depict thermodynamic stability of a compound and its competing solid

oxides, solid hydroxides, or soluble ions in aqueous solution as a response to changes in pH and applied electrode potential. Pourbaix diagrams are useful tools to understand redox active thermodynamic species in a hydrothermal or corrosion reaction. Diagrams are typically reported at the standard corrosion limit [1] of 10^{-6} aqueous ion activity and standard state temperature and pressure. The standard hydrogen electrode (SHE) is typically chosen as the reference electrode potential. Figure 2.1b shows an example pH-potential diagram of element A. The green region, existing at negative potentials and a range of pHs below approximately 14, is typically considered the immunity region. Here, the element or alloy should not oxidize or solubilize, and is thus considered stable in water. Solid oxidation regions, shown as two orange regions, indicates that a solid oxide or hydroxide scale should form on the surface of A. To engineer passivation, where oxide barriers can prevent further oxidation and solubilizing of an element, one will typically target the formation of a nonporous solid oxide region. Blue regions represent conditions where A should solubilize; thus, these are considered corrosion regions. Water stability regions are typically visualized, here with dotted blue lines. Above and below the lines water will oxidize and reduce, respectively. While the diagram here is shown only for element A, electrochemical diagrams can be extrapolated out to multiple elements following Gibbs' phase rule [33], as elucidated in W.T. Thompson *et al.* [53]. We note Pourbaix diagrams are thermodynamic in origin, and therefore do not take into account kinetics effecting reaction evolution. Nonetheless, these predominance diagrams are often used to understand how many variables interact to influence materials formation within aqueous systems.

2.4. Stability Diagrams

Stability diagrams presented within this work typically refer to solution pH versus aqueous ion concentration thermodynamic predominance diagrams [54, 55]. However, the broad name can be applied to aqueous predominance diagrams where other thermodynamic parameters vary. Stability diagrams have historically been leveraged to identify processing conditions for synthesis, including reactant concentration and pH [56]. Similarly to Pourbaix diagrams, standard state conditions are typically invoked. An applied potential of 0 V versus the standard hydrogen electrode can be assumed if none is specified. It should be noted that nonstandard state diagrams, particularly those where temperature is varied, should report aqueous ion concentrations in molality rather than molarity due to its invariance with pressure and temperature changes.

Figure 2.1c shows a typical stability diagram for element B. The salmon colored BO_2 represents a solid oxide phase, analogous to the potentially passivating scales formed in the orange Pourbaix diagram regions. There is a clear concentration and pH dependence of the solid region, as the stability of the solid is limited by low pH and low concentration of B ions in solution. At low concentrations, aqueous ions dominate within the green/teal corrosion regions. The B(II) hydrolysis series show B^{2+} stable at $pH < 6$, $B(OH)^{+}$ stable between approximately $6 < pH < 10$, and $B(OH)_2$ stable at $pH > 10$. Within pH-concentration stability diagrams, solids are generally found to be stabilized at higher aqueous ion concentrations, and aqueous ions at lower concentrations, due to the $-RT\ln(\eta_I)$ solubility term contribution to the chemical potential.

2.5. Applications

Redox, dissolution, and hydrolysis reactions occurring when elements come into contact with water dictate many significant processes for every day life. Herein, we focus on two primary areas of research surrounding aqueous materials formation: corrosion and synthesis applications.

2.5.1. Corrosion

Materials lifetime in aqueous systems is often bound by degradation via corrosion. The U.S. alone lost approximately $276 billion USD in corrosion related costs in 1998 (estimated at approximately $477 billion in January 2022) [57], and some public health hazards from toxic materials sources such as lead can be tied back to significant uncontrolled corrosion. Corrosion and general aqueous degradation progresses through reduction-oxidation (redox) reactions, which can lead to dissolution of the metal or alloy to create aqueous ions in solution. The formation of a solid (hydr-)oxide can also form, potentially providing a passive layer that protects the original compound from harmful corrosion processes. However, the prediction of which oxides will occur and their relative ability to protect is challenging to know *a priori*. Myriad factors influence corrosion, including temperature, ion concentration, pH, potential, scale identity, and surface crystallographic orientation. Additional considerations include chemisorption of ions in solution, surface and subsurface composition, and short range order can influence which oxide scales may form and any diffusion processes associated with dissolution and oxidation. Models and simulations to understand the variety of factors

influencing the formation of materials occurring during aqueous degradation are imperative to prolong the lifetime of better infrastructure and applications.

2.5.2. Synthesis

The development of novel synthesis methodology, such as hydrothermal synthesis of a new material, remains a paramount challenge in chemistry and materials science. Many synthesis methods, and in particular hydrothermal synthesis, often rely on a trial-and-error approach to establish. During experimental design, variables within the experiment are changed, such as temperature, pressure, pH, potential, mineralizer, reactant ratios and concentrations, and more. Expedited methodology optimization has the potential to unlock an increased number of realized compounds, in part because hydrothermal synthesis is particularly suitable for metastable material generation [58-60]. Design rules and computational modeling of synthesis conditions are current areas of research promising accelerated synthesis development [61-63].

One approach towards achieving predictive hydrothermal synthesis, extendable to corrosion resistance engineering, uses first-principles derived thermodynamic models, and avoids undertaking kinetic processes simulations accessible from panoramic-based studies [62,64-66] aimed at integrating nucleation and crystallization pathways. Pourbaix [28,37,45-50] and stability [54-56,67-71] diagrams have been applied successfully in the past to predict synthesis conditions through understanding the thermodynamic stability landscape of stable species at given condition ranges. However, historic use of predominance diagrams extends primarily to single-component homoanionic materials (simple oxides). In one study, J.M.R. Genin *et al.* explained the formation of different iron "green rust" scales through multi-ion Pourbaix diagrams [37]. More recently, M. Bianchini *et al.* explored how free energy mapping throughout the reaction and thermodynamic phase diagrams could help to explain previously perplexing polymorph formation over target reactants in the $Na_{0.67}MO_2$ (M=Co, Mn) materials family [62]. Moreover, phase diagrams, are useful in identifying potential byproducts or potential secondary corrosion products to better explain why a synthesis might have failed [4]. Despite reported success on isolated systems, the computational challenges for developing thermodynamic models are distinct: accurate and accessible phase-stability models under realistic hydrothermal conditions that connect phase equilibria to process variables, which can be selected in the laboratory, *e.g.*, temperature, reactant concentrations, and pH.

A rise in computational resources allows for ease of calculating multi-element and increasingly complex diagrams that were not feasible decades ago. In this work, we will leverage computational resources to develop thermodynamic models for aqueous materials formation in a variety of contexts. Furthermore, we develop a parameter, the maximum driving force (MDF) to aid in quantitative comparisons of phase formation in aqueous systems for systems with differing elements or compositions.

CHAPTER 3

Methodology

Modern applications of phase diagrams were first proposed by J.W. Gibbs in 1876 [33]. These diagrams broadly describe the most stable system configuration given certain degrees of freedom. Modern theory development has included the use of this work to model myriad systems, and generalized the phase diagram such that it can be expanded to multiple system conditions not previously captured [72]. While there are numerous previously reported uses of thermodynamic phase diagrams, we use and advance phase diagrams for materials under aqueous environments. Examples of relevant diagrams include the Pourbaix, stability, and yield diagrams. Variations on these diagrams are also presented, including (maximum) driving forces and predominance diagrams. Literature published in the past decades has reinvigorated the use of these phase diagrams for predicting aqueous materials formation, chiefly within the fields of synthesis science and corrosion science. In both cases, we allow the metal to be in a time-independent two phase equilibrium, and only dependent on intrinsic system variables (*e.g.*, solution pH, temperature).

We adopt a number of additional different computational and thermodynamic tools to propose ranges on synthesis and stable phase formation conditions. Key among these are density functional theory (DFT) for thermodynamic data sourcing, the revised Helgeson-Kirkham-Flowers (HKF) method for energy extrapolation to higher temperatures, and the implementation of the maximum driving force (MDF).

3.1. Energetic Sourcing

Generalized phase diagrams and thermodynamic modeling of aqueous species formation rely on accurately sourced thermodynamic data. Generally, most methods within this work use the Gibbs free energy of formation ($\Delta_f G$) to find the chemical potential for condition-dependent phase stability. Entropy (S), heat capacity (C), and vibrational free energy (F_{vib}) terms are used for some temperature-dependent evaluations. These values may be sourced either from experiment or computation.

Experimentally sourced thermodynamic data can be found from databases and previously published literature. Key databases include the NBS Tables [8], NIST Janaf Tables [73], Lange's Handbook of Chemistry [9], the OBIGT database [74], and the CRC Handbook of Chemistry and Physics [3]. However, $\Delta_f G$s may also need to be sourced from primary reports. Typically, aqueous ion thermodynamic data is always gathered from experimental sources, due to generally acceptable energetic accuracy and the relatively high cost of computing these values from first principles. On the other hand, values for solids are often associated with larger variance experimentally. Additionally, it can often be challenging or impossible to find thermodynamic data published for some or all components of a materials system. Therefore, some studies resort to sourcing their (bulk) solid $\Delta_f G$s from computational models.

Bulk or scale-constrained (translationally variant) solids may be sourced from computational modeling with relatively lower resource cost. Specifically, static density functional theory (DFT) in combination with phonon calculations provide the electronic, zero point, and vibrational energy contributions to the $\Delta_f G$, allowing for the creation of accurate and self-consistent thermodynamic data sets. Structural information is the only *a priori* knowledge needed for potential phases formed, and is often sourced from experimental sources such as the Inorganic Crystal Structure Database [30] or from high throughput DFT databases [22-24]. Structural prediction software is available, and includes bulk symmetry prediction programs such as CALYPSO [75] or alloy and complex oxide prediction codes [76-86].

Below, we review the broad computation methods used to source $\Delta_f G$ energetic data in this dissertation: (*i*) DFT and (*ii*) lattice harmonics and vibrational energy calculations. Then, we review the complimentary extrapolation of aqueous ion energies to nonstandard state with the (revised) HKF method.

3.1.1. Density Functional Theory

Density functional theory (DFT) is a method of atomistic materials modeling utilizing an electron density found from the Khon-Sham equation [87, 88] as an approximation for the quantum mechanical many-body problem. DFT is widely used throughout the materials science and physics communities to simulate materials ground states, structural phase transitions, electronic and optical properties, and more. We here use it because free energies of formation computed from DFT have been found to be highly accurate [4, 89-91], and are easily employed for systems where no experimentally-determined values are reported.

The basis of DFT resides in the Schrödinger Equation

$$i\hbar\frac{\partial}{\partial t}\Psi(x,t) = \left[-\frac{\hbar^2}{2m}\frac{\partial^2}{\partial x^2} + V(x,t)\right]\Psi(x,t)\,, \tag{3.1}$$

where $\psi(x,t)$ is a wave function, $V(x,t)$ is the potential, m is the particle mass, $\hbar$ is Planck's constant, and x,t are space and time, respectively. This equation describes the evolution of the wave function of a quantum mechanical system, with respect to space and time, as a function of the environment. While Equation 3.1 can be resolved analytically for a single particle system with some effort, interacting many electron systems must include approximations to solve.

In DFT, many electron-electron interactions are approximated with a Kohn-Sham density functional. Explicitly, each electron's interactions with other electrons are calculated based on a local or semilocal form given the electron density [87, 88]. Ultrasoft pseudopotentials can approximate the contribution of core electron states with a plane wave basis method [92, 93]. The exchange and correlation effects can be approximated with a number of different functionals, including a local density approximation or a generalized gradient approximation, which take into account the local electron density (and its derivative). Treating many body systems as sums of self-consistent, single electron systems in electron gas potentials drastically decreases the complexity of the problem such that it is feasible to solve with current computational resources available to most researchers. Generally, choice of functional in this work is based on weighing computational costs with how close key properties are to experimentally sourced values, such as free energies of formation.

Electronic energy, a key property necessary for our work, is found through the following equation for the ground state energy, $E_{\text{tot}}[n_0]$:

$$E_{\text{tot}}[n_0] = \langle\psi[n_0]|\hat{T} + \hat{V} + \hat{U}|\psi[n_0]\rangle \tag{3.2}$$

where n_0 is the ground state electron density, $\hat{T}$ is the kinetic energy, $\hat{V}$ is the potential energy, and $\hat{U}$ is the electron-electron interaction energy. The exact ground state electron density is unknown, necessitating approximations such as the orbital-based Khon-Sham equation. To better understand contributions to the electronic energy, it can be helpful to divide $E[n_0]$ into energetic components as:

$$E_{\text{tot}}[n] = E_{\text{T}}[n] + E_{\text{V}}[n] + E_{\text{J}}[n] + E_{\text{X}}[n] + E_{\text{C}}[n] \tag{3.3}$$

where $E_T[n]$ is the total kinetic energy in terms of Kohn–Sham orbitals [88], $E_V[n]$ is the total potential energy due to Coulombic attraction to atomic nuclei, $E_J[n]$ is the potential energy due to Coulombic repulsion for electron pairs, $E_X[n]$ is the mechanical exchange energy for electronics, and $E_C[n]$ is the electron correlation energy [94]. This equation, derived from work by Pierre Hohenberg, Walter Kohn, and Lu Jeu Sham [87, 88], demonstrates that the minimum of the total electronic energy and other observable ground state properties are a functional of the electron density. Completion of DFT structural relaxation calculations, followed by a static calculation yields the electronic energy (E_e) from Equation 3.2. E_e is a principal contribution to $\Delta_f G$ shown in Equation 3.5, and can be roughly approximated with the 0 K enthalpic contribution.

Errors associated with DFT simulations occur from functional approximation, and from electron density approximation [95]. More accurate exchange and/or correlation effects can be obtained using the plus U method or hybrid functionals, though the latter leads to significant computational cost increases. We note that some hybrid functionals will explicitly calculate exact exchange interactions at the Fock level within a close range (typically a couple Ångstroms) [91]. These screened Coulomb, range-separated functionals balance computational accuracy with resource availability by treating exchange interactions that occur at distances beyond the cutoff with a semilocal density functional to lower computational cost.

For this collection of works, density functional theory calculations are performed with the Vienna Ab initio Simulation Package (VASP) [96-99]. Functionals at different levels theory are utilized to optimize solid-state structures and obtain the ground state formation energy for each composition. For different projects, we employ the local density approximation (LDA), the generalized gradient approximation (GGA) by Perdew-Burke-Ernzerhof (PBE), the Perdew-Burke-Ernzerhof generalized gradient approximation revised for solids (PBEsol), the strongly constrained and appropriately normed semilocal density functional metagga (SCAN), and the hybrid exchange-correlation functional (HSE06) [91, 100-105]. K-points are converged to at least 3,000 k-points per reciprocal atom (KPPRA) and implemented with a Γ centered mesh. Generally, Guassian smearing is used with a small smearing width of 0.1 eV or less to accurately obtain any band gaps. Moleculear geometries, such as the oxygen molecule and hydrogen molecule gas bonds, are relaxed within a 15×15×15 $Å^3$ simulation cell vacuum. The initial magnetic moments, *e.g.*, for materials like copper

(II) oxide and oxygen gas, were chosen based on experiment [106, 107]. Total energy is converged to 10^{-7} eV and forces are converged to 10^{-3} eV Å^{-1} or less during relaxations. An energy cutoff of 450-700 eV is used for all calculations based on convergence criteria. Nonspherical gradient corrections within the PAW spheres are included. When necessary, Van der Waals forces are considered for solids implemented using the Tkatchenko-Scheffler method with iterative Hirshfeld partitioning for LDA and GGA functionals in VASP [108]. Van der Waals corrections for SCAN are implemented with the revised Vydrov and Van Voorhis nonlocal functional (rVV10) [109] and with the DFT-D3 dispersion correction for HSE06 [110]. Specific DFT settings employed by results chapters can be found in the Appendix.

3.1.2. Lattice Dynamics Calculations

Phonon calculations are necessary to perform in order to obtain the vibrational entropy and zero point energy contributions to $\Delta_f G$. Furthermore, these calculations permit assesment of the dynamical stability of a considered phase. In these works, lattice dynamics calculations are performed with VASP, utilizing plane wave calculations with PBEsol [92, 93, 100, 101], and Phonopy softwares [111]. We generate small displacements (displacement amplitude = 0.01-0.03 Å) within supercells with the frozen phonon method utilizing the harmonic approximation [112]. We calculate thermodynamic data for solid species through statistical thermodynamics expressions implemented with Phonopy. Phonon calculations are used to find the vibrational energy, written as the Helmholtz free energy

$$F = -k_B T \ln(Z) = \phi + \frac{1}{2}\sum_{\mathbf{q}\nu}\hbar\omega(\mathbf{q}\nu) + k_B T \sum_{\mathbf{q}\nu}\ln[1 - \exp(-\hbar\omega(\mathbf{q}\nu)/k_B T)]\,, \tag{3.4}$$

where the expression is written in terms of the Boltzman constant k_B, phonon frequency ω, temperature T, general q-points in the Brillion zone $\mathbf{q}$, and Planck's constant $\hbar$ [111]. For standard state systems, we use vibrational energies at 298.15 K to approximate the room temperature vibrational contribution [44].

The formation energy of each solid species is then

$$\Delta_f G(T) = H(T) - TS(T) = E_e + F_{\text{vib}}(T)\,, \tag{3.5}$$

where $F_{\text{vib}}(T)$ and $TS(T)$ are temperature-dependent terms, and $F_{\text{vib}}(T)$ is found from phonon calculations and given by Equation 3.4. When considered nonstandard state conditions, the $F_{\text{vib}}(T)$ term for the required temperature is calculated. In this way, the temperature-dependent free energies of formation for solid species can be obtained via first principles calculations [111].

3.1.3. Revised Helgeson-Kirkham-Flower Method

The (revised) Helgeson-Kirkham-Flowers is used to extrapolate thermodynamic information for aqueous ions, including entropy and Gibbs free energies of formation, from standard to nonstandard state. The calculations encompassed within the revised portion of HKF method are for charge neutral aqueous ions. Here, we use it to find nonstandard state ΔG values for aqueous ions considered for phase diagrams.

The HKF method encompasses a collection of works published from the 1970s through the 1990s, including the select articles highlighted here [113-119]. Several studies use the revised HKF method to account for different thermodynamic behavior of ions in solution at nonstandard state, including for the use of Pourbaix Diagrams [2, 120, 121]. The method is founded on the basis that the change in behavior of a solution can be derived from the sum of its solvated and nonsolvated contributions, and approximates the size of the ion radius and its subsequent Born coefficient through experimental observations and fitted data. Further dependence of solution structure based upon changes to the dielectric constant and effective volume are documented with temperature and pressure changes. Several parameters and functions, including the g-function and the dielectric constant of water, have been well documented. The entropy, enthalpy, heat capacity, and therefore formation energies of solutions can be calculated at nonstandard state. We utilized the following equations, similar to those those used by B. Beverskog *et al.* and C.C. Binter [120, 122], to find the entropy and heat capacity at elevated temperatures.

We start with the equation for the formation energy of a species at nonstandard state:

$$\Delta \bar{G}^{\circ} = \Delta \bar{G}^{\circ}_{f} + (\bar{G}^{\circ}_{P,T} - \bar{G}^{\circ}_{P_r,T_r}), \tag{3.6}$$

where the difference $(\bar{G}^{\circ}_{P,T} - \bar{G}^{\circ}_{P_r,T_r})$ is related to our definition of the Gibbs formation energy, which is dependent on the entropy, heat capacity, volume, and pressure:

$$\bar{G}^{\circ}_{P,T} - \bar{G}^{\circ}_{P_r,T_r} = -\bar{S}^{\circ}_{P_r,T_r}(T - T_r) + \int_{T_r}^{T} \bar{C}^{\circ}_{P_r} dT - T\int_{T_r}^{T} \bar{C}^{\circ}_{P_r} d\ln(T) + \int_{Pr}^{P} \bar{V}^{\circ}_{T} dP\,. \tag{3.7}$$

In this study we assumed the $\int_{Pr}^{P} \bar{V}^{\circ}_{T} dP$ term, describing the change in volume in the system at different pressure, is negligible. We therefore need the nonstandard state heat capacity in order to calculate the change in formation energy. We also assume that the integrated heat capacity can be approximated by the average temperature of the heat capacity at the given temperature range.

The equation for partial molar heat capacity, $\bar{C}^{0}_{P}$, is shown below as a sum of its solvated (s) and nonsolvated (n) contributions.

$$\bar{C}^{0}_{P} = \Delta\bar{C}^{0}_{P,n} + \Delta\bar{C}^{0}_{P,s}\,. \tag{3.8}$$

This ultimately gives us the final equation for the standard partial molal heat capacity as:

$$\begin{aligned}\bar{C}^{0}_{P} = \quad & c_1 + \frac{c_2}{(T-\Theta)^2} - \left(\frac{2T}{(T-\Theta)^3}\right) \times \left(a_3(P - P_r) + a_4 \ln\left(\frac{\Psi + P}{\Psi + P_r}\right)\right) \\ & + \omega T X + 2TY\left(\frac{\partial \omega}{\partial T}\right)_P - T\left(\frac{1}{\epsilon} - 1\right)\left(\frac{\partial^2 \omega}{\partial T^2}\right)_P\,,\end{aligned} \tag{3.9}$$

where $\bar{C}^{0}_{P}$ is given as a function of temperature and pressure. It accounts for changes in temperature and pressure through the inclusion of the dielectric constant and its dependent terms, the Born coefficient, and the coefficients of equations of state. The nonstandard state temperature and pressure are given by T and P respectively. Θ and Ψ are solvent parameters equal to 228 K and 2800 bar. Implementation of these equations yields the standard molar heat capacity at elevated temperatures and pressures.

We show the $\Delta\bar{C}^{0}_{P}$ is dependent upon parameters c_1, c_2, a_3, a_4, Z, and ω. Additional equations of state coefficients a_1 and a_2 are used for the approximation of other properties like nonstandard state entropy, but are not needed for this study. The values for the equations of state coefficients are derived from experiment, and are given in a variety of works [114, 115, 123]. In the case where parameters were not given, the coefficients were approximated by the coefficients provided for structurally and electronically similar ions found in works by E.L. Shock and H.C. Helgeson, particularly when modeling anionic copper complexes [114, 115, 118]. We

point out that the cuprite and cuprous hydrolysis series found to be stable in largely basic conditions, such as $Cu(OH)_3^-$ and $Cu(OH)_4^{2-}$, can also be written as the $HCuO_2^-$ and CuO_2^{2-}.

The series of ω and its partial derivatives with respect to temperature are given below, with a dependence on the g-function.

$$\omega_j = \omega_{e,j} - Z\omega_{H^+}\,, \tag{3.10}$$

$$\omega_j^{\text{abs}} = \frac{N^0 e^2 Z_j^2}{2r_{e,j}} = \frac{\eta_j^2 Z_j^2}{r_{e,j}}\,, \tag{3.11}$$

$$\omega_{e,j} = \frac{Z_{e,j}^2 \eta}{r_{e,j}}\,, \tag{3.12}$$

where Z is the formal charge on the ion, N is Avagadro's number, e is the absolute electronic charge equal to 4.80298×10^{-10} esu, and η is equal to 1.66027×10^5 Å cal/mol. An important point to note that neutral ions are often found to still behave as a charged ion in solution, but the revised HKF method for neutral atoms does not define a formal charge for these species. Values in the original works were found from experimental extrapolation exclusively. In this work, we define Z as 0 for electronically neutral ions, and extrapolate reported values for structurally similar ions to our own species. The value $\omega_{H}+$ is the Born coefficient of the H^+ ion, equal to approximately 5.387×10^4 cal/mol (225.4 kJ/mol) at standard state [115]. The effective radii of the j^{th} ion, $r_{e,j}$ is defined as

$$r_{e,j} = r_{x,j} + |Z_j|(k_z + g)\,, \tag{3.13}$$

where $r_{x,j}$ is the crystallographic radius of the ion, k_z is a charge dependent constant defined as 0.94 for cations and 0.0 for anions [114], and g is the g-function characterized in J.C. Tanger *et al.* [118]. The values of the g function are reported in E.L. Shock *et al.* and further in this section [123].

To calculate the C_p^0 value, we find the partial derivatives of the Born coefficient with respect to temperature. These are defined below, where each partial derivative similarly relies on the g-function and its partial derivatives:

$$\left(\frac{\partial\omega}{\partial T}\right) = -\eta\left[\frac{\text{abs}(Z^3)}{r_e^2} - \left(\frac{Z}{(3.082+g)^2}\right)\right]\left(\frac{\partial g}{\partial T}\right)_P^2\,, \tag{3.14}$$

$$\begin{aligned}\left(\frac{\partial^2\omega}{\partial T^2}\right) = 2\eta&\left[\frac{\text{abs}(Z^4)}{r_e^3} - \left(\frac{Z}{(3.082+g)^3}\right)\right]\left(\frac{\partial g}{\partial T}\right)_P \\ &-\eta\left[\frac{\text{abs}(Z^3)}{r_e^2} - \left(\frac{Z}{(3.082+g)^2}\right)\right]\left(\frac{\partial^2 g}{\partial T^2}\right)_P^2\,.\end{aligned} \tag{3.15}$$

We point out that the g-function, while defined elsewhere, was defined and then fit with a power series in J.C. Tanger *et al.* [118], and later E.L. Shock *et al.* [123]. As discussed in [123], the g-function is a solvent function that describes the effective electrostatic radii of pressure and temperature dependence of the solvent, in this case water [118]. We define it below:

$$g = a_g(1-\hat{\rho})^{b_g}\,, \tag{3.16}$$

$$a_g = a_1 + a_2 T + a_3 T^2\,, \tag{3.17}$$

$$b_g = b_1 + b_2 T + b_3 T^2\,. \tag{3.18}$$

Here, a_i and b_j are parameters given in a variety of texts, T is temperature, and $\hat{\rho}$ is the density of water divided by $1\,\frac{\mathrm{g}}{\mathrm{cm}^3}$ [122]. Qualitative trends and descriptions of the g-function can be found in [123].

The partial derivatives of the g-function with respect to temperature, at constant pressure, are necessary to find the final dependence of the Born coefficient on temperature, are shown below. Explicit values of the partial derivatives at different pressures and temperatures are found in [123]

$$\left(\frac{\partial g}{\partial T}\right)_P = g\left[\frac{\hat{\rho}\alpha b_g}{1-\hat{\rho}} + (b_2 + 2b_g T)\ln(1-\hat{\rho}) + \frac{a_2 + a_3 T}{a_g}\right], \tag{3.19}$$

$$\begin{aligned}\left(\frac{\partial^2 g}{\partial T^2}\right)_P = g\Bigg[&\frac{\hat{\rho}\alpha b_g}{1-\hat{\rho}}\left[\frac{2(b_2+2b_3T)}{b_g} + \frac{1}{\alpha}\left(\frac{\partial \alpha}{\partial T}\right)_P - \alpha - \frac{\hat{\rho}\alpha}{(1-\hat{\rho})}\right] \\ &+2b_3\ln(1-\hat{\rho}) + \frac{2a_g a_3 - (a_2+2a_3T)^2}{a_g^2}\Bigg] + \frac{1}{g}\left(\frac{\partial g}{\partial T}\right)_P^2\,,\end{aligned} \tag{3.20}$$

where α is the coefficient of thermal expansion for water.

Also necessary for the calculation of $\bar{C}_p^0$ are X, Y, and Z, which allow for the changes in the dielectric behavior of water, including its ability to stabilize solvents as temperature and pressure varies. We note that the Z in this case is dependent upon the dielectic constant of water, and is not the ion's formal charge. The definitions of X, Y, and Z are below, where ϵ is the dielectric constant of water:

$$Z = -\frac{1}{\epsilon}\,, \tag{3.21}$$

$$Y = \left(\frac{\partial Z}{\partial T}\right)_P = \left(\frac{1}{\epsilon^2}\right)\left(\frac{\partial \epsilon}{\partial T}\right), \tag{3.22}$$

$$X = \left(\frac{\partial Y}{\partial T}\right)_P = \left(\frac{1}{\epsilon^2}\right)\left(\frac{\partial^2 \epsilon}{\partial T^2}\right) - \left(2\epsilon Y^2\right), \tag{3.23}$$

Several researchers have documented the values of X, Y, and Z at a range of pressures and temperatures, including E.L. Shock *et. al.* [123].

Water's dielectric constant variation based on temperature, pressure and density has been well documented [122, 124].

$$\epsilon = \sum_{k=1}^{5} c_k D_w^{k-1}, \tag{3.24}$$

where c_k are fitting parameters for the density of water, given as D_w.

Therefore, the first and second partial derivatives with respect to temperature of Z used to calculate the Y and X functions are found to be:

$$\left(\frac{\partial \epsilon}{\partial T}\right)_P = \sum_{j=0}^{4} D_w^j \left[\left(\frac{dc}{dT}\right)_{j+1} - j\alpha c_{j+1}\right], \tag{3.25}$$

$$\left(\frac{\partial^2 \epsilon}{\partial T^2}\right)_P = \sum_{j=0}^{4} D_w^j \left[\left(\frac{d^2 c}{dT^2}\right)_{j+1} - j\left(\alpha\left(\frac{dc}{dT}\right)_{j+1} + c_{j+1}\frac{d\alpha}{dT}\right) - j\alpha\left(\left(\frac{dc}{dT}\right)_{j+1} - j\alpha c_{j+1}\right)\right]. \tag{3.26}$$

These equations are founded on established changes in the dielectric constant of water with respect to temperature and pressure. Needed to implement these equations are the coefficient of thermal expansion, α and its respective derivatives, which can be found in a variety of sources [113, 114, 117].

The thermodynamic behavior found for our studies should be viewed to be trends for the aqueous ions considered, and is not claimed to be exact values of the formation energies of these species at higher temperatures. We find agreement between our calculated entropies and heat capacities to those calculated by B. Beverskog *et al.* [121]. This approximation method for the formation energy temperature and pressure dependence also has been used in other works with success [119].

3.2. Phase Diagram Creation and Thermodynamics-based Analysis Tools

Phase diagrams and figures made from thermodynamics based analytics can be valuable tools to understand phase formation. To account for the multiple degrees of freedom (aqueous) environments allow for, countless

diagram types may be created. Here, we detail the creation of some of the main phase diagrams and tools used in these works.

3.2.1. Pourbaix Diagram

Pourbaix diagrams were first proposed by Marcel Pourbaix [1] to provide insight into aqueous redox corrosion reactions. Pourbaix diagrams are also commonly referred to as aqueous electrochemical diagrams and pH-potential diagrams. These figures illustrate the most stable phase(s) for a range of solution pHs and electrode potentials at a given temperature, pressure, and aqueous ion concentration. An example of a copper Pourbaix diagram is shown in Figure 7.1a, and contains all of the primary aspects of a typical diagram, including pH and potential-dependent stable elemental states (teal), solid oxide formation representative of copper scales (blues), and corrosive, soluble aqueous ions (oranges). While initially developed to understand corrosion, Pourbaix diagrams have more recently been framed to understand hydrothermal synthesis [63, 67].

Here, Pourbaix diagrams are created following methods originally implemented in a number of sources [1, 44, 53, 125]. Diagrams are calculated at standard state and at the standard corrosion limit of 10^{-6} solution activity (η_I) set by M. Pourbaix [1] except where specified. $\eta_I = 10^{-8}$ typifies many applications where low ion concentrations are expected, such as piping, refrigeration, and many plating applications [121]. $\eta_I = 10^{-2}$ or more represents solutions of high concentrations, more typical of synthesis environments. The ideal solution approximation ($\eta \approx$ concentration) is assumed except where specified. Approximations to account for nonideal solution effects are detailed in Section 3.2.1.1.

The electrode potential in solution is reported in reference to the standard hydrogen electrode (E_{SHE}), which is 0 V at pH = 0 at all temperatures. The temperature- and pressure-dependence of E_{SHE} is described through the following water redox reactions and Nernst equation:

$$2\mathrm{H}^+ + 2e^- \rightarrow \mathrm{H}_{2(\mathrm{g})}\,, \tag{3.27}$$

$$\mathrm{O}_2 + 4\mathrm{H}^+ 4e^- \rightarrow 2\mathrm{H}_2\mathrm{O}\,, \tag{3.28}$$

$$E = -\frac{2.303RT}{F}pH - \frac{RT}{2F}\ln\frac{p_{\mathrm{H}_2}}{p^0}\,, \tag{3.29}$$

where E is the potential in (V), and p^0 and $p_{\mathrm{H_2}}$ are the standard pressure and partial pressure of hydrogen in (Pa), respectively. While temperature change is allowed to modify the oxidation and reduction lines of water, we assume that the partial pressure of hydrogen does not vary substantially with temperature unless otherwise specified, and therefore do not include an explicit variation of it. The lines in the diagrams presented for water stability denote the oxygen evolution reaction (OER) and the hydrogen evolution reaction (HER), respectively. An important consideration for corrosion prediction can be excess O_2 or H_2 gas in solution, which can lead to stress corrosion cracking, and nonuniform corrosion. Explicit inclusion of gaseous species evolution will change the stability regions of species above and below the OER and HER lines [**126**].

$\Delta_f G$s for all species, solids and aqueous ions, were used to assess the chemical potentials of formation ($\Delta\mu$) at specific pH-potential (pH, U) points. In a single element system, the formation of a solid (hydr)oxide $\mathrm{M}_x\mathrm{O}_y\mathrm{H}_z$ is described using a generalized redox reaction of water with metal M as

$$X\mathrm{M} + Y\mathrm{H_2O} \rightarrow \mathrm{M}_x\mathrm{O}_y\mathrm{H}_z + (2Y - Z)e^- + (2Y - Z)\mathrm{H}^+ , \tag{3.30}$$

where X, Y, and Z provide stoichiometric mass balance. Then, the chemical potential ($\Delta\mu_{\mathrm{solid}}$) for the formation of a solid phase, *e.g.*, $\mathrm{M}_x\mathrm{O}_y\mathrm{H}_z$, from the reaction of water with its respective metal is

$$\begin{aligned}\Delta\mu_{\mathrm{M}_x\mathrm{O}_y\mathrm{H}_z} = \big(&\Delta_f G_{\mathrm{M}_x\mathrm{O}_y\mathrm{H}_z} - (2Y - Z)\cdot FU - (2Y - Z)\cdot RT\ln(10)\cdot \mathrm{pH} \\ &- X\cdot\Delta_f G_{\mathrm{M}} - Y\cdot\Delta_f G_{\mathrm{H_2O}}\big)/N ,\end{aligned} \tag{3.31}$$

where R is the ideal gas constant, T is the temperature, F is Faraday's constant, and N is the total number of metal elements per formula unit (here $N = X$).

Corrosion occurs through the solubilization of the solid and subsequent formation of aqueous ions $[\mathrm{M}_x\mathrm{O}_y\mathrm{H}_z]^{\delta}_{(\mathrm{aq})}$, shown below:

$$X\mathrm{M} + Y\mathrm{H_2O} \rightarrow [\mathrm{M}_x\mathrm{O}_y\mathrm{H}_z]^{\delta}_{(\mathrm{aq})} + (2Y - Z + \delta)e^- + (2Y - Z)\mathrm{H}^+ . \tag{3.32}$$

The reaction chemical potential to form the aqueous ion $\Delta\mu_{\text{aq. ion}}$ is therefore

$$\Delta\mu_{[\mathrm{M}_x\mathrm{O}_y\mathrm{H}_z]^{\delta}_{(\mathrm{aq})}} = \big(\Delta_f G_{[\mathrm{M}_x\mathrm{O}_y\mathrm{H}_z]^{\delta}_{(\mathrm{aq})}} + RT\ln(\eta_I) - (2Y - Z + \delta)\cdot FU \\ - (2Y - Z)\cdot RT\ln(10)\cdot \mathrm{pH} - X\cdot\Delta_f G_{\mathrm{M}} - Y\cdot\Delta_f G_{\mathrm{H_2O}}\big)/N\,, \tag{3.33}$$

where δ is the oxidation state and η_I is the solute activity. The first two terms of Equation 3.33 show that the chemical potential contributions to the aqueous ion include both its free energy of formation and some measure of solvation captured by the solute activity. Solid species with high solubility or that react with water are excluded from consideration. $RT\ln(\eta_I)$ is minimal at room temperature but increases substantially at elevated temperatures. It begins to dominate the chemical potential of aqueous ions as temperatures approach 300 °C when $RT\ln(\eta_I)$ decreases to below -0.6 eV at the typical corrosion limit.

To formulate the phase diagram, the intrinsic variables pH and potential are parametrically varied within a given set of conditions. Chemical potentials are enumerated at each pH, potential point, and then the most stable species with the most negative chemical potential is shown on the diagram. Phase boundaries therefore exist in lines or at triple points where the chemical potentials of two or three species are equal, respectively.

3.2.1.1. Nonideal Solution Effects. Nonideal solution effects are relevant any time the activity coefficient γ deviates from unity. The solution activity, sometimes referred to as the effective concentration, is designated within $\eta = \gamma\cdot c$, where c is the solution concentration. In ideal solutions, $\gamma = 1$ and therefore the solution activity and concentration are equal. Phase diagrams utilize solution activity, though most work will apply the ideal solution approximation and assume that $\eta = c$. The ideal solution approximation is most accurate for solutions at small concentrations. Other factors that more strongly introduce non-ideal effects include bulky ions, high absolute value of ion charges, and poorly soluble ions. Generally when constructing aqueous phase diagrams at concentrations higher than the standard corrosion limit ($\eta > 10^{-5}$ or 10^{-6}), it might be beneficial to apply straightforward calculations of γ to account for non-ideal solution effects, though this is an approximation made by the author and not the field standard.

It was necessary to approximate γ to more consistently represent solution activity across the wide range of concentrations considered for some studies in this work. We estimate γ through the Bromley equations when $c \leq 0.5$ m. Above this, a modified Debye-Hückel equation is used following the Robinson-Stokes

model [127]. Other approximations, including the general Debye-Hückel, may be used instead based on reported experimental data, resources, and needed accuracy of fit. We perform these calculations based on the work of L.A. Bromley [128], L.A. Bromley *et al.* [129], and R.H. Stokes *et al.* [127], and with some notation borrowed from M.M. Łenka *et al.* [67]

At moderate concentrations ($c \leq 0.5\,\mathrm{m}$), we can express the logarithm of the activity coefficient, $\log(\gamma)$, as dependent on the Debye-Hückel equation with an additional fitting term, BI:

$$\log\gamma_i = \frac{-A_y|z_+z_-|I^{1/2}}{1+I^{1/2}} + m_j\left[\frac{|z_i|+|z_i|}{2}\right]^2\left(\frac{(0.06+0.6B)|z_iz_j|}{(1+\frac{1.5I}{z_iz_j})^2} + BI\right) \tag{3.34}$$

where z_+ and z_- are the charge on the aqueous anions and cations in an electrolyte, A_y is the temperature-dependent Hückel coefficient, I is the ionic strength, m_j is the molality of oppositely charged species, and B is a temperature and ion dependent parameter to describe ion-ion interactions. B is constructed as

$$B = B_+ + B_- + \delta_+\delta_-\,, \tag{3.35}$$

where values for B_+, B_-, δ_+, and δ_- for each of the cations and anions, respectively, in an electrolyte are found from experiment (see L.A. Bromley [128] for many common ions) or approximated. We follow the standard from Bromley, where $B_{\mathrm{Na^+}} = 0.0$ and $B_{\mathrm{OH^-}} = -1.0$.

The model simulates long range ion-ion interactions with the first Debye-Hückel term. The summation is used to approximate short range ion-ion interactions based on the original Bromley equations and is considered the linear version of the Bromley-Zemaitis model, which neglects higher order polynomial terms [130]. We chose to neglect experimentally determined higher order terms because they are more challenging to find from past literature, and because the linear model has been shown to be successful in environments without incompletely ionized electrolytes, such as many sulfates and nitrates. Moreover, solution effect adjustments are typically smaller pieces of the total contributions of the aqueous ion chemical potential.

At high concentrations ($c \geq 0.5\,\mathrm{m}$), the logarithm of the activity coefficient, $\log(\gamma)$, is dependent on the adjusted Debye-Hückel equation introduced by the Robinson-Stokes model [127]:

$$\log\gamma_i = \frac{-0.5092|z_+z_-|I^{1/2}}{1+0.3286\,\text{å}\,I^{1/2}} - \frac{n}{\nu}\log a_w - \log\left[1-0.018(n-\nu)m\right] \tag{3.36}$$

where a_w is the activity of water, å is the mean nearest neighbor ion distance (set to 4 Å for all species), n is the hydration parameter, *i.e.*, the net number of coordinated water molecules for both cations and anions, and ν is the number of ions created by dissociating a single solvent molecule. At a given concentration, this method only relies on the experimental parameters å and n. This method may be used up to $I \approx 5\,\mathrm{m}$. The approximation of these constants (rather than being deduced from experiment) and calculating the activity of water for an ideal solution will introduce some error into the activity. We expect it to be small for the activity coefficient. The error should also be even smaller for the thermodynamic phase diagrams with this scheme in comparison to the full ideal solution approximation ($\gamma = 1$, $\eta_I = m$).

3.2.1.2. Solid Energetic Corrections. Energetic corrections are introduced by the authors [26] and elsewhere [28] for DFT-sourced data sets, which may be used if there is substantial deviation between DFT sourced and experimental sourced $\Delta_f G$s of a solid phase. An energetic correction term, $\mathrm{E_{correction}}$, may be found from DFT and experimental sources to ensure that experimental dissolution energy of solids is accurate. $\mathrm{E_{correction}}$, as part of the correct relative chemical potential (CRCP) scheme was proposed by K.A. Persson *et al.* [28] to combine aqueous ion and computational data efficiently. $\mathrm{E_{correction}}$ is calculated via the difference:

$$E_{\text{correction}} = (\Delta_f G_{\text{oxide, DFT}} - \Delta_f G_{\text{oxide, Exp}})/N\,, \tag{3.37}$$

Where the same solid oxide's free energies of formation are subtracted. N is equal to the number of metal atoms in each oxide. The $\Delta_f G_{\text{oxide, Exp}}$ may be substituted for a free energy of formation for the oxide sourced from a more accurate, higher level DFT-sourced free energy of formation, such as a hybrid functional [26].

Most Pourbaix diagrams have a number of stable solid oxidation phases, however, little literature exists on which solid to choose, and arguments could be considered for choice of an oxide which exhibits (*i*) the correction that is the smallest based on energy differences, (*ii*) the largest stability area given the condition ranges probed, and (*iii*) the lowest free energy of formation per atom. The work presented in this collection leverage use of the solid species with the largest stability area, but more research should be completed on the effect of this choice.

The formation energy for aqueous ions is corrected by:

$$\Delta_f G_{\text{aqueous ion, Calculated}} = \Delta_f G_{\text{aqueous ion, Exp.}} + N' \cdot E_{\text{correction}}\,, \tag{3.38}$$

for all aqueous ions with the same cation as the oxide. For polyatomic ions, N' is the number of cations per aqueous ion; otherwise, $N' = 1$. For multiple cation systems (such as a systems with a binary A-B alloy) oxides should be chosen for the A and B atom separately, and the energy difference correction applied separately to ions of different cations. Therefore, for an n-H_2O element Pourbaix diagram, there will be n different energy corrections that should be applied if the $E_{\text{correction}}$ method is utilized. Note that this correction is not defined for ions with multiple cation types.

3.2.1.3. Extension to Multi-Elements. Pourbaix diagrams can be extrapolated to multiple metal elements for intermetallic and alloy systems within a corrosion context, or a multiple element hydrothermal synthesis. We here utilize the concepts of W.T. Thompson *et al.* [53] to write the chemical potential for solid species and aqueous ions combinations at different pHs, applied potentials, and concentrations. We allow up to the number of cationic metal elements involved in the system to be the maximum number of stable phases considered at a given set of conditions. For example, in a ternary alloy, up to three solid oxidation products, solid elements, or aqueous ions may be considered to be the most stable (though less is also possible). This follows the field standard for Pourbaix diagram creation, which is derived from Gibbs' phase rule [33, 72]. In these multi-element systems, species combinations are only considered which can follow a mass balance constraint [53]. In other words, each diagram is given a overall percentage of each element in the system (*e.g.*, 20% M_1 and 80% M_2) where there is assumed to be an infinite reservoir of H_2O. Any set of products chosen must be able to have formation reactions mass balanced such that the overall composition of the system is preserved.

The generalized creation of a multi-element (hydr)oxide scale, $A_wB_xO_yH_z$, here written as an oxidation reaction from elements, is

$$WA + XB + YH_2O = A_wB_xO_yH_z + (2Y - Z)e^- + (2Y - Z)H^+ \tag{3.39}$$

where A and B are cations (often transition metal or group 13 or 14 p-block elements), and W, X, Y, and Z are balancing, stoichiometric coefficients. Then, the chemical potential for the formation of a solid species

from the reaction of water and its respective metal is written

$$\Delta\mu_{\mathrm{A_wB_xO_yH_z}} = (\Delta_f G_{\mathrm{A_wB_xO_yH_z}} - (2Y - Z)\cdot FU - (2Y - Z)\cdot RT\ln(10)\cdot pH - W\cdot\Delta_f G_{\mathrm{A}} - X\cdot\Delta_f G_{\mathrm{B}} - Y\cdot\Delta_f G_{\mathrm{H_2O}})/N \tag{3.40}$$

where N is the total number of metal elements per formula unit (here equaled to $W + X$).

For aqueous ions in an A-B-H_2O system, we write the reaction of the elements leaving the solid and undergoing solubilization as

$$WA + XB + YH_2O = A_wO_{y'}H_{z'}^{\delta'} + B_xO_{y''}H_{z''}^{\delta''} + (2Y - Z + \delta' + \delta'')e^- + (2Y - Z)H^+ \tag{3.41}$$

where $\mathrm{A_wO_{y'}H_{z'}^{\delta'}}$ are the $\mathrm{B_xO_{y''}H_{z''}^{\delta''}}$ ions formed, and δ' and δ'' are the ionic charges. We note that $Y' + Y'' = Y$ and $Z' + Z'' = Z$. Then, the reaction chemical potential is

$$\Delta\mu_{\mathrm{A_wO_{y'}H_{z'}^{\delta'}+B_xO_{y''}H_{z''}^{\delta''}}} = ([\Delta_f G_{\mathrm{A_wO_{y'}H_{z'}^{\delta'}}} + RT\ln(\eta_A)] + [\Delta_f G_{\mathrm{B_xO_{y''}H_{z''}^{\delta''}}} + RT\ln(\eta_B)] - (2Y - Z + \delta' + \delta'')\cdot FU - (2Y - Z)\cdot RT\ln(10)\cdot pH - W\cdot\Delta_f G_{\mathrm{A}} - X\cdot\Delta_f G_{\mathrm{B}} - Y\cdot\Delta_f G_{\mathrm{H_2O}})/N\,. \tag{3.42}$$

Then, in this two element system, combinations of up to two aqueous ions, elements, and oxidized solids are considered (which can fulfill the mass balance constraint) to find the species combination which yields the lowest chemical potential at specific pH, potential points.

The above equations can be extrapolated to more elements as long as additional mass balance and species number constraints can be fulfilled. However, efficiencies in creating and reading diagrams are ideal for three or more elements, and required for five or more [131].

3.2.1.4. Solid Phase Filtration Choices for Improvement in Pourbaix Diagram and MDF Calculations. Solid filtration methods are often necessary to preserve the physicality of reported thermodynamic models when applied to real aqueous materials formation. Moreover, filtering solids can increase calculation efficiency. Filtration refers to phase inclusion, and systematic methods of filtering or removing unphysical phases that should not form from consideration. Here, we briefly compare different filtration methods

associated with currently available filters (PyMatgen module PourbaixDiagram, version v2022-0-11), and our reasoning for our own solid filtration methodology leveraged in Chapter 7.

For a single metallic element M-O-H system, the widely used high throughput DFT database Materials Project [25] can contain over 100 different solid entries. This includes entries with the same composition as well as moderately adjusted compositions not commonly seen in experiment. In order to increase program execution efficiency and prevent unphysical, highly oxidized or reduced phases from appearing, the "PourbaixDiagram" module in pymatgen and the Materials Project [132-134] uses a solid filter that places all the entries into a convex hull and selects only those on the thermodynamic hull, thus limiting the number of chemical potential calculations necessary. This method prioritizes calculation efficiency only, and can remove vital experimentally-found compounds like CoO_2 and Ni_3O_4 from consideration when comparing driving force planes.

Within Chapter 7, we implement our own filter that checks for oxidation states stable in water, removes hydrides (often reactive in most aqueous conditions), and selects the most stable entry per composition. In doing so, we attempted to ensure that solid phases are only considered for visualizing thermodynamically stable elements which are stable in water. The final selection criteria, stability per composition, aides in computational feasibility. Other works herein implicitly employ the above filtration criteria through thermodynamic data set construction.

Figure 3.1 shows the range of compounds which a negative (stable) driving forces within a wide condition window of -2≤pH≤16 and applied potential between -3 V ≤ V_{SHE} ≤ 3 V. Without any solid phase filter, hydrides like CoH_3 and NiH_3 have extremely negative driving forces, indicating thermodynamic stability. This is an unphysical result to report because transition metal hydrides are generally unstable and react vigorously with water in most aqueous conditions [135]. Therefore these phases are not practical to report as solid phase scales that should form in aqueous conditions. In the cobalt and nickel systems, both our and MP's filters do not allow hydride formation. Moreover, our filter includes a wide range of solid oxide candidates, such as CoO_2, while preventing specific unrealistic compositions from appearing, such as NiO(OH).

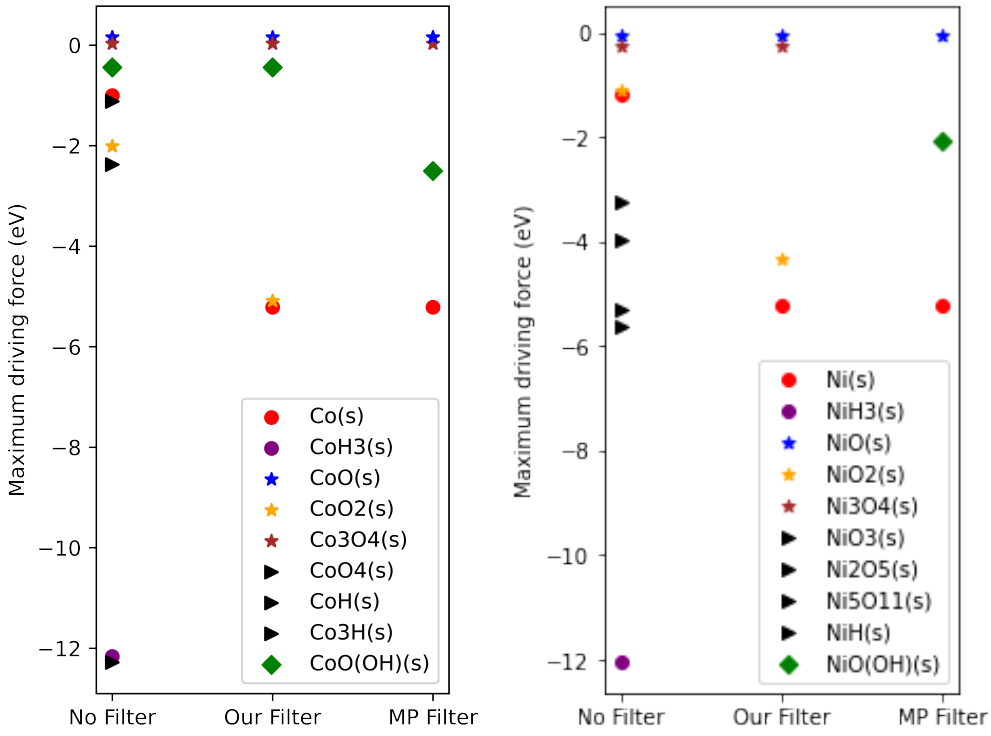

(a) Co system (b) Ni system

Figure 3.1. Comparison of MDFs across Ni and Co systems with different solid filters. Cobalt and nickel hydrides are shown to be the most thermodynamically stable if included, leading to an unphysical model for solid materials formation. While our model and Materials Project (MP) predict both $Co_{(s)}$ and $Ni_{(s)}$ to have the highest thermodynamic driving forces for formation, the second most stable solid, an oxide, in both systems is distinct for different filtration choices.

Figure 3.2 shows how drastically the Ni Pourbaix diagrams can change by implementing a solid phase filter. Common nickel oxides like NiO_2 and Ni_3O_4 are included with our filter while making sure compounds not often observed in experiment like Ni_5O_{11}, NiH, and NiH_3 are omitted from consideration.

3.2.2. Generalized Stability and Yield Diagrams

Stability diagrams typically refer to more generalized aqueous, thermodynamically-based predominance phase diagrams. Traditionally, stability diagrams compare solution pH to solution concentration/activity, however, these diagrams may be allowed to vary with mineralizer amount added, temperature, pressure, or other environmental variables. Stability diagrams are often used to identify experimental conditions that

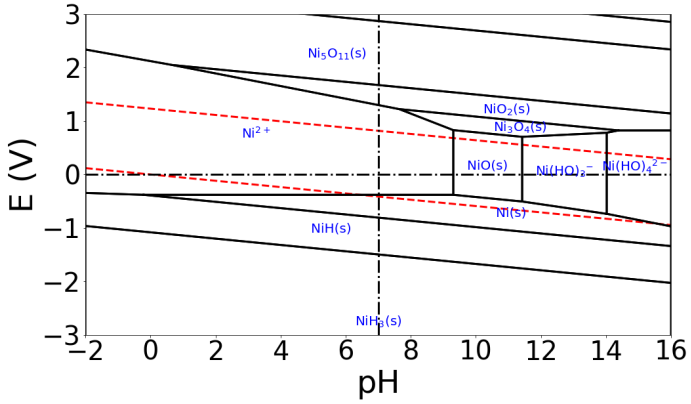

(a) No filter.

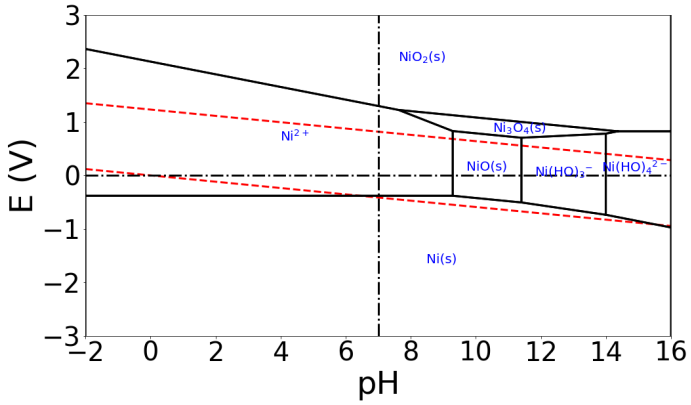

(b) This work.

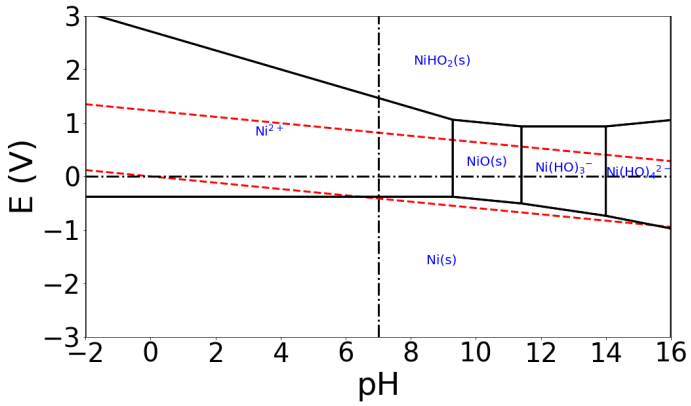

(c) Material Project filter.

Figure 3.2. Comparing Ni Pourbaix diagrams with different solid filters. NiH_3 dominates negative applied potentials if not filtered. However, by only filtering through the convex hull method such as in MP's filter, important phases like Ni_3O_4 may not be predicted.

might foster synthesis in a hydrothermal environment, but applications also exist within corrosion science. Use of stability diagrams in synthesis-condition prediction has been applied successfully in a variety of literature [54-56, 67-71].

Stability diagrams are computed following the methods described by M.M. Łencka *et al.* and A. Anderko *et al.* [56, 67]. As in the creation of Pourbaix diagrams, predominance lines are defined when the chemical potentials $\Delta\mu_A = \Delta\mu_B$, for two species (solids and/or ions in solution) comprising A and B within a phase field on either side of the thermodynamic boundary. The steps for their creation, nearly identical to those for Pourbaix diagrams listed in the previous section, are as follows: (*i*) list potential species and find all $\Delta_f G$s, either from computational and/or experimental sources, (*ii*) enumerate the chemical potentials of all species or sets of species that might form (*e.g.*, Equations 3.31, 3.33, 3.40, 3.42), and (*iii*) within a range of pH and concentrations/activities (or other environmental variables) find the most stable species or set of species. In the case of multi-element stability diagrams, the mass balance constraint laid out in Section 3.2.1.3 must be fulfilled.

Yield diagrams are used depict the predicted yield of a specific product throughout a given region of space, and are often overlaid on stability diagrams to further clarify regions of high product yield. Here, we define yield diagrams within their traditional use in a concentration-solution pH context [67], but this method could be extrapolated to handle other intrinsic environmental variables. Within the context of phase diagrams, we define yield as the ratio of the number of moles of the target product(s) $\mathcal{N}$ recovered, $\mathcal{N}(\text{actual})$, to the theoretical number of moles, $\mathcal{N}(\text{theoretical})$, calculated from the complete reaction of the limiting reagents (100 % transformation). Rather than computing theoretical yields from reaction stoichiometry, we utilize previously computed chemical potentials (*e.g.*, Equations 3.31, 3.33) by maintaining that within stable regions of the target product, the average composition of the system is also the most probable composition of the system. Therefore, the predicted yield $\mathcal{N}(\text{actual})$ for the target product J is given by the canonical ensemble of the chemical potentials

$$\mathcal{N}_J = \exp\left(-\frac{\Delta\mu_J}{k_B T}\right)\left[\sum_j \exp\left(-\frac{\Delta\mu_j}{k_B T}\right)\right]^{-1}, \tag{3.43}$$

where j is a sum over the chemical potentials of considered formation reactions. The yield is also defined to be zero at the dissolution boundaries, in accordance with previous literature [56, 68]. Therefore, the actual yield for product J is

$$\mathcal{N}(\text{actual}) = \mathcal{N}_J - \sum_j \mathcal{N}_j = 2\mathcal{N}_J - 1\,. \tag{3.44}$$

These yield values are then used to predict quantitatively the pH ranges, or ranges of other environmental variables, for which aqueous reaction will provide the target phase with high purity and minimal secondary phases. Intuitively, the 0% yield line corresponds to the boundary where chemical potentials between the target product and byproducts are equivalent. Then, x percentage yield of $\mathcal{N}_J$ is equal to the probability of finding $\mathcal{N}_J$ less the probability of finding all other stable species.

3.2.3. Driving Forces and the Maximum Driving Force

Thermodynamic driving forces, *i.e.*, chemical potential differences, can be useful to understand the thermodynamic force propelling a certain product to form. Driving force diagrams are created by calculating the chemical potential planes (Equations 3.31, 3.33, 3.40, 3.42) for each of the individual products or product combinations in the system. In 2D, the planes are typically visualized within an independent x-axis corresponding to a varying intrinsic variable, and a dependent, y-axis displaying the associated product chemical potential. Figure 7.1b shows an example of a single element driving force diagram for aqueous copper behavior. The diagram depicts the driving forces to form different copper aqueous ions or solids at a constant 100 mV applied potential, consistent environmental conditions shown by the dotted line on Figure 7.1a. The stable phases appearing here are obtained by examining the chemical potentials of stable and metastable species at the constant potential contour from the Pourbaix diagram.

As in phase diagrams, there can be multiple products corresponding to one plane for multi-element systems in a driving force diagram, which leads to exponentially increasing possible combinations as further elements are added. Thus, reduction schemes such as those introduced in L.N. Walters *et al.* [136] and A.M. Patel *et al.* [131] can ensure computational feasibility while preserving necessary and probable species combinations. Generally, only lower chemical potential species are visualized to ensure readability.

Next, we define the maximum driving force (MDF) for system, first introduced by L.N. Walters *et al.* [136]. The MDF for solid phases that would nucleate on the surface of a metal in an aqueous system is defined as

$$\Delta\mu_{\max} = \max\left(\Delta\mu_{\text{solid}} - \Delta\mu_{\text{aq.ion}}\right) \equiv \text{MDF}\,, \tag{3.45}$$

where $\Delta\mu_{\max} \leq 0$ is the optimized driving force, $\Delta\mu_{\text{solid}}$ is the reaction chemical potential for solid phase formation, *e.g.*, an alloy or (hydr-)oxide, obtained from Equation 3.31, and $\mu_{\text{aq. ion}}$ is the reaction chemical potential for the most stable aqueous ion(s) at a given set of environmental conditions found in Equation 3.33.

Environmental condition boundaries must be defined prior to calculating the MDF. The constraints are required because the calculated stability of solid scales and aqueous ion species evolves through the environmental condition space, including pH, potential and concentration ranges. Figure 3.3 shows the drastic MDF change depending on condition ranges. Very low or no driving force for solid phase formation exists at moderate applied potentials, while more extreme positive or negative applied potentials can yield MDFs of -3 eV or greater. Given most operating conditions for corrosion resistant materials might not need to include such extreme redox potentials, we suggest limiting the range of considered potentials to that which is approximately what a material might be exposed to. Therefore, unless otherwise noted, we defined the default set of conditions as: $2.5 \leq \text{pH} \leq 12.5$, $-500\,\text{mV} \leq \text{V}_{\text{SHE}} \leq 750\,\text{mV}$, $\eta_I = 10^{-6}$, T = 25°C, and P = 1 atm, here termed the standard corrosion limit window.

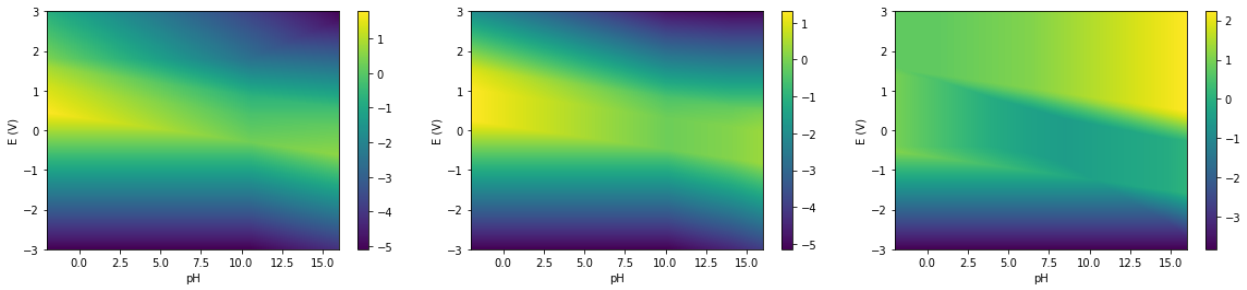

(a) Co system (b) Ni system (c) Cr system

Figure 3.3. Heatmaps representing the driving force for formation of the most stable species across pH-potential space for Co, Ni, and Cr. The most stable species are shown to occur at low and high applied potentials. At moderate applied potentials, the MDF is ≥0 and therefore aqueous ion formation is thermodynamically preferred.

Concentration can also play a key role in the mangitude of the MDF calculated. As seen in Figure 3.4, the MDF increases with higher concentrations. In dilute solutions $\eta_I \approx 10^{-8}$, the MDF of the Fe system, given by Fe_2O_3 scale formation, is about -0.22 eV. At the standard corrosion limit of $\eta_I = 10^{-6}$, the MDF is about -0.34 eV. Then finally, at more concentrated solutions $\eta_I \approx 10^{-2}$, the MDF further decreases to about -0.57 eV. Therefore, the more ions in solution, the larger the equilibrium driving forces that push the system to create solid phases.

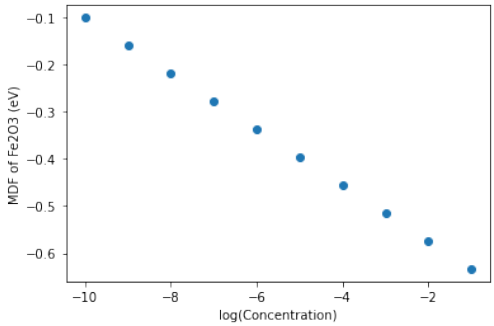

Figure 3.4. The MDF of Fe_2O_3 vs. concentration (η_I). The MDF is located at pH= 4.28, and applied potential= 0.67 V. The most stable ion at this pH is $Fe(OH)_{3(aq)}$, with associated reaction $Fe + 3H_2O = Fe(OH)_{3(aq)} + 3H^+ + 3e^-$. The associated reaction for Fe_2O_3 is $2Fe + 3H_2O = Fe_2O_3 + 6H^+ + 6e^-$.

Finally, the MDF can be extrapolated to multiple metal elements for simulation of intermetallic, alloy, and complex oxide systems. We here utilize the concepts of W.T. Thompson *et al.* [53] to write the chemical potential for solid species combinations, and for aqueous ions at different pHs, applied potentials, and concentrations. Unlike other popular predominance diagrams such as the Pourbaix diagram, we use a model that can be unconstrained at the surface, with fast reaction rates due to mobile water and ions, and without knowledge of the solid bulk composition [62]. Therefore, in these multi-element systems, species combinations do not need to follow a mass balance constraint for initial surface species formation. Future studies of surface transformation or subsurface species selection requires that species combinations be considered, which would follow a mass balance constraint [53].

We allow up to the number of cationic metal elements involved in the system to be the maximum number of stable phases considered at a given set of conditions. For example, in a ternary alloy, up to three oxides or

aqueous ions may be considered to be the most stable (though less is also possible). This follows the field standard for Pourbaix diagram creation, which is derived from Gibbs' phase rule.

In a multi-element system, the chemical potential of solid elements in their most stable phase at standard state is $\mu = \Delta_f G = 0$, where $\Delta_f G$ is the bulk Gibbs free energy of formation. We write the creation of (hydr)oxide scales, here $A_w B_x O_y H_z$ as an oxidation reaction from elements

$$W\mathrm{A} + X\mathrm{B} + Y\mathrm{H_2O} = A_w B_x O_y \mathrm{H}_z + (2Y - Z)e^- + (2Y - Z)\mathrm{H}^+ \tag{3.46}$$

where A and B are cations (typically transition metal or group 13 or 14 p-block elements), and W, X, Y, and Z are balancing and stoichiometric coefficients. This equation can be written and then balanced for up to two solid species, as discussed in the proceeding paragraph. This equation can also be easily changed to include alloy or intermetallic systems reacting. Mass balance constraints can always be fulfilled within the step [53].

Then, the chemical potential for the formation of a solid species from the reaction of water and its respective metal is written

$$\begin{aligned}\Delta\mu_{\mathrm{A_wB_xO_yH_z}} = (\Delta_f G_{\mathrm{A_wB_xO_yH_z}} - (2Y - Z)\cdot FU - (2Y - Z)\cdot RT\ln(10)\cdot pH \\ -W\cdot\Delta_f G_{\mathrm{A}} - X\cdot\Delta_f G_{\mathrm{B}} - Y\cdot\Delta_f G_{\mathrm{H_2O}})/N\end{aligned} \tag{3.47}$$

where N is the total number of metal elements per formula unit (here, $W + X$).

For aqueous ions in an A-B-H_2O system, we write the reaction of the elements leaving the solid and undergoing solubilization as

$$W\mathrm{A} + X\mathrm{B} + Y\mathrm{H_2O} = \mathrm{A_wO_{y'}H_{z'}^{\delta'}} + \mathrm{B_xO_{y''}H_{z''}^{\delta''}} + (2Y - Z + \delta' + \delta'')e^- + (2Y - Z)\mathrm{H}^+ \tag{3.48}$$

where $\mathrm{A_wO_{y'}H_{z'}^{\delta'}}$ are the $\mathrm{B_xO_{y''}H_{z''}^{\delta''}}$ ions formed, and δ' and δ'' are the ionic charges. We note that $Y' + Y'' = Y$ and $Z' + Z'' = Z$. Then, the reaction chemical potential is

$$\begin{aligned}\Delta\mu_{\mathrm{A_wO_{y'}H_{z'}^{\delta'}+B_xO_{y''}H_{z''}^{\delta''}}} = ([\Delta_f G_{\mathrm{A_wO_{y'}H_{z'}^{\delta'}}} + RT\ln(\eta_A)] + [\Delta_f G_{\mathrm{B_xO_{y''}H_{z''}^{\delta''}}} + RT\ln(\eta_B)] \\ -(2Y - Z + \delta' + \delta'')\cdot FU - (2Y - Z)\cdot RT\ln(10)\cdot pH \\ -W\cdot\Delta_f G_{\mathrm{A}} - X\cdot\Delta_f G_{\mathrm{B}} - Y\cdot\Delta_f G_{\mathrm{H_2O}})/N\end{aligned} \tag{3.49}$$

Misfit product combinations (combinations of solids and aqueous ion species) may be considered. However, in implementations of the MDF presented here, we do not allow conditions where these phases combinations are the most stable to be part of the MDF calculation. In other respects, the MDF for multiple element systems is calculated identically to single element systems, though filtration methods may need to be employed to ensure computational feasibility.

3.2.4. Probability Diagrams

Probability diagrams, which may also be referred to as ensemble diagrams, show the general probability of any one species or set of species appearing at a given condition. Here, 1 is equal to a 100% probability a material will form. These probabilities can then be used to visualize and analyze potential metastable phases. Probabilities are calculated from the chemical potential ensemble of all possible species sets. We define the probability of species combinations J as a function of pH or potential at a fixed activity as

$$P_J = \frac{\exp\left(-\frac{\Delta\mu_{\mathrm{rxn},J}}{k_B T}\right)}{\sum_j^M \exp\left(-\frac{\Delta\mu_{\mathrm{rxn},j}}{k_B T}\right)}, \tag{3.50}$$

where M is the number of total species combinations and k_B is Boltzmann's constant, Here, the chemical potentials of reaction $\Delta\mu_{\mathrm{rxn},J}$ are calculated via the previously introduced Equations 3.31, 3.33, 3.40, and 3.42. Systems with many potential phase combinations may experience a lack of efficiency for probability diagram calculation. To increase calculation speed, reduce resource cost, and avoid summing errors, it maybe necessary to calculate the demoninator as follows: $\Delta\mu_j$ is to be sorted in descending order of magnitude such that the largest contributions are included within $\sum_j$ first. We found truncating the sum at $M = 100$ led to general numerical convergence and reduced the overall computational time in calculating P_J.

3.2.5. Simple Models of Nucleation Barriers

First introduced in the 1930s [137], classical nucleation theory (CNT) may be leveraged to further understand specific phase nucleation. It is helpful leverage particularly for hydrothermal synthesis problems, where it is

expected that initial nucleate formation should lead to a growth stage for successful syntheses, and because comparison of reaction pathways are easiest when targeting a single material.

The nucleation barrier for a given product may be written as

$$W = V \cdot \Delta G_v + A\sigma = \frac{4}{3}\pi R^3 \Delta G_v + 4\pi R^2 \sigma \,, \tag{3.51}$$

where W is the work necessary to create a nucleate, G_v is the bulk free energy of the nucleate's compound, A is the surface area of the nucleate, V is the nucleate volume, σ is the specific surface area energy of the nucleate's compound, and R is the radius of the nucleate. The first term represents the volumetric contribution to the work, or in other words the energy lost (nucleate stablization) due to the creation of a stable compound. The second term is associated with the interfacial energy, and the energy needed to be input (destabilization) due to creating a new interface. These terms compete against each other, and often yield a critical radius R^* associated with a work barrier W^* that is necessary to overcome to create a stable nucleate (Figure 3.5). Without reaching these critical conditions, the nucleate is likely to disappear or solubilize.

For the works included herein, G_v is equated to the bulk $\Delta_f G$ of the target product. σ is approximated due to the fact that it may be computationally expensive to compute, and will not be reported in literature for new compound synthesis. When comparing reaction nucleation barriers for the same nucleate, testing σ at multiple magnitudes can ensure that any trends found (comparison of different pathway) is invariant with regard to surface area energy choice.

3.2.6. The Effective Chemical Potential

Previously, the $\Delta\mu_{\max}$ was introduced in Subsection 3.2.3 to assess oxide formation at the surface of a material from a difference in stability between the solid and aqueous phases. However, subsurface oxidation exclusively occurs as a solid-state transformation. Below this initial layer, time-dependent oxidized solid formation is reflective of the compositionally-constrained subsurface environment. Therefore, we assume the subsurface system to be isothermal and isobaric, and an open system to oxygen but closed to other elements.

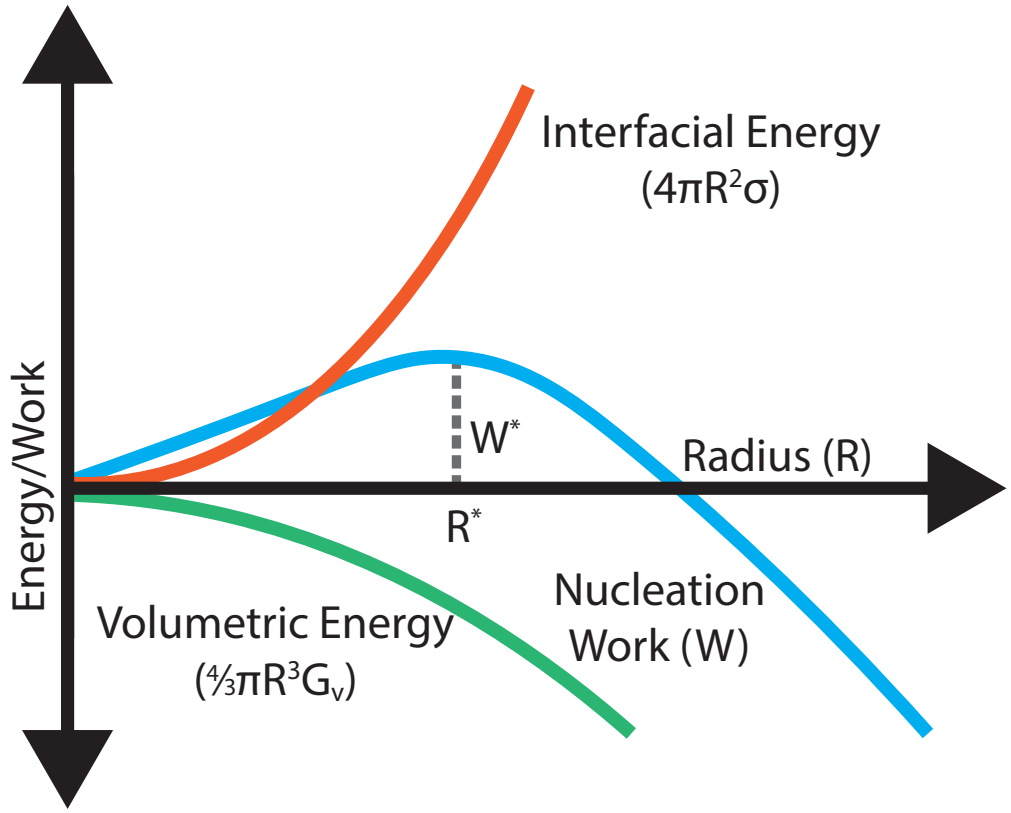

Figure 3.5. The nucleation work W for forming a nucleate based on CNT. Here, the energy associated with volumetric and interfacial contributions are oppositely signed, leading to a critical radius R^* with the work barrier W^* needed to form a stable nucleate.

Following Ref. [62] and [138], the grand canonical free energy for a given (solid) product, *e.g.*, oxide or hydroxide, below the surface is

$$\bar{\phi}^{\text{eff}}_{\text{solid}} = \frac{\Delta_f G_{\text{solid}} - N_{\text{O}}\mu^{\text{eff}}_{\text{O}}(x)}{\sum N_{\text{metal}}} \tag{3.52}$$

where $\Delta_f G_{\text{solid}}$ is the free energy of formation of the solid subsurface product, N_{O} and N_{metal} is the number of oxygen and metal atoms per formula unit, respectively, and $\mu^{\text{eff}}_{\text{O}}(x)$ is the depth-dependent effective oxygen chemical potential. Here, we parametrically decrease $\mu^{\text{eff}}_{\text{O}}$ (or another ion such as hydrogen, $\mu^{\text{eff}}_{\text{H}}$) with scale depth to reflect declining oxygen content below a solid's surface, for which the true depth dependence is a consequence of diffusion during active corrosion and/or changes in oxygen solubility from alloy processing. In other words, as is shown in Figure 7.1d, the oxygen chemical potential decreases accordingly with the

reduction in local oxygen composition. The chemical potential of the product will then decrease according to oxygen composition.

3.3. Publicly Available Code And Programs

Numerous codes and programs associated with this dissertation were developed to advance specific projects, and are now available publicly:

(1) Data and code related to algorithms that implement Equation 3.31-3.45 and are used in the calculation of multi-element and compositionally-dependent MDFs and driving-force diagrams are deposited on Github.

(2) Data and code used in the construction of lead (Pb) thermodynamic diagrams have been deposited in a Github Repository.

(3) Code to evaluate BiMOQ stable species at a given pH and potential value and sample data sets are available on Github.

(4) Sample scripts to create disordered Cr_2O_3 structures with cation substituted Al point defects, and then to calculate compositionally dependent scale stability is available on Github.

CHAPTER 4

Constructing Thermodynamic Models of Aqueous Copper Oxidation

Much of the work presented in the following chapter is available as a peer reviewed publication in *The Journal of Physical Chemistry C* [26]. Contributing researchers to the project, also listed as authors on the paper, include Dr. Liang-Feng Huang and Dr. James M. Rondinelli. Reprinted (adapted) with permission from L.N. Walters, L.F. Huang, J.M. Rondinelli "First-Principles-Based Prediction of Electrochemical Oxidation and Corrosion of Copper under Multiple Environmental Factors", *Journal of Physical Chemistry C*, 125, 25, 14027–14038 (2021) [26].

4.1. Introduction and Literature Review

Scientists and engineers use the familiar Pourbaix diagram as a tool to explain the thermodynamic stability regions of metals and oxides in aqueous environments [1, 4]. The phase diagram depicts species predominance and dissolution boundaries in the pH-potential phase space, and it can be divided into regions of corrosion, solid oxidation phase formation (often passivation), and immunity. Further, they allow us to decouple kinetics and thermodynamics, which is challenging in experiment Corrosion behavior is successfully described by Pourbaix diagrams in a variety of systems [1, 27, 44, 120, 139]. Pourbaix diagrams provide clear thermodynamic models of Pourbaix diagrams also aid the successful prediction of conditions for stable materials synthesis, including for magnesium oxide and delafossite $CaGaO_2$ systems [37, 45-50, 140].

The accuracy of these diagrams relies on careful sourcing of the Gibbs free energies of formation ($\Delta_f G$) to calculate reaction chemical potentials. Generally copper is a rather noble element that forms corrosion products only in highly basic and acidic conditions, and at applied overpotentials [1, 141]. Traditional techniques to find the $\Delta_f G$ values of solids include combustion calorimetry, which has been associated with significant errors [4, 6, 27]. Previous studies have found that materials or compounds that are prone to sample

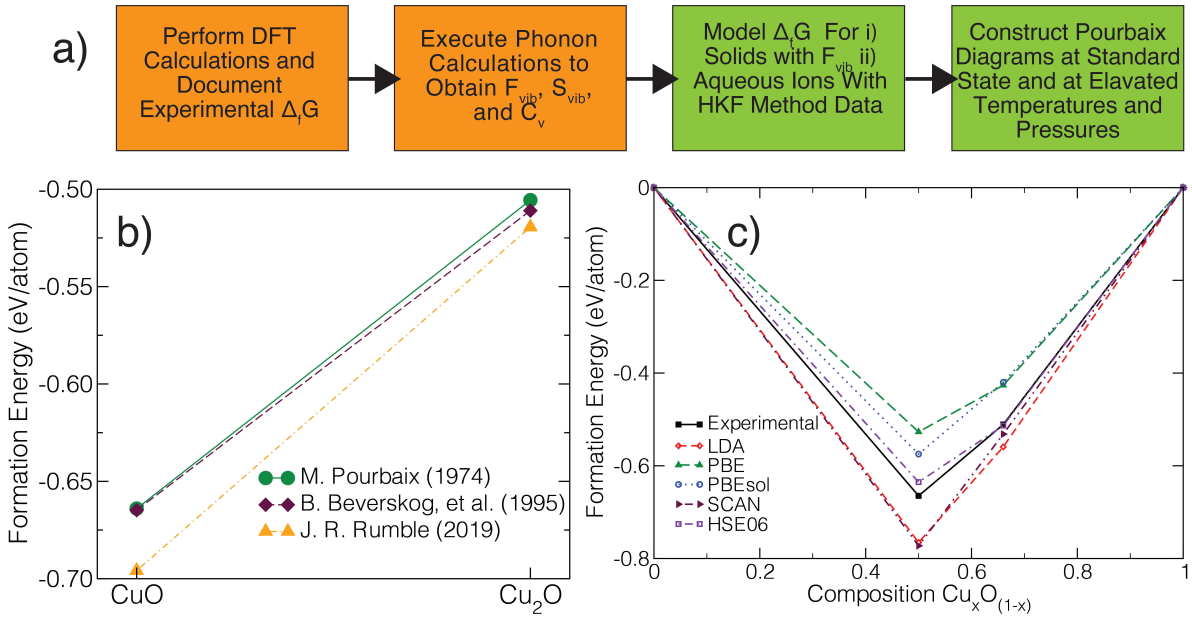

Figure 4.1. (a) The work flow summary for the creation of Pourbaix diagrams utilizing first principles density functional theory. The orange boxes (left) focus on the calculation of energetic and thermodynamic quantities, and the subsequent green boxes (right) on post processing and the analysis of the relative chemical potentials in the context of evolving aqueous environments. (b) The standard state free energies of formation of $CuO_{(s)}$ and $Cu_2O_{(s)}$ from a variety of experimental sources (M. Pourbaix, 1974 [1]; B. Beverskog *et al.*, 1995 [2]; J.R. Rumble, 2019 [3]). Discrepancies exist between each phase for all sources, consistent with $\Delta_f G$ values reported for other transition metal compounds [4]. (c) $\Delta_f G$ versus composition for the copper-oxygen system obtained from a variety of DFT functionals. HSE06 is shown to most closely fit the experimental free energies of formation energies. SCAN and LDA consistently overestimate the $\Delta_f G$, while PBE and PBEsol underestimate the energies compared to experimental sources [1].

defects, such as $NiO_{(s)}$, often lack correct experimentally determined free energies of formation to generate physically exact Pourbaix diagrams [27]. In other cases, the DFT formation energies are preferred to create an accurate version of *shallow* convex hulls or when there is a lack of experimental data across a composition or material family [27, 44]. In the case of copper, the deepest composition in the hull, shown in Figure 4.1c, exhibits a modest experimental formation energy of ≈66 meV/atom. In comparison, these studies also found success using $\Delta_f G$ values generated from bulk first principles calculations, which allow for defect free sample analysis and meticulous control over simulation quality when moving to high-level exchange-correlation functions [4, 27, 44]. The free energy of formation and thermodynamic data of aqueous ions typically rely on experiments, as the $\Delta_f G$ values of aqueous ions are computationally intensive to calculate. Moreover,

experimental techniques for aqueous ions are associated with much smaller errors than solid state formation energy methods [4].

Importantly, previous studies have found significant dependence of dissolution boundaries on aqueous-ion concentration and temperature, creating a complex phase space to study corrosion [2, 121, 142-144]. For applications like piping, coatings, or nuclear waste disposal, the need for alloys and conditions that support complete immunity and passivation of copper is paramount. While the $\Delta_f G$ values of aqueous ions are prevalent at standard conditions, high temperature $\Delta_f G$ data are scarce [145, 146]. The revised Helgeson-Kirkham-Flowers (HKF) model addresses this issue and is able to successfully estimate the $\Delta_f G$ values for aqueous ions at elevated temperatures [121, 142-144, 147]. It extrapolates room temperature data to predict the entropy and heat capacity of aqueous ions at elevated temperatures. In all cases, highly accurate knowledge of corrosion and solid oxide formation (passivation) behavior of copper is crucial.

Copper plays a key role in much of our daily lives, from electronics and energy applications to buildings and shipping. Therefore, its use, or misuse in terms of applications, has wide reaching effects. The recent coronavirus pandemic COVID-19 has pointed out the need for further understanding and developing anti-microbial coatings, for which copper and its corrosion properties show promise [148, 149]. In addition, public reliance on proper corrosion control within copper pipes to prevent poisoning remains a large public health issue [150-152]. The corrosive behavior of copper also plays a vital role in industrial applications including steal reactors, catalysts in flow reactors and specialized alloys [140, 153-156]. Copper-nickel alloys, in particular 70:30 Cu-Ni alloys with small concentrations of aluminum or iron, show high corrosion resistance in addition to favorable mechanical properties, allowing them to be used in seawater and piping applications [157, 158]. Copper processing techniques include chemical mechanical polishing and electrochemical-mechanical polishing in aqueous environments [159]. Etching of copper with acidic or basic solutions is also common for fabricating devices, particularly in the electronics industry [160-162]. Recovery of copper by smelting copper dust has been in great demand, and can be used to create nanoporous copper [163, 164].

One of the most important potential applications of copper is as a thick coating for steel containers designed for permanent disposal of radioactive waste (radwaste) [165-167]. Several proposed repository systems utilize Cu as a noble, corrosion resistant layer within a multi-barrier approach to yield long-term

waste isolation. These deep geological repositories (DGR) must last between approximately 10,000 to one million years, depending on national government regulation [168, 169], and copper's persistent corrosion resistance must be absolute. While long-term laboratory conditions and natural copper deposits indicate stability for thousands of years [170], some questions remain about elevated copper corrosion and oxidation behavior at the broader conditions that nuclear waste depositories are subjected to.

Although the corrosion behavior of copper is well studied, with several reports published by Pourbaix alone [1, 2] and copper being rumoured to be a favorite research target of Marcel Pourbaix himself [1, 2], there are neither any detailed first principles studies focused on copper, nor any broad reports of computationally determined pressure and temperature dependent copper corrosion studies. To that end, we explore the thermodynamic behavior of copper in an O_2 free environment under a broad electrochemical phase space. We expand our study to include nonstandard state behavior by employing the HKF method to obtain the necessary $\Delta_f G$ values of aqueous ions under these conditions. The extent to which we leverage DFT calculations is unique in terms of Pourbaix diagrams sourced from *ab initio* calculations. Finally, the generation of accurate nonstandard state and sulphur-containing Cu phase diagrams enforces the applicability of the study to understand phase stability in many of its typical use conditions in various industries.

4.2. Results

4.2.1. Computational Methods Development and Structure Enumeration

Structure and (redox) reaction enumeration are foundational for Pourbaix diagram creation. Phases are considered if they are stable in water, in accordance with principles laid out by Pourbaix. Therefore, the stability regions shown within these diagrams should depict the compounds and species that would be found within water after a long time. This approach ensures the pH-potential diagrams provide a a map of the aqueous phase space for experimental validation.

Generally, copper oxidation states of 0, I, and II are known to be stable in water [145, 146]. Therefore, we consider the solid-state compounds $Cu_{(s)}$, $Cu_2O_{(s)}$, $CuO_{(s)}$, $Cu(OH)_{2(s)}$, as well as the aqueous ion species Cu^+ and Cu^{2+}, and their respective cuprous and cupric anionic complexes (*e.g.*, $Cu(OH)_2^-$, $Cu(OH)_3^-$, and $Cu(OH)_4^{2-}$) as given in Table 4.1. Additionally we introduced multinuclear copper ions (*e.g.*, $Cu_2(OH)_2^{2+}$, $Cu_3(OH)_4^{2+}$). The Cu(III) oxidation state is known to be unstable in water; no aqueous ion or solid species

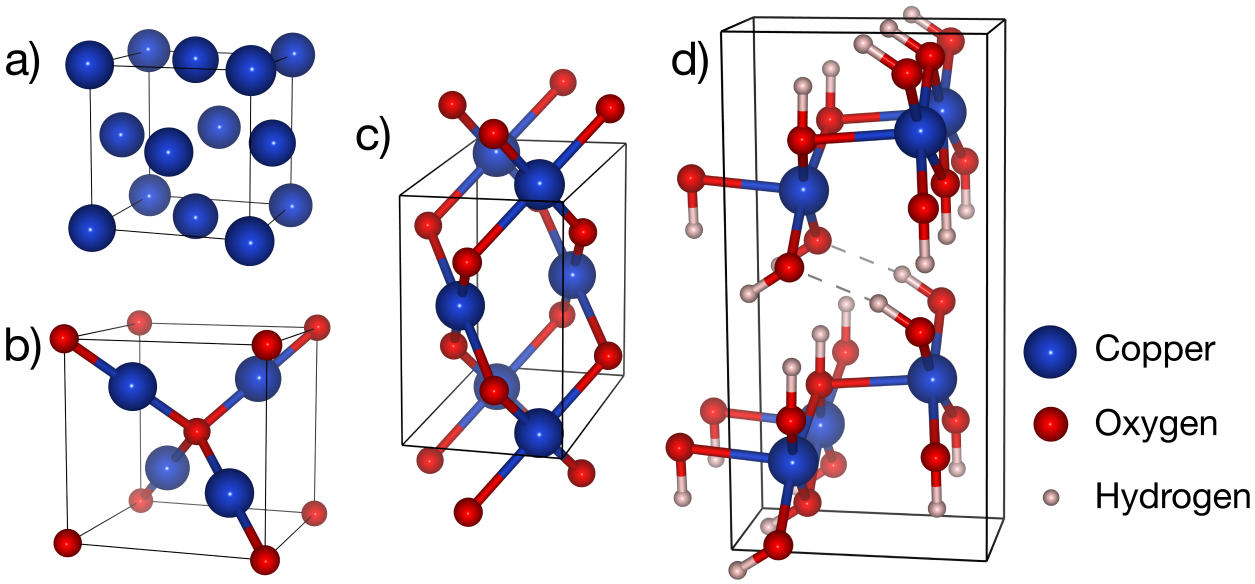

Figure 4.2. The crystal structures of copper compounds considered: (a) fcc elemental copper (b) cubic Cu_2O (c) monoclinic CuO, and (d) hydrated $Cu(OH)_2$. Structures were relaxed with DFT.

at this oxidation state were included. Additionally, the hydrated solid cuprice phase ($CuOH_{(s)}$) was not included; although the phase has been predicted [171], it is not known to be stable in water and is not commonly observed in electrochemical studies of copper [141, 172-175].

Density functional theory calculations were performed with the Vienna Ab initio Simulation Package (VASP) [96-99]. We benchmarked bulk solid phase electronic and energetic behavior with different density functionals: the local density approximation (LDA), the generalized gradient approximation (GGA) by Perdew-Burke-Ernzerhof (PBE), the Perdew-Burke-Ernzerhof generalized gradient approximation revised for solids (PBEsol), the strongly constrained and appropriately normed semilocal density functional metaGGA (SCAN), and the hybrid exchange-correlation functional (HSE06) [91, 100-105]. The initial antiferromagentic moment for copper (II) oxide was chosen based on experiment [106, 181], and single-point-energy calculations showed the experimental magnetic moment was consistent with the DFT ground state. The total energy was converged to 10^{-7} eV and forces were converged to less than 1^{-3} meV Å^{-1} during relaxations. Nonspherical gradient corrections within the PAW spheres were included. Van der Waals forces were considered for all solids implemented using the Tkatchenko-Scheffler method with iterative Hirshfeld partitioning. As Van der

Table 4.1. Copper compounds and species consideration in constructing the Pourbaix diagrams. Crystal structure or solubility information by oxidation state is provided where available. No structures with a Cu(III) were considered.

Solid species considered			
Composition	Oxidation State	Crystal Structure (space group)	Considered
Cu	0	Cubic ($Fm\bar{3}m$)	yes
Cu_2O	I	Cubic ($Pn\bar{3}m$)	yes
CuOH	I	Orthorhombic ($Aem2$)	no
CuO	II	Monoclinic ($C2/c$)	yes
$Cu(OH)_2$	II	Orthorhombic ($Cmc2_1$)	yes
Cu_2O_3	III	Tetragonal ($P4_2/mmc$)	no
Aqueous Ions Considered			
Composition	Oxidation State	$\Delta_f G$ (eV)	Considered
Cu^+	I	0.5182 [3]	yes
CuOH	I	-1.2678 [121, 176]	yes
$Cu(OH)_2^-$	I	-3.4518 [121, 176]	yes
Cu^{2+}	II	0.6747 [177, 178]	yes
$CuOH^+$	II	-1.2966 [178-180]	yes
$Cu(OH)_2$	II	-3.2666 [178, 180]	yes
$Cu(OH)_3^-$	II	-5.1716 [178, 179]	yes
$Cu(OH)_4^{2-}$	II	-6.8233 [178, 179]	yes
$Cu_2(OH)_2^{2+}$	II	-2.9424 [178, 180]	yes
$Cu_3(OH)_4^{2+}$	II	-6.5678 [178]	yes
Cu^{3+}	III	No Available Data	no
CuO_2^-	III	No Available Data	no

Waals interactions corrections are only explicitly handled in LDA, GGA, and the HSE06 functionals in VASP, cell optimization with SCAN did not augment the specific correction. Instead, SCAN intrinsically includes the nonlocal interactions necessary to simulate solid hydrated phases [182]. The hydrated solid $Cu(OH)_{2(s)}$ was found to exhibit the largest van der Waals corrections to the energy.

The oxygen molecular and hydrogen molecular bonds were relaxed within a simulation cell with $15 \times 15 \times 15\,\text{Å}^3$ vacuum. A triplet state ferromagnetic moment was preserved in the end of the $O_{2(g)}$ relaxations for all functionals, as shown in Figure 4.3b. The electronic energies E_e of elemental oxygen and hydrogen gas have a significant impact on the $\Delta_f G$ reported for each solid oxide and hydroxide. Systematic errors associated with ab initio calculations of gaseous molecules are well reported [183-186]. The magnetic moment for oxygen is consistently determined to be $2.00\,\mu_B$ for each functional, which is in agreement with experiment [107]. The binding energies reported from different functionals for gaseous hydrogen and oxygen are fairly consistent (Figure 4.3). The exception is SCAN, which predicts the binding energy to be around ≈1.5 eV greater for

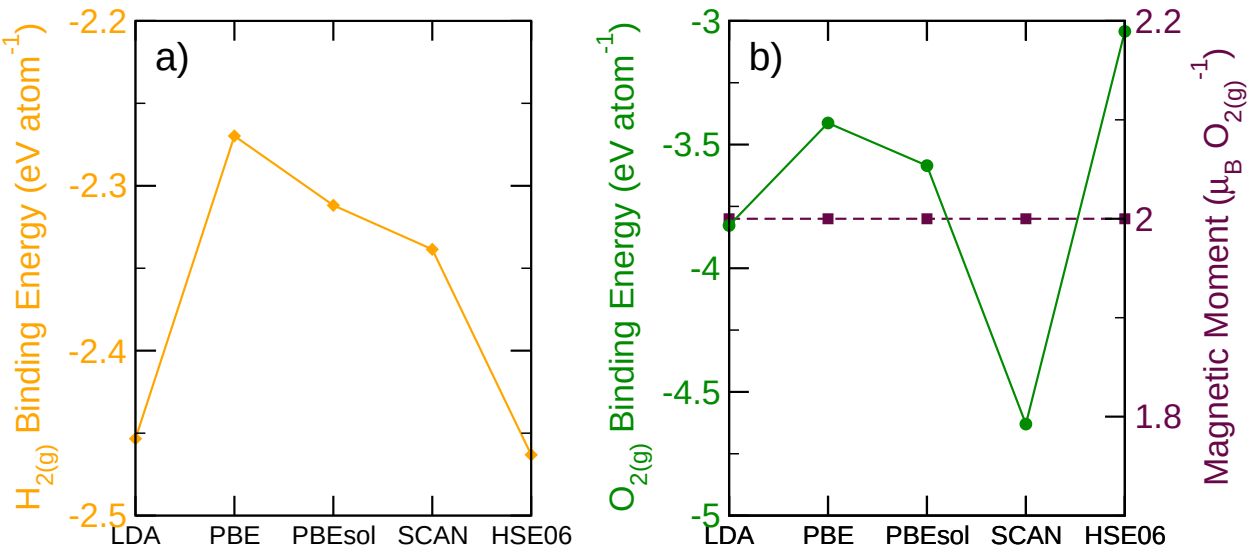

Figure 4.3. Binding energies and magnetic moments for hydrogen and oxygen gas with various exchange-correlation functionals to DFT. No zero point corrections are added. (a) The binding energies of the diamagnetic hydrogen molecule show small variations with functional. (b) The binding energies and magnetic moments of the oxygen molecule. All functionals predict the triplet ground state (magnetic moment of $2.0\,\mu_B$. The DFT energy per atom is consistently predicted to be ≈ -3 eV [5]. SCAN severely overestimates the binding energy of $O_{2(g)}$, while HSE06 most closely matches the experimental binding energy.

$O_{2(g)}$ than what is predicted for HSE06. On the other hand, HSE06 gives an $O_{2(g)}$ binding energy that is closest to the experimental binding energy of -2.56 eV/atom [186, 187]. Other GGA functionals and LDA have larger binding energies, consistent with documented problems associated with overbinding [185, 186].

Crystal structures for the experimental ground state phase were obtained from the International Crystal Structures Database (ICSD) [30]. The ground state structure, based upon the DFT electronic energy of each composition, was used to determine the convex hull and ultimate chemical potential of each species. Materials that are reactive with or very soluble in water were not included in the DFT calculations or later post processing steps, such as $Cu_2O_{3(s)}$. The materials considered and not considered for the simulate copper Pourbaix diagrams are found in Table 4.1. The considered electrochemical reaction pathways that connect all of the involved species are given in Table 4.2, where elemental Cu is used as the reference for calculating the reaction chemical potentials $\Delta\mu$ of the species.

Lattice dynamics calculations were performed with VASP and the Phonopy software [111]. All solid-state phases were found to be dynamically stable. We calculated thermodynamic data for them using statistical

Table 4.2. Formation reactions for passivation and corrosion products considered. Elemental copper is selected as the reference state ($\mu(\mathrm{Cu}) = 0$). U is the applied potential for the system, where the standard hydrogen electrode (SHE) potential is used as the reference. F is the Faraday constant. Reactions energies in units of kJ/mol.

Reaction Path	Chemical Potential Change ($\Delta\mu$)
$Cu \rightarrow Cu^{+} + e^{-}$	$\Delta\mu(Cu - Cu^{+}) = \mu(Cu) - \mu(Cu^{+}) + FU$
$Cu \rightarrow Cu^{2+} + 2e^{-}$	$\Delta\mu(Cu - Cu^{2+}) = \mu(Cu) - \mu(Cu^{2+}) + FU$
$2Cu + H_2O \rightarrow Cu_2O_{(s)} + 2e^{-} + 2H^{+}$	$\Delta\mu(Cu - Cu_2O) = \mu(Cu) - \frac{1}{2}\mu(Cu_2O) + \frac{1}{2}\mu(H_2O) + FU + RT\ln(10)\cdot pH$
$2Cu + H_2O \rightarrow CuOH^{+} + e^{-} + H^{+}$	$\Delta\mu(Cu - CuOH^{+}) = \mu(Cu) - \mu(CuO) + \mu(H_2O) + FU + RTln(10)\cdot pH$
$Cu + H_2O \rightarrow CuO_{(s)} + 2e^{-} + 2H^{+}$	$\Delta\mu(Cu - CuOH^{+}) = \mu(Cu) - \mu(CuOH^{+}) + \mu(H_2O) + 2FU + 2RT\ln(10)\cdot pH$
$Cu + 2H_2O \rightarrow Cu(OH)_2^{-} + e^{-} + 2H^{+}$	$\Delta\mu(Cu - Cu(OH)_2^{-}) = \mu(Cu) - \mu(Cu(OH)_2^{-}) + 2\mu(H_2O) + FU + 2RT\ln(10)\cdot pH$
$Cu + 2H_2O \rightarrow Cu(OH)_{2(s)} + 2e^{-} + 2H^{+}$	$\Delta\mu(Cu - Cu(OH)_{2(s)}) = \mu(Cu) - \mu(Cu(OH)_{2(s)}) + 2\mu(H_2O) + 2FU + 2RT\ln(10)\cdot pH$
$Cu + 2H_2O \rightarrow Cu(OH)_2 + 2e^{-} + 2H^{+}$	$\Delta\mu(Cu - Cu(OH)_2) = \mu(Cu) - \mu(Cu(OH)_2) + 2\mu(H_2O) + 2FU + 2RT\ln(10)\cdot pH$
$Cu + 2H_2O \rightarrow Cu(OH)_{2(s)} + 2e^{-} + 2H^{+}$	$\Delta\mu(Cu - Cu(OH)_2) = \mu(Cu) - \mu(Cu(OH)_2) + 2\mu(H_2O) + 2FU + 2RT\ln(10)\cdot pH$
$Cu + 3H_2O \rightarrow Cu(OH)_3^{-} + 2e^{-} + 3H^{+}$	$\Delta\mu(Cu - Cu(OH)_3^{-}) = \mu(Cu) - \mu(Cu(OH)_3^{-}) + 3\mu(H_2O) + 2FU + 3RT\ln(10)\cdot pH$
$Cu + 4H_2O \rightarrow Cu(OH)_4^{2-} + 2e^{-} + 4H^{+}$	$\Delta\mu(Cu - Cu(OH)_4^{2-}) = \mu(Cu) - \mu(Cu(OH)_4^{2-}) + 4\mu(H_2O) + 2FU + 4RT\ln(10)\cdot pH$
$2Cu + 2H_2O \rightarrow Cu_2(OH)_2^{2+} + 4e^{-} + 2H^{+}$	$\Delta\mu(Cu - Cu_2(OH)_2^{2+}) = \mu(Cu) - \mu(Cu_2(OH)_2^{2+}) + 2\mu(H_2O) + 4FU + 2RT\ln(10)\cdot pH$
$3Cu + 4H_2O \rightarrow Cu_3(OH)_4^{2+} + 6e^{-} + 4H^{+}$	$\Delta\mu(Cu - Cu_3(OH)_4^{2+}) = \mu(Cu) - \mu(Cu_3(OH)_4^{2+}) + 4\mu(H_2O) + 6FU + 4RT\ln(10)\cdot pH$

thermodynamics expressions implemented in Phonopy. For standard state systems, we used vibrational energies at 298.15 K to approximate the room temperature vibrational contribution [44]. To describe the behavior of solid copper species at nonstandard state conditions, we further utilize DFT lattice dynamics calculations. Phonon calculations are used to obtain the vibrational energy, written as the Helmholtz free energy, where the heat capacity and entropy of each solid species is found as partial derivatives of the harmonic phonon energy, E, and Helmholtz free energy, F, respectively [111]. In this way, thermodynamic quantities in addition to formation energies for solid species can be obtained via first principles calculations [111]. We then use the temperature-dependent quantities to calculate the formation energy at elevated temperatures [111, 112].

The temperature dependence of aqueous ions was approximated with the semi-empirical revised Helgeson-Krikham-Flowers (HFK) method. The revised HKF method has been successfully employed in a variety of pH-potential phase diagram studies [121, 142-144, 147]. It is valid for aqueous ion states when the dielectric constant and density of water are below their critical values and up to 1000 °C and 500 MPa, which is well above our outlined conditions [117, 188]. Briefly, the standard state thermodynamic properties are calculated using property based constants, termed coefficients of equations of state, including c_1, c_2, and the Born coefficient ω [117, 118, 123]. We choose equations-of-state coefficients for aqueous ions based upon structural and charge similarities of ions, consistent with previous works [120]. We then obtain the nonstandard state heat capacity and used this to calculate the apparent standard partial molal Gibbs free energies of formation

($\Delta\bar{G}^\circ$) at a nonstandard state pressure and temperature:

$$\Delta\bar{G}^\circ = \Delta_f\bar{G}^\circ + (\bar{G}^\circ_{P,T} - \bar{G}^\circ_{P_r,T_r}) \tag{4.1}$$

We refer readers to Subsection 3.1.3 for a brief overview of the revised HKF implementation.

Pourbaix diagrams were created following Subsection 3.2.1 using the activities of $\eta_I = 10^{-2}$, $\eta_I = 10^{-6}$ (the standard corrosion limit), and $\eta_I = 10^{-8}$. $\eta_I = 10^{-8}$ typifies many applications where low concentrations of copper are expected, such as piping, refrigeration, and many plating applications [121]. $\eta_I = 10^{-2}$ represents situations of high copper concentrations. The solvation term $-RT\ln(\eta_I)$ is omitted for the solid species which are assumed to have negligible solvation in water. This solvation term is minimal at room temperature but increases substantially at elevated temperatures. It begins to dominate the chemical potential of aqueous ions as temperatures approach 300 °C when $-RT\ln(\eta_I)$ decreases to below -60 meV at the typical corrosion limit.

We further examine use of an energetic correction term, $E_{\text{correction}}$, which is found from examining energetic differences between lower-resource DFT and experimental sources to ensure that the experimental dissolution energy of solids is accurate. Calculation of $E_{\text{correction}}$ is described in Subsubsection 3.2.1.2. $E_{\text{correction}}$ associated with $Cu_2O_{(s)}$ and $CuO_{(s)}$ and calculated from accurate experimental and HSE06 reference energies are shown in Table 4.3.

4.2.2. Properties of Copper and Its Oxides and Hydroxides

To create thermodynamic phase diagrams from computed $\Delta_f G$ values, first we established a methodology to accurately model aqueous electrochemical behavior. Solid species were simulated with a range of exchange-correlation functionals to DFT [189]. We compared functionals based on the location of compounds within the convex hull, conventional cell volumes, magnetic moments, and electronic band gaps, as shown in detail in Table 4.4. We underestimated the band gaps of $Cu_2O_{(s)}$ and $CuO_{(s)}$ by approximately 1.5 eV and 1.4 eV, respectively, consistent with well-known DFT limitations. $CuO_{(s)}$ is metallic with local and semi-local LDA, PBE, PBEsol, and SCAN functionals [182]. Each functional predicted a nonzero band gap, with an average value of 0.57 eV for $Cu_2O_{(s)}$, which is much less than the experimental 2.1 eV band gap. The HSE06 functional

Table 4.3. Corrections added to the free energy of formation of aqueous ions, which vary by by source. Historically, energy corrections are added to experimental $\Delta_f G$ values [28] to ensure that each solid dissolves at an accurate energy relative to the aqueous ions. For both oxides, HSE06 achieves the smallest corrections for aqueous ions. Corrections based on $Cu_2O_{(s)}$ exhibit the largest corrections for PBE and PBEsol, while SCAN and LDA demand the largest $E_{\text{correction}}$ when based on $CuO_{(s)}$.

Corrections added to aqueous species based upon Cu_2O			
Functional	Cu_2O Energy (eV/f.u.)	Experimental $E_{\text{correction}}$ (eV/Cu f.u.)	HSE06 $E_{\text{correction}}$ (eV/Cu f.u.)
Experimental	-1.5329	0.0000	-0.0026
LDA	-1.6777	-0.0724	-0.0750
PBE	-1.2788	0.1271	0.1245
PBEsol	-1.2597	0.1366	0.1340
SCAN	-1.5951	-0.0311	-0.0337
HSE06	-1.5277	0.0026	0.0000
Corrections added to aqueous species based upon CuO			
Functional	CuO Energy (eV/f.u.)	Experimental $E_{\text{correction}}$ (eV/Cu f.u.)	HSE06 $E_{\text{correction}}$ (eV/Cu f.u.)
Experimental	-1.3230	0.000	-0.0559
LDA	-1.5311	-0.2081	-0.2640
PBE	-1.0536	0.2694	0.2135
PBEsol	-1.1494	0.1736	0.1177
SCAN	-1.5448	-0.2218	-0.2777
HSE06	-1.2671	0.0559	0.0000

predicted nonzero band gaps for both oxides (1.30 eV for $Cu_2O_{(s)}$ and 1.80 eV for $CuO_{(s)}$), which were both closest to the experimental values.

The magnetic moments are underestimated for paramagnetic $CuO_{(s)}$ for all functionals. LDA, PBE and PBEsol predict a magnetic moment for $CuO_{(s)}$ of $< 0.01\,\mu_B$. SCAN and HSE06 both lead to magnetic moments within $0.1\mu_B$ of the experimental value. Paramagnetic $Cu(OH)_{2(s)}$ experimentally did not show a substantial band gap or local magnetic moment, so there was no substantial differences for these properties based on functional. Elemental copper was predicted by DFT to be a diamagnetic metal, which is consistent with experiment.

Table 4.4. Properties calculated with DFT using different functionals. Free energy of formation, conventional unit cell volume, electronic band gap, and any magnetic moments stabilized are included. Experimental data on each solid is provided for comparison from the NIST Janaf Tables [6] and a variety of other sources. Energetically, small deviations were seen between experimental and DFT data.

SOLID-STATE COMPOUNDS				
Cu, Cubic				
Functional	Energy (eV/f.u.)	Volume (Å^3)	Band Gap (eV)	Magnetic Moment μ_B
Experimental	0.000	47.1633	0.00	0.000
LDA	0.000	43.7453	0.00	0.000
PBE	0.000	47.9865	0.00	0.000
PBEsol	0.000	45.4433	0.00	0.000
SCAN	0.000	45.0705	0.00	0.000
HSE06	0.000	48.0609	0.00	0.000
Cu_2O, Cubic				
Functional	Energy (eV/f.u)	Volume (Å^3)	Band Gap (eV)	Magnetic Moment μ_B
Experimental	-1.5327 [6]	77.7725	2.1 [190, 191]	0.000
LDA	-1.6777	72.8722	0.73	0.000
PBE	-1.2788	79.8630	0.48	0.000
PBEsol	-1.2597	75.7100	0.57	0.000
SCAN	-1.5951	76.4457	0.48	0.000
HSE06	-1.5277	77.7725	1.30	0.000
$Cu(OH)_2$, Orthorhombic				
Functional	Energy (eV/f.u.)	Volume (Å^3)	Band Gap (eV)	Magnetic Character
Experimental	-3.7303 [1, 6, 180]	164.0976	0.00 [192-194]	0.000 (weakly AFM/FM) [194, 195]
LDA	-4.9031	143.3151	0.00	0.000
PBE	-3.4995	171.0463	0.00	0.000
PBEsol	-3.8374	152.1084	0.00	0.000
SCAN	-3.6525	181.2558	0.00	0.000
HSE06	-5.4102	159.6701	0.00	0.000
CuO, Monoclinic				
Functional	Energy (eV/f.u.)	Volume (Å^3)	Band Gap (eV)	Magnetic Moment μ_B
Experimental	-1.3297 [6]	81.4014	1.4 [196, 197]	0.69 [181]
LDA	-1.5311	82.4583	0.00	0.001
PBE	-1.0536	89.8508	0.00	0.002
PBEsol	-1.1494	85.5860	0.00	0.003
SCAN	-1.5448	84.9546	0.00	0.586
HSE06	-1.2671	81.4014	1.80	0.680

Volume discrepancies between experiment and calculations were minimized with the use of HSE06 for both oxides. PBE exhibited the closest volume to experiment for elemental copper. SCAN yielded properties very close to experiment for all solid species with the exception of the free energy of formation of $CuO_{(s)}$, which was overestimated. This trend follows benchmark studies on SCAN [182, 198]. Therefore, HSE06 predicts the chosen properties (volume, band gap, and magnetic moment) best when compared to that reported in previous studies. Other lower level functionals were unable to capture the broad range of properties needed to describe the behavior of these copper phases.

Table 4.5. The free energies of formation for $Cu(OH)_{2(s)}$ at different levels of theory and from two different experimental sources. We note that van der Waals (VDW) interactions are included for all functionals except SCAN, where specified.

Functional	$\Delta_f G$ (eV/f.u.)
Experimental (NIST-Janaf Tables [6])	-3.8623
Experimental (Puigdomenech [121])	-3.7303
LDA	-4.8798
PBE	-3.4995
PBEsol	-3.8374
SCAN with VDW	-1.8177
SCAN without VDW	-3.6544
HSE06	-3.8215

We base our functional selection on the location of the dissolution boundaries determined from direct electrochemical observation in experiment and comparison with experimental $\Delta_f G$ values. Figure 4.1c shows the convex hulls obtained from different functionals in relation to experiment, as well as the deviations of copper oxide experimental formation energies reported by different sources (e.g., LDA, PBE, PBEsol, SCAN, HSE06). Immediately, it is apparent that SCAN and LDA estimate the free energies of formation of the copper oxides to be as much as 170 meV/atom greater than the experimental values, while PBE and PBEsol underestimate the formation energy of each oxide by as much as 90 meV. Moreover, the $Cu(OH)_2$ formation energy varies widely based on the experimental and DFT source, as shown in Table 4.5. PBEsol underestimates the free energy of formation of copper (II) hydroxide by only 1 meV/atom when compared to one experimental sources [6]. SCAN and PBE were within 46 and 77 meV/atom of the experimental formation

energies, respectively. The large overestimation for the hydroxide stability with the latter functionals deviates substantially from previously reported formation energies [1, 3, 6, 121]. As with the oxides, HSE06 is closest to experimental sources as the simulated $\Delta_f G = -3.78\,\text{eV/f.u.}$ Therefore, we identify HSE06 to be the most physically consistent functional when considering the free energies of formation of the solid species. All data and nonstandard state diagrams are then based on HSE06 computed $\Delta_f G$ values unless stated otherwise.

4.2.3. Standard State Corrosion of Copper

Figure 4.4 shows the standard state Pourbaix diagrams calculated from experimental and DFT $\Delta_f G$ values. The standard state Pourbaix diagrams with copper hydroxide included are shown in Figure 4.8. When compared to experimental free energies of formation, we find that PBE, PBEsol and HSE06 allow for larger regions of corrosion. PBE and PBEsol both exhibit $CuOH^+$ and $Cu(OH)_3^-$ at the expense of $CuO_{(s)}$ stability regions in neutral pHs. The $CuO_{(s)}$ dissolution boundary at basic pH was lower for HSE06 than it was for the experimental Pourbaix diagram, leading to the emergence of the $Cu(OH)_3^-$ corrosion product. The overestimation of formation and binding energies found in SCAN lead to stability regions that are quite different from the experimental case, and vast passivation regions.

Stability regions ranged greatly for the corrosion-passivation phase spaces in Figure 4.4. The immunity region is relatively stable. We see that the overestimation of the copper oxide phases intuitively lead to larger passivation regions at standard conditions. Lower aqueous ion concentration like those shown in Figure 4.5, associated with applications such as piping, was found to give a stronger preference for aqueous ion stability. This is consistent with chemical understanding of equilibrium constants, and with past studies that explored the role of activity on copper Pourbaix diagrams [1, 2, 121]. Figure 4.6 depicts higher aqueous ion concentrations of copper, which lead to larger solid stability regions.

Available experimental species stability data affirms that HSE06 is in agreement with direct experimental observations from a variety of sources [141, 172-174]. A study by J. Kunze *et al.* found small applied overpotentials and slight underpotentials lead to consistent observance of $Cu_2O_{(s)}$ at a pH ≈ 9.3 [173]. Other studies also found a broad range of potentials supporting some formation of $Cu_2O_{(s)}$, possibly supporting a larger stability region for copper (I) hydroxide than has been previously reported [1, 121]. Moreover, the same studies found higher applied voltages lead to mixed phases of $CuO_{(s)}$ and $Cu(OH)_{2(s)}$. A solubility

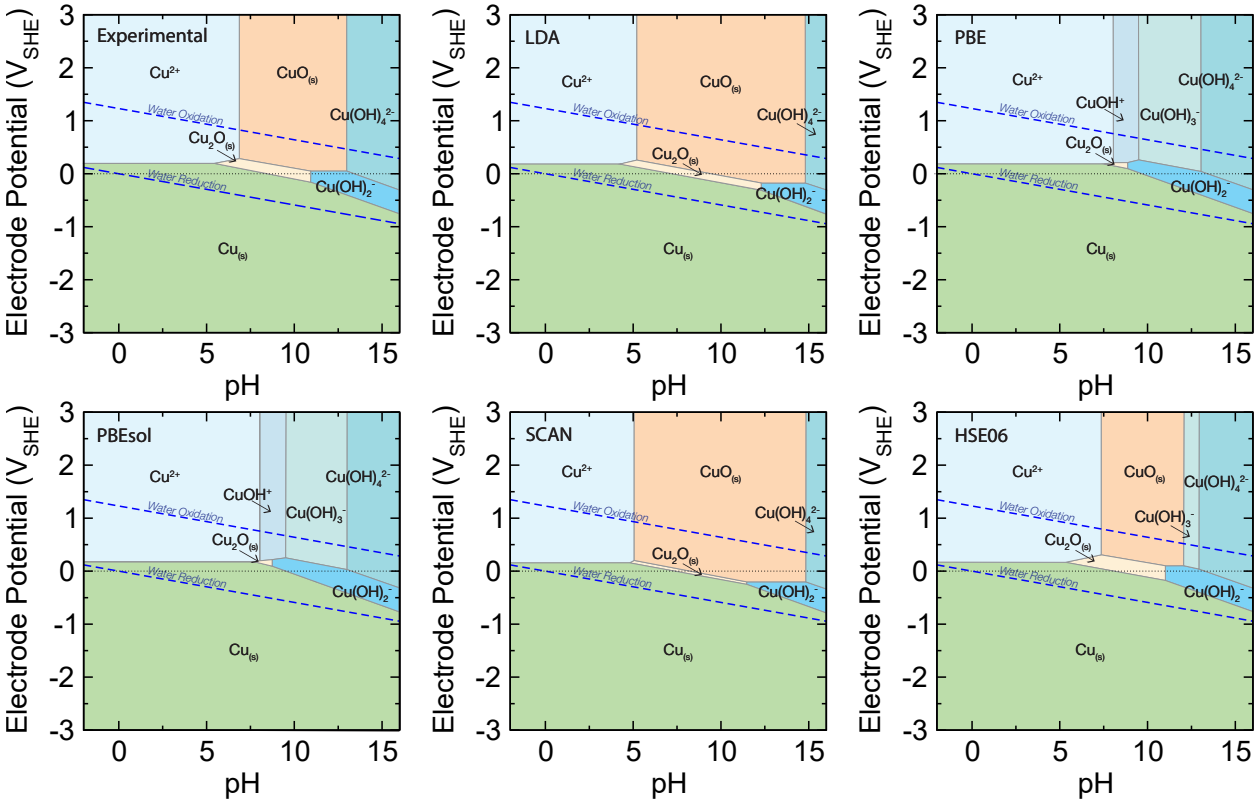

Figure 4.4. Pourbaix diagrams at standard state calculated using different formation energy sources as indicated in the upper left of each diagram. Copper activity in solution is set to the typical corrosion limit, $\eta_I = 10^{-6}$ and no $E_{correction}$ is incorporated. Experimental free energies of formation are sourced from the NIST-Janaf Thermochemical Tables [6]. Dotted lines are drawn to represent the oxidation and reduction of water. SCAN and LDA clearly overestimate the $\Delta_f G$ of the copper oxides, which leads to the large CuO passivation region. The GGA functionals, PBE and PBEsol, underestimate the formation energy of the oxide phases when compared to experiment and lead to nearly no passivation. HSE06 closely matches the formation energies found from experiment for $Cu_2O_{(s)}$ and $CuO_{(s)}$; therefore, the dissolution boundaries obtained from HSE06 most closely match experiment.

study by D.A. Palmer showed that the $Cu(OH)_3^-$ ion is also a prominent ion at high pH values at room temperature [199]. Therefore, the DFT-HSE06 calculated Pourbaix diagram gives the best agreement with the direct experimental observations.

Next, we evaluate driving forces based on differences in chemical potentials between various components to probe the formation and relative stability of stable and metastable phases. Figure 4.7 presents the relative chemical potential differences between species at the DFT-HSE06 level, where copper is used as the zero chemical potential standard. At no applied potential ($U = 0\,\mathrm{V}$), elemental $Cu_{(s)}$ is stable until about pH = 7.5,

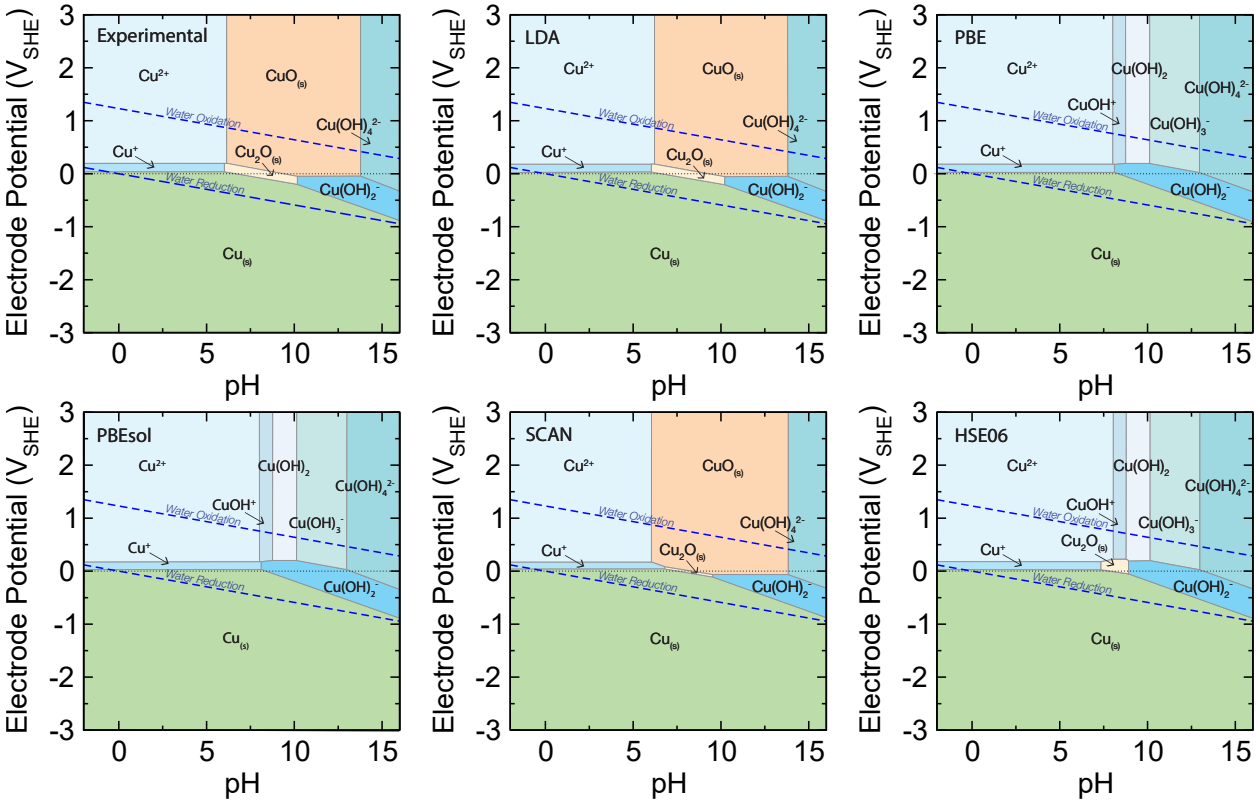

Figure 4.5. Copper Pourbaix diagrams at standard state for low solute activity (η_I=10^{-8}). No energy corrections are added. Functional dependence follows similar trends to diagrams created at the typical corrosion limit. SCAN and LDA overestimate the stability range of the solid copper compounds. Conversely, PBE and PBEsol do not allow for stability of solid species. HSE06 does not predict $CuO_{(s)}$ to be stable, but does allow for a small region of $Cu_2O_{(s)}$ stability around neutral pHs. Diagrams shown here are applicable to standard state conditions for relatively pure water, with approximate copper concentrations at 10^{-8} mol/L copper.

after which $Cu_2O_{(s)}$ and then the $Cu(OH)_2^-$ ion is favored in basic conditions. At applied under potentials, the pH range that stabilizes $Cu_{(s)}$ expands, and the driving force to create and protect elemental copper is substantial. Therefore, at standard conditions, elemental copper should be protected at all but very high pH values. At applied over potentials, the opposite trend occurs: the Cu^{2+} ion is stable in acidic conditions, and $CuO_{(s)}$ is stable at around pH = 7. Near neutral pHs, the passivation and corrosion products have similar chemical potentials, and the driving forces to create one over the other decreases.

Traditionally $Cu(OH)_{2(s)}$ was not present in published copper Pourbaix diagrams. The hydrated phase exhibits limited solubility in water, which increases substantially over pH ≈ 9.6 [200]. There is

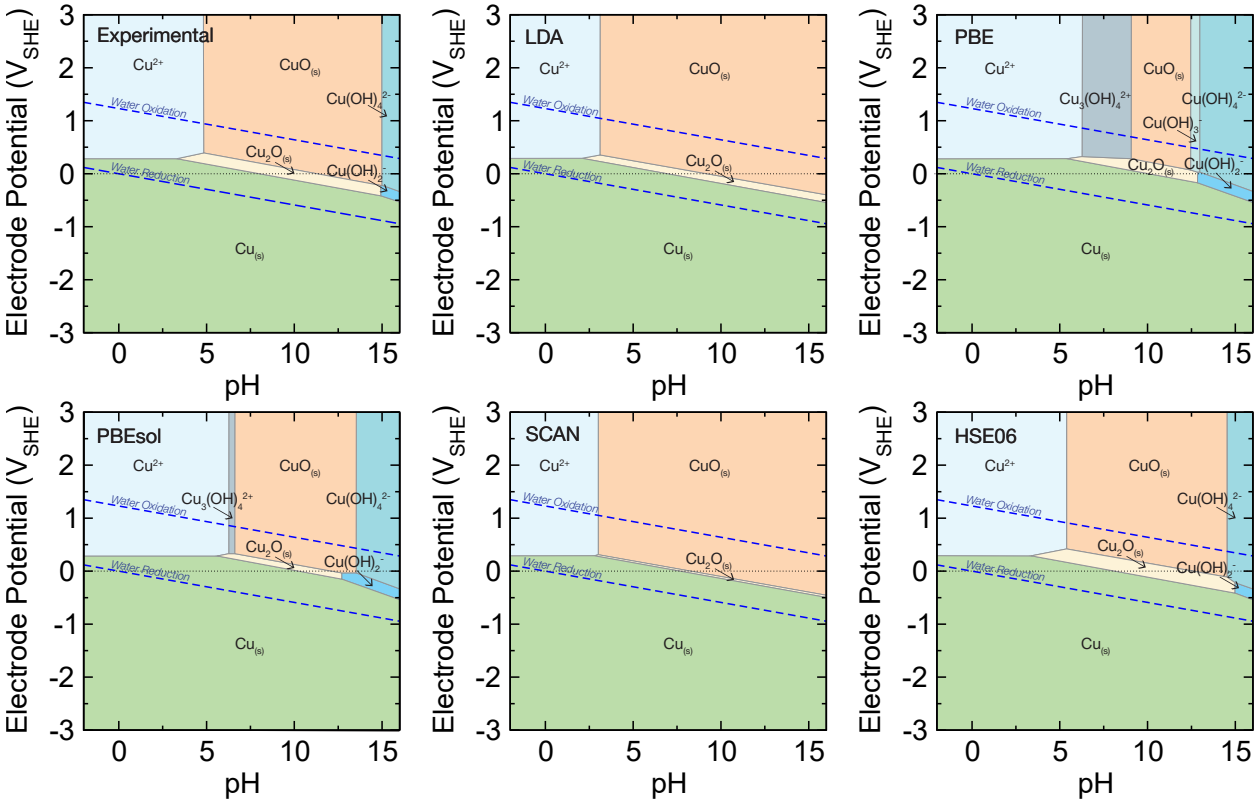

Figure 4.6. Copper Pourbaix diagrams at standard state for high solute activity (η_I=10^{-2}). No energy corrections are added. Functional dependence follows similar trends to diagrams created at the typical corrosion limit. SCAN and LDA overestimate the size of the $CuO_{(s)}$ region, and do not predict corrosion to occur at high pHs. PBE and PBEsol underestimate the passivation region. The GGA functionals also allow for the formation of additional aqueous ions at intermediate pHs. $Cu_3(OH)_4^{2+}$ occurs in acidic conditions for diagrams based on PBE and PBEsol energies. PBE also stabilizes $Cu(OH)_3^-$ at around pH = 12. HSE06 and the experimentally derived diagrams are in good agreement. Both show large copper oxide passivation regions, and predict immunity of elemental copper at neutral pHs and potentials. These diagrams are relevant for situations where copper activity is large, corresponding to approximate concentrations of 10^{-2} mol/L copper.

little experimental observation of the formation for copper hydroxide as a prominent solid scale. However, computationally, some DFT functionals like LDA estimate a much higher free energy of formation for $Cu(OH)_{2(s)}$ than experimental sources report [6, 121]. In Figure 4.8, we show the standard state Pourbaix diagrams calculated from $\Delta_f G$ values (in Table 4.5) where $Cu(OH)_{2(s)}$ is considered.

PBEsol, HSE06, and the experimentally-sourced diagrams stabilize for aqueous ions at low and high pHs (approximately pH≤6 and pH≥14). The passivisation regime only allows for copper (II) hydroxide and

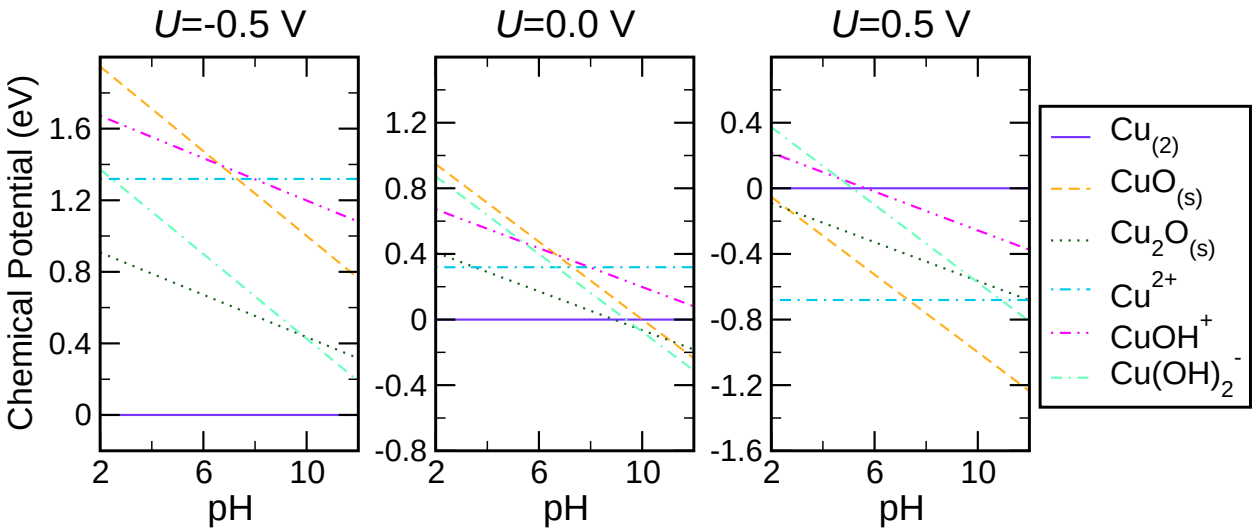

Figure 4.7. Changes in the chemical potential of different components from the free energies of formation calculated with HSE06 (no energy corrections added). Select solid oxidation and corrosion products are shown in relation to elemental copper, corresponding to 0 eV. At low underpotentials, copper is squarely in its immunity region, where the driving forces to create elemental copper is largest in acidic conditions. At $U = 0.0$ V and no $E_{correction}$, $Cu_{(s)}$ is stable until pH ≈ 8, where $Cu(OH)_2^-$ becomes stable. At basic pHs, the driving force to create $Cu(OH)_2^-$ instead of the metastable $CuO_{(s)}$ is minimal. Overpotentials demonstrate a highly stable Cu^{2+} corrosion region. The driving force to create the Cu^{2+} ion gradually decreases until the chemical potential difference is equal for the corrosion and passivation regions ($\Delta\mu_{Cu^{2+}} = \Delta\mu_{CuO_{(s)}}$). After this, a passivation region dominated by $CuO_{(s)}$ emerges.

$Cu_2O_{(s)}$ to form, and the protection region itself is much larger than it is when $Cu(OH)_{2(s)}$ is suppressed. We note that the $Cu_2O_{(s)}$ region is not observed for PBEsol. SCAN will not show the $Cu(OH)_{2(s)}$ phase with or without the van der Waals correction included because the $CuO_{(s)}$ solid has such a low formation energy. We note that with the rVV10 van der Waals energy correction method, the free energy of formation is much lower than experiment (by nearly 2 eV/f.u.), necessitating future benchmarking of the use of van der Waals corrections for transition metal hydroxides with SCAN.

The LDA-sourced Pourbaix diagram shows overestimated $Cu(OH)_{2(s)}$ domains. In this case, the presence of copper hydroxide greatly increases the solid oxidation stability regions, and does not allow for well-known corrosion or passivisation behavior at extreme pHs. The only Pourbaix diagram without a stable copper hydroxide domain is that sourced from the PBE functional, as the $Cu(OH)_{2(s)}$ free energy of formation is low (about 0.2 eV/f.u. below the experimentally-sourced range).

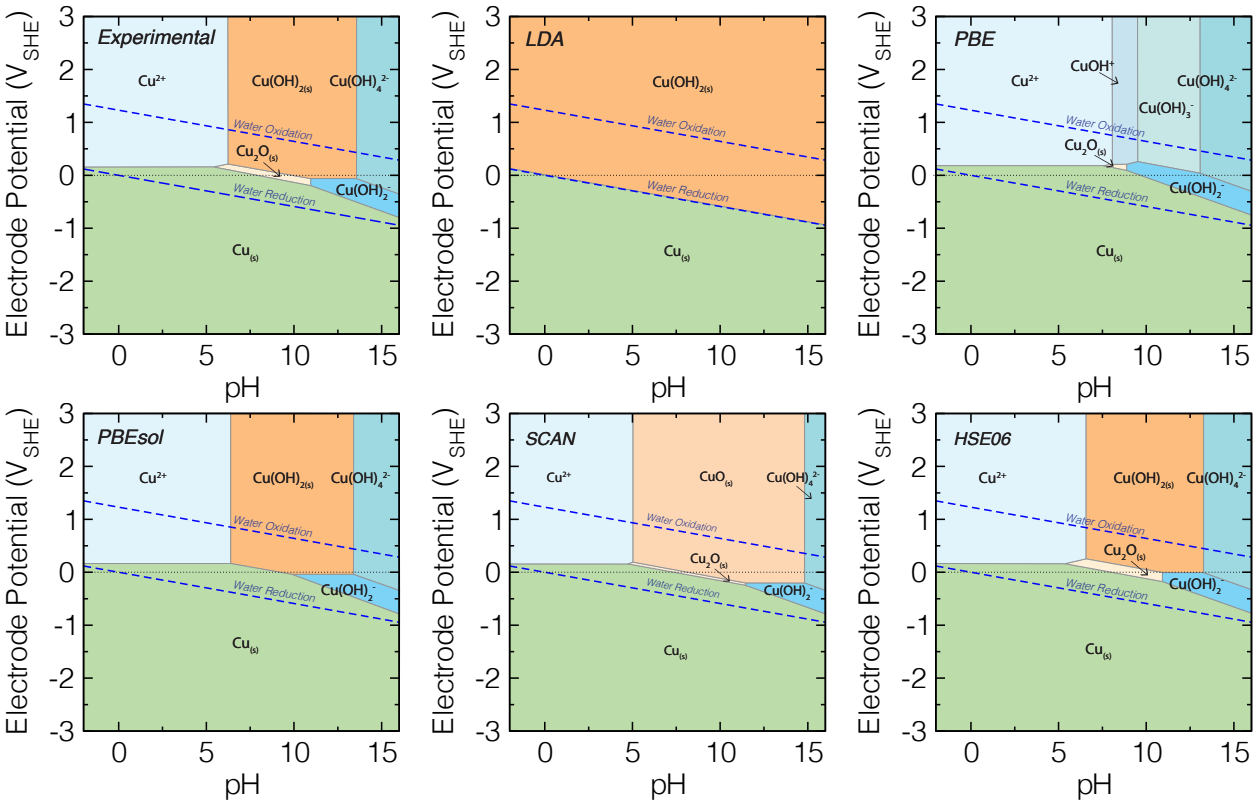

Figure 4.8. Copper Pourbaix diagrams shown at standard state and the typical corrosion limit (η_I=10^{-6}), where the hydrated $Cu(OH)_{2(s)}$ is included. No energy corrections are added. Experimental solid free energies of formation were sourced from the NIST-Janaf Tables [6], as other experimental sources do not allow for a $Cu(OH)_{2(s)}$ predominance region. We see HSE06 and LDA Pourbaix diagrams demonstrate large $Cu(OH)_{2(s)}$ passivation regions, and do not allow for stable corrosion regions at extreme pH values. Additionally, in both cases the passivation impedes the immunity region of elemental copper. The inclusion of copper hydroxide does not change the PBE Pourbaix diagram, as the free energy of formation of the hydrated phase is severely lower than experiment. Pourbaix diagrams calculated using experimental energies, PBEsol, and SCAN demonstrate passivation regions at ranges of intermediate pHs, and corrosion at highly acidic or basic conditiuons. The immunity region in all cases is preserved. $Cu_2O_{(s)}$ has a region of stability in the experimentally and SCAN calculated diagrams, but does not appear in the PBEsol diagram.

Pourbaix originally published two copper diagrams, one with only $CuO_{(s)}$ and one with the hydroxide passivisation phase also considered [1]. Both experimentally sourced diagrams presented in this study are consistent with his work [1]. However, we note that experimental $\Delta_f G$ value for $Cu(OH)_{2(s)}$ varies by as much as 0.2 eV/f.u. [1, 6, 121]. Past studies do not identify $Cu(OH)_{2(s)}$ as a primary product formed on copper in solution, and identify $CuO_{(s)}$ as the most stable solid oxidation phase in most cases. Other experiments

specify that while the initial solubility constant of $Cu(OH)_{2(s)}$ is small, over a large amount of time the scale breaks down and dissolves in solution or transitions into $CuO_{(s)}$, pointing to instability of the solid [200-202].

4.2.4. Computationally Sourced Correct Relative Chemical Potential Benchmarking

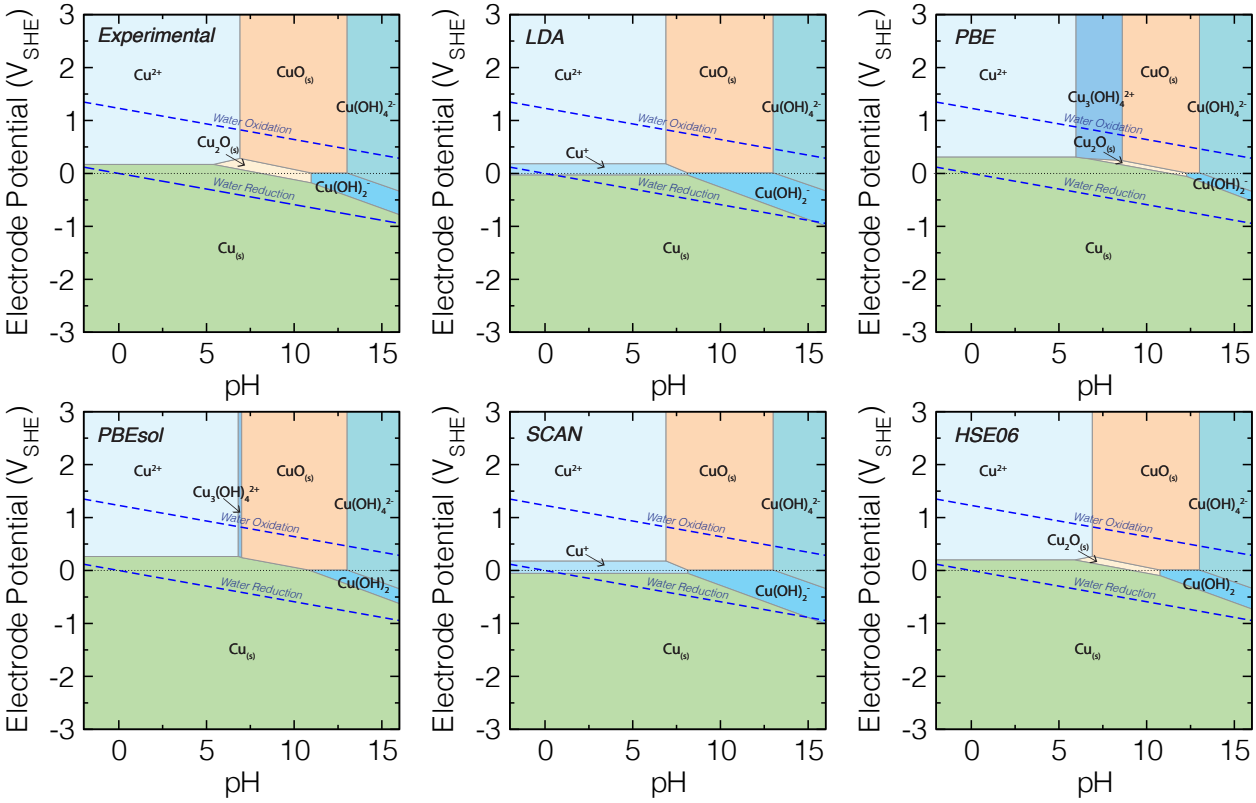

Figure 4.9. The CRCP method implemented from experimentally sourced $E_{\text{correction}}$ at standard state. The typical corrosion limit was used. $E_{\text{correction}}$ was based on the $\Delta_f G$ of $CuO_{(s)}$ from experiment.

We subsequently explored the implementation of the popular correct-relative-chemical-potential (CRCP) method [28]. The CRCP method is important for approximating electrochemical behavior via Pourbaix diagrams if accurate $\Delta_f G$ sources such as the hybrid HSE06 functional cannot be used due to a large number of considered solid species or limited computational resources. Energy corrections, shown in Table 4.3, are based on the $CuO_{(s)}$ phase. $CuO_{(s)}$ was chosen because it is the passivating species with the largest stability region. Use of $Cu_2O_{(s)}$ $\Delta_f G$ values would have led to small variations in the ion corrections. Figure 4.9 shows Pourbaix diagrams with applied energy corrections, $E_{\text{correction}}$, within the CRCP method from experimental

$\Delta_f G$ values to each of the exchange-correlation functionals explored. Upon employing the corrections we find that HSE06 reproduces the experimentally sourced Pourbaix diagram almost exactly, except for a slight underestimation of the size of the $Cu_2O_{(s)}$ stability region. LDA, PBEsol, and SCAN all produce phase diagrams with the same corrosion products as the experimental diagram, albeit small regions of Cu^+ or $Cu_3(OH)_4^{2+}$ emerge. PBE, however, introduces a large $Cu_3(OH)_4^{2+}$ region which inhibits the formation of protective $CuO_{(s)}$. Furthermore, LDA, PBE, PBEsol, and SCAN do not allow for a stable $Cu_2O_{(s)}$ phase. The immunity region of solid copper is largely correct in all Pourbaix diagrams in Figure 4.9 by employing the CRCP method given availability of the experimental $\Delta_f G$ values. Although there are minor differences, all diagrams sourced from local or semi-local functionals (LDA, PBE, PBEsol, and SCAN) better simulated the general immunity, solid oxidation, and corrosion regimes than they did without the corrections, and are therefore in better agreement with the experimental and HSE06 reference diagrams. Therefore, experimentally-based CRCP corrections are a moderately accurate and robust method to describe copper corrosion behavior.

Based on this analysis, we propose that the use of a high-level functional, such as HSE06, may be used for the reference energy of a compound in the CRCP method for a novel system instead of experimental $\Delta_f G$ values. This reference energy could later be used to find a $E_{\text{correction}}$ suitable for the creation of accurate phase diagrams for a previously unsynthesized or measured material to enable accurate phase predictions. To probe this idea, we explored the different phase emergence of PBE sourced energies corrected with either HSE06 or experimental $\Delta_f G$ values. Figure 4.10 shows CRCP corrected PBE regions and their experimental reference phases for (left) experimental sources and (right) HSE06 regions at three different applied potentials. In both cases, PBE+CRCP robustly reproduces the reference regions. Exceptions include the $Cu_3(OH)_4^{2+}$ region that was incorrectly produced when using either experimental or HSE06 based corrections. Moreover, PBE+CRCP predicts the $Cu(OH)_2^-$ at too low applied potentials. Otherwise, use of energy corrections from either experimental or HSE06 produce shifted immunity, passivation, and corrosion domains with the same chemical identities as those in the original phase diagrams. Therefore, the use of highly accurate HSE06 allows for a self-consistent first principles method to correct $\Delta_f G$ sets sourced from lower levels of DFT theory. As multi-element Pourbaix diagrams present a unique challenge, including the ballooning computational

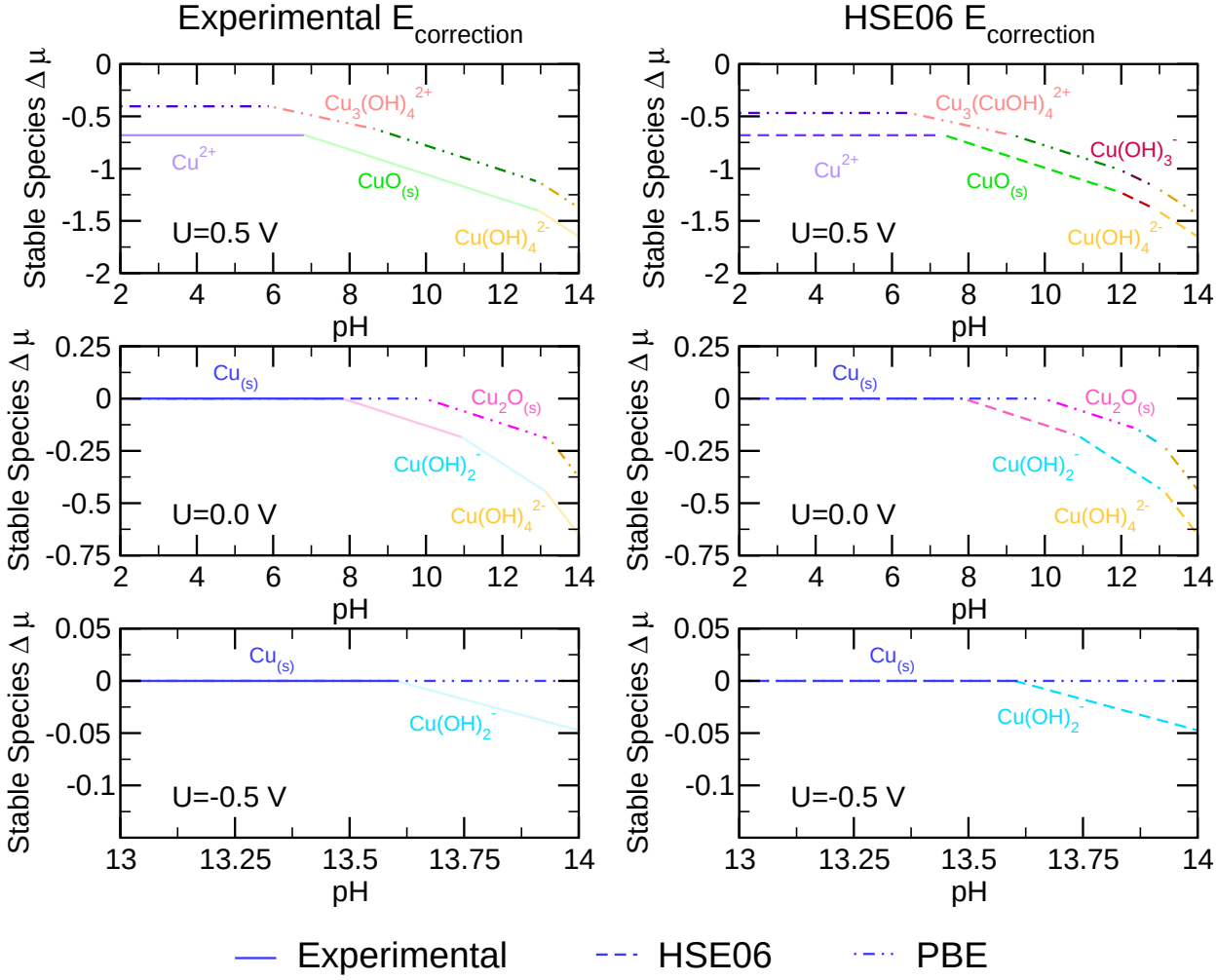

Figure 4.10. CRCP corrections added to aqueous ion free energies of formation according to Table 4.3 with experimental and with HSE06 $\Delta_f G$ values as the reference. Corrections were based on the free energy of formation of $CuO_{(s)}$, as it is the dominant passivation phase in the standard state Pourbaix diagram. There is substantial agreement between the HSE06 and experimentally sourced energy corrections. PBE (dotted and dashed line) corrected with HSE06 agrees well with PBE energies corrected with the experimental $E_{\text{correction}}$. The largest differences occur at a large applied over potential, where PBE stabilizes the $Cu(OH)_3^-$ ion only with the HSE06 correction added. Additionally, at U=0.0 V the PBE energies with an HSE06 correction only show a $Cu(OH)_2^-$ stability region. The similarities PBE shows with HSE06 corrections support the approach that higher level theory calculations can be used to correct cheaper functionals in first principles Pourbaix diagram.

cost for image rendering and number of phases to consider with DFT, we believe this will help lower the computational and resource costs associated with first principles Pourbaix diagram generation [4, 125].

Additionally generating the $E_{\text{correction}}$ from computation will be useful when experimental formation energies for a system are not known.

4.2.5. Nonstandard State Corrosion of Copper

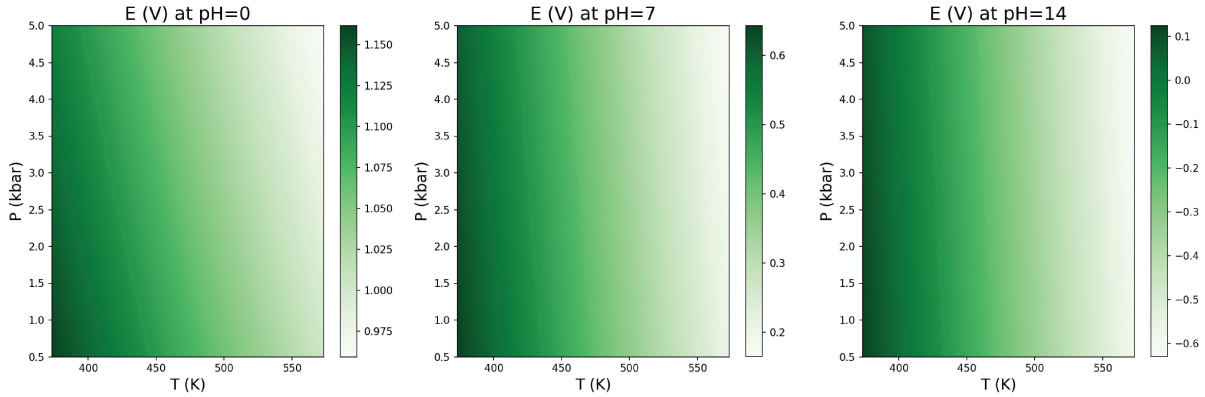

Figure 4.11. The oxidation potential of water E calculated for temperatures from 373.15 K to 573.15 K (100 °C to 300 °C) and 0.5 kbar to 5 kbar. E depends on the $\Delta_f G$ of water, which was interpolated between calculated values [7].

We next examine temperature dependencies of the system recognizing HSE06 as the functional in best agreement with direct experimental stability observations.

First, we evaluate any changes to the water stability region, defined as the region between the reduction and oxidation potentials of water. This region varies with pH, temperature, and pressure. The potential is reported in reference to the standard hydrogen electrode (E_{SHE}), which is 0 V at 0 pH at all temperatures. The temperature T and pressure P dependencies of E_{SHE} are described through the Nernst equation (Equation 3.29). We can implement the Nernst equation and calculate E^0 as 0 and $\Delta_f G(\text{H}_2\text{O})/2F$ for water reduction and oxidation, respectively.

Figure 4.11 presents two-dimensional heat maps of how the potential E approximately varies with temperature and pressure at pH = $0, 7,$ and14. The $\Delta_f G$ for water at specific temperature and pressure points are sourced from H. Halbach *et al.* [7] Potentials were found as interpolations from the previously calculated $\Delta_f G$. We see that temperature has the most substantial effect on E. As temperature and pressure

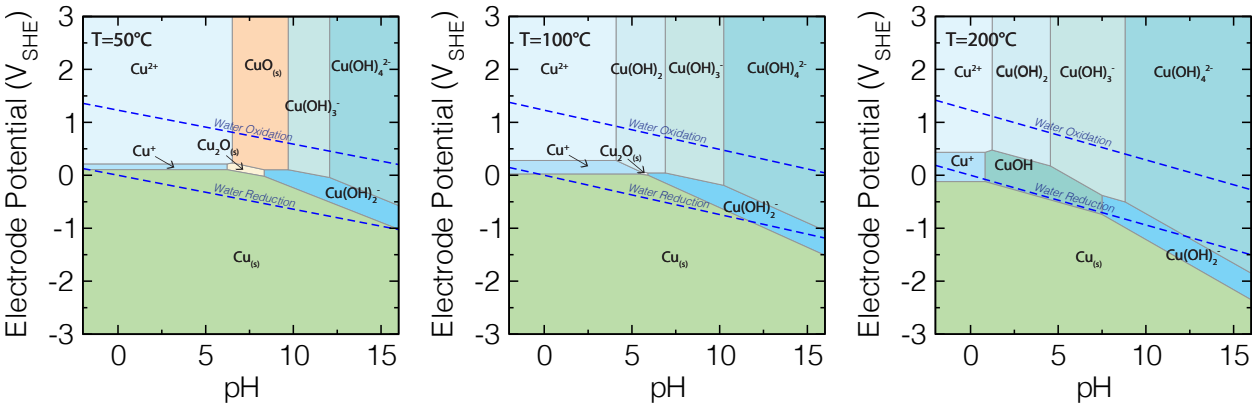

Figure 4.12. The nonstandard state Pourbaix diagrams created with $\Delta_f G$ values from the hybrid HSE06 functional. Diagrams shown are at the standard corrosion limit and no $E_{\text{correction}}$ is incorporated. The dissolution boundaries for the aqueous ions in solution expand at elevated temperatures. $CuO_{(s)}$ disappears near 100 °C, while the $Cu_2O_{(s)}$ region shrinks substantially. Elemental copper further loses its nobility as the temperature rises. Dotted lines represent the oxidation and reduction of potential of water compared to the standard hydrogen electrode.

increases, E decreases. Therefore, temperature is shown to have a much stronger effect on E, and therefore the stability region of water, than pressure. This is incorporated in to later diagrams.

Figure 4.12 presents Pourbaix diagrams calculated with HSE06 using temperature-dependent $\Delta_f G$ values. The diagrams at higher temperatures show a similar increase in the stability of aqueous ions as corrosion products, but smaller $Cu_2O_{(s)}$ passivation regions at the neutral pHs [1,121]. It should be noted that previous studies found significant differences in the reported nonstandard state free energies of formation, particularly for aqueous ions, which could account for these deviations [199]. As the temperature increases, the regions in the Pourbaix diagram corresponding to protective copper oxide shrink and the existing corrosion boundaries push into neutral pHs. Predominance of the copper oxyhydroxide ions is marked with increases as much as 3 pH units per 50 °C increase. The emergence of a stable Cu^+ ion occurs early ($T < 50$ °C) at low pHs and small applied potentials. Additionally, a hydrolysis product, CuOH, emerges just above $T = 100$ °C and $2 < \text{pH} < 7$. Solubility studies also support the increase in region of area of $Cu(OH)_3^-$ and $Cu_2O_{(s)}$ over $CuO_{(s)}$ at higher temperatures [199]. This behavior is consistent with our knowledge of aqueous ions exhibiting more stable chemical potentials at increased temperatures. We also find that the driving forces to create aqueous ions are much higher at elevated temperatures, due to the identified increase in $\Delta_f G$ calculated with the revised HKF

method (Figure 4.13). In particular, Cu^+, CuOH, $Cu(OH)^+$, and $Cu(OH)_2$ all become stabilized at higher temperatures. Together these results indicate that copper protection and immunity is severely infringed upon, even in oxygen free environments, at high temperatures.

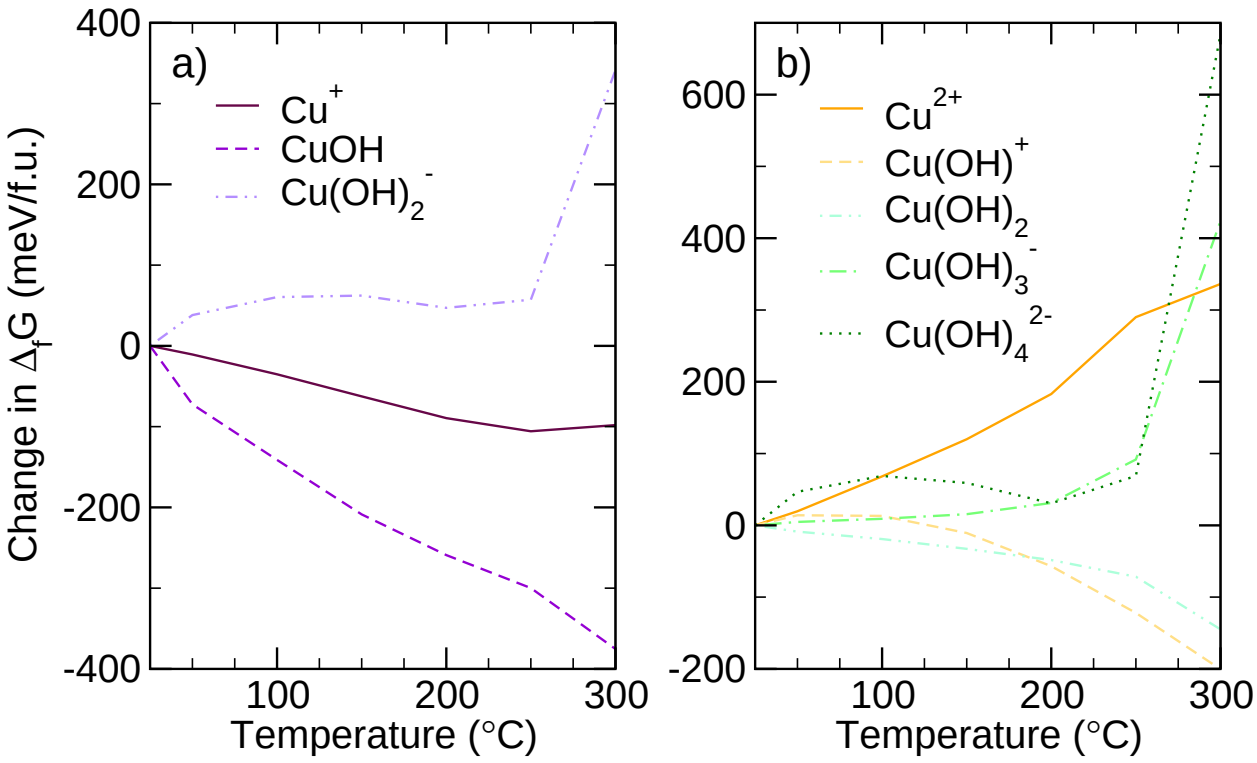

Figure 4.13. Change in aqueous ions $\Delta_f G$ as a function of temperature for the (a) Cu^+ and (b) Cu^{2+} hydrolysis series. We see the largest change in the $Z = 2^+$ series (e.g., $Cu(OH)_4^{2-}$ as part of the Cu^{2+} series) at elevated temperatures. We observe charged species generally become less favorable at higher temperatures, consistent with the smaller dielectric constant and decreased structure of water. This effect is more pronounced with larger species, particularly with the $Cu(OH)_3^-$ and $Cu(OH)_4^{2-}$ ions. The neutral species in each series, $Cu(OH)_2$ and CuOH, both show small increases in stability at high temperatures.

Next, we explored the effect of varied pressure on the Cu aqueous electrochemical behavior. External pressure leads to a small effect on the room-temperature stability, but plays a significant role at elevated temperatures as shown in the Cu Pourbaix diagrams at 300 °C for 500 bar and 5,000 bar (Figure 4.14). Here the shifts in the dissolution boundaries are apparent; the stability ranges of aqueous ions are more strongly effected than the solid phases at higher pressures. The Cu^{2+} region grows in predominance slightly at higher pressures around 1 pH point. The stability regions of neutral $Cu(OH)_2$ and CuOH shrink at elevated pressures,

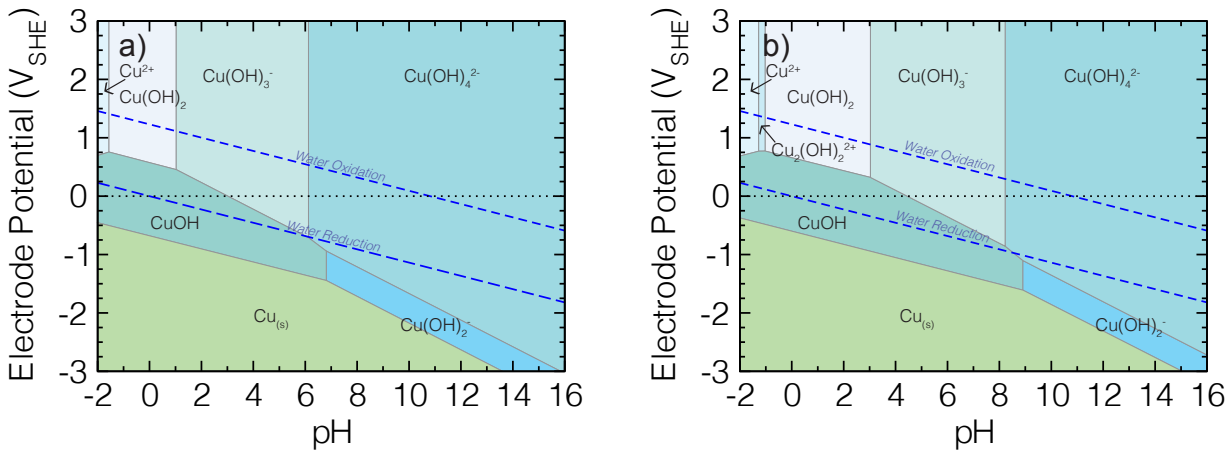

Figure 4.14. Pressure dependent Pourbaix diagrams for elemental copper at (a) 500 bar and (b) 5,000 bar at 300 °C, the $\eta_I = 10^{-6}$, and no $E_{\text{correction}}$. Diagrams use free energies of formation calculated with the HSE06 functional. Dotted lines represent the oxidation (upper) and reduction (lower) of potential of water compared to the standard hydrogen electrode.

while the charged $Cu_2(OH)_2^{2+}$ region eventually disappears at over 500 bar. Conversely, the large, negatively charged $Cu(OH)_4^{2-}$ ion area decreases such that it is stable from very alkaline regions through to pH = 8. Finally, the immunity region of copper at high pressures recovers slightly at most pHs by requiring less negative applied potentials to stabilize elemental copper.

We attribute these changes in stability to the change in heat capacity of ions, specifically charged copper hydroxides, as pressure increases; at elevated temperatures, the heat capacity fluctuates less at high pressures than at the saturation pressure (P_{sat}). At 200 °C, this change is ≈1.67 kJ/mol·K between saturation pressure and 5,000 bar for $Cu(OH)_4^{2-}$, and can be even larger [123]. High temperatures transform water into a nonpolar, unstructured solvent. Applied pressure conserves some structure and polarity in high temperature H_2O, allowing for improved stability of charged ions. The dielectric constant (ϵ) and g-function (a quantitative description of the ion-water relationship in terms of pressure and temperature) of water decline less at high temperatures when the system is also at elevated pressures. Therefore, increasing pressure can lead to the emergence of alternate aqueous ion stability regions. In the case of copper, applied pressure favors the stability regions of charged ions, and leads to the loss of regions defined by neutral species.

Selective control of which ions form in water is important for many applications. In particular, many transition metals and alloys, including copper, are susceptible to chlorine attack on their passivation

layers [203, 204]. Aggressive anions like Cl^- can target elemental copper as well as passivating scales and are connected with detrimental corrosion mechanisms such as pitting and crevice corrosion [203, 205]. Furthermore, the presence of some ions like OH^- can lead to the copper surface reconstructions, even at slight underpotentials where copper is within its immunity region [173]. The inclusion of oxidizing agents, such as Cu^+ or Cu^{2+}, promotes anodic dissolution and pitting. Favoring non-aggressive anions or complexed anions through the evolution of pressure could lead to greater corrosion control by promoting uniform corrosion mechanisms. Evaluation of pressure-dependent Pourbaix diagrams will be important for future extreme high pressure and temperature applications such that pressure ranges can be chosen that prioritize corrosive species and stable ions tied to uniform corrosion, and not to pitting, crevice corrosion, or other harmful mechanisms.

Table 4.6. Solid sulphur phases considered in the simulated phase diagrams. Crystallographic information was calculated using the PBEsol functional, and $\Delta_f G$ values are listed at the HSE06 level from our DFT calculations.

Material	Considered?	Copper Oxidation State	Computational $\Delta_f G$ (eV/f.u.)	Experimental Reference (eV/f.u.)
$S_{(s)}$	yes	I	0	0
$Cu_2S_{(s)}$	yes	I	-0.7697	-0.8934 [206]
$Cu_{1.6}S_{(s)}$	yes	I/II	-0.4966	-
$Cu_{1.7}S_{(s)}$	yes	I/II	-0.5509	-
$Cu_7S_{4(s)}$	yes	I/II	-19.0306	-23.2148 [206]
$Cu_{1.8}S_{(s)}$	yes	I/II	-0.6111	-
$Cu_{1.9}S_{(s)}$	yes	I/II	-0.6297	-
$CuS_{(s)}$	yes	II	-0.4795	-0.5565 [206]

4.2.6. Effects of Cl^- and HS^- on Copper Corrosion

Finally, we explore the effect of sulfide and chloride ions on copper thermodynamic corrosion behavior. Free energies of formation at (non)standard state for copper solids were sourced from L.N. Walters *et al.* [26], B. Beverskog *et al.* [121], and I. Puigdomenech *et al.* [206] $\Delta_f G$ values for $Cu_2S_{(s)}$, $CuS_{(s)}$, and $S_{(s)}$ were calculated within this study from DFT. We note that disordered structures $Cu_{2-x}S_{(s)}$, $0.1 \leq x \leq 0.4$ ($Fm\bar{3}m$, Cu_2Se defect structure) were created and their free energies are reported herein for future work. Initial

solid state crystal structures were sourced from the International Crystal Structures Database (ICSD) [30], where only oxides and sulfides and oxysulfides with stable oxidation states were considered. Moreover, due to computational feasibility, compositions with formula units greater than 50 atoms were excluded. A full list of compositions identified are shown in Table 4.6.

Structures were optimized with PBEsol such that total energies were converged to 10^{-7} eV and forces were converged to less than 1 meV Å^{-1}. The Brillouin zones of all structures were sampled with a minimum of 3,000 k-points per reciprocal atom (KPRRA) and used a Γ-centered mesh. Electronic energies (E_e) were found from an HSE06 calculation on the optimized structure. Lattice dynamical (phonon) calculations used the PBEsol functional to obtain the vibrational energies (F_{vib}). Thermodynamic data for aqueous ions, reported in Table 4.7 were found from B. Beverskog *et al.* [121], I. Puigdomenech *et al.* [206], Pourbaix [1], Lange's Handbook of Chemistry [9], and E.L. Shock [29].

Table 4.7. Aqueous ion phases considered in sulphur and chloride containing diagrams.

Material	Considered?	Copper Oxidation State	$\Delta_f G$ (eV/f.u.)
$CuCl_2^-$	yes	I	-2.5455
$CuCl_3^{2-}$	yes	I	-3.8605
$Cu_3Cl_6^-$	yes	I	-7.5865
Cu_2Cl_4-	yes	I	-5.0517
$CuCl^+$	yes	II	-0.7235
$CuCl_2$	yes	II	-2.0599
$CuCl_3^-$	yes	II	-3.3295
$CuCl_4^-$	yes	II	-1.7324
$CuClO_3^+$	yes	II	0.5714
Material	Considered?	Oxidation State	$\Delta_f G$ (eV/f.u.)
Cl−	yes	-1	-1.7324
S_5^{2-}	yes	-0.4	0.4838 [1]
S_4^{2-}	yes	-0.5	0.5940 [1]
S_3^{2-}	yes	-0.67	0.7227 [1]
S_2^{2-}	yes	-1	0.8707 [1]
H_2S	yes	-2	-0.5157 [1, 115, 207, 208]
HS^-	yes	-2	0.0366 [1, 207, 208]
S^{2-}	yes	-2	0.94756 [1, 207, 208]

$H_2S_2O_3$	yes	II	-5.8855 [1]
$HS_2O_3^-$	yes	II	-5.8671 [1, 208]
$S_2O_3^{2-}$	yes	II	-5.5981 [1, 114, 208]
$S_5O_6^{2-}$	yes	II	-10.1961 [1, 208]
$S_4O_6^{2-}$	yes	2.5	-11.0534 [1, 208]
$HS_2O_4^-$	yes	III	-6.1719 [207]
$S_2O_4^{2-}$	yes	II	-6.1152 [1, 207]
$S_3O_6^{2-}$	yes	3.33	-10.1646 [1]
H_2SO_3	yes	IV	-5.8329 [1]
HSO_3^-	yes	IV	-5.7150 [1, 208]
SO_3^{2-}	yes	IV	-4.9349 [1, 208]
$S_2O_5^{2-}$	yes	IV	-8.1958 [114]
$S_2O_6^{2-}$	yes	V	-10.2292 [1]
H_2SO_4	yes	VI	-6.3865 [1, 207, 208]
HSO_4^-	yes	VI	-8.0265 [1, 208, 208]
SO_4^{2-}	yes	VI	-7.7162 [1, 207, 208]
$S_2O_8^{2-}$	yes	VII	-11.7990 [1, 114, 208]
HSO_5^-	yes	VIII	-6.6074 [114]

Figure 4.15 displays a complete pH-potential Pourbaix diagram of Cu-S-Cl in pure water at $\eta_I = 10^{-6}$ and at standard state. Cl^- is additionally stabilized at all conditions, and therefore not shown for clarity. Color coordinated regions represent the thermodynamic stability of copper and sulfur containing species, where greens are immunity for copper, oranges contain copper sulfides or oxides, and blue regions stabilize corrosive copper aqueous ions. At near neutral potentials, native or passive copper will be stabilized at $pH \leq 11$. Therefore, upon initial inspection, copper should be thermodynamically protected for broad conditions, such as the presence of aqueous sulphur and chloride, assumed by a deep geological repository.

Upon closer inspection of Figure 4.15, we find similar trends to those identified earlier in the chapter. Near neutral pHs, copper exhibits either an immunity region or one of two scales: $Cu_2O_{(s)}$ and $Cu_2S_{(s)}$. Both Cu(I) phases are formed through anodic reactions to form passive surfaces. $Cu_2S_{(s)}$ (chalcocite) is a common solid copper sulfide within aqueous systems. Some studies report chalcocite to be passive and protective,

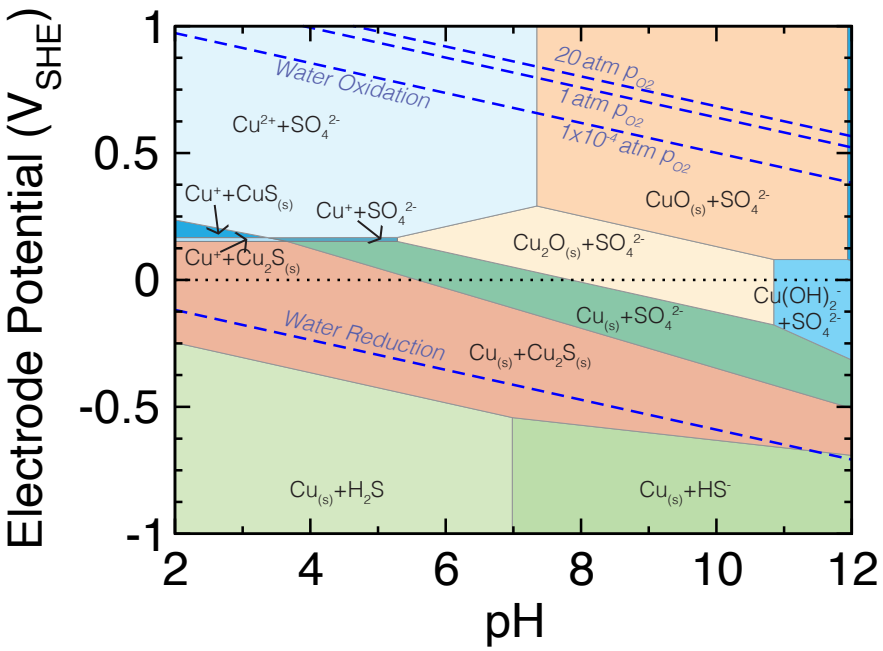

Figure 4.15. A Cu-S-Cl-H_2O electrochemical (Pourbaix) predominance diagram. Regions of stability are labeled for Cu and S containing species. All regions additionally include the Cl^- ion, not shown in labels for clarity. Diagrams were created at $\eta_I = 10^{-6}$ activity and standard state. Regions are colored in blues when a copper aqueous ion is stabilized, green if the only copper species is elemental copper (immunity regions) and oranges if a copper suphide or oxide is present. Aqueous Cu ions are generally stabalized at acidic pHs and higher applied potentials (except for the $Cu(OH)_2^-$ dissolution boundary near pH = 11, $E \approx 0\,V$. Copper sulfides are dominated by Cu_2S, which demonstrates a large stability window between approximately -0.5 V and 0.2 V. An additional immunity region separates copper sulfide formation and and oxide film formation leading to these films being unlikely to coexist, and demonstrating scale identity variation based on possible DGR conditions.

including D. Kong *et al.* [209] and F. Mao *et al.* [210]. These and other works supported passivity with electrochemical impedance spectroscopy and potentiodynamic polarization curves from a conventional three electrode cell to find that $Cu_2S_{(s)}$ thin films form in dearated sodium sulfide solutions. $Cu_2S_{(s)}$ films generally demonstrate a passive potential between -0.86 to -0.33 V_{SCE} for up to 75 °C. Challenges to $Cu_2S_{(s)}$ possible protection lie in poor mechanical properties, for which flow or other strain could lead to sloughing [211], Cl^- attack at positive potentials [211], and condition dependent porosity [212].

Other (metastable) copper sulfides include $CuS_{(s)}$ and cation deficient $Cu_xS_{(s)}$ where x is approximately $1.2 < x < 2$ within the fluorite ($Fm\bar{3}m$) and anilite ($Pnma$) defect structures. Future work will investigate the effects of including these phases into predominance diagrams.

4.3. Conclusion

Here, we develop a thermodynamic model for copper corrosion in an O_2 free environment at standard and non-standard state conditions. We leverage previous work to create aqueous electrochemical phase diagrams from computation, and propose a modified CRCP correction scheme for high throughput Pourbaix diagram creation and instances where values for experimental references states are unknown. Our study finds that elevated temperatures and high purity water support decreased passivation regions. Small stability region variances are seen with changing pressures, which could be used to engineer the presence of certain aqueous ions at elevated temperatures. Basic conditions severely limit the protection regime for elemental copper. Additionally, the stabilization of corrosion products at neutral pHs is concerning for applications that rely on the formation of copper oxides for protection at elevated temperatures. Even at intermediate temperatures ($T \leq 100\,^{\circ}\mathrm{C}$) where $Cu_2O_{(s)}$ layers should still form, the driving forces for copper oxides materials are no longer substantial when compared to other relatively stable copper ions. Finally, strong competition with metastable phases and at low concentrations of copper should also be a concern.

We also identify that the experimentally derived diagrams and those computed from first principles calculations exhibit a few inconsistencies which merit direct experimentation. At standard state, the dissolution boundary of $CuO_{(s)}$ at an over potential and its high pH point (pH $\approx$ 11-14) should be re-examined. In addition, the effect of high temperature on the stability of both $Cu_2O_{(s)}$ and $CuO_{(s)}$ should be probed. Of particular interest are regions and temperatures where first-principles simulation has predicted corrosion, but the experimentally sourced diagrams suggest passivation behavior (T = 100 °C, pH $\approx$ 6-8). In the future the presence of specific ions at neutral pHs at high temperatures and pressures should be examined. We predict lower pressures to stabilize neutral ions (*e.g.*, CuOH, $Cu(OH)_2$) more readily than charged ions as pressure increases ($P \approx$ 500-5,000 bar, $T >$ 100 °C, pH$\approx$7). Last, we demonstrate how the foundations understood from copper electrochemical Pourbaix diagrams can be used to map out the corrosion conditions of a number of key infrastructure systems, including deep geological repositories storing spent nuclear waste.

CHAPTER 5

Understanding the Effects of Water Chemistry Treatments for Lead Release Control Strategies Though Thermodynamic Models of Scale Formation

Much of the work presented in the following chapter is available as a peer reviewed publication in *Journal of Physical Chemistry C* [213]. Contributing researchers to the project, also listed as authors on the paper, include Alex T. Tai, Dr. Raymond J. Santucci, Dr. John R. Scully, and Dr. James M. Rondinelli. Reprinted (adapted) with permission from L.N. Walters, A.T. Tai, R.J. Santucci, J.R. Scully, and J.M. Rondinelli "Density Functional Theory-Based Thermodynamic Model for Stable Scale Formation in Lead-Water Systems", *Journal of Physical Chemistry C*, 126, 39, 16841–16850 (2022) [213]. Copyright 2022 American Chemical Society.

5.1. Introduction and Literature Review

Lead was applied throughout much of human industrialization in energy, construction, beauty products, and more. Two of the largest lead water crises in recent decades, in Flint, MI and in Washington, DC, drew national attention to the dangerous amounts of lead release from legacy pipes into the public and private water supplies [214] of communities across the world [18,215-217]. With 6-10 million active lead service lines and countless lead-based private well systems in the U.S. alone, indigestible lead in drinking water remains a public health concern—particularly for under-served communities [218]. The Environmental Protection Agency (EPA) has attempted to preserve nominal lead levels through the Lead Copper rule approved in 1991 and revised in 2021, which requires systematic intervention for lead levels above 15 μg/L and specific planning for lead level reduction when concentrations reach 10 μg/L [219].

Indigestible lead released from pipes may occur via soluble lead present as aqueous ions in solution and as particulate lead. Solid lead particulates are insoluble nanometer or micrometer scale lead particles

created through precipitation of lead solids in solution or scale sloughing from pipe walls [220-222]. High soluble and particulate lead concentrations have been measured in water systems undergoing partial piping replacement due to galvanic couples with remaining pipe, and from lead or lead-containing pipes and solders with entrapped lead, demonstrating that newer or replacement infrastructure may not guarantee Pb-free water [223]. As global water resources become scarcer and infrastructure continues to age, establishing fundamental knowledge of the processes through which aqueous, bioavailable lead forms is of upmost public health importance.

Strategies implemented to control lead release are based on decades of water treatment and sampling, and through experimental studies of the effectiveness of corrosion inhibitors [224, 225]. Governments increase health outcomes for communities by incorporating water additives to reduce bacteria growth such as include chlorine and chloramines [226]. Common corrosion-control strategies include filtration (particularly for particulate lead), the addition of phosphates and adjustment of solution pH in order to induce passivation by the formation of an insoluble solid layer (scale) inside the pipe that blocks lead corrosion. However, myriad of tunable variables within aqueous systems have contributed to widespread failures due the confounding dependencies of corrosion on multiple environmental factors, including electrode potential changes due to changing disinfectant additives (Washington, DC) and water source switching accompanying corrosion inhibitor omission (Flint, MI) [217].

Models which account for the diverse, interconnected mechanisms of lead release, including bulk thermodynamic and kinetic factors, the effects of environmental changes (e.g., temperature, increased salinity from rising sea levels), additives, disturbances in pipe lines, and flow rates are lacking [227-230]. In particular, the ultimate structure and mechanisms by which corrosion inhibitors form solid scales in pipes that limit lead (II) release are not fully understood [225, 231, 232]. For example, it has been shown that the addition of orthophosphate as a corrosion inhibitor causes the formation of scales dominated by hydroxylpyromorphite and $Pb_3(PO_4)_2$ [225, 231, 233]. Although studies have directly observed lead carbonate scales to form on pipes expected under operating conditions, other data on lead phosphate scales are unable to identify such scales despite current models predicting their stability [17, 225]. We note that characterizing the growth of scales is challenging, in part because of limited spectral ranges for Raman spectroscopy [17], inadequate

solution control, little initial starting scale monitoring [234], and the *ex-situ* testing nature due to removal and recovery of scales on pipe for laboratory characterization. These limitations necessitate the integration of literature covering multiple experimental techniques here and elsewhere to best support solid lead phase formation.

First-principles calculations based on density functional theory (DFT) have been shown to be a rigorous electronic structure method from which to construct predictive and descriptive thermodynamic models of corrosion, including the evaluation and design of corrosion inhibitors for transition and post-transition metal compounds [27, 235]. This approach constructs electrochemical pH-potential diagrams, also called Pourbaix diagrams [1, 53, 227], using quantum-mechanically computed Gibbs free energies of formation [236]. Herein, we utilize our recently implemented computational workflow to assess the stability of relevant lead compounds with varying environmental conditions and evaluate the effects of prevalent phosphate and carbonate ions on lead scale formation [216, 225]. We show that relativistic spin-orbit effects and non-ideal solution interactions [67, 127, 128] are required to formulate an accurate thermodynamic model consistent with experimentally observed phases (such as those reported in Table 5.3). Our models suggest that the reported success of water chemistry treatment with orthophosphates likely depends on water lead levels (transiently) exceeding the LCR or secondary trace elements, e.g., Ca and other divalent cations, in promoting the Pb orthophosphate stability. It is recognized that systems in the field are far from equilibrium; nonetheless, thermodynamics models are a necessary starting point. Our work provides improved understanding of the thermodynamic factors and boundary conditions governing soluble Pb(II), and which influence scale formation and therefore release of particulate lead.

5.2. Results

5.2.1. Lead Oxide Formation Energies

Accurate Pourbaix diagrams require high quality Gibbs free energies of formation values $\Delta_f G$ for all solid compounds and aqueous species possible in solution. For the Pb-H_2O system, we first compute the $\Delta_f G$ values for native Pb oxides using multiple levels of DFT with spin-orbit coupling (SOC) by using the following exchange-correlation functionals: LDA, PBE, PBEsol, and SCAN. (See methods for a brief description of the functionals.) Figure 5.1a compares our results against experimentally reported $\Delta_f G$ values. The stable

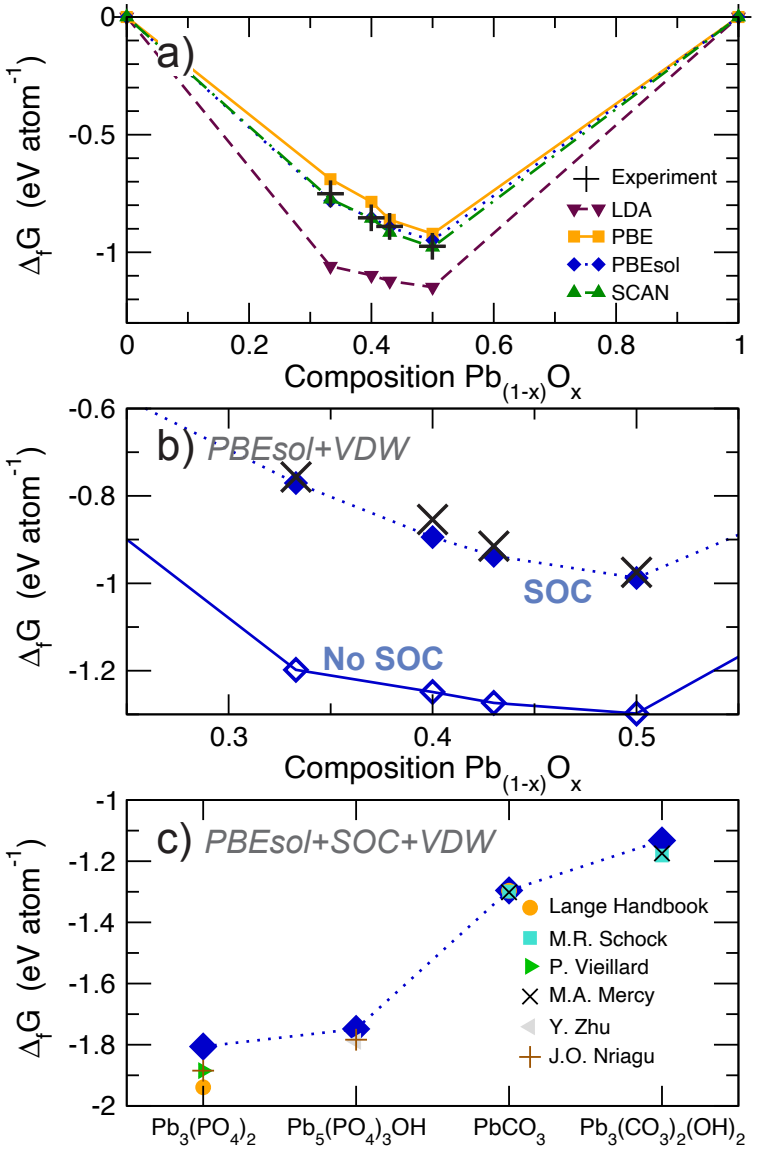

Figure 5.1. (a) Calculated free energies of formation for solid lead oxides at $T = 298.15\,\mathrm{K}$ with different functionals compared to experimental $\Delta_f G$ reported from a number of sources [1,8-14]. Stable and metastable oxides include PbO_2, Pb_2O_3, Pb_3O_4, and PbO. (b) Detailed comparison over a narrower composition range showing the sizeable overestimation in $\Delta_f G$ compared to experiment when spin-orbit coupling (SOC) is not included in the DFT-PBEsol calculations with van der Waals interactions. (c) Calculated $\Delta_f G$ values with SOC and VDW interactions for the most stable solid lead phosphates and carbonates compared to experiment.

lead oxides, in order of mole fraction, are PbO_2, Pb_3O_4, and PbO for all levels of theory. Pb_2O_3 is always stable or above the hull by a few meV per formula unit (f.u.), while Pb_2O is unstable. LDA gives large

$\Delta_f G$ values, while PBE Gibbs free energies of formation are slightly below experimental and average DFT values. In contrast, the semi-local functionals PBEsol and SCAN give free energies of formation closest to experiment; they are within a few percent or less for each compound. For example, PBEsol gives Pb_2O and Pb_2O_3 to be 446 meV/f.u. above the convex hull and on the hull, respectively. Equilibrium reaction information supports the assignment of Pb_2O_3 as a stable phase on the hull [1]; however, the corresponding thermodynamic data is unavailable for Pb_2O. Therefore, we formulate our thermodynamic models using PBEsol to balance computational feasibility and accuracy.

Accurate Pourbaix diagrams require high quality Gibbs free energies of formation values $\Delta_f G$ for all solid compounds and aqueous species possible in solution. For the Pb-H_2O system, we first compute the $\Delta_f G$ values for native Pb oxides using multiple levels of DFT with spin-orbit coupling (SOC) by using the following exchange-correlation functionals: LDA, PBE, PBEsol, and SCAN. (See methods for a brief description of the functionals.) Figure 5.1a compares our results against experimentally reported $\Delta_f G$ values. The stable lead oxides, in order of mole fraction, are PbO_2, Pb_3O_4, and PbO for all levels of theory. Pb_2O_3 is always stable or above the hull by a few meV per formula unit (f.u.), while Pb_2O is unstable. LDA gives large $\Delta_f G$ values, while PBE Gibbs free energies of formation are slightly below experimental and average DFT values. In contrast, the semi-local functionals PBEsol and SCAN give free energies of formation closest to experiment; they are within a few percent or less for each compound. For example, PBEsol gives Pb_2O and Pb_2O_3 to be 446 meV/f.u. above the convex hull and on the hull, respectively. Equilibrium reaction information supports the assignment of Pb_2O_3 as a stable phase on the hull [1]; however, the corresponding thermodynamic data is unavailable for Pb_2O. We also find that resource-intense exact Fock-exchange does not improve the level of agreement (see Table 5.1). Therefore, we formulate our thermodynamic models using PBEsol to balance computational feasibility and accuracy.

The excellent quantitative agreement in $\Delta_f G$ values is a consequence of our treatment of the relativistic SOC interactions for Pb. [237]. Figure 5.1b shows the effects of including SOC on the DFT-PBEsol free energies of formation. Although all values reported include van der Waals (VDW) interactions, the correction is minor for the native Pb oxides (< 45 meV/atom, less than 5 % and within 4 % of the experimental value). We find $\Delta_f G$ values for PbO_2 and PbO are within approximately 14 meV/atom of the experimentally reported

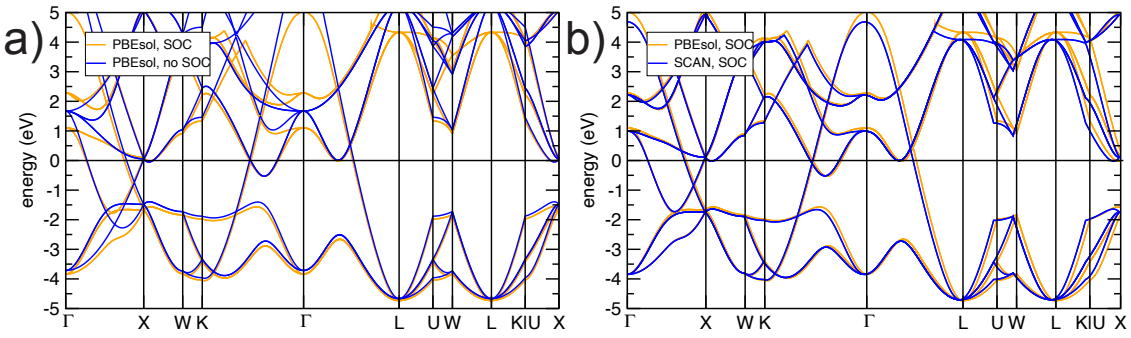

Figure 5.2. Overlaid electronic band structures for elemental lead comparing (a) calculations with and without spin-orbit coupling (b) inclusion of PBEsol or SCAN functionals.

values. Pb_2O_3 and Pb_3O_4 are within 40 meV/atom. Without SOC, our energies increase by more than 200 meV/atom, corresponding to a 20 % increase in $\Delta_f G$, which would lead to spurious relative stability of the oxide against other compounds or species. This improvement is due to SOC decreasing the electronic energy of Pb by 539 meV/Pb with SOC, which also affects the electronic band structure (Figure 5.2a), while other phases are only stabilized by at most 439 meV/Pb. We find the SOC corrections are equally important to our DFT-SCAN data (Figure 5.2b), indicating SOC inclusion is necessary to accurately model the lead oxide system. We note that our structural and electronic data is also in general agreement with R.T. Grimes *et al.* [238], though we attribute some structural differences and any reported crystalline $\Delta_f G$s to SOC not being explicitly included.

Figure 5.1c shows $\Delta_f G$ calculated with the PBEsol functional, and SOC and VDW interactions for the most energetically stable solid phases of lead carbonates and lead phosphates. PBEsol+SOC+VDW achieves good agreement with the experimental $\Delta_f G$ values [13,14], in part because the VDW interactions improve the hydrogen-bonding description in these phases; for example, $Pb_5(PO_4)_3OH$ is further stabilized by 105 meV/f.u. owing to its stacked O-H bonds in the [001] direction. This stabilization shifts the calculated $\Delta_f G$ values closer to experiment. The calculated free energy of formation of $PbCO_3$ is very well reproduced (<1 meV difference), whereas the $\Delta_f G$ for $Pb_3(PO_4)_2$ presents the largest difference from experiment at 134 meV/atom from one source [9], although others report closer $\Delta_f G$ values (<80 meV/atom difference) [11, 13]. The $\Delta_f G$ of $Pb_3(CO_3)_2(OH)_2$ also exhibits minor deviation from experiment (within 5 meV/atom). We attribute this discrepancy to ambiguity over the H positions in the hydrocerussite structure, which are statistically

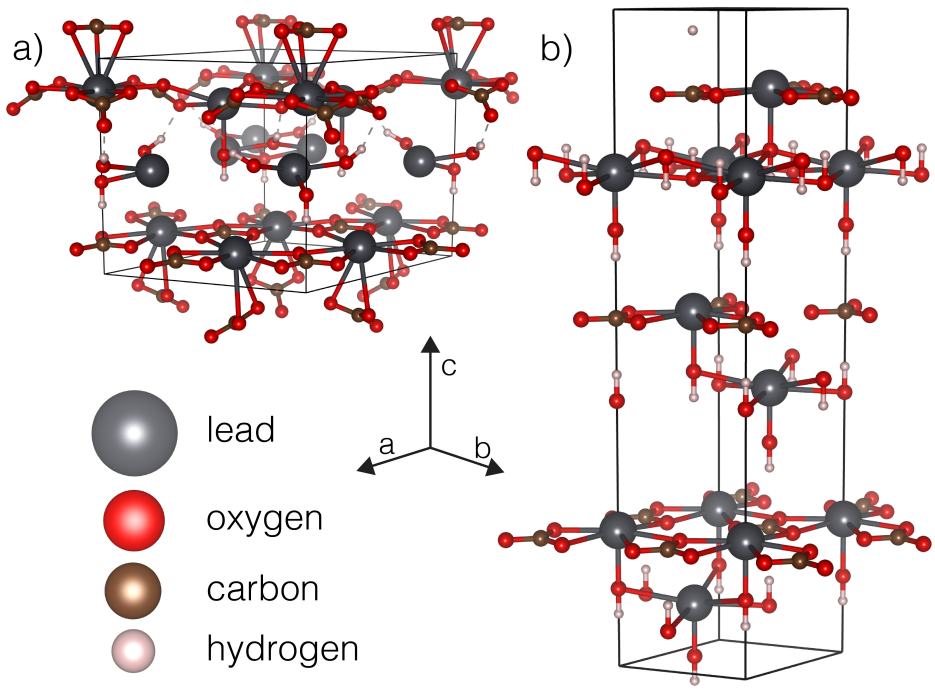

Figure 5.3. The considered structures for hydrocerussite, sourced from previous literature are shown [15, 16]. The structure in (a) exhibits a lower $\Delta_f G$/atom and $\Delta_f G$/Pb.

disordered. Material composition and structures have varied in literature between naturally occurring and synthetic sources [15, 16, 239]. Additionally, characterization of the location of hydrogen in the material has not been reported. Therefore, we incorporated hydrogen into the structure of two previously reported hydrocerussite compounds based on hypothesized H locations reported in previous literature. The methods used to select probably hydrogen positions follows that used in similar apatite structures from A. Slepko *et al.* [240] Crystallographic information for the chosen phase is reported in [213] and the relaxed DFT structures are shown in Figure 5.3.

We probed the necessity of resource-intense exact exchange to model lead and lead oxides using the hybrid exchange-correlation functional (HSE06) [91]. Other literature which sources free energies of formation from DFT for Pourbaix diagrams has found a Fock-exchange term for short-range interactions to be necessary to correctly capture electrochemical passivation behavior [4, 26, 27]. HSE06 relaxations and static calculations were used to find the electronic energies of lead oxides on or near the convex hull. Convergence tolerances of a 400 eV plane wave energy cut off and 2,500 KPPRA were used. The total energy of the system was

converged to 10^{-5} eV. We note these tolerances were lowered compared to other functionals in this work to make the computations finish within a reasonable time frame. Furthermore, SOC was not included. We find that because the HSE06 functional underestimates the formation energies of lead oxides (Table 5.1), there is not a clear advantage for using the high-resource-cost functional in place of a semi-local functional that would also allow SOC interactions to be included.

Table 5.1. The formation energies of lead oxides which appear on or near the convex hull, calculated with the hybrid functional HSE06. For comparison, the difference between experimental [1] and HSE06 $\Delta_f G$s are also listed.

Material	HSE06 $\Delta_f G$ (eV/f.u.)	Difference Between Experimental $\Delta_f G$ (eV/f.u.)
$PbO_{(s)}$	-1.8463	-0.1295
$Pb_2O_{3(s)}$	-3.9012	-0.5703
$Pb_3O_{4(s)}$	-5.9895	-0.5713
$PbO_{2(s)}$	-2.1135	-0.1984

5.2.2. Capturing Non-Ideal Solution Effects

Subsequent sections illustrate phase diagrams at elevated concentrations where nonideal solution effects may be significant. Therefore, use of the extended Debye-Hückel equations and Robinson-Stokes model were used to calculate the activity coefficients for various aqueous ions. The Bromely parameters necessary for these equations are shown in Table 5.2. We note that PbH_2, H_3PO_4, and H_2CO_3 are not included, because the Bromley model is not valid for electrically neutral aqueous ions. Instead, the activity was approximated as unity following field standard.

Table 5.2. The Bromley parameters, B and δ are shown below. Information for each ion were found from previous literature or estimated (values shown in parenthesis).

Ion	z	$B_{\pm}$	$\delta_{\pm}$
$PbOH^{+}$	1+	(0.05)	(0.2)
Pb^{2+}	2+	-0.104	0.25
Pb^{4+}	4+	(-0.1)	(0.27)
$HPbO_2^{-}$	1-	(0.05)	(0.2)
PbO_3^{2-}	2-	(0.05)	(-0.7)
H^{+}	1+	0.0875	0.103
OH^{-}	1-	0.076	-1.0
$H_2PO_4^{-}$	1-	-0.052	0.20
HPO_4^{2-}	2-	-0.010	-0.57
PO_4^{3-}	3-	0.024	-0.70
HCO_3^{-}	1-	(0.05)	(0.2)
CO_3^{2-}	2-	0.028	-0.67

Within the Robinson-Stokes model, we estimated a_w as the molar fraction of water in solution X_w, following methods by O. Miyawaki et al. [241] We approximated n from values provided by R.H. Stokes *et al.* [127], calculated values of hydrated Pb(II) ions [242, 243], and the other acids and bases [244]. The approximated hydration numbers for each ion used in this study are as follows: 7 (Pb^{2+}), 8 (Pb^{4+}), 5 (PbO_2^{-}), 3 (PbO_3^{2-}), 4 (H^{+}), 0.5 (OH^{-}). The total n was found from a sum of the individual ions in the electrolyte.

5.2.3. Lead Pourbaix Diagrams

We next explore possible thermodynamically stable solid scales and ions, and their dependencies on electrode potential, pH, and concentration to assess lead's electrochemical immunity, corrosion, and solid-oxide formation. Figure 5.4 presents the Pb-H_2O Pourbaix diagrams obtained using experimental $\Delta_f G$ values [1] and our DFT PBEsol+SOC+VDW calculated values with variable aqueous ion concentrations (m_{Pb}), where all diagrams are calculated within a non-ideal solution model (see Section 3.2.1.1) and the electrode potential is reported

versus the standard hydrogen electrode (SHE). In particular, nonideal solution effects are important to fine tune dissolution boundaries by approximating factors such as ion charge, ion size, and ion-ion interactions into the model with little requisite computational resources. Independent of concentration, all Pourbaix diagrams show that $Pb_{(s)}$ is stable at negative (reducing) potentials. Insoluble $PbO_{2(s)}$ is stable at positive (oxidizing) potentials, except in extreme alkaline conditions and low lead concentrations where the PbO_3^{2-} ion is stable. $Pb_3O_{4(s)}$ also appears in all diagrams around 500 mV and neutral to alkaline pH. Experimentally, no $Pb_3O_{4(s)}$ and $Pb_2O_{3(s)}$ phases were found in surface measurements by R.J. Thibeau *et al.* due to limited potential and pH control [17], which could be supported by their relatively smaller domain sizes in the calculated diagrams.

The Pourbaix diagram constructed from experimental free energies of formation (Figure 5.4a) and from our first-principles calculated $\Delta_f G$ values (Figure 5.4b) at high lead concentrations ($m_{Pb} = 1$ m) show excellent agreement with each other and with direct experimental observations (solid symbols). For specified potential-pH values, stable elemental lead is indicated with black circles, whereas solid lead oxide phases observed during aqueous corrosion are indicated with purple triangles [17]. We note this study experienced characterization limitations due to the stable $PbO_{2(s)}$ having no infrared absoprtion bands or Raman spectra in the region tested. Nonetheless, oxides were observed to occur where the triangle points are found at high applied potentials. We accurately capture the dissolution boundaries among species compared to experiment with a difference of ~0.2 pH units for each ion by employing the Robinson-Stokes model to approximate the effect of high concentration electrolyte (soluble lead) solutions [127]. The Bromley model is utilized to effectively handle lower concentrations ($m_{Pb} \leq 0.1$ m). The experimentally sourced diagram in Figure 5.4a exhibits a slightly smaller $PbO_{(s)}$ area because of the minor but more positive lead oxide free energy of formation. Although a passive $Pb_2O_{3(s)}$ region appears in a narrow stability window between $PbO_{(s)}$ and $Pb_3O_{4(s)}$, near 500 mV in our calculated diagram (Figure 5.4b), it has not been conclusively verified as a stable oxide in experiment.

Our DFT-PBEsol+SOC+VDW model accurately describes the direct observations of immunity and solid oxide formation in lead films for high soluble lead concentrations at standard state. This initial comparison

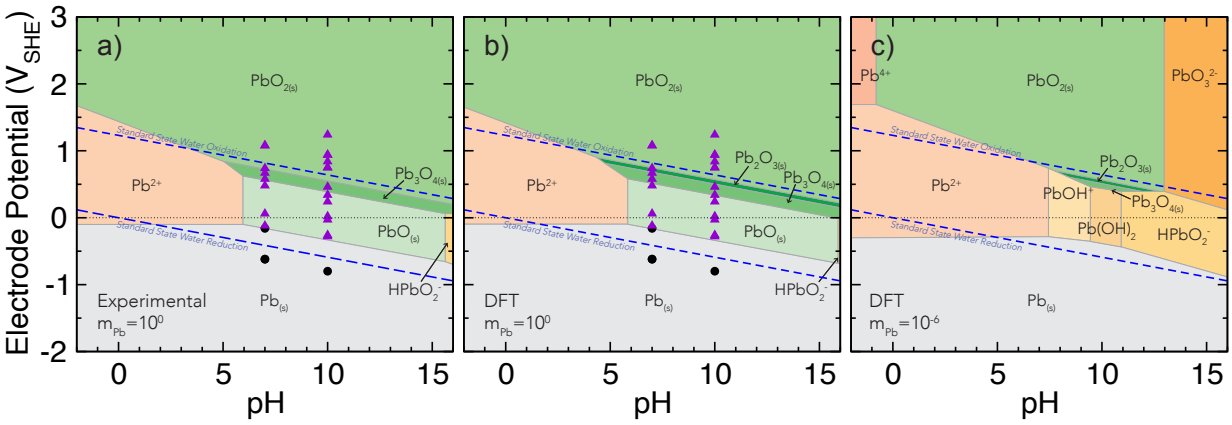

Figure 5.4. Aqueous Pb-H_2O Pourbaix diagrams in pure water at standard state and with non-ideal solution effects for high Pb concentration ($m_{Pb} = 10^0$ m) using (a) experimental $\Delta_f G$ values from Refs. [1,8,9] and (b) our DFT-PBEsol+SOC calculated $\Delta_f G$ values. Black circles and purple triangles indicate direct experimental film growth observations of $Pb_{(s)}$ (black circles) and $PbO_{(s)}$ (purple triangles) [17]. Note that unambiguous experimental phase identification of $PbO_{2(s)}$ was not possible owing to the absence of first-order infrared absorption bands and Raman activity in the spectral range probed. (c) Pourbaix diagram at the standard corrosion limit ($m_{Pb} = 10^{-6}$ m) obtained from our DFT-PBEsol+SOC calculated $\Delta_f G$ values. Lead corrosion is predicted to occur at these low lead concentrations without an applied potential through the formation of aqueous Pb^{2+} (pH < 7), $PbOH^+$ (7 < pH < 9.5), $Pb(OH)_2$ (9.5 < pH < 11), or $HPbO_2^-$ (pH > 11).

allows us to justify use of our computational scheme to further probe thermodynamic corrosion propensities at more dilute concentrations and with additional additives, which will form solid phases in solution.

Figure 5.4c shows our simulated Pourbaix diagram at the standard corrosion limit of ($m_{Pb} = 10^{-6}$ m). As in the high soluble lead concentration regions, our work employs a non-ideal solution model to more accurately capture the phases boundaries in the Pourbaix diagram, particularly at moderate lead concentrations. The use of an ideal solution model in Pourbaix's original report and Ref. [228] over or under stabilize boundaries such as Pb^{2+} by 0.3 pH points or more. At these lower concentrations, elemental Pb is immune to corrosion below approximately -0.12 V, above which lead oxidizes to form ionic aqueous ions. Pb^{2+} ions are found over acidic conditions (pH < 7), while highly alkaline solutions (pH > 10.5) stabilize aqueous $HPbO_2^-$. Differently from Pourbaix's original report in 1966, for which more recent Pb-corrosion models base the selection of aqueous ions on, we include additional Pb(II) ions. Specifically, we include $PbOH^+$ and $Pb(OH)_2$, which have been observed in Pb-H_2O solubility studies [245-247] and dominate at approximately 7 < pH < 9.5 and 9.5 < pH < 11, respectively (Figure 5.4c). An important implication of our predicted $PbOH^+$ stability at the

standard-corrosion limit is that it requires other scale-formation and precipitation-product models to consider it a viable aqueous Pb(II) dissolution product in addition to the commonly reported Pb^{2+} ion.

5.2.4. Role of Additives on Electrochemical Solid Oxidation

We now examine thermodynamically the electrochemical phase formation and Pb corrosion arising from the presence of two common ions directly measured in water systems throughout the U.S., orthophosphates (PO_4^{-3}) and carbonates (CO_3^{-2}) [10, 233]. Phosphate is used as a common lead release limiting additive, and carbonates commonly leach into water system through organic matter and as calcium carbonate salts. Phosphates can react with dissolved cations in water, including aqueous Pb ions, to form metal phosphate salts that can nucleate on internal surfaces of pipes to produce protective coatings, as well as promote direct scale formation of passive Pb compounds on piping and solder joints. Previously, added scales from orthophosophates were reported to establish protective surface layers which isolate native lead and establish kinetic barriers from lead dissolution, while the presence of carbonates did not sufficiently impede lead release [10, 216, 221]. Typical concentrations of added phosphates in water are around 1-3 mg/L [18] ($m \approx 10^{-5}$) and carbonates are typically measured near 60-180 mg/L [19] ($m \approx 10^{-3}$–10^{-4}). Consequently, $Pb_3(PO_4)_2$, $Pb_5(PO_4)_3OH$, $PbCO_3$, and $Pb_2(CO_3)_2Pb(OH)_2$ are the expected primary solid phases arising from these additives. Therefore, we performed high-fidelity DFT-PBEsol+SOC+VDW calculations on each phase to obtain reliable free energies of formation. We identified $Pb_5(PO_4)_3OH$ and $PbCO_3$ as the most thermodynamically stable solid phases on a per Pb atom basis. These data are then used to simulate the additive-based Pb Pourbaix diagrams.

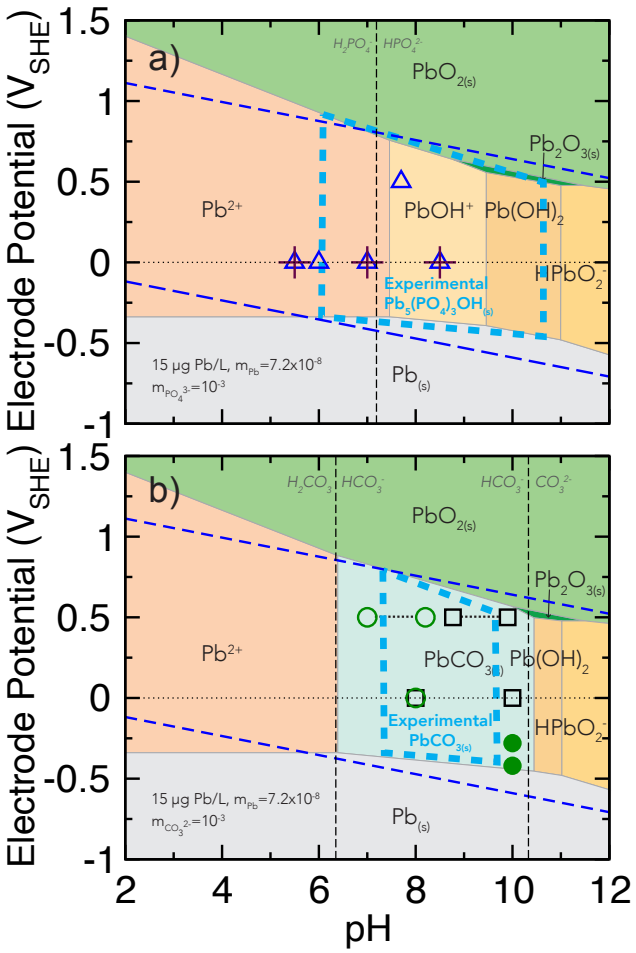

Figure 5.5. Simulated standard state Pourbaix diagrams including (a) phosphate and (b) carbonate additives at the specified Pb and additive concentrations. No solid lead phosphate regions are predicted at the low permitted lead concentration level. Carbonate additives cause a dominant cerussite ($PbCO_3$) solid oxidation region, replacing portions of the Pb^{2+} corrosion region and shifting the lead oxidation potential for scale formation potential lower by nearly -450 mV with respect to the SHE. The broken vertical black lines represent phosphate and carbonate aqueous ions in solution with zero, one, or two protons. The dark blue broken lines represent the stability region of water. The thick, light blue broken polygons show the stability region of lead phosphates and carbonates based on experimental formation free energies. Green symbols in (b) correspond to experimentally observed conditions for lead carbonate phase formation [17].

Figure 5.5 shows our calculated Pourbaix diagrams for both additives at standard state with EPA acceptable soluble lead concentrations, $m_{Pb} = 7.24 \times 10^{-8}$, and approximate additive concentrations, $m_{CO_3^{-2}} = m_{PO_4^{-3}} = 10^{-3}$, of those currently in use [18, 19]. Many of the same lead stability regions from the additive

free Pb-H_2O Pourbaix diagrams appear in Figure 5.5, including $Pb_{(s)}$, Pb^{2+}, and $PbO_{2(s)}$. We find, however, that phosphate ions do not supplant the formerly stable $PbOH^+$ and $Pb(OH)_2$ (corrosive) species at low Pb concentrations, low potentials, and neutral pHs (Figure 5.5a). Note that when lead carbonates or phosphates do not appear in a stability region, they are assumed to be aqueous ions in solution with zero, one, or two protons as specified by the broken vertical black lines. There is no solid oxidation phase at the low water lead levels shown, which follow the accepted EPA lead action level of 15 μg Pb/L [**219**]. We find that our calculated orthophosphate film stability, even at higher lead concentrations (Figure 5.6), is smaller than that predicted by others [**216**].

The absence of hydroxylpyromorphite $Pb_5(PO_4)_3OH_{(s)}$ scale as reported in experimentally derived Pourbaix diagrams for low potentials and neutral pH values could be attributed in part to dissolution rate suppression as in hydrocerussite [**248**]. Based on the quality of our first-principles data presented in Figure 5.1c, however, we attribute the absence of $Pb_5(PO_4)_3OH_{(s)}$ in Figure 5.5a to overestimated $\Delta_f G$ values extracted from experiment. The measured dissolution equilibrium gives $\Delta_f G$ values that vary by as much as 95 meV/atom in a single study, which is more than our DFT calculated energy varies from the average experimental values. The average experimental free energy of formation is 30 meV/atom lower for $Pb_5(PO_4)_3OH_{(s)}$ than our DFT calculated value, which is enough to stabilize solid hydroxylpyromorphite at 15 μg/L [**13**, **14**].

Lead phosphate films have not been observed (or were under-observed relative to model calculations based on experimental formation free energies) under several different environmental conditions: in real legacy piping treated with orthophosphates (black square at some approximate conditions in Figure 5.5a) [**225**], in direct aqueous film growth at high lead concentrations [**17**, **232**], and in new lead pipes tested using synthetic tap water conditions in a long-term laboratory setting [**234**]. A more exhaustive list of references on reported solid lead phosphate formation is given in Table 5.3. Here, high variability could arise from changes in pH, uncertainty in phase crystallography, defects, and ion concentrations, or the underlying DFT structural model where hydroxide partial Wyckoff site occupancy is not fully captured, leading to configurational entropy loss (estimated to be small). Furthermore, other competing phases with similar $\Delta_f G$ values may be present in real solutions and scales. $Pb_3(PO_4)_{2(s)}$, which has a slightly lower $\Delta_f G$ per Pb atom, has been observed to

form upon reconstruction of a synthetic hydroxylpyromorphite in some dissolution studies and in mineral growth studies [14, 232].

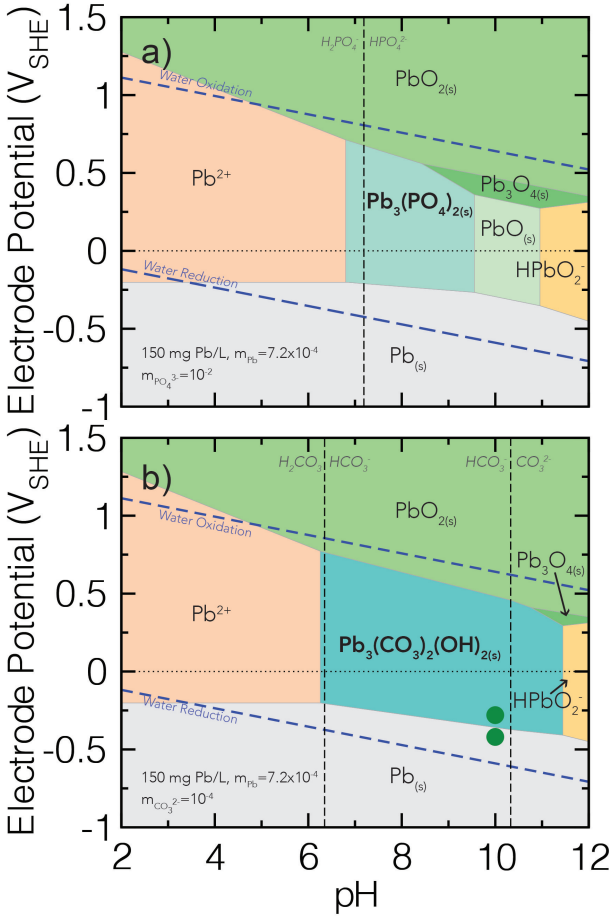

Figure 5.6. The multi-element Pourbaix diagrams sourced from DFT free energies of formation at $m_{Pb} = 7.24 \times 10^{-4}$, $m_{CO_3^{-2},PO_4^{-3}} = 10^{-4}$ and standard state: (a) lead orthophosphate, showing the $Pb_3(PO_4)_2$ phase while the $Pb_5(PO_4)_3OH$ phase is suppressed, and (b) lead carbonate, showing hydrocerussite while the cerussite phase ($PbCO_3$) is suppressed. In (a), the passivation region ranges from approximately $7 < pH < 11$ and $-0.3 < V < 0.75$ (pH dependent). The hydrocerussite stability region extends farther into basic conditions, reaching almost a pH of 6.

Other reports suggest that trace metals often found in hard drinking water, e.g., alkaline earth metals, may be necessary to realize a lead-phosphate scale through the formation of a substituted calcium phosphate solid hydroxyapatite (HA) scale [14, 222, 231, 234, 249, 250]. These studies propose that when moderate Ca concentrations are present (hard water contains $m_{Ca} \geq 10^{-4}$ [19]), the very stable apatite $Ca_5(PO_4)_3OH_{(s)}$ scale

will form. Surface absorption and a fast exchange reaction, $Ca_5(PO_4)_3OH + xPb^{2+} \rightarrow Ca_{10-x}Pb_x(PO_4)_6OH_2 + xCa^{2+}$, is thought to occur [222, 234, 249, 250], in part because of entropic stabilization [14], though we note surface HA could lead to higher lead solubilities [251]. Other studies have suggested lead precipitate reactions form dissolved HA to grow hydroxylpyromorphite [250]. This rapid phase transformation is not accounted for in our thermodynamic model (Figure 5.5a). Lead phosphate scales like $Pb_5(PO_4)_3OH$, which are not as energetically stable as HA, have not been observed or were under-observed within isolated models of direct aqueous film growth [17, 232] and in some legacy piping treated with orthophosphates [225] (see also Table 5.3). On the other hand, calcium-lead apatite scales are known to occur in phosphate-treated systems with Ca present [231, 234, 250]. Therefore, past findings support the validity of the electrochemical diagram in Figure 5.5a, rather than that sourced from energies from experiment, and point to likely effects of unintentional trace elements like Ca on stability of a passivating phosphate surface through (*i*) fostering a HA dissolution to hydroxylpyromorphite percipitation mechanism and (*ii*) Pb^{2+}-Ca^{2+} cation exchange [250].

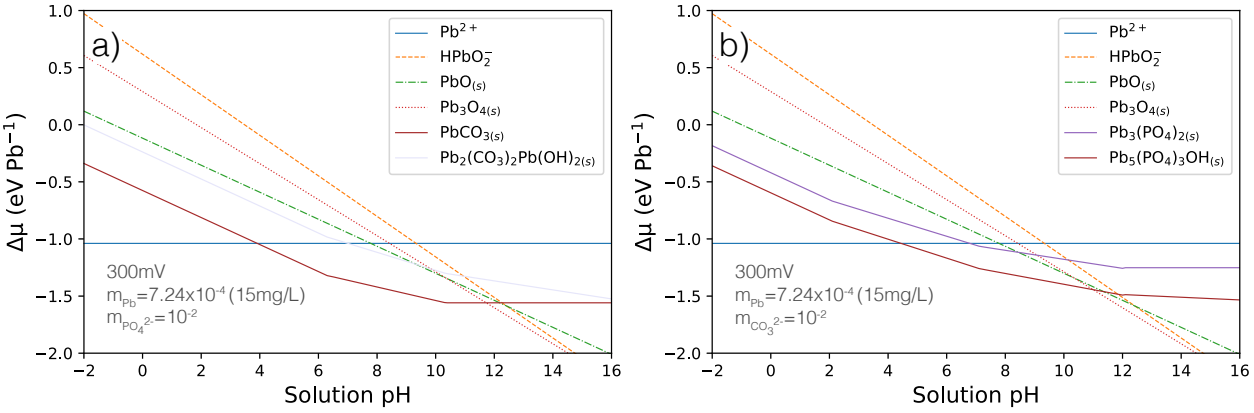

Figure 5.7. Driving forces for (a) lead phosphate and (b) lead carbonate systems at high concentrations. The driving forces to create a lead carbonate scale are greater for $PbCO_3$ than $Pb_5(PO_4)_3OH$.

In contrast to phosphate addition, aqueous carbonate is relatively effective at thermodynamically stabilizing a film at low soluble lead concentrations and moderate to high pHs (Figure 5.5b), consistent with several reports finding that lead carbonate scales form readily at numerous conditions [17, 225, 234]. However, we emphasize that studies have found that effects other than thermodynamics, such as diffusivity, porosity, and morphology, have made lead carbonate experimentally ineffective at lowering lead concentrations below

15 μg/L [216]. We find that cerussite replaces the formerly stable $PbOH^+$ and $Pb(OH)_2$ (corrosion) and $PbO_{(s)}$ (non-protective scale) to form a phase region from about $6.4 < pH < 10.4$ and $-0.5 < V < 0.5$ (pH dependent), and extends stability into the lead immunity region. The strong thermodynamic stability seems to indicate that there are greater thermodynamic driving forces to create a stable $PbCO_{3(s)}$ surface among all of the phases tested with the two different additives; therefore, it is probable to form in real solutions but is dependent upon reaction kinetics and other solution factors such as the concentration of trace elements. Some studies have found higher amounts of cerussite rather than hydrocerussite to be prominent in real piping systems [225, 232]. Although the lack of a ($Pb_3(CO_3)_2(OH)_2$) hydrocerussite region in Figure 5.5b is due in part to dissolution rate suppression not accounted for in our model [248], direct thin film growth experiments (filled green dots) in Figure 5.5b) support our finding of stable $PbCO_{3(s)}$ near the alkaline solid oxidation-immunity boundaries [17]. Moreover, phase characterization from real pipe samples are shown with open symbols: $PbCO_3$ (green circles), $Pb_3(CO_3)_2(OH)_2$ (black squares), $Pb_5(PO_4)_3OH_{2(s)}$ (blue triangles), $Pb_3(PO_4)_2$ (purple pluses) in Figure 5.5 to provide greater context on reported materials formation. However, we note that the conditions labelled are tentative due to the transient, sometimes undefined sample histories and ambiguity in the aqueous environment. In particular, due to the similar driving forces for cerussite and hydrocerussite (Figure 5.7), it is reasonable that condition variability not considered in our model (e.g., kinetics) leads to the scattered phases recorded within the lead carbonate stability region as some of these reports are taken from experiments which have not reached equilibrium.

5.2.5. Environmental Boundary Condition Optimization for Scale Formation

We next vary the environmental boundary conditions to assess the robustness of the lead scales. Figure 5.8a-d map the critical Pb-activity value for the general dissolution boundary between a lead compound and soluble Pb ions. It is determined by self-consistently obtaining the terminal pH-potential value for a two phase equilibrium (line) or a three phase equilibrium (point) for a given lead activity (η_{Pb}). This critical value for the multi-element systems is visualized by the marked × labelled *solids stability bound* in Figure 5.8e-f. The immunity-dissolution boundary in Figure 5.8a delineates the lead activity below which dissolution is thermodynamically driven, as a function of critical potential. All diagrams (except Figure 5.8a) were calculated at the standard electrode potential of lead's half cell reaction $Pb \rightarrow Pb^{2+} + e^-$, -126 mV versus

Table 5.3. Summary of key studies on solid lead phosphate formation and identification by: (*i*) film growth, precipitation, and cation-substitution studies, (*ii*) synthetic piping studies, and (*iii*) real pipe extraction studies.

Film growth, precipitation, and cation-substitution studies				
Authors	Title	Journal	Summary	Notes
R.J. Thibeau, C.W. Brown, A.Z. Goldfarb, and R.H. Heidersbach	Infrared and Raman spectroscopy of aqueous corrosion films on lead [17]	J. Electrochem. Soc.	Lead films were held in phosphate solution at varying pHs and potentials	Raman spectra may have been too narrow to capture lead phases
X. Li, B. Azimzadeh, C.E. Martinez, and M.B. McBride	Pb Mineral Precipitation in Solutions of Sulfate, Carbonate and Phosphate: Measured and Modeled Pb Solubility and Pb^{2+} Activity [232]	Minerals	Lead precipitates were synthesized and characterized in sulfate, carbonate, and phosphate solutions	
J.D. Pasteris, Y. Bae, D.E. Giammar,S.N. Dybing, C.H. Yoder, J. Zhao, and Y. Hu	Worth a Closer Look: Raman Spectra of Lead-Pipe Scale [252]	Minerals	Discusses use of Raman to characterize lead precipitates, including substituted lead phosphate scales	Review paper with some original information
Y. Takeuchi, T. Suzuki, and H. Arai	A study of equilibrium and mass transfer in processes for removal of heavy-metal ions by hydroxyapatite [249]	J. Chem. Eng. Japan	Pb^{2+} substitution rates are found for hydroxyapatite in solution	
Q.Y. Ma, S.J. Traina, T.J. Logan, and J.A. Ryan	In situ lead immobilization by apatite [250]	Environ. Sci. Technol.	Hydropyromorphite was found to occur precipitation of aqueous Pb and HA	Dissolved HA was the only source of phosphate
S.M. Vesecky J. Liu, R.M. Friedman, F. Pacholec, and J.B. Lechner	Comparison of film formation using phosphate inhibitors in systems with comparable water qualities [253]	J. N. Engl. Water Works Assoc.	Investigation of efficacy of different phosphate inhibitors on forming lead scales	
G.P. Lobo and A.J. Gadgil	Preventing leaching from lead water pipes with electrochemistry: an exploratory study [254]	Environ. Sci. Water Res. Technol.	The scales of lead coupons and reclaimed pipes subjected to orthophosphate synthetic tap water were characterized	
B.P. Boffardi and A.M. Sherbondy	Control of Lead Corrosion by Chemical Treatment [255]	Corrosion	Lead pipe sections were subjected to water treatments, including orthophosphates and characterized	
Synthetic piping studies				
Y. Bae, J.D. Pasteris, and D.E. Giammar	The Ability of Phosphate To Prevent Lead Release from Pipe Scale When Switching from Free Chlorine to Monochloramine [234]	Environ. Sci. Technol.	Piping system was set up and solutions were run through to evaluate scales that formed	Phosphate solution was inadequately monitored, piping began solution exposure with PbO_2 scale
J. Zhao, D.E. Giammar, J.D. Pasteris, C. Dai, Y. Bae, and Y. Hu	Formation and Aggregation of Lead Phosphate Particles: Implications for Lead Immobilization in Water Supply Systems [222]	Environ. Sci. Technol.	Pilot piping systems are used to study lead phosphate aggregation and scale formation	
Y. Bae, J.D. Pasteris, and D.E. Giamma	Impact of orthophosphate on lead release from pipe scale in high pH, low alkalinity water [256]	Water Res.	Piping system was built from extracted LSL piping. Scales were analyzed after multi-month of orthophosphate treatment	
Real pipe extraction studies				
J. Tully, M.K. DeSantis, and M.R. Schock	Water quality–pipe deposit relationships in Midwestern lead pipes [225]	AWWA Wat. Sci.	Pipes from real lead service lines were extracted and internal scales characterized.	Phosphate was used irregularly (not controlled) to treat pipes
J.D. Hopwood, G.R. Derrick, D.R. Brown, C.D. Newman, J. Haley, R. Kershaw, and M. Collinge	The Identification and Synthesis of Lead Apatite Minerals Formed in Lead Water Pipes [231]	J. Chem.	Calcium substituted lead apatites were synthesized and identified in real piping	
M.K. DeSantis and M.R. Schock	Ground Truthing the 'Conventional Wisdom' of Lead Corrosion Control Using Mineralogical Analysis [257]	Proc. AWWA 2014 Water Quality Technology Conference	Over 300 pipe samples were taken from LSLs were taken and scales characterized	
L.W. Wasserstrom, S.A. Miller, S. Triantafyllidou, M.K. Desantis, and M.R. Schock	Scale Formation Under Blended Phosphate Treatment for a Utility With Lead Pipes [258]	J. Am. Water Work. Assoc.	Over 340 pipes from LSLs and steel piping systems were extracted and scales were characterized	Phosphate solution was not controlled or documented precisely within long term pipe treatment

SHE [259]. However, the diagrams are identical when the electrode potential is chosen to be the approximate solution potential of non-disinfected tap water (300 mV) [260] or at the lower potentials reported in some systems with high lead water levels (≈-250 mV) [220]. Because there is no change in Pb oxidation state, this activity boundary occurs at a fixed pH, although it is dependent on additive concentration (Figure 5.8c,d). It is linear in the potential-lead activity space and the critical potential value shifts to more negative voltages with decreasing lead activity. At $\eta_{Pb} = 10^{-7}$, which is still above the accepted lead action level, the potential drops to less than -300 mV, or 600 mV below the potential of tap water.

The critical Pb activity also decreases with elevated temperatures in the Pb-H_2O system, corresponding to a pH-dependent critical point for the $PbOH^+$-$Pb(OH)_2$-$PbO_{(s)}$ equilibrium (Figure 5.8b). At pH = 9.51, -126 mV (the standard electrode potential for lead [259]), and at standard state, the critical lead activity to stabilize any $PbO_{(s)}$ is $\eta_{Pb} = 1.86 \times 10^{-4}$. The Pb activity difference between near freezing temperatures (5°C) and high summer temperatures (≥ 40°C), however, is an increased by 95% at elevated temperatures (about 3.88 mg/L) and also occurs. These results emphasize that minerals and oxidizing disinfectants (leading to potential changes), and temperature volatility introduce significant variability on the boundary conditions of lead corrosion. Thus, control-mechanism modeling and lead-level testing should not be performed only at standard conditions.

Figure 5.8c,d show the most stable lead-phosphate and lead-carbonate triple points with respect to additive concentrations and lead activity. The triple points are calculated at the solid phase boundary intersecting with the Pb^{2+} to $PbOH^+$ predominance line near pH = 7. Here, the most probable solid scales at low lead levels are $Pb_5(PO_4)_3OH_{(s)}$ and $PbCO_{3(s)}$ for phosphate and carbonate addition, respectively. The minimum aqueous lead levels required to thermodynamically stabilize a scale are highly dependent upon additive concentration. The decrease of either additive concentration by an order of magnitude indicates an increase in soluble lead by approximately an order of magnitude. High enough levels of additive are imperative to foster thermodynamic driving forces for scale formation, but we note excess additives can also lead to harmful health and environmental implications. Consistent with our simulated Pourbaix diagram, the cerussite region is stabilized at lower lead concentrations, down to the lead-action level or below at reasonable carbonate concentrations. In contrast, lead levels are half an order of magnitude above the lead-action level, even at $m_{PO_4^{-3}} = 10^{-3}$, to stabilize a phosphate scale.

Finally, we present standard concentration-pH stability diagrams for orthophosphate (Figure 5.8e) and for carbonate (Figure 5.8f) addition at the lead action level (15 μg/L). For both additives, we find Pb^{2+}, $PbOH^+$, $Pb(OH)_2$, and $HPbO_2^-$ dominate at low and high pHs, respectively, at Pb concentrations below the critical value for solid oxide formation. We find very high orthophosphate concentrations $m > 10^{-3}$ are required to thermodynamically stabilize a protective $Pb_5(PO_4)_3OH_{(s)}$ scale at acceptable aqueous lead levels. At lower concentrations comparable to that in real pipes ($m \approx 10^{-5}$), no solid should form, again leading to

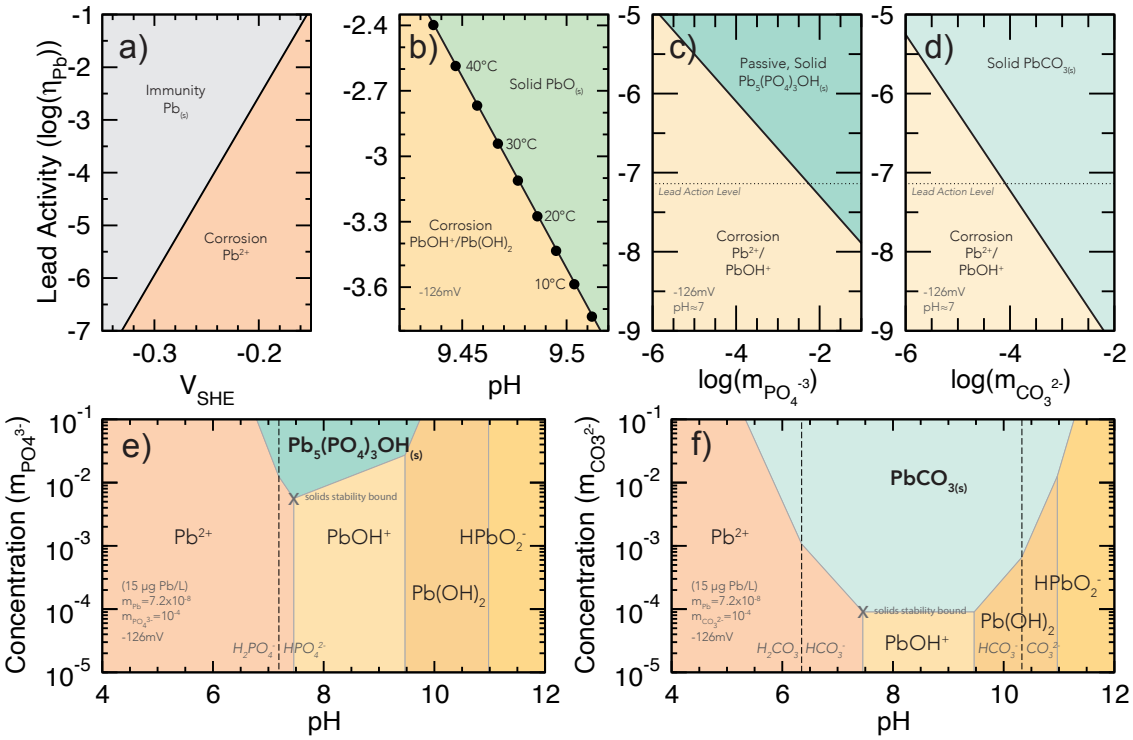

Figure 5.8. Phase diagrams showing environmental changes on lead corrosion, focusing on changes in the low lead activity boundary as function of (a) potential, (b) temperature and pH, and additive (c,d) concentrations. The concentration versus pH diagram (stability diagram) for (e) lead-orthophosphate and (f) lead-carbonate. The low pH boundary near pH $\approx 6-8$ for elemental lead is found to be too high, particularly for high temperatures and low lead concentrations. All diagrams other than in panel (a) were calculated at -126 mV versus SHE, the standard electrode potential of lead. All diagrams other than panel (b) were calculated at standard state. Note that typical phosphates added to water are around 1-3 mg/L ($\approx 10^{-5}$ m) [18] and carbonates from calcium-containing sources are near 60-180 mg/L ($\approx 10^{-3}$ to 10^{-4} m) [19].

discrepancies between our ab initio model using defect-free, solute-free phosphate phases and the known success of orthophosphate addition as a lead release inhibitor which lowers the lead oxidation rate [220, 255]. We would expect small shifts in the stability boundaries towards smaller stability ranges upon defect and structural distortion inclusion. This inconsistency could be due to other effects such as particle aggregation in hard water from high zeta potentials [216, 222]. In contrast, we find carbonates foster $PbCO_{3(s)}$ even at low lead concentrations ($m > 10^{-4}$).

5.3. Discussion and Future Work

Our work within this chapter provides the first stability maps, generated from thermodynamic data sourced from DFT calculations, for compounds (solid scales and aqueous ions) expected under equilibrium conditions at the potential and pH anticipated for lead pipes in drinking water. We demonstrated that first principles thermodynamic models for lead release via corrosion based on semi-local density functional theory with spin-orbit coupling and van der Waals interactions included capture experimentally-verified stability regions of native Pb oxides in the Pb-H_2O system. The stability/dissolution boundaries for the oxides were found to vary by as much as 6 pH points without SOC included and with an ideal solution model, leading to dangerous overestimation of scale formation if the interactions are not included. This poses a challenge for generating reliable electrochemical models using computational data obtained with current high-throughput DFT databases. Nevertheless, DFT-sourced thermodynamic models reported here and those found elsewhere are one reasonable tool for streamlining analysis of a material's chemical and electrochemical behavior [27].

Our model shows that solid lead oxides scales exhibit a limited stability range under many aqueous conditions, and especially at acceptable EPA action levels (15 μg/L, m $\approx 7.24\times10^{-8}$ mol/kg Pb(II)) [219]. We predict soluble Pb phases are thermodynamically stable at aqueous lead levels below higher concentrations such as m $\approx 10^{-4}$ without an appropriate oxidizing potential to promote the formation of a tetravalent lead film. The driving forces that spur lead release are further increased with varying water hardness and temperatures above 25 °C, which is a reality for many U.S. cities in the spring, summer, and fall [261]. These trends are revealed by the higher incidence of lead poisoning in the summer than in any other season [214].

Nonetheless, inclusion of additives such as phosphates and carbonates increase the stability domains of protective oxide scales, and consequently, limit soluble lead in potable water. Although $Pb_5(PO_4)_3OH_{(s)}$ and $PbCO_{3(s)}$ are the most probable scales to form on pipes with water treated with these additives, respectively, our models predict that carbonates provide the broadest solid phase region for oxidized scale stability at the low lead concentrations imposed by current policy. This is reflected in the lower pH dissolution boundary and high maximum driving forces for forming solid $PbCO_{3(s)}$ (Figure 5.7), though passivation and protection is not obtained by cerussite scales, potentially due to kinetic effects [10, 216]. Our phosphate-containing models are inconsistent with the practical success of orthophosphate scale as a corrosion inhibitor [216, 232, 233, 255] in

city water systems and earlier models that predicted orthophosphate scales when few were found experimentally in highly controlled experiments. Although we cannot identify a singular source for the discrepancies, possible factors include: overestimated free energies of formation, $\Delta_f G$, the presence of additional elements like Ca to stabilize more complex Pb solids not previously considered and difficult to experimentally identify, chloride-sulfate mass ratios, and kinetic effects [216].

Our thermodynamic models highlight the need for more comprehensive atomistic/nanoscale studies with coupled kinetic models to clarify under what circumstances scales may form, in part because Pb-P solid formation has been tied to mitigating Pb dissolution rates [220, 262]. It should also be noted that phosphate anions may inhibit corrosion kinetics without detection of stable phosphate-based scales. At the center of the lead-release problem is the kinetically dependent accumulation of consumable lead in the drinking water, whether through direct dissolution of the pipe or through a multi-step pipe-film-electrolyte process. Furthermore, lead particulate release may be limited by consistent orthophosphate treatment [221, 222]. There is the critical need to define whether leaded distribution systems supporting potable water of a certain chemistry ever reach thermodynamic equilibrium or whether accumulation is instead kinetically mediated, e.g., possibly by clean water flushing, an inhibiting ion, or a scale that protects the surface or acts as a chemical sink for lead ions.

Future work should continue to establish reliable thermodynamic models describing scale stability within aqueous lead systems. DFT modeling helps advance the field by providing a better thermodynamic understanding of the probability of compound formation as a function of select water chemistry variables. State of the art computational tools make available probing of scale-dependent and amorphous solids, which will be imperative to increased accuracy of modeling solid oxidation formation. Furthermore, projects could examine the effect of other common ions in solution, such as calcium, chlorides, and sulfates, which are known to impact corrosion in other systems [263]. For example, calcium and magnesium concentrations are variables used to calculate water hardness. However, water hardness is often reported indiscriminately as equivalent $CaCO_3$ concentration. This ignores the possibly important effect calcium (and perhaps magnesium) may have in stabilizing lead films, as discussed above. Future advances to our models should include complex aqueous ion components, however, further experiments or advanced computation is required to the high-fidelity

thermodynamic data on multiple-cation complexes that might form. Mapping the effect of common additives and trace elements and minerals in water on scale formation in Pb pipes would bring the ability to forecast whether certain compounds might be expected to exist over long-term exposures. An increased understanding of lead-water chemistry and scale formation thermodynamics will aid lead release studies and improve practices for corrosion mitigation in the presence of multiple scales, which is often neglected.

As the industry conducts batch analysis of soluble lead collected at sampling intervals unlikely to catch episodic events that release lead, establishing a causal connection between water chemistry, compound formation, and soluble lead content is challenging but of of utmost importance. Factors to consider include, but are not limited to: structural and compositional disorder, Mg/Ca-associated hardness, chloride-to-sulfate mass ratio, phosphate and carbonate concentration, electrode potential, and lead film/scale chemistry, morphology, thickness, surface energy, etc. Additionally, the sources of consumable lead—bioavailable soluble lead as well as particulates—must be understood on the materials science length scale, whether from electrochemical ejection from lead pipe, chemical dissolution of lead corrosion products and scales, or particulate spallation. Finally, due to the complexity of the flowing drinking water systems and the grave consequences associated with lead release predictions, experimental work should also continue to explore these same questions, like the role of calcium in lead film formation and the presence/absence of phosphate-based films [252]. The most compelling framework involves computational modelling working in harmony with experimental analysis. Future work will evaluate the effects of further additives common in piping systems, including the effects of chlorine, chlorides, and sulfates in scale formation.

5.4. Conclusions

Here we presented a computationally-sourced, experimentally-reinforced first principles thermodynamic model of aqueous lead corrosion. We varied environmental conditions to assess corrosion suppression dependencies to acceptable concentrations in legacy water distribution systems through phase diagrams with state-of-the-art theory and non-ideal solutions. We found a collection of lead oxides and multi-element lead oxides and hydroxides are energetically stable. PBEsol with spin orbit coupling provides the best DFT model choice for matching experimental free energies of formation and reproducing directly observed solid phases at specific conditions while conserving computational resources. Pourbaix and stability diagrams generated

with $\Delta_f G$s calculated from DFT indicated that standard state conditions at low water lead levels promote thermodynamically driven corrosion in the absence of a corrosion inhibitor. We further found that although aqueous carbonate or orthophosphate additions promote solid lead-additive scales, only very high aqueous ion concentrations can substantially support an increase the total passivation at conditions similar to those in piping. Carbonate has high probable thermodynamic efficacy through the creation of a stable $PbCO_{3(s)}$ region even at very low lead concentrations and at a wide range of pHs. Moreover, we suggest that the disconnect between previous studies on absence of solid lead phosphate even when predicted by stability models may be due to overestimated free energies of formation, and the need for calcium to form a substituted $Ca_{10-x}Pb_x(PO_4)_6OH_2$ hydroxyapatite scale. We anticipate this chapter will provide thermodynamic guidance for scientists attempting to first understand and then suppress lead corrosion in legacy piping. Additionally, our investigation contributes a baseline for lead oxide computational work through our identification of the inclusion of spin-orbit coupling as necessary to capture lead system energetics. Future work should evaluate the effects of further additives common in piping systems, including the effects of chlorine, chlorides, and sulfates in scale formation.

CHAPTER 6

Synthesis Prediction and Optimization of Thermoelectric, Heteroanionic BiMOQs

Much of the work presented in the following chapter is available as peer reviewed publications in (*i)* *Chemistry of Materials* and (*ii) Journal of the American Chemical Society* [20, 63]. Contributing researchers to the project, also listed as authors on the paper, include Dr. Chi Zhang, Dr. James Rondinelli, Dr. Vinayak Dravid, Dr. Kenneth Poeppelmeier, Dr. Jiangang He, Dr. Rebecca McClain, Hongyao Xie, Songting Cai, Jiahong Shen, Fenghua Ding, Xiuquan Zhou, Dr. Christos Malliakas, Dr. Mercouri Kanatzidis, Dr. Christopher Wolverton. Article (*i*) was reprinted (adapted) with permission from L.N. Walters, C. Zhang, V.P. Dravid, K.R. Poeppelmeier, J.M. Rondinelli "First-Principles Hydrothermal Synthesis Design to Optimize Conditions and Increase the Yield of Quaternary Heteroanionic Oxychalcogenides", *Chemistry of Materials*, 133, 8, 2726–2741 (2021) [63]. Copyright 2022 American Chemical Society. Article (*ii*) was reprinted (adapted) with permission from C. Zhang, J. He, R. McClain, H. Xie, S. Cai, L.N. Walters, J. Shen, F. Ding, X. Zhou, C.D. Malliakas, J.M. Rondinelli, M.G. Kanatzidis, C. Wolverton, V.P. Dravid, K.R. Poeppelmeier "Low Thermal Conductivity in Heteroanionic Materials with Layers of Homoleptic Polyhedra", *Journal of the American Chemical Society*, 144, 6, 2569–2579 (2022) [20]. Copyright 2022 American Chemical Society.

6.1. Introduction and Literature Review

Heteroanionic materials are compounds comprising two or more anions for which one is typically the oxide anion [60, 264]. Many heteroanionic materials exhibit structures similar to their homoanionic counterparts, fluorides, nitrides, and other chalcogenides; however, the change in chemical bonding afforded by the additional distinct anions increases structural diversity [265, 266] and accessible electronic, magnetic, and optical properties making them a desirable composition space for materials design [58, 267-269]. Recent progress in heteroanionic materials research led to development of oxynitrides for water splitting applications

and bismuth oxychalcogenide materials for thermoelectric applications [270-273]. Yet, understanding of the synthesis methods of heteroanionic oxides with methods beyond solid-state synthesis is less developed than their homoanionic counterparts.

Hydrothermal synthesis methods are one promising approach to achieve fast and tailorable crystal growth of heteroanionic materials [274-278] because they offer control over morphology and composition through changes in the interactions among the involved species [279]. Dynamic processes active in hydrothermal synthesis, however, remain difficult to model as they involve complex sets of cooperative and/or competing reactions. In addition, there are local spatial and temporal variations in pressure, chemical potentials, and solubilities, which may explain why the design of reaction protocols often use trail-and-error approaches. Predictive design of synthesis is further complicated because process conditions that yield successful synthesis of targeted *homoanionic* materials may not result in similar synthesis fidelity for compositionally-derived *heteroanionic* materials, owing to how the additional anion changes the hydrothermal environment [59].

One approach towards achieving predictive hydrothermal synthesis procedures uses first-principles derived thermodynamic models, and avoids undertaking modeling of kinetic processes accessible from panoramic-based studies [62, 64-66] aimed at integrating nucleation and crystallization pathways. The computational challenges for the former are distinct: accurate phase-stability models under realistic hydrothermal conditions and suitable processing models that connect phase equilibria to process variables, which can be selected in the laboratory, *e.g.*, temperature, reactant concentrations, and pH.

The aforementioned models can be constructed using electrochemical (Pourbaix) phase diagrams [1], in combination with stability diagrams, respectively. As mentioned in previous chapters, Pourbaix diagrams depict phase stability of a compound and its competing oxides, hydroxides, or ions in aqueous solution as a response to changes in pH and potential, which makes it a useful tool to understand redox active thermodynamic species in a hydrothermal reaction. Stability diagrams can be used to identify processing conditions for synthesis, including reactant concentration and pH [56], because pH becomes a dependent variable (rather than an independent variable as in a Pourbaix diagram) that is determined self-consistently by H^+ or OH^- ions in solution. Furthermore, it permits more accurate modeling of acids and bases through non-ideal solution behavior expected to occur in realistic hydrothermal reactions. Although Pourbaix [28, 37, 45-50]

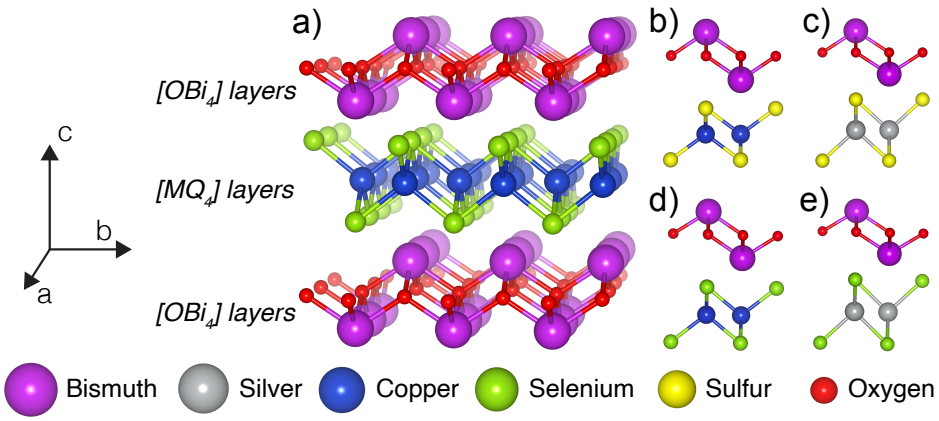

Figure 6.1. The structures of the layered bismuth oxychalcogenide BiMOQ (M = Cu, Ag; Q = S, Se) family, including (a) the typical layered oxychalcogenide structure for (b) copper bismuth oxysulfide, (c) silver bismuth oxysulfide, (d) copper bismuth oxyselenide, and (e) silver bismuth oxyselenide. Layers extend in the a-b plane and are formed by (OBi_4) and (MQ_4) tetrahedra.

and stability [54-56,67-71] diagrams have been applied successfully in the past to predict synthesis conditions, their use extends primarily to single-component homoanionic materials.

Here we implemented these tools within a first-principles framework to predict and understand hydrothermal synthesis of the quaternary heteroanionic bismuth oxychalcogenides family, BiMOQ (M = Cu, Ag; Q = S, Se). Although the physical properties of these layered 2D semiconductors have been studied before, owing to their use as p-type semiconductors, thermoelectrics, and photoluminescent materials, [31,32,272,273,280-284] minimal efforts have focused on understanding their synthesis. The ternary Bi_2O_2Q (Q = S, Se, Te) materials [285-287] have been pursued with hydrothermal synthesis whereas the quaternary BiMOQ compounds, and particularly BiCuOSe, have largely been pursued through solid-state synthesis [280,283,284,288-290]. Owing to the vast space of temperature and pH processing conditions accessible in the laboratory, we constructed first-principles phase diagrams to select synthesis parameters and identify when hydrothermal reactions would lead to high yield. We also calculated the driving forces for the formation of competing phases to understand where secondary metastable phases were in strong energetic competition with our target products. Our collaborators then hydrothermally synthesized pure BiCuOS, BiAgOS, BiCuOSe, and BiAgOSe crystals and assessed phase purity with scanning electron microscopy (SEM) and powder X-ray diffraction (PXRD). This experimentation further aids in discussion of chemical

distinctions among the bismuth oxychalcogenides. We explain differences in reaction conditions and changes in secondary phase competition. This work provides a strategy to develop first-principles based synthesis procedures for hydrothermal reactions, which should accelerate the time from computational prediction of novel materials to laboratory discovery.

6.2. Results

6.2.1. Dependencies at Standard State

Multi-element Pourbaix diagrams were computed for relevant systems, *i.e.*, Bi-Cu-S-H_2O, Bi-Ag-S-H_2O, Bi-Cu-Se-H_2O, and Bi-Ag-Se-H_2O, in the BiMOQ family. Target phase stability regions were observed for each of our four Bi-M-Q-H_2O systems (Figure 6.2 and Figure 6.3), indicating potential synthesizability through hydrothermal methods. Further inspection shows the target BiMOQ phases are bordered by relatively large regions comprising either homoanionic oxides or single-cation comprising heteroanionic materials near zero potential ($-0.25 < V_{\mathrm{SHE}} < +0.25$). We find that large pH ranges, varying from acidic to alkaline, promote target product stability for both copper and silver oxyselenides (Figure 6.2), with the domain of stability larger for Cu than Ag. The prominent selenate ion appears only at very basic pHs or high potentials. Therefore, only competing solid phases limit the stability range in the oxyselenides except for very alkaline solutions ($\mathrm{pH} > 14$). In contrast, the BiMOS oxysulfides exhibit smaller regions of stability (Figure 6.3). Within the Bi-Cu-S and Bi-Ag-S systems, ions and solid secondary phases are found to be stable near electrochemical conditions similar to the target heteroanionic materials. As with the BiMOSe oxyselenides, BiCuOS exhibits a larger domain of stability near 0 V compared to BiAgOS by ≈ 3 pH units; however, this behavior is amplified in the oxysulfides because the SO_4^{2-} ion infringes upon the stabilization of BiAgOS. For all materials, a higher concentration of all species in solution at $\eta_I{=}10^{-2}$ versus $\eta_I{=}10^{-6}$ leads to a substantial increase in pH stability ranges of the target BiMOQs, consistent with the increase in solubility term [**63**].

To understand the stability differences appearing in the Pourbaix diagrams, we examined in detail the multi-dimensional convex hull diagrams of the quaternary Bi-M-O-Q systems (Figure 6.4). The $\Delta_f G$ values of both target heteroanionic copper oxychalcogenides are more negative with respect to the hull, indicating increased stability compared to the corresponding BiAgOQ materials. BiCuOS is 4.5 meV above the hull, while BiAgOS is 68.4 meV above it. Furthermore, BiCuOSe is on the hull while BiAgOSe lies above the hull

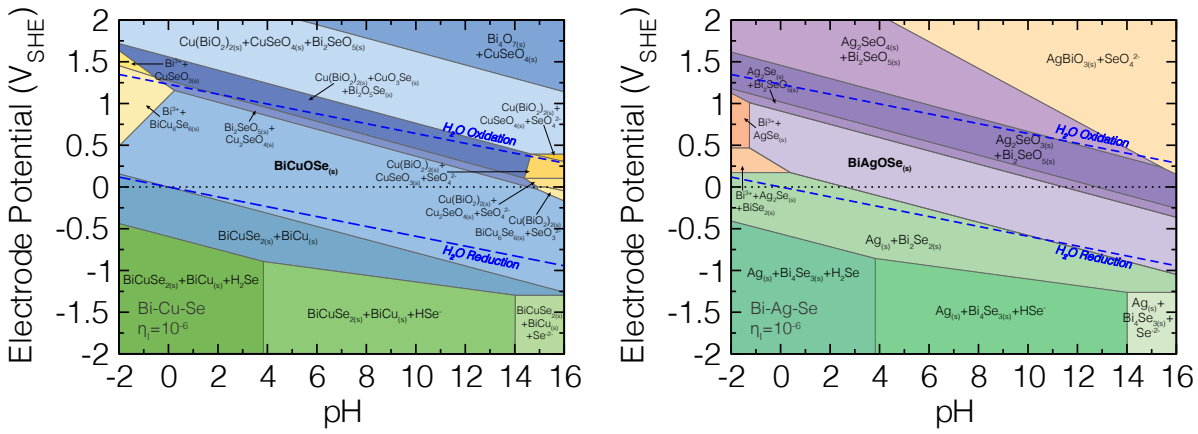

Figure 6.2. Multi-element Pourbaix diagrams for the (left) Bi-Cu-Se and (right) Bi-Ag-Se systems. Diagrams were calculated with an activity of $\eta = 10^{-6}$ and Bi:Ag:Se=1:1:1 mass ratio at standard state with V_{SHE} in units of Volts. At no applied electrode potential, both BiCuOSe and BiAgOSe are stable from acidic to alkaline pH. This crossover point occurs at pH ≈14 for BiCuOSe, and pH ≈11 for BiAgOSe.

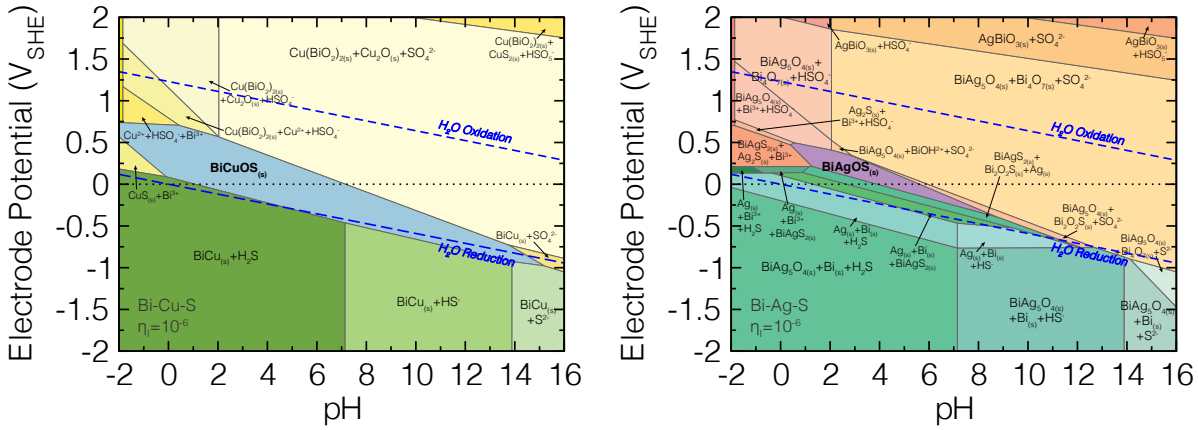

Figure 6.3. Multi-element Pourbaix diagrams for the (left) Bi-Cu-S and (right) Bi-Ag-S systems. Diagrams were calculated with an activity of $\eta = 10^{-6}$ and 1:1:1 mass ratio at standard state with V_{SHE} in units of Volts. At no applied electrode potential, both BiCuOS and BiAgOS exhibit narrow ranges of stability with respect to pH.

by 9 meV per atom. The increased thermodynamic stability of the copper oxychalocogenides correlates with larger pH stability ranges for the copper target phases in the Pourbaix diagrams.

We can further clarify key differences in the copper and silver containing Pourbaix diagrams through the nobility of each transition metal. Although both BiMOSe phases are stable across large pH ranges, the range for BiCuOSe is about 5 pH units greater. Similarly, BiCuOS has a wider stability region than BiAgOS at no

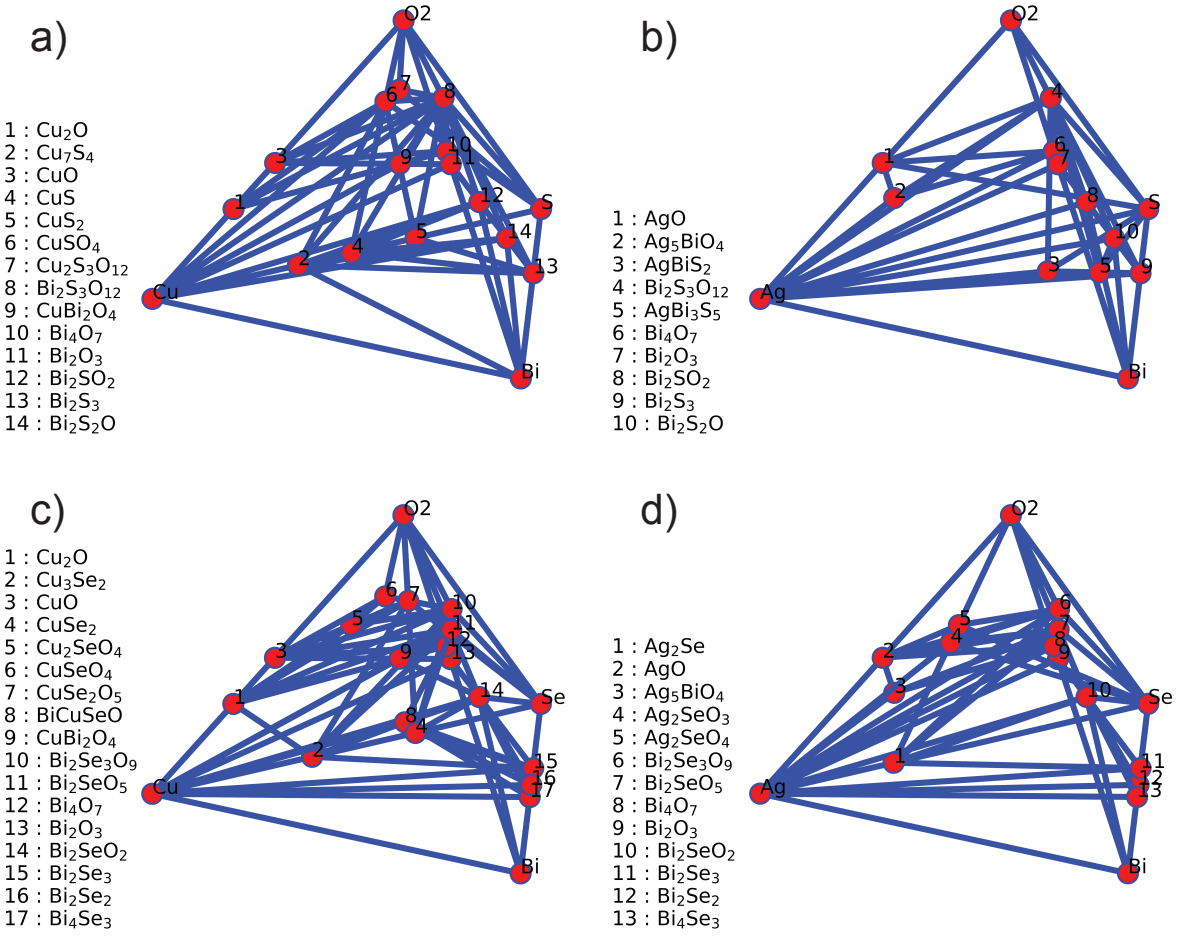

Figure 6.4. The convex hulls for each of the four BiMOQ species: (a) Bi-Cu-S-O (b) Bi-Ag-S-O (c) Bi-Cu-Se-O (d) Bi-Ag-Se-O. The target BiCuOSe phase is stable regarding the 4 dimensional hull. All other target phases are metastable.

applied potential by about 4 pH units. This variation is reflected in the single element Pourbaix diagram of Cu and Ag [1, 63]. Ag is a more noble metal such that it resists oxidation at a wide range of pHs and applied potentials. Despite evolving pH and redox potentials, we prioritize setting up the initial conditions of our reaction to be within stability regions for the target phase. For acidic pHs, oxidation of silver into Ag^+ occurs at $V_{SHE} = 0.5\,V$ instead of $V_{SHE} = 0.1\,V$. Similarly, at a pH of 16, Ag begins to corrode at $V_{SHE} = 0.0\,V$

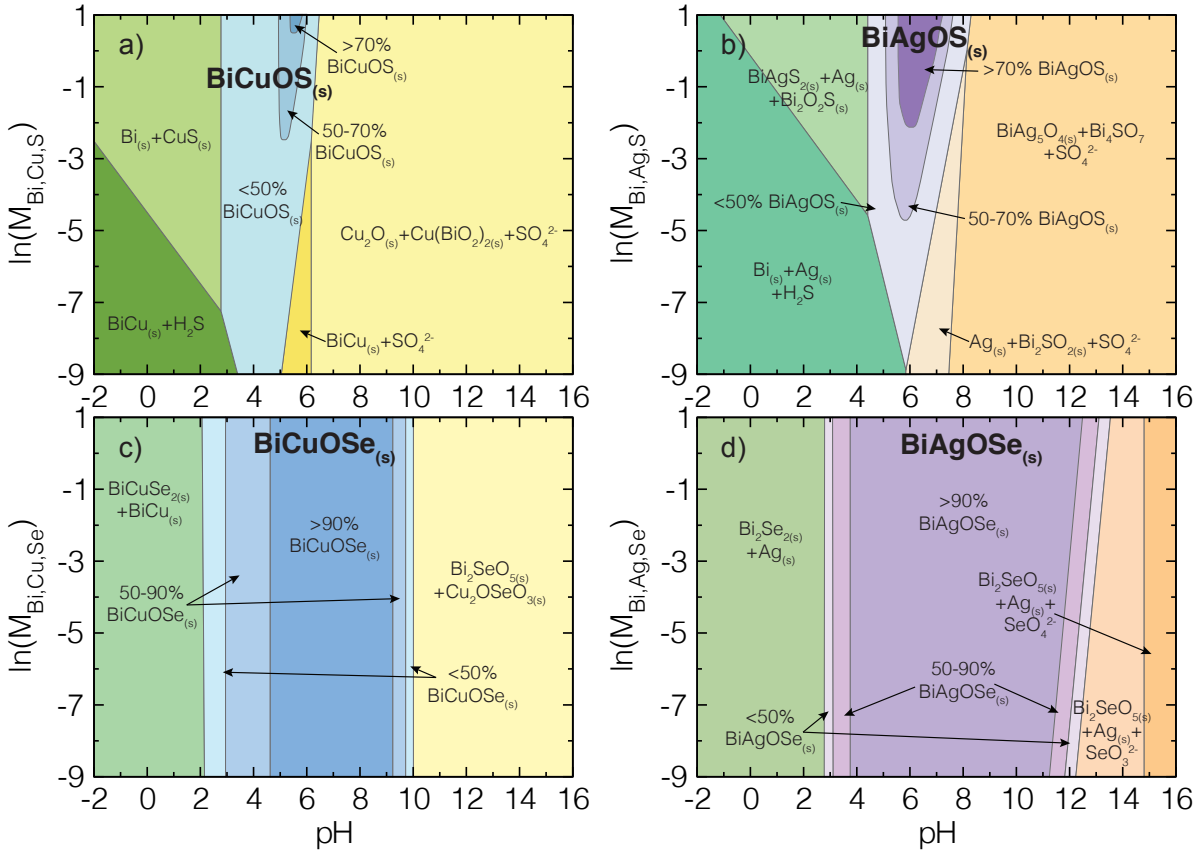

Figure 6.5. Multi-element stability and yield diagrams for the (a) Bi-Cu-O-S (b) Bi-Ag-O-S (c) Bi-Cu-O-Se (d) Bi-Ag-O-Se systems. Diagrams were calculated with a 1:1:1 ratio of elements, and the ideal solution approximation at standard state. The yield for the BiMOQ compounds is maximum at high concentration. Reagents considered were the elemental chalcogenide (S or Se), the elemental transition metal (Cu or Ag) and Bi_2O_3. High yield regions for the target phases, shown in darker purple or blue, are larger for the oxyselenides than the oxysulfides.

while Cu corrodes at any potentials $V_{\mathrm{SHE}} > -0.5\,\mathrm{V}$. Therefore, silver is less reactive, a fact which leads to suppressed elemental ion transport and silver oxide formation.

Next, we examine the standard state stability and yield diagrams sourced from the same $\Delta_f G$s as the multi-element Pourbaix diagrams above. These constant potential (V_{SHE}) diagrams present the dependence of phase stability with concentration of the elements in solution and pH. Here, aqueous ions with molar concentrations ranging from very dilute (10^{-9} mol/L) to strong (10^{1}) mol/L were used along with the ideal solution approximation [27] to further refine the synthetic processing variables required for the BiMOQ

materials. It should be noted that there are approximately 55 mol/L in pure water, which sets the maximum theoretical solute molarity.

Percent actual yield values, determined by Equation 3.44, are then projected into the same phase space to obtain a yield diagram (Figure 6.5); here, we only overlay the yield diagrams on the stability maps in the space spanned by the target BiMOQ compounds. These hybrid stability-yield diagrams may be interpreted similarly to Pourbaix diagrams; they present electrochemical equilibria with dividing lines between different phases and/or species indicating equivalent reaction chemical potentials. Within the target phase regions, lines are drawn to indicate conditions that produce the specified yield values. Relevant yield ranges for the oxyselenide systems were chosen to be 0-50 %, 50-90 %, and over 90 % yield. The BiMOS target products never reach 90 % yield, and thus a maximum yield range of > 70 % was chosen. To optimize hydrothermal product yield, reactions should be completed within the maximum percent yield region.

Figure 6.5 shows numerous boundaries occur between the target BiMOS oxysulfides and simpler homoanionic solids or intermetallics in combination with aqueous ions in solution. In contrast, only two boundaries (one at low and one at high pH) occur for the BiMOSe compounds, presumably due to a decreased number of stable competing phases for the oxyselenide systems. We find that the higher the total concentration of Bi, M, and S in solution ($M_{Bi,M,S}$), the broader the range of pH that is able to precipitate the target oxysulfides. For BiCuOS and BiAgOS, these high concentration-limited pH values range from approximately pH 3 to 6.5 and pH 4.5 to 8.5, respectively. Conversely, the phase boundaries for the oxyselenides are markedly different; they are largely concentration independent, except at alkaline solutions in BiAgOSe. The concentration independence stems from the stable precipitate regions of both systems. Note that such vertical, concentration independent, boundaries occur whenever all reacting species on either side of the target phase's dissolution boundary are solids. The silver oxyselenide system also exhibits the largest target phase stability area, owing to the small number of competing phases that have relatively lower competing $\Delta\mu_{rxn}$ when compared to the other Bi-M-Q systems.

Figure 6.5 also shows yield percentages (shaded regions) inside the BiMOQ phases where the target oxychalcogenide will precipitate from the solution within the specified yield range. We find that the oxysulfides do not reach their maxima yield until the aqueous ion concentration is at least 10^{-2} mol/L. In contrast,

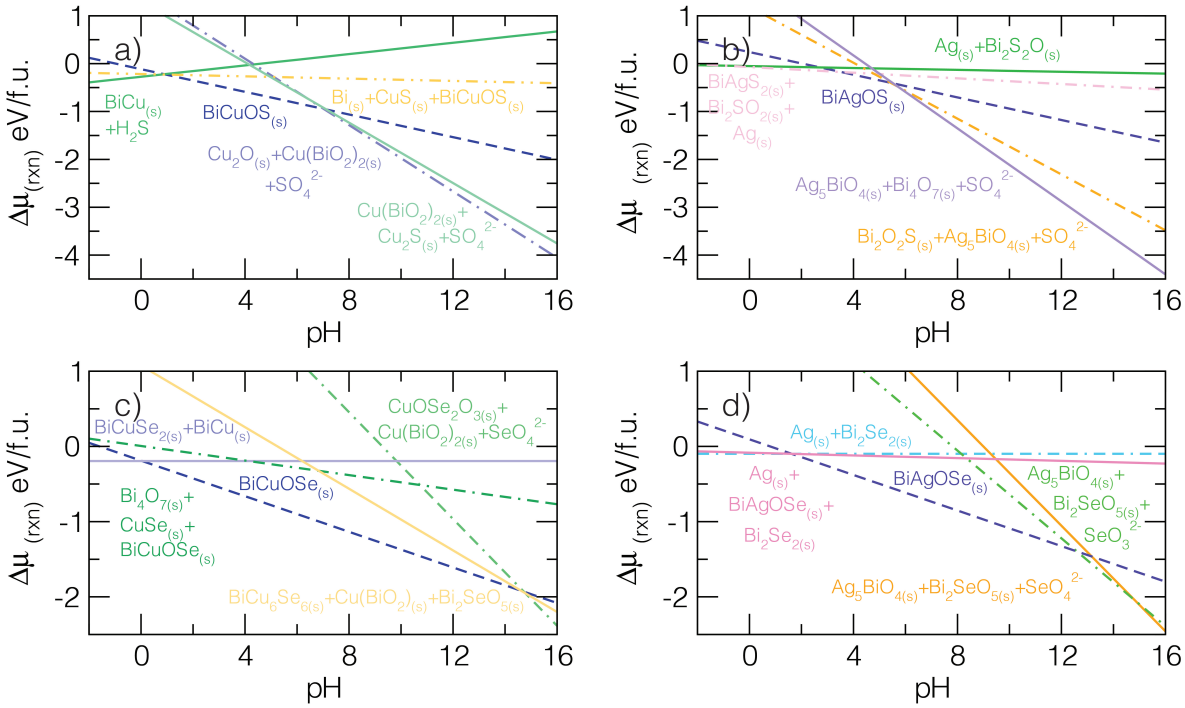

Figure 6.6. Driving forces for each BiMOQ oxychalcogenide at the standard corrosion limit, V_{SHE} = 0.0 V, and at standard state obtained from the $\Delta\mu_{\mathrm{rxn}}$ for stable and metastable species combinations in the (a) Bi-Cu-S (b) Bi-Ag-S (c) Bi-Cu-Se (d) Bi-Ag-Se systems.

maximum yields of > 90 % occur in large ranges of pH and ion concentration in the BiMOSe oxyselenides. Because the maximum yield region of BiMOS is relatively small and limited to high pH values compared to BiMOSe, we expect that phase pure oxyselenides should be experimentally easier to realize.

Based on the above thermodynamic phase diagrams we recommend neutral pHs at no applied potential for synthesis of the bismuth oxychalcogenides. Because there could be difficulty preserving Bi-O bonds at low pHs, deviations from neutral pHs to optimize yield should be performed at higher pHs.

An important consideration to note is that the primary chemical substitution in the target phases also leads to variations in driving forces of the systems, which influences the real-time progression of experimental reactions [39, 291]. The driving forces are defined by $\Delta\mu_{\mathrm{rxn},i} - \Delta\mu_{\mathrm{rxn},j}$, where i and j are two formation reactions comprising two different species combinations. At the dissolution boundaries, chemical equilibrium requires $\Delta\mu_{\mathrm{rxn},i} = \Delta\mu_{\mathrm{rxn},j}$ such that the driving force is zero; however, near the boundary there is a small finite driving force for one of the forward or reverse reactions, i and j, to occur. The driving forces are

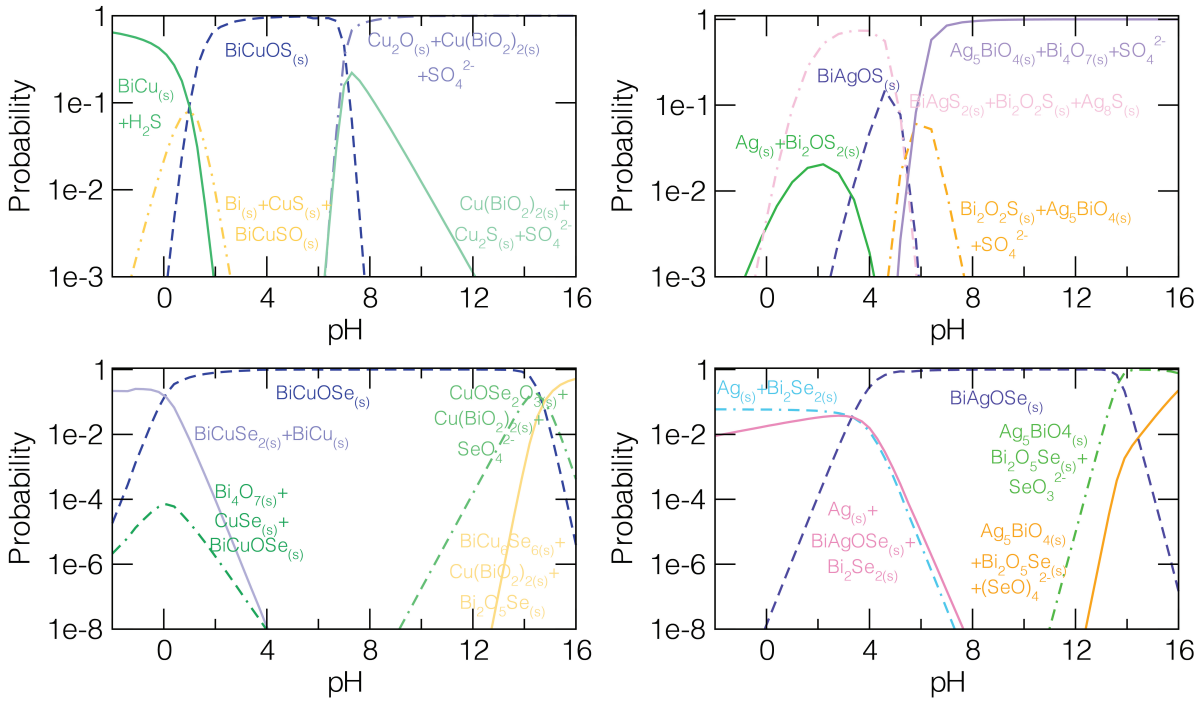

Figure 6.7. Standard state probability profiles for the BiMOQ compounds and potential byproducts with respect to pH ($V_{\mathrm{SHE}} = 0\,\mathrm{V}$, $\eta_I = 10^{-6}$), and equal elemental ratio. Only the most stable and metastable species are presented at all pHs. The target BiMOQ products are indicated by broken, dashed lines in dark purple or blue. Common hydrothermal byproducts are those that appear with high probabilities near the pH boundaries of each BiMOQ material.

strongly influenced by the $\Delta_f G$ of the reactants and products, and the solution pH. From our analysis of the $\Delta\mu_{\mathrm{rxn},i}$ values (Figure 6.6), we find that the driving forces to precipitate copper containing BiCuOQ phases are larger than those for the silver containing analogues. For instance, at pH = 5 and $V_{\mathrm{SHE}} = 0.0\,\mathrm{V}$ within the middle of the target phase stability regions, the BiCuOQ compounds exhibit a 0.16 eV larger driving force. This is largely tied to the larger $\Delta\mu_{\mathrm{rxn}}$ of the copper containing target phases. Furthermore, many of the byproducts in the oxysulfide systems, such as SO_4^{2-}, have $\Delta\mu_{\mathrm{rxn},i}$ values comparable to the BiMOS target phases, which reduces the magnitude of the driving force to create the BiMOS target products. In contrast, among the possible bismuth oxyselenide species, there are few competing energetically favorable phases, ensuring a large driving force for BiMOSe formation. These aforementioned differences in driving forces suggest then that hydrothermal synthesis of the copper oxychalcogenides will likely be easier than that of the silver variants, and similarly the oxyselenides should be easier to synthesize than the oxysulfides.

Last, we examine important metastable species that could appear as secondary phases (alternative reaction by-products) in the context of the driving forces and probability diagrams. Figure 6.7 shows the probability that specific species combinations will precipitate under a given reagent ratio and ion activity. A decrease in probability by one order of magnitude corresponds to an approximate increase in the reaction chemical potential of 0.1 eV or less. Phases closer to 1 are the most stable for a given pH, while those indicated by lines with intermediate probabilities indicate that multiple secondary metastable phases may be observed during laboratory synthesis. We point out that this analysis is based only on thermodynamic arguments, and thus attempts to identify potential byproducts in the absence of a kinetic model.

In Figure 6.6 and Figure 6.7, both oxyselenide systems demonstrate large regions where pure BiCuOSe and BiAgOSe are the most stable phases to form, *e.g.*, pH from about 0 to 14 and 3.5 to 12.5, respectively. Competing metastable secondary phases with similar $\Delta\mu_{\text{rxn}}$s include $BiCuSe_2$, Bi_2SeO_5, and elemental Ag, and thus may appear during hydrothermal synthesis of BiMOSe oxyselenides. The oxysulfides exhibit a narrower range of phase pure stability and more prominent potential byproducts. BiAgOS is the most stable species for less than a single pH unit. Strong competition with a number of other metastable compounds, *e.g.*, Ag and SO_4^{2-}, decrease the stability region of the BiAgOS target phase. Therefore, we collectively learn from the driving force and probability plots in combination with the stability and yield diagrams that the reaction conditions most conducive to precipitating the targeted BiMOQ phases requires simultaneously achieving large ion concentrations (Figure 6.5) with pH values at the center of the BiMOQ domain where the relative $\Delta\mu_{\text{rxn}}$ of BiMOQ is greatest.

6.2.2. Dependencies at Nonstandard State Reaction Conditions

We now examine the effect of nonstandard state conditions on phase equilibria in the BiMOQ family by simulating Pourbaix diagrams and stability-yield diagrams at T = 200 °C and $P = P_{sat}$ to approximate hydrothermal reaction conditions. Experimental increases in temperature allow for reagents to more readily dissolve in solution due to the increase in entropy and solubility within solution and the greater $\Delta_f G$ values of the aqueous ions. The justification for simulating nonstandard state conditions is that if the thermodynamics favors the targeted phase at nonstandard state, then kinetic processes leading to nucleation and growth (precipitation) should be sufficiently rapid for the formation of small target phase nuclei. This is principally

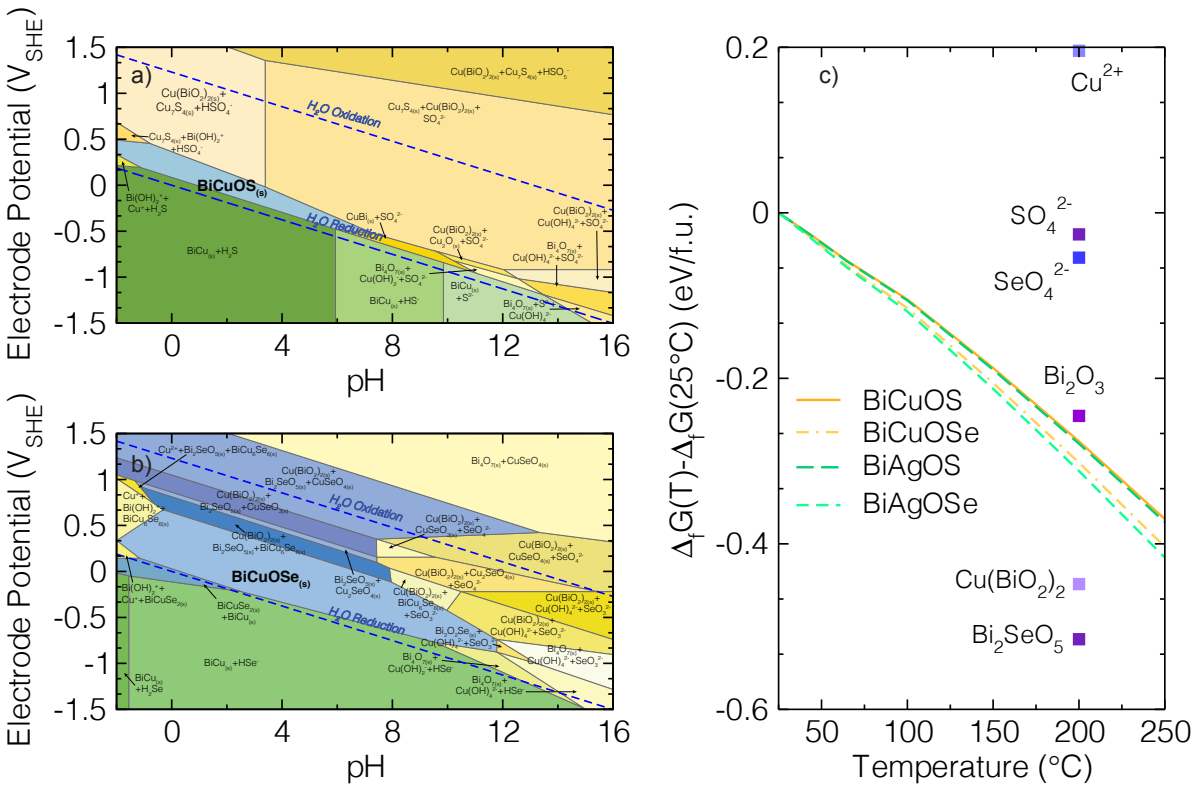

Figure 6.8. Nonstandard state multi-element Pourbaix diagrams for the (a) Bi-Cu-S and (b) Bi-Cu-Se systems. Diagrams were calculated at $T = 200\,^{\circ}\mathrm{C}$ and $P = P_{\mathrm{sat}}$ with an activity of $\eta = 10^{-6}$ and a 1:1:1 mass ratio of Bi:Cu:Q. Stable domains of BiCuOQ appear at acidic pH values, where BiCuOSe demonstrates a larger stability domain than BiCuOS. A significant factor in the decrease of the BiCuOS region resides in the prominent aqueous ions regions bordering the target phase. (c) Temperature dependence of $\Delta_f G$, as shown by the change in the Gibbs free energy of BiMOQ target phases at elevated temperature minus the standard state Gibbs free energy of formation ($\Delta_f G(T) - \Delta_f G(T = 25^{\circ}\mathrm{C})$). The change in free energy of formation is also shown at $T = 200^{\circ}\mathrm{C}$ for common byproducts. Most byproducts, such as Bi_2SeO_5 and the SO_4^{2-} ion, decrease in energy while the Cu^{2+} ion increase in Gibbs free energy of formation at elevated temperatures.

important, because there is an increase in the stability of aqueous ions with temperature, which effectively increases their concentration in solution. Upon cooling, if the BiMOQ phase remains stable (or metastable), the percent transformation to it from species in solution will increase, ultimately leading to nuclei growth and crystallization with minimal byproducts as the ion concentration decreases.

Nonstandard state Pourbaix diagrams are presented in Figure 6.8a and Figure 6.8b for BiCuOS and BiCuOSe, respectively. The corresponding nonstandard state silver oxychalcogenide phase diagrams are found in Figure 6.9. Immediately, we find large stable regions for the Cu(I) and Ag(I) oxidation states, particularly

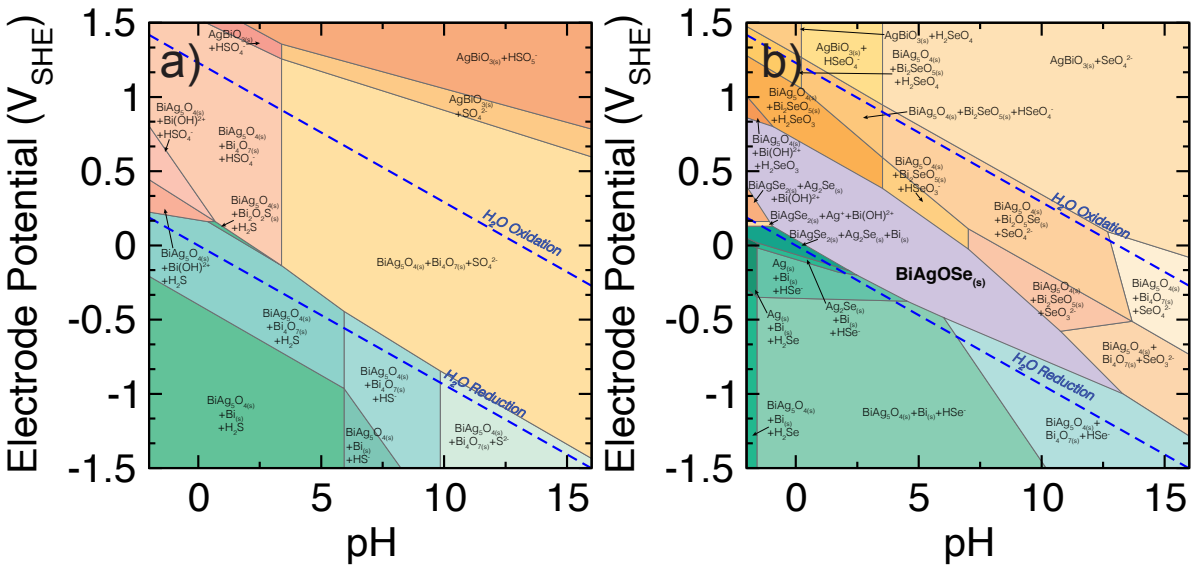

Figure 6.9. Nonstandard state multi-element Pourbaix diagrams calculated at $T = 200\,^{\circ}\mathrm{C}$ and $P = P_{\mathrm{sat}}$, an activity of $\eta = 10^{-6}$, and Bi:M:Q=1:1:1 mass ratio for the (a) Bi-Ag-S and (b) Bi-Ag-Se systems. For BiAgOSe compounds, the target phase occurs at lower pHs. BiAgOS does not exhibit a higher temperature stability region due to high stability of ion species like SO_4^{2-}. In general, sulfate and selenate species largely dominate applied oxidizing potentials. The HS^- and HSe^- ions are generally stable at applied potentials below the stable region of the target phase at a given pH.

when compared to standard state. This may be explained by *in situ* experimental evidence, which shows lower oxidation states become stable with increasing temperature for transition metals with variable oxidation states [292]. Additionally, water becomes a less dense and nearly nonpolar liquid at increased temperatures, which energetically penalizes higher oxidation states and large aqueous ions. The increase in the +1 oxidation state is principally important for the successful reaction of copper containing products with variable aqueous oxidation states, as Cu(II) is usually the most common oxidation state in aqueous solutions. Therefore, the phase diagrams support the use of increased temperature to improve the prevalence of appropriate oxidation states for efficient synthesis.

As we move our focus to the target phases, we notice the dissolution boundaries of the BiCuOQ phases shrink at 200 °C, leading to the formation of ions in solution near $V_{\mathrm{SHE}} = 0\,\mathrm{V}$ and alkaline pH values. The reduction in the relative stability of solid phases occurs as a consequence of the increase in the solute activity term within the free energy of formation, $RT\log_{10}(\eta_I)$, which leads to a dramatic decrease in the chemical potentials for the aqueous ions ($\approx 600\,\mathrm{meV}$). Moreover, the dielectric constant of water decreases and its

molar volume increases with increasing temperature, which generally leads to a more drastic stabilization of large and neutrally charged ions [**115**, **118**, **293**, **294**]. Nonetheless, the BiMOQ species are energetically more stable at higher temperatures as well. The free energy of formation for all target compounds increase by ≈ 400 meV from room temperature to T =250°C (Figure 6.8c), which allows for the solid BiMOQ phases to preserve much of their pH stability ranges at elevated temperatures. In comparison, the free energy of formation of other solid phases increased from about 100 meV to 600 meV, while the $\Delta_f G$ for aqueous ions changed from -400 meV to 400 meV. For example, BiCuOS and BiCuOSe each exhibit a decrease in stability region by about 3 and 8 pH units, respectively. BiCuOS retains much of its stabilizing region at elevated temperatures. For BiCuOSe, this dramatic decrease in pHs that stabilize the target phase support performing the synthesis at relatively neutral pHs, and none greater than ≈8.

Figure 6.9 shows all nonstandard state Pourbaix diagrams, including BiAgOS and BiAgOSe, which both demonstrate stability decreases at V_{SHE} = 0.0 V. The stability region for BiAgOS was not found at the standard corrosion limit, meaning that at the current theory level of DFT+SOC we are unable to predict BiAgOS even at high temperatures. BiAgOSe exhibits a decrease in its pH range of stability, shifting from approximately 2.5 < pH < 11 to 1 < pH < 7.5. Therefore, basic condition should only stabilize BiAgOSe at lower temperatures. As with the copper diagrams, stable aqueous ions impede upon the stabilty regions of both target phases, and particularly for BiAgOS.

The nonstandard state stability diagram for all systems is shown in Figure 6.10. The target phases appear for all systems, although generally with a smaller stabilizing pH range than those shown from the Pourbaix diagrams. This supports the idea that increasing temperature, which is necessary for solubilization and transport of reagents, can nucleate the target phase. Both oxyselenide systems remain widely independent of concentration, with target phases at nearly neutral pHs and at all concentrations considered. On the other hand, the oxysulfide systems demonstrate strong concentration dependencies. Below a critical concentration of aqueous ions the BiMOS phases will not form, similarly to what we found at standard state conditions. We found this concentration to be about 10^{-5} M and 10^{-3} M at their maxima for BiCuOS and BiAgOS, respectively. Finally, the median pH value within each target phase shifted towards the right with respect to the standard phase pH regions. This change indicates that the pH needed to generate target phase production

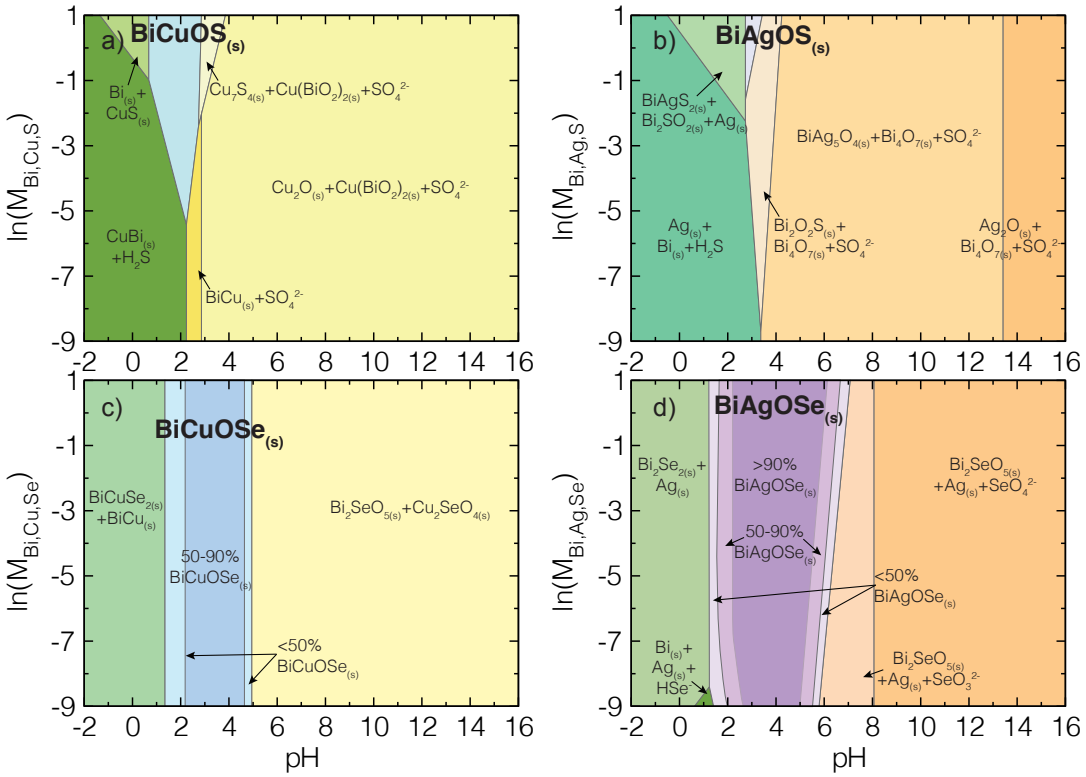

Figure 6.10. The stability diagram at T = 200°C, P=P_{sat}, and V_{SHE} = 0.0 V for (a) Bi-Cu-S (b) Bi-Ag-S (c) Bi-Cu-Se and (d) Bi-Ag-Se. As with the nonstandard state Pourbaix diagrams, the oxyselenides (BiCuOSe and BiAgOSe) demonstrate larger stability and yield regions, which indicates relative ease of nucleation even at higher temperatures. The oxysulfides, BiCuOS and BiAgOS, might not need such high temperatures to solvate reactants and nucleate target phases.

is dynamic and is flexible throughout the experiment as the temperature varies. Additionally, such high temperature may not be as necessary or effective for nucleating BiMOS target phases.

Therefore, hydrothermal synthesis of the target oxychalcogenides is supported by Figure 6.8, Figure 6.9, and Figure 6.10. They suggest that nucleation of the target phases should occur even at high temperatures. Stable regions exist at T =200°C for all systems, except BiAgOS in the Pourbaix diagrams at the DFT+SOC level of theory. The most prominent stable regions are at neutral and acidic pHs, demonstrating that very little mineralizer should be necessary to obtain viable pH environments for successful reactions. It is important to emphasize that these conditions rationalize and support previous hydrothermal synthesis methods of BiCuOQ target phases, including Refs. [272, 273] which used a 1Bi:1M:1Q reagent ratio, relatively neutral solution pHs, and no applied potential. Moreover, while prominent aqueous ion byproducts are expected to

Table 6.1. Reaction formation energy differences for BiAgOSe, BiCuOSe, and relevant side reactions as calculated with Δ_fGs from DFT (solids) and experimental literature (aqueous ions). Revised from original table produced in the supplemental materials of C. Zhang *et al.* [20]

Reaction	**Reaction Formation Energy (meV/f.u.)**
$Bi_2O_2Se + Cu_2Se \rightarrow 2BiCuOSe$	-793.3
$Bi_2O_2Se + Ag_2Se \rightarrow 2BiAgOSe$	-72.2
$Bi_2O_3 + 2Ag^+ + 2Se^{2-} + H_2O \rightarrow 2BiAgOSe + 2OH^-$	-2,129.5
$Bi(OH)_4^- + Ag^+ + Se^{2-} \rightarrow 2BiAgOSe + 2OH^- + H_2O$	-2,700.7
$2Bi(OH)_4^- + Se^{2-} \rightarrow Bi_2O_2Se + 4OH^- + 2H_2O$	-2,127.8

occur, we know from the standard state thermodynamic phase diagrams that decreases in temperature will only lead to broadening of the solid BiMOQ phases boundaries. Heteroanionic chemistry changes lead to a decline in the stability region of the BiMOQ target product. The BiCuOS phase in particular demonstrated a very small change in the stable region with temperature, indicating that it should be produced independent of reaction temperature.

6.2.3. Understanding Two-Step Subtractive Synthesis for High Yield BiAgOSe

Later sections report that a complex two-step, subtractive synthesis methodology is necessary to generate high yield BiAgOSe and to eliminate the formation of secondary phases. In general, our collaborators obtain multiple phases from the initial BiAgOSe hydrothermal synthesis reported in L.N. Walters *et al.* [63] owing to several concurrent, highly thermodynamically favorable reactions, and the residue of reagents with low solubilities in water. Therefore, additional synthesis steps are necessary. Our group utilized DFT-sourced Δ_fGs, phase diagrams, and classic nucleation theory arguments to improve understand of the complex BiAgOSe synthesis. In particular, we answered (*i*) the most probable reactions taking place in the hydrothermal system (*ii*) why a two step synthesis is required (*iii*) why the second synthesis step necessitates target phase seeding.

First, we formed an aggregate list from our previous computational work [63] and our collaborators' experimental observations describing the most common products formed from reactions after both synthesis steps. This demonstrated that $Bi_2O_2Se_{(s)}$, $Ag_{(s)}$, $Bi_2O_{3(s)}$, $BiAgOSe_{(s)}$ were the most common byproducts and occured at the largest amounts. Based on the high pHs and relatively neutral potentials imposed upon

the system, the most likely aqueous ions were assumed to be $Bi(OH)_{3(aq)}$, $Bi(OH)^-_{4(aq)}$, $Ag^+_{(aq)}$, $AgO^-_{(aq)}$, $HSe^-_{(aq)}$, $Se^{2-}_{(aq)}$, and $SeO^{2-}_{4(aq)}$. Combinations of potential reactions were probed for phase stability at reaction conditions and energetic driving force to determine the most probable system progression. An abbreviated list of chemical reactions considered is shown in Table 6.1.

Based on experimental and computational results [20, 63], we present two likely reactions and one side reaction that progress within our synthetic route. Our initial synthesis advances through the competition of Reaction R 1 and the energetically favorable side Reaction R 3, which happen concurrently owing to comparable, highly favorable reaction energies (see Table 6.1):

$$Bi(OH)_4{}^- + Ag^+ + Se^{2-} \longrightarrow BiAgOSe_{(s)} + 2\,OH^- + H_2O \tag{R1}$$

$$Bi_2O_2Se_{(s)} + Ag_2Se_{(s)} \longrightarrow 2\,BiAgOSe_{(s)} \tag{R2}$$

$$2\,Bi(OH)_4{}^- + Se^{2-} \longrightarrow Bi_2O_2Se_{(s)} + 4\,OH^- + 2\,H_2O \tag{R3}$$

Therefore, Reaction R3 diverts some bismuth to create Bi_2O_2Se. In the second synthesis step, Reaction R2 utilizes the Bi_2O_2Se and other byproducts, such as Ag_2Se, to create BiAgOSe. Note that these reaction are not written as standard half cell reactions, as OH^- will be the reacting species in basic solutions rather than H^+.

Next, we explore why a two-step reaction is necessary to create high yield BiAgOSe. Other BiMOQ materials, particularly the most widely reported BiCuOSe, can be produced hydrothermally at high yield in a single step with similar reagents [63]. First, we compare the inital reaction formation energies of BiCuOSe and BiAgOSe with the most probable reactants. For simplicity, we assume that substitution of copper for silver only modifies the final target phase and leads to a substitution of Ag^+ for Cu^+ as a reactant, as shown in

$$Bi(OH)_4{}^- + Cu^+ + Se^{2-} \longrightarrow BiCuOSe_{(s)} + 2\,OH^- + H_2O \tag{R4}$$

We find that BiCuOSe has a reaction free energy of -6.65 eV/f.u., versus -2.70 eV/f.u. for BiAgOSe. This indicates a much more substantial driving force for the formation of BiCuOSe. Accordingly, side reactions such as Reaction R3 are able to better compete against formation of BiAgOSe. Moreover, the free energy of

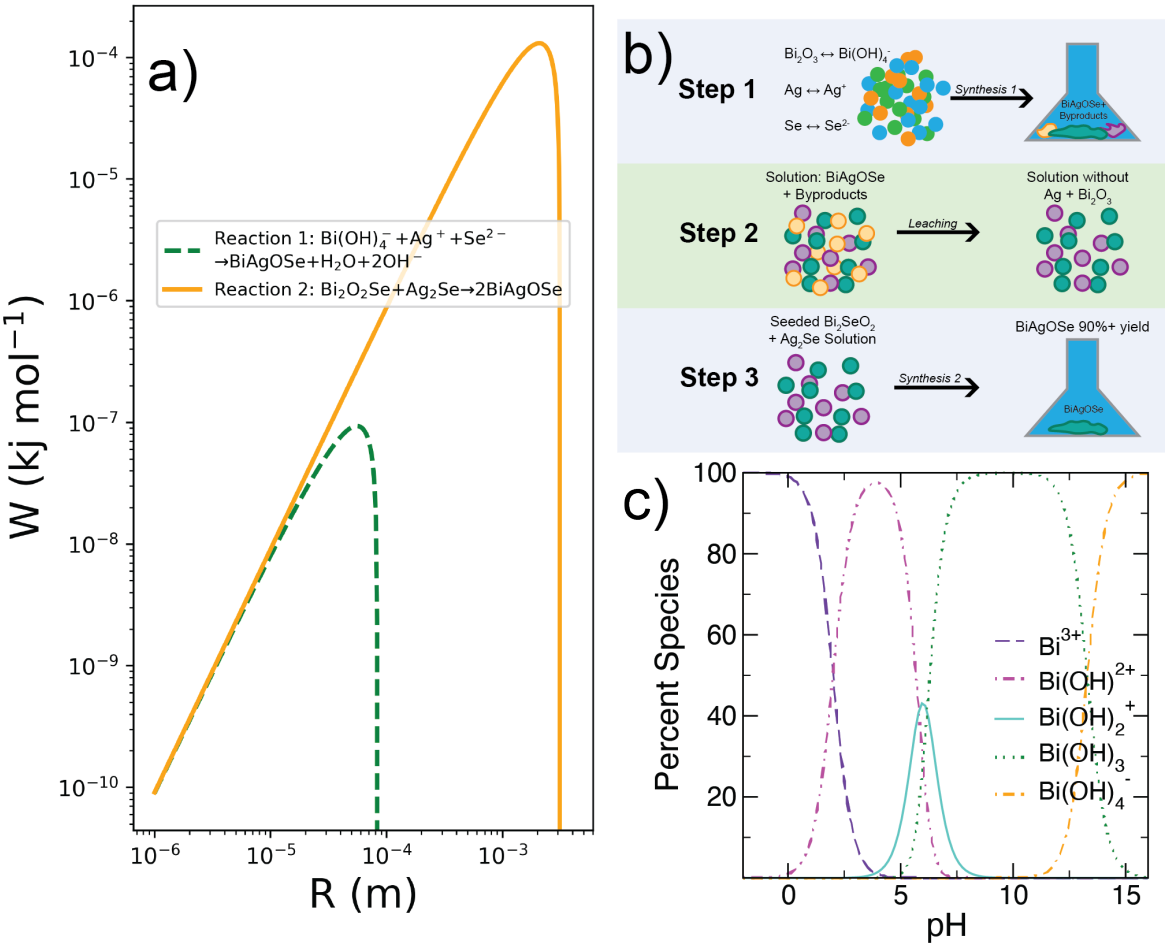

Figure 6.11. (a) The reversible work for Reaction R1 and Reaction R2 as part of the two step subtractive synthesis methodology presented in [20]. Reaction R1 (dotted green line) is shown to have a three order of magnitude smaller nucleation barrier than Reaction R2. (b) Schematic of two step subtractive synthesis method. In step 1, reactants form target BiAgOSe and byproducts. Step 2 removes unnecessary byproducts and left over reactants, such as Bi_2O_3. Finally, step 3 shows the reaction of the two main byproducts, Bi_2SeO_2 and Ag_2Se seeded with target phase to complete the high yield synthesis. (c) The hydrolysis series of Bi^3 demonstrates the stable aqueous Bi(III) ions at a range of pHs.

formation of BiCuOSe, which is on the composition-energy convex hull, is lower (more stable) at -2.6258 eV/f.u. BiAgOSe is 8.2 meV/atom over the hull and considered metastable with a $\Delta_f G$ of -2.3675 eV/f.u. Finally, we note that Ag is more noble with lower solubility than Cu under the reaction conditions. This is supported by the silver and copper Pourbaix diagrams [1] and their solubility equilibrium constants. Therefore, copper solubilization and ion transport is more accessible in bismuth oxychalcogenide synthesis. Therefore, the

decrease in silver solubility and reaction driving forces to create target BiAgOSe compared to BiCuOSe provides support for understanding why there is not high yield of BiAgOSe after Reaction R1.

Finally, we consider the seeding requirement for the second synthesis step. We utilized classical nucleation theory to calculate the nucleation barrier associated with each step in the reaction process. Figure 6.11a shows the nuclei size needed to reach over the reaction work barrier W^*. Reaction R1 necessitates a moderate nucleus size to get over a relatively small nucleation barrier of approximately 10^{-9} eV (10^{-7} kJ/mol). On the other hand, Reaction R2 must reach a size of approximately two orders of magnitude larger to overcome a reversible work barrier that is three orders of magnitude larger. Therefore, seeding Reaction R2 (the second synthesis step) with the target phase aides in overcoming the nucleation barrier and allowing bulk thermodynamic driving force to foster high yield BiAgOSe production.

We show a schematic of the proposed reaction sequence in Figure 6.11b. The initial evolution of Reaction R1 and Reaction R3 leads to BiAgOSe accompanied with Bi_2O_2Se. To design a high-yield methodology, Bi_2O_2Se obtained in Reaction R3 must be subsequently reacted with Ag_2Se to produce BiAgOSe, show in in Reaction R2. However, the energetic driving force of Reaction R2 is quite small (-72.2 meV/f.u., shown in Table 6.1). Most of the formation energy of the desired quaternary phase in this route is consumed by the formation of the Bi_2O_2Se and Ag_2Se intermediates, which limits formation of subsequent BiAgOSe and must be overcome through seeding. Therefore, Reaction R2 can reach completion when no additional Bi_2O_2Se is produced by Reaction R3.

Based on these concepts and experimental constraints, our collaborators formally introduced a "subtraction strategy" to facilitate target product formation through chemically removing the remaining Bi_2O_3 and additional aqueous bismuth ions after the initial reaction period [**20**]. The synthesis method contains the above mentioned three steps: (*i*) Ag, Se, and Bi_2O_3 react in a hydrothermal vessel via Reaction R1 and Reaction R3 to produce target BiAgOSe in parallel with undesired Bi_2O_2Se, Ag_2Se, and remaining Bi_2O_3; (*ii*) production of Bi_2O_2Se is halted through Reaction R3 termination by removing aqueous bismuth ions and unreacted Bi_2O_3; and (*iii*) Bi_2O_2Se and Ag_2Se react as demonstrated in Reaction R2 with seeded BiAgOSe produced in Reaction R1. Our collaborators reported successful, high yield BiAgOSe target material recovery.

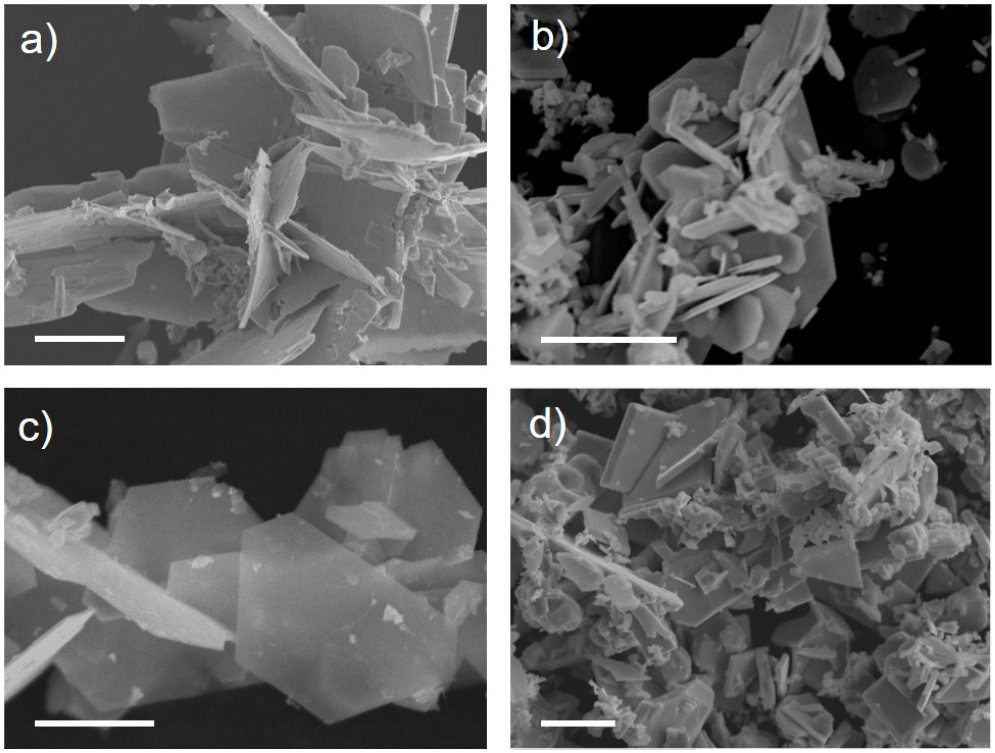

Figure 6.12. SEM images of the target (a) BiCuOS (b) BiAgOS (c) BiCuOSe and (d) BiAgOSe heteroanionic materials. The scale bar is set to 10 μm.

The peer-reviewed study provides the characterization of the product after each step via PXRD and the SEM images illustrate their morphology [20].

6.2.4. Computationally Guided BiMOQ Synthesis: Summary of Collaborative Experimental Efforts

Computational models shown above suggested a number of hydrothermal conditions for optimal synthesis. Therefore, our collaborators probed the possibility for the systems to facilitate nucleation of BiMOQ species at high temperatures, and found that all exhibited a range of pHs and concentrations where the emergence of the target phases could occur. Successful synthesis of the heteroanionic BiMOQ materials as confirmed by PXRD and SEM (Figure 6.12) [63]. BiCuOS, BiAgOS, and BiCuOSe were obtained as phase pure compounds without secondary byproducts, whereas BiAgOSe coexisted with Ag_2Se and Bi_2O_2Se phases after leaching with HCl to remove Bi_2O_3. As the synthesis methodology was optimized, many of the detected

secondary phases, such as $BiCuSe_2$ and elemental Ag, were the same as those observed in the driving force, probability, and thermodynamic phase diagrams. The dependencies of the hydrothermal synthesis on environmental variables, including the choice of mineralizer, pH sensitivity, and ratio of reagents, on the ultimate BiMOQ purity and yield were detailed in the peer-reviewed manuscript [63]. The study focused on these key optimization approaches, which were found to be most significant for the bismuth oxychalcogenides, while emphasizing how *a priori* knowledge and computationally sourced phase diagrams work together for synthesis design.

6.3. Discussion

This section lays out primary takeaways and trends found from our computationally lead synthesis efforts. Future work on complex hydrothermal methods should add to this list, providing intuition with which to design initial experiments. This is important, as heteroanionic materials are often metastable and require greater synthesis optimization than their homoanionic analogs. We note that, during hydrothermal synthesis, different anions can facilitate or hinder reagent transportation, while the presence of additional ions can change the potential, solubility, and pH of the reaction environment. Often these intricacies are further complicated by mineralizer and temperature selection, demanding additional time and resources. Here, we discuss how to design and optimize future hydrothermal synthesis of heteroanionic materials by examining in further detail the solution pH and byproducts formed in our bismuth oxychalcogenides.

An effective indicator to understand hydrothermal heteroanionic materials synthesis is by understanding propensity to oxide byproduct formation. Although oxides form frequently at various conditions, oxide precipitates appear most prominently in high pH regions where the potential needed to reduce water is much lower than it is at acidic pHs. Most elemental metals, including copper, silver, and bismuth are also more likely to create oxide solids and OH^- coordinated ions at high pH values, making the incorporation of the oxygen-metal bond into a target phase more likely to occur in basic conditions. This is supported by our computationally generated electrochemical phase diagrams, where complex oxides and oxygen containing ions dominate in alkaline environments.

Conversely, we found both in Pourbaix diagrams and in our collaborators' experiments that at extremely low pHs, all BiMOQ systems favor homoanionic species without oxygen. Solid secondary phases at low

pHs included transition metal sulfides and selenides, *e.g.*, $BiMQ_2$ (M = Cu, Ag; Q = S, Se) could be made from similar reactants but in an acidic environment. Future reactions may consider lower pHs in order to favor homoanionic products without oxygen. Therefore, to form heteroanionic oxide containing products, we recommend a median pH that balances the bonding of both O and Q anions.

We further recommend the use of driving force and probability diagrams to identify likely prominent byproducts and assess synthesis design and pH selection. For example, in the oxyselenide systems the BiMOSe target phases were most often produced with CuSe, $Cu(BiO_2)_2$, and Bi_2O_3 as byproducts (see Figure 6.6 and Figure 6.7), and these phases are stable at the same conditions as the target phase. Connecting which species form at conditions near the target phase, therefore, helps us to better understand and optimize the processing parameters. Moreover, these probability diagrams can be used to guide synthesis of many different homoanionic products within the same materials family through changes in pH, temperature, and pressure.

Finally, the additional chalcogenide species in heteroanionic materials can change the thermodynamic regions that normally stabilize solid products towards conditions favoring aqueous ions. The impeding effects of including stable sulfur or selenium anions on ion transport and precipitate formation are illuminated from the multi-element electrochemical and stability diagrams. For instance, when considering oxysulfide systems, our collaborators found the formation of stable heteroanionic precipitates are prevented due to the formation of sulfate ions. Furthermore, introduced ions can form weakly basic or acidic byproducts that influence the pH beyond a typical metal-oxide system, such as the introduction of the S^{2-} anion and its respective hydrolysis. Therefore, altering the type or amount of mineralizer is necessary for the reaction to proceed effectively. It is therefore important to use *a priori* knowledge and thermodynamic diagrams to obtain a coherent picture of anion behavior and to minimize the complexity of synthesis optimization.

6.4. Conclusions and Future Work

There are many different considerations that go into the development of new synthesis methods of novel complex compounds. Here, we focused on hydrothermal synthesis, where *a priori* knowledge of the synthesis methods of similar materials is often insufficient to guide a new synthesis. The massive complexity introduced from multiple ions in heteroanionic materials synthesis necessitates the use of theoretical approaches and computational phase diagrams. We showed that thermodynamic analyses based on electrochemical Pourbaix

and stability-yield phase diagrams afford a view into the active species present during realistic reaction conditions, providing guidance for rational synthesis design. Our successful hydrothermal syntheses of the layered bismuth oxychalcogenides, based on theory-informed pH, metastable species, reactant ratios, temperature, and mineralizer choices, reinforces the utility of a first-principles parametric simulation approach in selecting processing parameters. Subsequent work to optimize experimental reaction conditions iteratively and interactively with computation during synthesis development will lead to adaptive implementation of the methods and improved knowledge of material synthesizability, including use of nucleation barriers and solubility to further fine tune understanding. Future development of models of transient and/or competing phases near phase boundaries could be developed based on the results presented herein, which connect reaction pathways and simultaneous reactions within the closed synthesis system. We hope that our work both standardizes the use of computation to guide *de novo* inorganic materials synthesis and ultimately facilitates the efficient synthesis of important new technological materials.

CHAPTER 7

Development of Quantitative Thermodynamic Descriptors of Solid Phase Formation In Aqueous Environments

Much of the work presented in the following chapter is available as a peer reviewed publication in *Journal of Physical Chemistry Letters* [136]. Contributing researchers to the project, also listed as authors on the paper, include Emily L. Wang and Dr. James M. Rondinelli. Reprinted (adapted) with permission from L.N. Walters, E.L. Wang, J.M. Rondinelli "Thermodynamic Descriptors to Predict Oxide Formation in Aqueous Solutions", *Journal of Physical Chemistry Letters*, 13, 26, 6236–6243 (2022) [136]. Copyright 2022 American Chemical Society.

7.1. Introduction and Literature Review

Quantitative comparisons of protective oxidized solid formation in corrosion-resistance alloy design remains a grand challenge in materials and corrosion sciences. Corrosion resistant materials often rely on the creation of these stable, solid (hydr)oxides, termed scales, to limit any release of soluble ions or larger particulates. A general approach to predict scale formation is to rely on free energies of formation of the bulk oxide, $\Delta_f G$, and its location on the convex hull (composition-energy diagram) to predict which oxide is most likely to form. This technique omits key aspects of the oxidation problem at the nanoscale, such as diffusion, kinetics, and the relative energetic stabilities of competing phases. Initial ($\leq 10^{-7}$ s) and kinetically-controlled film growth can be described by decoupled kinetic models, such as percolation and diffusion models [295-297], however, these rely often on experimentally-derived parameters that are challenging to extract. On the other hand, thermodynamic phase diagrams have demonstrated success as predictive tools for understanding scale growth [21, 89, 121, 298-300]. Predominance diagrams, including Pourbaix [1, 53] and stability diagrams [54, 55, 67], compare how the environment, described by pH, potential, concentration, and temperature, changes the stability regions of ions and solids. Figure 7.1a shows the stable phases in the

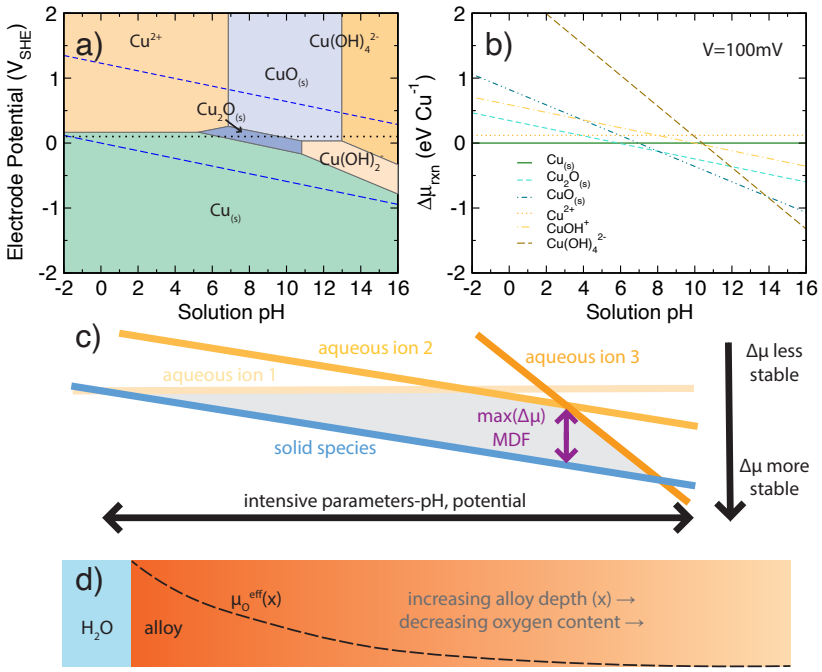

Figure 7.1. (a) Cu Pourbaix diagram showing the pH and potential ranges, elemental states (teal), solid oxide formation representative of copper scales (blues), and corrosive aqueous ions (oranges). (b) Driving force diagram at 100 mV for pHs in between -2 and 16. (c) Schematic multidimensional driving force diagram projected onto two-dimensions showing how the MDF is calculated by computing differences between driving force planes that appear here as lines. (d) Schematic of $\mu_{\mathrm{O}}^{\mathrm{eff}}(x)$, where oxygen content and chemical potential decrease with increasing depth into the alloy.

potential–pH space for the Cu-H_2O system. The phase diagram-based models, however, are computationally intensive to calculate for multiple-element systems, *e.g.*, binary or multi-principal elemental alloys. They also do not provide a direct route to compare oxide-phase stabilities among different alloy systems; they only convey the size of the stability fields.

Within this chapter, we develop the concept of thermodynamic driving forces, *i.e.*, chemical potential differences ($\Delta\mu$), as a way to quantitatively describe aqueous stable (hydr)oxide formation during electrochemical oxidation. High thermodynamic driving forces, evidenced by large, negative $\Delta\mu$s, are likely to indicate which initial phases will appear, and may also describe phase evolution and the final equilibrium microstructure that forms. For example, steel-process design (quenching or annealing) to achieve diffusionless transformations for the creation of martensitic transformation-induced-plasticity steels may be informed by driving forces, determined from chemical potential lines with respect to temperature and composition [301, 302]. Recently,

the synthesis science community has used chemical potential predominance mapping to select the most successful precursors for target-phase synthesis [37, 63, 67] and mapping of the initial reaction steps verified by *in situ* characterization support the use of thermodynamic driving forces [62, 138]. Our utilization of driving forces is similar to that proposed by M.J. McDermott *et al.* for solid-state reactant selection [303], which relies on maximization of the system thermodynamic free energy difference upon product formation; our work, however, proposes an extension of this concept towards aqueous two-medium systems.

In situations where early solid-oxide growth may be followed by aqueous dissolution, a high driving force for scale formation would likely produce a solid-liquid equilibrium with an oxide phase at the boundary separating the alloy from the aqueous environment. Herein, we formulate the maximum driving force (MDF) descriptor to characterize solid phase oxide or hydroxide formation in an aqueous metal-H_2O system. We calculate it from the chemical potential difference between the solid element or (hydr)oxide and the most stable aqueous ion over a range of pH and potentials. Our workflow leverages existing computational materials science frameworks and experimental thermodynamic databases to determine the MDF for systems with $n \leq 5$ elements in equilibrium with H_2O. We also introduce a second metric to account for oxide growth parametrically through effective oxygen chemical potential changes (μ_O^{eff}) without explicitly treating the kinetics of nucleation and growth. To justify the use of our descriptors, we interpret experimental film growth studies of the aqueous nickel (hydr)oxide system. Furthermore, we examine the MDF trends for transition-metal and main-group elements, focusing on correlations between the MDF and enthalpy of formation. Following, we apply the MDF to simple TM-substituted Cr_2O_3 corrundum scales demonstrated to form on a set of cantor alloy systems, thus debuting our models for multiple cation oxides. Finally, we propose the MDF parameter can further be used in a predictive manner to assess oxide phase evolution from different metals, thereby informing alloy composition design for selective oxidation.

7.2. Results

7.2.1. Thermodynamic Descriptor Formulation

To build the formalism of our thermodynamic descriptors, we first establish that materials in aqueous environments may be stable or react with water or other dissolved ions to form aqueous dissolution products or solids, most commonly in the form of oxides or hydroxides. Then, solid native (hydr)oxide $M_xO_yH_z$

formation can be described using a generalized redox reaction of water with metal M as

$$X\mathrm{M} + Y\mathrm{H_2O} \rightarrow \mathrm{M}_x\mathrm{O}_y\mathrm{H}_z + (2Y - Z)e^- + (2Y - Z)\mathrm{H}^+$$

where X, Y, and Z provide stoichiometric mass balance. To predict if a solid phase forms, we calculate the chemical potentials (μ) for each species. The chemical potential of elements in their most stable phase at standard state (T = 298.15 K, P = 1 atm) is $\mu = \Delta_f G = 0$, where $\Delta_f G$ is the bulk Gibbs free energy of formation. The chemical potential ($\Delta\mu_{\mathrm{solid}}$) for the formation of a solid phase, *e.g.*, $\mathrm{M}_x\mathrm{O}_y\mathrm{H}_z$, from the reaction of water with its respective metal is

$$\begin{aligned}\Delta\mu_{\mathrm{M}_x\mathrm{O}_y\mathrm{H}_z} = \big(&\Delta_f G_{\mathrm{M}_x\mathrm{O}_y\mathrm{H}_z} - (2Y - Z)\cdot FU - (2Y - Z)\cdot RT\ln(10)\cdot \mathrm{pH} \\ &- X\cdot\Delta_f G_{\mathrm{M}} - Y\cdot\Delta_f G_{\mathrm{H_2O}}\big)/N\,, \end{aligned} \tag{7.1}$$

where R is the ideal gas constant, T is the temperature, F is Faraday's constant, and N is the total number of metal elements per formula unit (here $N = X$).

Corrosion occurs through the solubilization of the solid and subsequent formation of aqueous ions $[\mathrm{M}_x\mathrm{O}_y\mathrm{H}_z]^{\delta}_{(\mathrm{aq})}$, for which the reaction chemical potential $\Delta\mu_{\mathrm{rxn}}$ to form the aqueous ion $\Delta\mu_{\mathrm{aq.\,ion}}$ is

$$\begin{aligned}\Delta\mu_{[\mathrm{M}_x\mathrm{O}_y\mathrm{H}_z]^{\delta}_{(\mathrm{aq})}} = \big(&\Delta_f G_{[\mathrm{M}_x\mathrm{O}_y\mathrm{H}_z]^{\delta}_{(\mathrm{aq})}} + RT\ln(\eta_I) - (2Y - Z + \delta)\cdot FU \\ &- (2Y - Z)\cdot RT\ln(10)\cdot\mathrm{pH} - X\cdot\Delta_f G_{\mathrm{M}} - Y\cdot\Delta_f G_{\mathrm{H_2O}}\big)/N\,, \end{aligned} \tag{7.2}$$

where δ is the molecular charge and η_I is the solute activity. The first two terms of Equation 7.2 show that the chemical potential contributions to the aqueous ion include both its free energy of formation and some measure of solvation captured by the solute activity. Equation 7.1 and Equation 7.2 may be formulated to include different reacting species known to be present in water, such as OH^- (alkaline conditions), H^+ (acidic conditions), and common aqueous ions (*e.g.*, M^{δ}).

These expressions are used commonly to construct Pourbaix diagrams and certain driving force diagrams, including within this work. For example, taking a constant potential contour through Figure 7.1a (dotted line at applied potential of 100 mV), the stable phases appearing here are obtained by examining the relative

chemical potentials of aqueous copper species at varying pH values and identifying those with lowest $\Delta\mu_{\text{rxn}}$ (Figure 7.1b). The small chemical potential differences between the first and second most stable species in Figure 7.1b indicate there are small driving forces for Cu formation at low pH values, whereas there are moderate driving forces to stabilize a solid oxide for $6 \leq \text{pH} \leq 14$. This missing variation in magnitude of the driving force to form oxides in Figure 7.1a is what motivates us to compute the potential and pH-dependent MDF.

The maximum driving force (MDF) for solid phases that would nucleate on the surface of a metal in an aqueous system is defined as

$$\Delta\mu_{\text{max}} = \max\left(\Delta\mu_{\text{solid}} - \Delta\mu_{\text{aq.ion}}\right) \equiv \text{MDF}\,, \tag{7.3}$$

where $\Delta\mu_{\text{max}} \leq 0$ is the optimized driving force, $\Delta\mu_{\text{solid}}$ is the reaction chemical potential for solid phase formation, *e.g.*, an alloy or (hydr-)oxide, obtained from Equation 7.1, and $\Delta\mu_{\text{aq. ion}}$ is the reaction chemical potential for the most stable aqueous ion(s) at a given set of environmental conditions found in Equation 3.33. Although Equation 7.3 does not have any interfacial or kinetic terms explicitly included, we make the ansatz that rapid formation of the solid is expected whenever there are large driving forces, because the liquid provides sufficiently fast transport of ions.

Computing the MDF requires: (*i*) identifying the most stable solid-aqueous ion pair and then (*ii*) calculating the chemical potential difference at the specific electrochemical conditions, *i.e.*, pH, potential, concentration, for which the greatest difference occurs. Similar to P.K. Todd *et al.*, while the $\Delta\mu$ difference is maximized with respect to solid species selection, the $\Delta\mu$ Euclidean distance is minimized with respect to aqueous ion selection [**132**]. Environmental conditions will restrict the ion most likely to form in solution, thus requiring the MDF to incorporate the known most stable soluble ion for the considered aqueous phase, which leads to the minimized distance than if an unstable ion had been chosen. Subsection 3.2.3 provides additional details on free energy of formation sources and numerical evaluation details. A schematic of the MDF, shown in Figure 7.1c, illustrates that the chemical potential lines enclose a range of conditions (shaded area) that stabilize an oxide more than aqueous ions. The purple arrow indicates the difference in solid phase

and aqueous ion chemical potential at maximizing conditions. Details for extrapolating the MDF to multiple elements are provided in Subsection 3.2.3.

Initial solids most likely to form at the surface are the most thermodynamically stable species based on the overall highest driving force within a chemical potential window. Although $\Delta\mu_{\max}$ assesses oxide formation at the surface of a material from a difference in stability between aqueous and solid species, subsurface oxidation exclusively occurs as a solid-state transformation. Below this initial layer, time-dependent solid-state oxidation is reflective of the compositionally-constrained subsurface environment. Therefore, we use a model that is unconstrained at the surface, with fast reaction rates due to mobile water and ions, and without knowledge of the solid bulk composition [**62**]. We assume the subsurface system to be isothermal and isobaric, and an open system to oxygen (or other active diffusing ions) but closed to other elements.

Following Ref. [**62**] and [**138**], the grand canonical free energy for a given (solid) product, *e.g.*, oxide or hydroxide, below the surface is $\bar{\phi}^{\text{eff}}_{\text{solid}} = (\Delta_f G_{\text{solid}} - N_{\text{O}}\mu^{\text{eff}}_{\text{O}}(x))(\sum N_{\text{metal}})^{-1}$, where $\Delta_f G_{\text{solid}}$ is the free energy of formation of the product, N_{O} and N_{metal} is the number of oxygen and metal atoms per formula unit, respectively, and $\mu^{\text{eff}}_{\text{O}}(x)$ is the depth-dependent effective oxygen chemical potential. Here, we parametrically decrease $\mu^{\text{eff}}_{\text{O}}$ (or another ion such as hydrogen or a transition metal, TM, $\mu^{\text{eff}}_{\text{H}}$ or $\mu^{\text{eff}}_{\text{TM}}$) with scale depth to reflect declining oxygen content below a solid's surface, for which the true depth dependence is a consequence of diffusion during active corrosion and/or changes in oxygen solubility from alloy processing. In other words, as is shown in Figure 7.1d, the oxygen chemical potential decreases accordingly with the reduction in local oxygen composition. The chemical potential of the product will then decrease according to oxygen composition.

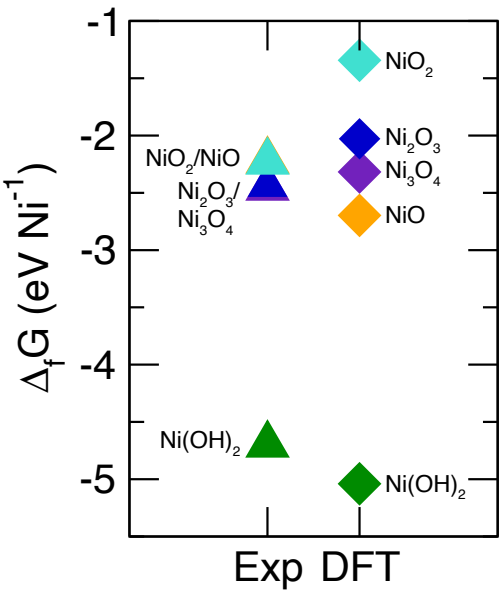

Figure 7.2. $\Delta_f G$s of solid Ni phases from experiment [1] and DFT calculated with the hybrid functional HSE06 [21]. $Ni(OH)_2$ exhibits the lowest free energy of formation per nickel.

7.2.2. Bulk and pH/V Dependent Ni Film Growth

Next, we develop the use of the MDF by applying it to understand scale formation of nickel (hydr-)oxides thin films. Generally, $Ni(OH)_{2(s)}$ initially grows at the surface and then $NiO_{(s)}$ evolves beneath it at moderate pHs and potentials (approximately $7 \leq pH \leq 15$, $-0.5\,V \leq V_{SHE} \leq 1\,V$) (Figure 7.3a) [21, 304, 305]. Surface $NiO_{(s)}$ initiates at lower pHs between 5 and 7. L.F. Huang *et al.* characterized this pH-dependent and depth-dependent nickel scale formation by reporting film identity and thickness at $pH = 4.9$ and 12.0 for distinct potentials in the range of $-600\,mV \leq V_{SHE} \leq 800\,mV$ [21]. Figure 7.3b shows their experimental Ni thin film depths, $\Delta h_{Ni_{(s)}}$, at $pH = 12$ decrease nearly 2 nm with increasing oxidation potential from about -0.6 V to 0.8 V. Simultaneously, the subsurface $NiO_{(s)}$ film depth increases in magnitude from only 0.8 nm to 2.4 nm. The thickness $h_{Ni(OH)_{2(s)}}$ starts at ≈ 5 nm, demonstrating fast initial growth, but plateaus during further oxidation potential change. This and other past literature utilizing model Pourbaix diagrams to interpret this phase evolution could not fully capture the pH-dependent and depth-dependent scale formation [21, 89, 126]. Historically, predicting the phases of aqueous Ni surface scales has been challenging and led to contradicting reports. This was due in part to discrepancies in $\Delta_f G$s reported in literature, shown in Figure 7.2, where

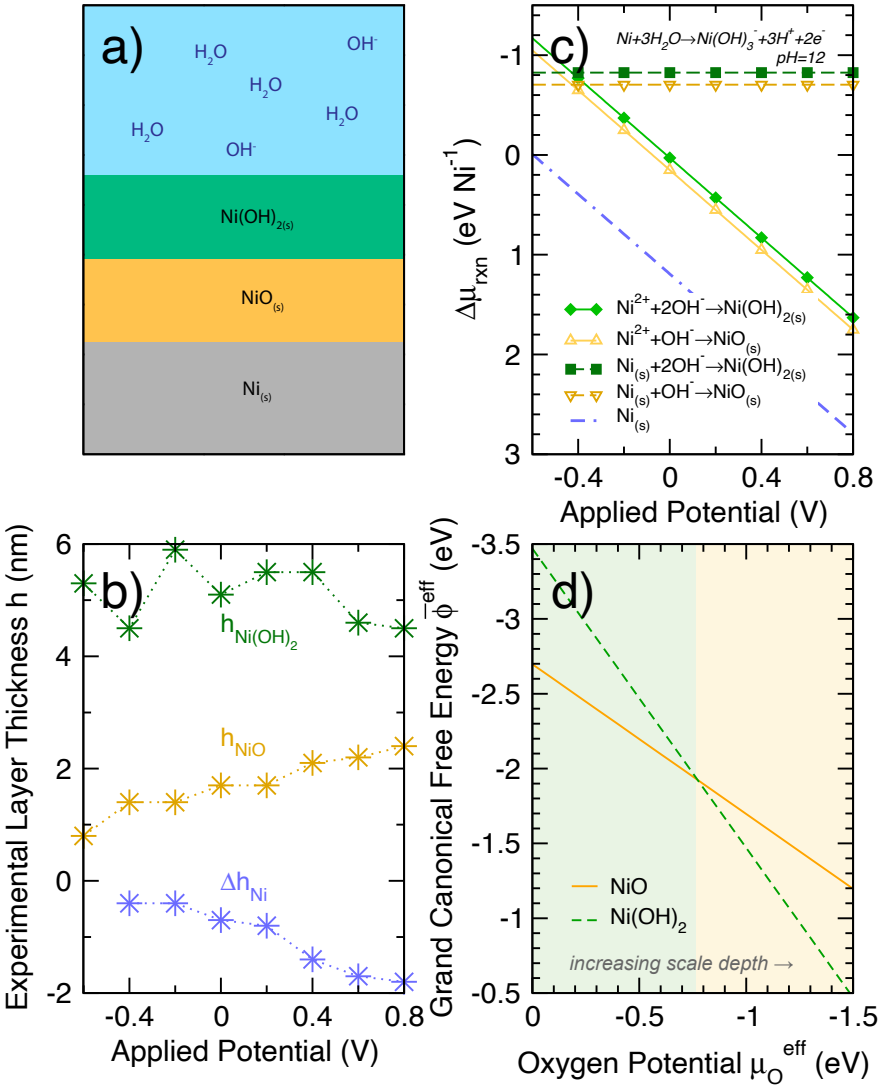

Figure 7.3. (a) Schematic of the Ni thin film system constructed by L.F. Huang *et al.* [21], where Ni films are subjected to specific pHs and then characterized at distinct applied potentials. At most pHs, $Ni(OH)_{2(s)}$ forms at the surface and it then transforms to $NiO_{(s)}$ below the surface $Ni(OH)_{2(s)}$ layer. (b) Ni thin film depth (h) dependence at pH = 12 measured in L.F. Huang *et al.* [21]. (c) The driving forces of thin films as a function of applied potential, -600 mV $\leq V_{SHE} \leq$ 800 mV, calculated in comparison to the most stable ion $Ni(OH)_3^-$. $Ni(OH)_{2(s)}$ exhibits the maximal (most negative) driving forces to form at all voltages, and results in the deepest film depth of any solid. (d) $NiO_{(s)}$ and $NiOH_{2(s)}$ depth-dependent stability, calculated from $\bar{\phi}^{eff}$ as μ_O^{eff} is varied. At a relatively low oxygen chemical potential of μ_O^{eff} = −0.7 eV with limited oxygen, $NiO_{(s)}$ becomes the most stable solid. Note the chemical potential axes are flipped.

DFT and experimental sources demonstrate qualitative and quantitative differences in solid (hydr)oxide stability.

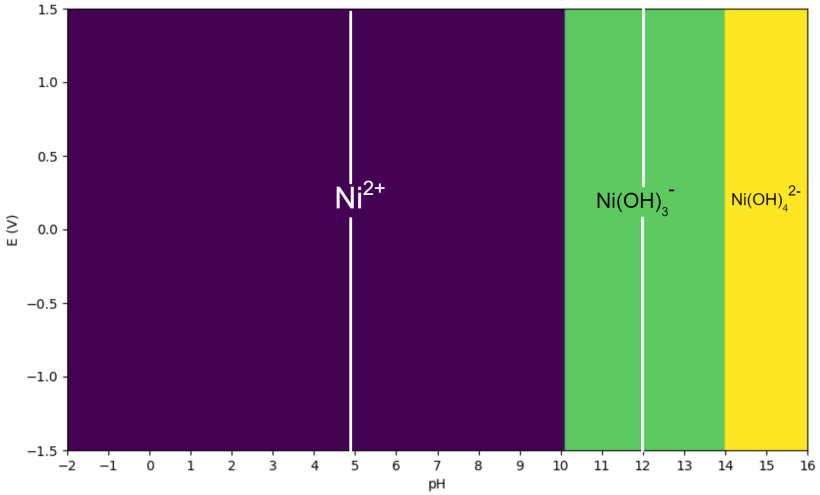

Figure 7.4. Aqueous ion predominance diagram for Ni. At pH = 12, $Ni(OH)_3^-$ is the most predominant aqueous ion. Dissolution boundaries for Ni^{2+} occur at pH ≈ 10 and for $Ni(OH)_4^{2-}$ at pH ≈ 14.

Figure 7.3c presents the calculated driving forces found through the subtraction of the chemical potential of $Ni(OH)_3^-$ from the formation of solid oxides and elemental Ni. $Ni(OH)_3^-$ was found to be the most stable aqueous ion at the pH tested (Figure 7.4). Consistent with previous reports [21,89], we choose $\Delta_f G$s calculated from DFT HSE06 calculations to better model the aqueous electrochemical behavior of nickel. Surface energy corrections are not included here, but could be through inclusion of surface electronic energy [21]. We find the most stable solid scales to be $Ni(OH)_{2(s)}$ and $NiO_{(s)}$, in agreement with previous thermodynamic predictions [1, 21, 89]. At alkaline pHs, OH^- (rather than H_2O) and Ni^{2+}/Ni (potential-dependent) exhibit the highest (most negative) driving forces, fostering $Ni(OH)_{2(s)}$ scale formation. $Ni(OH)_{2(s)}$ exhibits higher unconstrained (bulk) driving forces than $NiO_{(s)}$ formation at all potentials, consistent with its initial significant growth on the Ni film ($h_{Ni(OH)_{2(s)}} \approx 5$ nm). The dot-dash line reveals that elemental Ni is increasingly unstable and prone to oxidation as the potential increases, through either solubilization into $Ni(OH)_3^-$ or scale formation, which agrees with the disappearance of Ni film depth in Figure 7.3b. The initial and stable nickel hydroxide surface film is a product of the large chemical potential difference between $Ni(OH)_{2(s)}$ and the most stable ion, $Ni(OH)_3^-$. The less negative driving forces for surface nickel oxide formation appear in Figure 7.3d, where

NiO forms as the most thermodynamically stable product under subsurface composition constraints at a critical point for constrained $\mu_{\mathrm{O}}^{\mathrm{eff}}$. Finally, we exhibit calculated driving forces for thin films grown at pH = 4.9 in Figure 7.5. At lower pHs, L.F. Huang *et al.* [21] reports an experimental switch to favor $\mathrm{NiO}_{(s)}$ surface growth instead of $\mathrm{Ni(OH)}_{2(s)}$. When pH = 4.9, the most stable ion is Ni^{2+}. Driving forces in Figure 7.5 correctly predict that the most stable surface solid is $\mathrm{NiO}_{(s)}$ (orange solid line). The dotted lines represented driving forces for surface nickel hydroxide formation are less negative, indicating less thermodynamic drive for formation. Therefore, the MDF and $\bar{\phi}_{\mathrm{solid}}^{\mathrm{eff}}$ successfully describe the experimentally demonstrated external and internal oxidation of the Ni film.

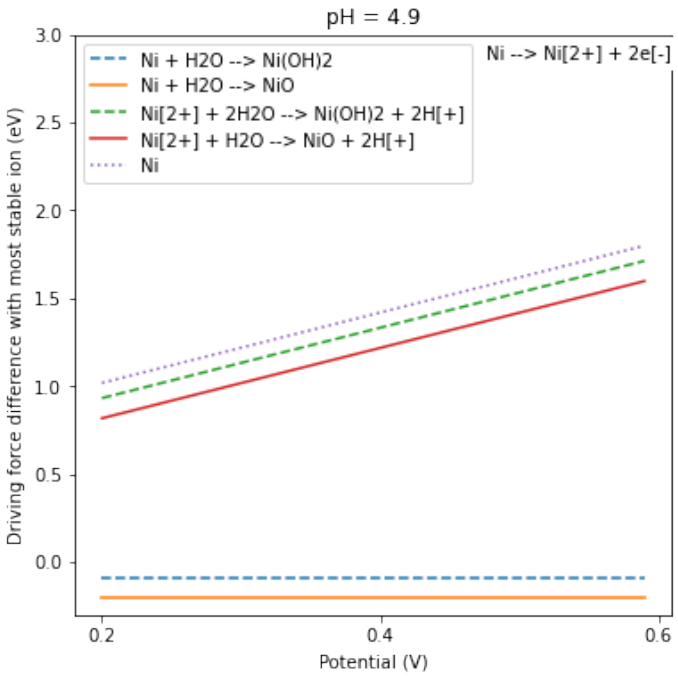

Figure 7.5. Ni driving force diagram at pH= 4.9 and potential range consistent with experimental thin film characterization presented in L.F. Huang *et al.* [21].

7.2.3. Mapping Elemental Corrosion Trends

We next explore MDF trends for elements by calculating the MDF for 3*d*, 4*d*, and select main group metals, using $\Delta_f G$ values sourced from Pourbaix's Atlas [1]. Figure 7.6a-b shows the stable solid (element, oxide, hydroxide, or oxyhydroxide) with the highest MDF in the standard corrosion window. The MDFs are plotted

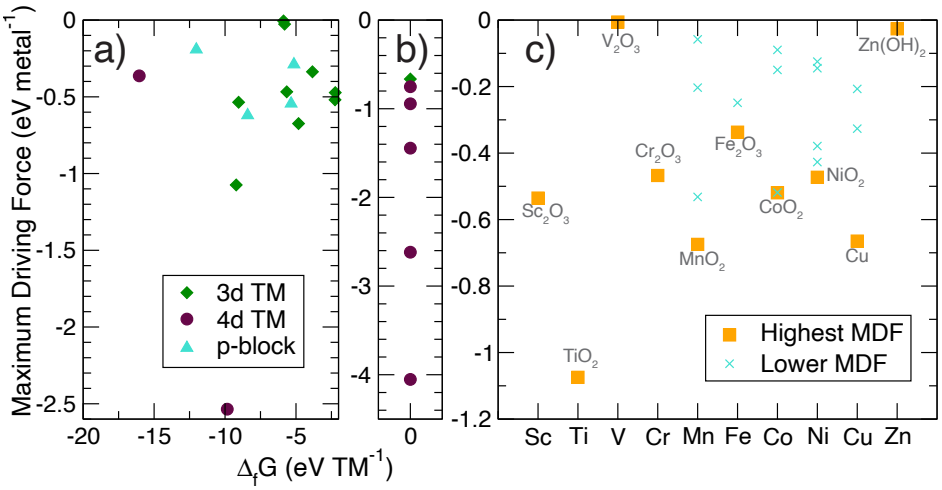

Figure 7.6. (a) Calculated MDF versus free energy of formation for $3d$ and $4d$ transition metals (TM), and select p-block elements (Al, Ga, Sn, In) whose solid product is an oxide, hydroxide, or oxyhydroxide. (b) The calculated MDF for $3d$ and $4d$ elements whose MDFs are calculated from their elemental states, *i.e.*, $\Delta_f G$ = 0. (c) Calculated MDF for each of the transition metals, including the most stable (orange, ■) and any other stable (teal, ×) solid products. All calculations are performed for the standard corrosion window with thermodynamic data sourced from experimental $\Delta_f G$ values [1].

against Gibbs free energy of formation for the solid, which has been utilized as a "rule of thumb" guide for assessing phase stability [306]. First, we note that MDF and $\Delta_f G$ show little correlation. The elements group within one of three categories according to the two energy descriptors: (*i*) $\Delta_f G \approx 0$ and MDF < 0, demonstrating little thermodynamic drive for general oxidation despite the MDF indicating solid stability in water, (*ii*) $\Delta_f G < 0$ and MDF ≈ 0, occurring for an oxidized solid that readily might form outside of water, but is an unstable or metastable scale within an aqueous environment, or (*iii*) $\Delta_f G < 0$ and MDF < 0, where there is high thermodynamic drive within and outside aqueous conditions to generate a solid oxidation product. The MDF, as it represents a driving force for scale formation (solid oxidation) over aqueous ion formation (corrosion), is a unique descriptor which captures behavior missing in $\Delta_f G$.

Figure 7.6a-b demonstrates also the variability in scale stability and corrosion behavior that exists within the periodic table. $4d$ elements exhibit the largest MDFs, such as Ru and Ag, whose elemental metals have MDFs of -4.05 eV and -2.61 eV, respectively. The $4d$ row also contains two elements, Nb and Cd, that have an MDF close to 0, indicating metastable oxide or hydroxide scales that may be more susceptible to other effects (*e.g.*, kinetic effects) within the standard corrosion window. This leads to a discrepancy between the

MDFs of Nb and Cd and their reported solid oxide phase formation in water, which we attribute to inclusion of the $Nb(OH)_{5(aq)}$ and $Cd(OH)_{2(aq)}$ ions in our dataset, whose very negative $\Delta_f G$ values limit the known solid stability. This inconsistency highlights the need for high-fidelity energies and the importance of data sources, particularly for high-throughput studies that may employ the MDF for predictive purposes.

Nearly all the $3d$ transition metals exhibit MDFs ranging from -0.25 to -0.75 eV/metal. All $3d$ TMs but copper find their largest driving forces with a (hydr)oxide product. Moreover, V_2O_3 is the only oxide scale predicted from the $3d$ series, again demonstrating the need for accurate sourcing of $\Delta_f G$ values, and particularly hydroxide values from DFT, which exhibit greater uncertainty (Figure 7.7). Main group metals also show moderate MDFs. $In(OH)_3$ exhibits the largest MDF at -0.62 eV/In and the smallest MDF is for hydrated Al_2O_3 with -0.19 eV/Al. Finally, as expected many noble metals, such as Ag and Cd, have a high driving force to resist oxidation (≥ 1 eV), despite $\Delta_f G = 0$ (Figure 7.6b).

To further explore variation in the $3d$ row, we plot all solids with MDF ≤ 0 for each element in Figure 7.6c. Data shown in squares indicate the species with the highest MDF per element. The crosses represent any solids with MDFs less than the most stable species. We find that TiO_2 has the largest driving force of all $3d$ oxidized phases explored. Most other $3d$ transition metals exhibit MDFs ranging from approximately -0.4 to -0.7 eV per transition metal. Cu is the only $3d$ metal whose elemental form is most stable within the standard corrosion window with respect to oxidized products. Furthermore, between Mn and Cu, we find multiple oxides, hydroxides, and oxyhydroxides provide sizeable MDFs. This data suggests that Mn, Fe, Co, Ni, and Cu are more likely prone to multiphase competition during electrochemical oxidation. Further use of $\bar{\phi}^{\text{eff}}_{\text{solid}}$ applied to these metals may provide insight into subsurface compound formation, particularly for materials with multiple metastable phases.

7.2.4. Multiple Element Driving Forces to Describe Cantor Alloy Films

Multicomponent cantor alloys are known for their excellent mechanical properties and synergistic behavior produced from the unique chemical interactions of the different alloying elements [307, 308]. Collaborators have synthesized a CrMnFeCoNi-Al Cantor alloy system and characterized its corrosion behavior. They found complex Al-Cr oxides form on the surface at a range of compositions. We therefore apply the MDF to understand the oxide scale formation with respect to Al-Cr concentration.

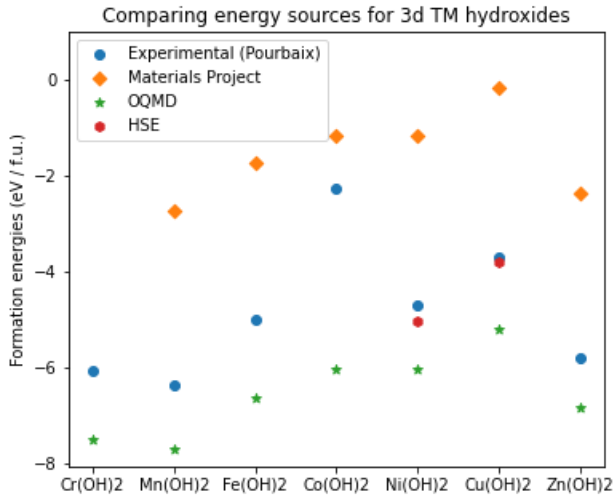

Figure 7.7. Comparison of experimental [1], high throughput DFT calculations from the Materials Project (corrected values) and OQMD databases [22-25], and HSE06 hyrbrid functional taken from L.N. Walters *et al.* [26] and L.F. Huang *et al.* [27] for some $3d$ transition metal hydroxides.

To apply the MDF, we first make a number assumptions about the system: (*i*) Al^{3+} and Cr^{3+} are the most stable aqueous ions in solution, (*ii*) the structure of the scale forming is a corundum $Cr_xAl_{2-x}O_3 (x \leq 1.4)$ structure ($R\bar{3}c$), (*iii*) the scale is substitutionally disordered for cations within a single phase, and (*iv*) the effect of modeling the oxide formation from elements instead of its respective alloy will only quantitatively alter the MDF value, and not change the MDF trend within the oxide set. Future work should evaluate the validity of these assumptions, in particular (*iii*) and (*iv*). We note that within this study, experimental collaborators provided evidence for a single phase scale. Studies to establish energetic landscape of alloy reference states will aid in understanding when (*iv*) can be safely adopted.

To simulate the cation-disordered corundum scale, we first create special quasi-random structures (SQS) between 8-60% Al, to fully explore the experimental composition limits of approximately 10-40% Al. The implementation of IceT [82-86] and Supercell methods [309] were used to create structures ranging from 30 to 60 atoms to accommodate multiple cation orders and compositions. DFT calculations implemented the generalized gradient approximation PBEsol, a 600 eV plane wave cutoffs, and 4,000 KPPRA to evaluate the electronic energy contribution to the enthalpy of formation (ΔH) as an approximation for $\Delta_f G$. SQS were

relaxed to ensure structural optimization within 0.01 eV/Å, followed by a static calculation with tetrahedron method smearing and Blöchl corrections to ensure accurate energies.

First, we benchmark the calculated enthalpies of formation, as well as an average of all energies, shown in Figure 7.8. The enthalpy sets tested were IceT structures of 50 atom supercells, IceT structures of 30 atom supercells, and Supercell generated structures of 60 atom supercells. We demonstrate that substitution of Al leads to a decrease in enthalpy by approximately 300 meV per metal atom with an additional 10% Al substitution with all methods and supercell sizes. There is some variation in ΔH magnitude between each energy set. Both IceT methods exhibit lower enthalpies at a given composition than any Supercell generated structure. Furthermore, there is a larger difference in magnitude between all energetic sets with lower Al content, particularly $\leq 35\%$ Al. Finally, the noise appearing in the linear dependence of ΔH on Al content is due to the simulated disorder by the SQS. Owing to the noise and magnitude variation between energetic sets, the average of all sets includes significant noise as well. In order to model MDF, we chose to use ΔH from the IceT 50 atom set and the Supercell 60 atom set. This is due to the larger supercell sizes within these sets, known to better accommodate disorder, and the larger number of composition, enthalpy points in these sets. Due to the significant amount of noise and different magnitude variations, we will not combine data sets or utilize the average enthalpies for the subsequent calculations.

Next, we calculate the MDF utilizing the IceT 50 atom structure enthalpy set (Figure 7.9a) and the Supercell 60 atom structure ΔH (Figure 7.9b). Approximate experimental conditions are pH = 5, U = 100 mV, and $\eta = 10^{-6}$, which are used herein. We note the graphical trends are preserved with lower pHs and varying potentials and concentrations. Driving forces are calculated with respect to the most stable aqueous ions, therefore, at the given conditions the solution is composed of a compositionally identical combination of aqueous Al^{3+} and Cr^{3+}. At very low ($\leq 15\%$) and high ($\geq 55\%$) aluminum content, both enthalpy sets experience increasing (more positive) driving forces, meaning that the scale is thermodynamically less stable than scales with intermediate Al content. Experimentally, our collaborators found that the most protective scales contained approximately 25% aluminium. The minimum of the IceT set is 40% Al, and 50 %Al for Supercell. Both graphs exhibit several local minima, which we attribute to the imperfect simulation of disorder by the limited SQS cell size. Moreover, the large DF range, such as 250 meV difference between the

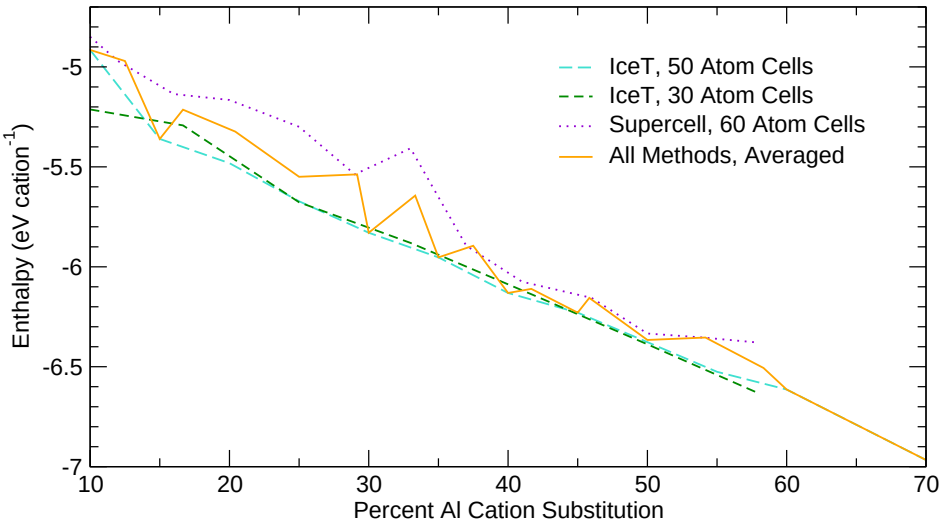

Figure 7.8. Enthalpies from supercell calculations of substituted $Cr_xAl_{2-x}O_3 (x \leq 1.4)$ scales. Supercell and IceT SQS generators were used with different supercell sizes and show roughly the same magnitude enthalpies of formation. Enthalpies are shown to decrease with increasing Al content.

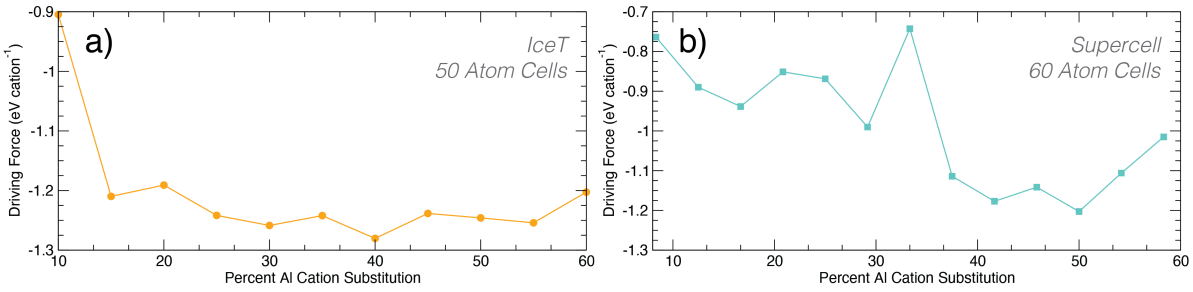

Figure 7.9. The driving forces of substituted $Cr_xAl_{2-x}O_3 (x \leq 1.4)$ scales calculated at the approximate experimental conditions of pH = 5 and U = 100 mV for (a) the IceT method and (b) the Supercell method. DF minima occurs near 40% Al and 50% Al for (a) and (b) respectively, with local minima near 20-30% Al corresponding to the most protective scales found in experiment. Driving forces are calculated with respect to the most stable aqueous ions, therefore, at the given conditions the solution is composed of a compositionally identical combination of aqueous Al^{3+} and Cr^{3+}.

two methods at approximately 30% Al , demonstrates the significant difference that local (dis)order can play on the MDF, structural energetics, and thermodynamic scale stabilization.

Through this initial investigation into multi-element MDF, we demonstrate that the possibility of leveraging MDF to show quantitative trends in compositionally varying systems, which is not easily available with traditional predominance diagram tools. Future work should explore the use of SQS with controlled

short range order to understand energetic variance, the effect of alloy versus from-element formation reference states when calculating chemical potentials, and attempt to establish best practices for sourcing disorder from SQS to limit computational and structural artifacts within energy sets.

7.3. Discussion

Finally, we discuss additional considerations for the inclusion of the MDF and effective potential parameters, focusing on systems with many different elements or varying compositions that may benefit from easy to interpret and low resource-requirement predictions. This is particularly relevant to advanced alloy systems, such as multi-principal element alloys (MPEAs) with five or more elements, for which recent research focuses on multi-component interactions, but is resource demanding [**310**, **311**]. It has been shown that the superior corrosion resistance of some MPEAs can be linked to mixed-metal oxides formed via higher driving forces than relevant binary oxides [**312**]. To that end, effects of alloying elements or alloy composition may be compared with the MDF to understand any increased or suppressed driving force, in addition to any changes to scale composition or structure. One approach to capture the configurational entropy contribution central to phase stability in MPEAs or other high entropy materials is through computational techniques such as DFT, which allow researchers to probe how atomic scale differences and local orderings may change formation energies, leading to measurable differences in the MDF, scale identity, and/or dissolution boundaries. The very beginning of this idea is what was attempted in Subsection 7.2.4, but which must extrapolated on to include more physical structure generation, the alloy species, and more oxide structures. In practice, thermodynamic competition between solids of similar (M)DFs may also provide insight into complex or phase-separated scales. Last, we note that because this approach requires either calculated or experimentally determined, accurate energies for new alloying systems or compositions, energetic sourcing becomes the bottleneck to using the MDF broadly, as it is for predominance diagram creation.

Reaction kinetics can play a dominant role in the formation of new materials. We propose two kinetically driven aspects of the system for which the MDF may approximate: (*i*) reaction rate of the initial surface species formation, and (*ii*) sub-surface, depth-dependent scale formation. As in Ref. [**62**], we argue that the initial species to form will be that with the highest driving force. Because a reaction rate is often approximated as the ratio of the thermodynamic driving force to a generalized resistance, the spatial or

temporal effects hindering the transformation must be defined. At the solid-liquid boundary, there should be little or different resistances for the transformation. Thus, the thermodynamic driving force can account for a large portion of the system dynamics. Solid-solid transformations, described next, would require defining resistance terms to evaluate whether a transformation would proceed; examples include anion and cation transport, defect density, interfacial reaction rates, and thickness, among others. Furthermore, state-of-the-art protection attributes, which can tune resistance terms such as sacrificial cathodic protection in the presence of Cl^-, may be incorporated by modifying the potential to account for additional ions, leaving of any less noble metallic species, and additional reactions to form complex soluble ions or multiple-anion solid surface phases within Equation 3.40 and Equation 3.42 [**313**].

Internal (subsurface) oxidation within aqueous thin film growth are limited by ion mobility, *e.g.*, diffusion barriers of redox agents such as H^+ and OH^- below the liquid-solid interface. Oxidized products that occur subsurface have not been described by widely used, easily-calculable parameters. Spatially-dependent chemical potentials can describe concentration gradients, as used in phase field models [**314-316**], for example $\mu_{\mathrm{O}}^{\mathrm{eff}}(x)$ and $\mu_{\mathrm{H}}^{\mathrm{eff}}(x)$, to examine internal/external oxidation and serve as a resistance proxy for diffusional barriers of O and H from the aqueous medium. Furthermore, cation (M) diffusion may be included with a variance of $\mu_{\mathrm{M}}^{\mathrm{eff}}(x)$ within an open system towards the cation element. By graphing the driving forces with respect to constrained chemical potentials, we can examine species evolution both from reaction of elements/alloys and from the transformation of initial surface products. Future experimental work to characterize depth-dependent oxygen content or film formation through use of x-ray photoelectron spectroscopy, time of flight secondary ion mass spectrometry, or reflectometry measurements may be used to assess the bounds on $\mu_{\mathrm{O}}^{\mathrm{eff}}(x)$.

7.4. Conclusions and Future Work

In conclusion, we formulated quantitative descriptors for solid-phase formation in aqueous environments using free energies of formation for solids and ions. We showed the maximum driving force parameter enables a comparison of the tendency for solid-phase formation in aqueous electrochemical environments among different materials systems, which is difficult to achieve from classic pH–potential diagrams alone. The MDF and depth-dependent descriptors are versatile and easily-calculable based on available thermodynamic

databases, and are therefore ideal for implementation in high-throughput workflows, particularly where free energies of formation are already available.

We propose using the MDF to guide the selection for alloying elements and composition to control corrosion behavior, for understanding depth-dependent scale growth, and to aide in devising solvothermal synthesis methodologies.

CHAPTER 8

Summary and Outlook

8.1. Summary

This dissertation developed models for predicting materials formation in aqueous environments. Here, we review the overarching questions introduced by the project chapters alongside results-driven responses.

- What benchmarking is necessary to establish a level of DFT that can create accurate Pourbaix diagrams? Are there methods we can develop to improve the accuracy and efficiency of Pourbaix diagram creation? Are there further analyses tools that we can develop beyond the Pourbaix diagram still using DFT-calculated free energies of formation?

  For copper free energies of formation, hybrid HSE functionals are required to generate an accurate thermodynamic model. This is established through comparison of free energies of formation, electronic behavior, structural parameter differences, and the location of dissolution boundaries from DFT-simulated Pourbaix diagrams. Other functionals that require less time resources may be sufficient for other materials systems. Inclusion of energy corrections, such as fitting aqueous ion thermodynamic data with the difference of hybrid functional- and gga functional-sourced DFT energies, can limit the time resources necessary to construct a DFT-based free energy of formation set for a give materials family. Further analysis tools, such as driving force diagrams, can provide supplementary information on aqueous materials formation. Wider spread inclusion of diverse thermodynamic tools presents an area of future work for the computational corrosion science field.

- Do calculated lead predominance diagrams match what we know about lead release, particularly in legacy water systems? Can we learn anything new about limiting Pb corrosion through studying the thermodynamic contributions to lead solubilization?

No, our calculated lead predominance diagrams are inconsistent with the dissolution and phase stability regions previously published. The most significant deviations occur for multi-element systems with water additives. These differences suggest thermodynamic contributions to scales previously thought to be stable within legacy water systems, such as hydroxylpyromorphite, may rely on other environmental conditions to form, such as Ca^{2+} ions, not explicitly modeled in our work.

- Can we effectively utilize predominance diagrams to understand and optimize hydrothermal synthesis methods for multiple element compounds? Are there ways that we can bridge the gap between traditional thermodynamics and kinetics modeling of materials formation?

  Yes, synthesis methodologies for a family of four element, layered, heteroanionic bismuth oxychalcogenides was rationalized through thermodynamic models such as Pourbaix, stability-yield, driving force, and probability diagrams. This presents an opportunity for synthetic-process design and optimization of other chemically complex products. One way that thermodynamic and kinetic modeling can be bridged are critical radii of nucleation calculations based on classic nucleation theory. Other opportunities to probe the interplay of kinetics and thermodynamics should be explored with future work.

- Are there further models or descriptors we could develop to provide quantitative information for aqueous materials formation? What ways could we ground this descriptor in physical observation and experiment?

  Within this work we attempted to develop two new descriptors, the maximum driving force (MDF) and effective chemical potential, which we believe provide valuable quantitative information about surface and subsurface scale formation, respectively. Further studies which carefully control and characterize the aqueous ion concentration, temperature, potential, and solution pH of aqueous thin film growth would provide significant insight into the utility of these descriptors. Furthermore, benchmarking these descriptors for multiple element systems would help discern how well single value descriptors can simulate more chemically complex environments.

8.2. Outlook

Based on experience in the field of thermodynamic modeling, I propose a few frontier opportunities for aqueous materials formation research. I hope to be able to participate in some of these directions in the future, and look forward to progress made in these and other directions.

8.2.1. Frontier 1: Synthesis Design and Development

Accelerating materials discovery will yield new energy, electronic, and health care solutions to transform society for the better. Necessary to achieve this is efficient use of time, experimental, and human resources. Computational modeling may be used as an optimization tool to provide *a priori* understanding of prospective syntheses. Thermodynamic diagrams connect the multiple interacting factors that influence hydrothermal synthesis, such as solution pH, temperature, pressure, potential, reactant choice, and reactant concentration. Incorporation of other variables, such as non-aqueous solutions and mineralizer contents, would provide key steps towards mapping these diagrams onto the systems they attempt to replicate. Widespread use of these models, and making them more accessible to laboratories without computational expertise, could rapidly change synthesis development and success product yield.

8.2.2. Frontier 2: Better Access and Standards for Benchmarking Thermodynamic Data

A bottleneck for utilizing thermodynamics modeling is the creation of a comprehensive free energy of formation data set, regardless of the use of experimental or computational solid phase energies. It is time consuming to identify and assemble experimental values, and this data may contain errors due to defects in samples. On the other hand, DFT-sourced solid phase $\Delta_f G$s are known to contain systematic errors, and the time and expertise necessary to execute relaxation and phonon calculations can be a significant obstacle. For both solid and aqueous ion phases, it may not be clear what all known phases are. Comparison of many well respected high throughput DFT and experimental databases often yield different included phases, likely in part due to incomplete knowledge of the materials system at the time of publication.

Future creation of accessible thermodynamic models will rely on building better databases, which accumulate knowledge of all known phases in a material set and their respective free energies of formation.

Furthermore, though DFT has provided computational researchers with a way to model systems before synthesis and thus provide *a priori* system knowledge for new materials. Providing accuracy standards for energy sets found with DFT will increase the fidelity of reported diagrams. We here acknowledge that high accuracy energetic calculations have been a significant thrust of computational chemistry within the last decade [**317-319**]. Leveraging benchmarks and methods within this field may allow for additional insight during future establishment of best practices for calculating accurate free energies of formation with reasonable resource availability.

8.2.3. Frontier 3: Bridging Kinetics and Thermodynamics

Thermodynamic models are limited in their description of phase stability simulating only thermodynamic contributions. Improved models could include kinetic effects to materials formation as well. Within some of our works, such as within Chapter 6, we make an initial attempt to bridge these theories with classic nucleation theory's critical radii analysis paired to driving forces and bulk free energies of formation. However, models which incorporate diffusion, reaction rates, scale dependence of products, surface free energies and identification of nucleation and growth sites, could provide valuable information towards for materials formation predictions.

8.2.4. Frontier 4: Model Extrapolation to Further Descriptors

Inclusion of more parameters to adjust predominance diagrams for different environments would allow this subfield to increase its predictive capabilities. Frontier 1 discusses modifying theory to include mineralizer and nonaqueous solutions. Moveover, better incorporation of scale dependence, surface orientation, multiple cation aqueous ion complexes, and continuously varying nonstandard state conditions are available paths. For widest spread use, tools such as ASE and Materials Project that provide materials scientists with access to free, open source post processing of datasets, could incorporate such tunability into phase diagram creation libraries.

8.3. Concluding Statements

To wrap up this disertation, I would like to share a few additional concluding remarks and takeaways with readers. First, that this work would not have been possible without the significant contributions of foundational thermodynamic literature in the 19^{th} and 20^{th} centuries by Gibbs, Pourbaix, and countless others. Furthermore, modern scientists within the last decade made important contributions to the use of phase and predominance diagrams within peer reviewed literature, one of which, Dr. Wenhao Sun, cannot be cited enough as inspiration for many of the projects included herein. Libraries, scripts, databases, and information made available particularly by Dr. Liang-Feng Huang and the Materials Project allowed DFT-sourced Pourbaix diagrams to accessible from the start of this works 5 years ago, without which the extrapolations presented in the project chapters would not have been able to be made.

This dissertation attempted to make a modest contribution to the field of computational DFT-sourced Pourbaix diagrams and wider thermodynamic tools, which I believed should be used in the future for aqueous materials formation prediction and rationalization. Accessible materials discovery will occur only when more research groups across the world are able to contribute. I believe this will transpire when we can preserve experimental and time resources where possible with colloquial use of computation and thermodynamic tools. Furthermore, phase and predominance diagrams can cultivate intuition about a new system to scientists unlike many other data reporting schemes. I look forward to seeing the incredible strides sure to be made by materials scientists in the future, for which this work will hopefully add a small founding piece to.

Vita

Publications During PhD

1. N.J. Szymanski*, **L.N. Walters***, D. Puggioni, J.M. Rondinelli, "Design of a Heteroanionic Material Exhibiting a Peierls Metal-Insulator Transition" *Phys. Rev. Lett.*, 2019. **authors contributed equally* [link]
2. **L.N. Walters***, C. Zhang*, V.P. Dravid, K.R. Poeppelmeier, J.M. Rondinelli, "First-principles Hydrothermal Synthesis Design and Verification of Quaternary Heteroanionic Oxychalcogenides" *Chem. Mater.*, 2021. **authors contributed equally* [link]
3. **L.N. Walters**, L.F. Huang, J.M. Rondinelli, "First-Principles-Based Prediction of Electrochemical Oxidation and Corrosion of Copper under Multiple Environmental Factors" *J. Phys. Chem. C*, 2021. [link]
4. C. Zhang, J. He, R. McClain, H. Xie, S. Cai, **L.N. Walters**, J. Shen, J.M. Rondinelli, M. Kanatzidis, C. Wolverton, V.P. Dravid, K.R. Poeppelmeier, "Low Thermal Conductivity in Heteroanionic Materials with Layers of Homoleptic Polyhedra" *J. Am. Chem. Soc.*, 2022. [link]
5. **L.N. Walters***, E.L. Wang*, J.M. Rondinelli, "Development of a Quantitative Down-selection Descriptor for Corrosion Resistant Materials Design" *J. Phys. Chem. Lett.*, 2022. **authors contributed equally* [***featured with supplemental cover***] [link]
6. **L.N. Walters**, A.T. Tai, R.J. Santucci, J.R. Scully, J.M. Rondinelli, "Density Functional Theory-Based Thermodynamic Model for Stable Scale Formation in Lead Water Systems" *J. Phys. Chem. C*, 2022. [link]
7. **L.N. Walters**, J.M. Rondinelli, "Revealing Anti-Anatase as a Robustly Metallic Advanced Ceramic Through a First-Principles Investigation of Tetragonal Mo_2N" *J. Phys. Mater.*, 2022. (*In preparation*)

8. J. Zhang, S. Shen, M. Wang, D. Puggioni, W. Xing, X. Xu, Y. Lyu, **L.N. Walters**, L. Liu, Y. Wang, H. Peng, H. Ishizuka, D. Yi, T. Nan, Z. Sheng, Q. He, S. Zhou, R. Yu, N. Nagaosa, C.W. Nan, Y. Tokura, J.M. Rondinelli, P. Yu, "An intrinsic Ferromagnetic Polar Metal by Design", 2022. (*In preparation*)
9. **L.N. Walters**, J.R. Scully, J.M. Rondinelli, "Revealing Aqueous Thermodynamic Models of O_2-Free Copper Corrosion for Deep Geological Repositories" 2023. (*In preparation*)

Other Publications

1. N.J. Szymanski, **L.N. Walters**, O. Hellman, D. Gall, S.V. Khare. "Dynamical Stabilization in Delafossite Nitrides for Solar Energy Conversion" *J. Mater. Chem. A*, 2018. [link]
2. X. Lang, E. X. Xu, Y. Wei, **L.N. Walters**, M.J.A. Hore, "Isomeric and Structural Effects in Polymer Cononsolvent Systems" *Polymer*, 2019. [link]

Bibliography

[1] M. Pourbaix, Atlas of Electrochemical Equilibria in Aqueous Solutions, 2nd Edition, National Association of Corrosion, 1974.

[2] B. Beverskog, I. Puigdomenech, Revised pourbaix diagrams for copper at 5-150 °C, SKI-R–95-73 (1995) 1–67.

[3] e. John R. Rumble, CRC Handbook of Chemistry and Physics, CRC Press/Taylor & Francis, 2019.

[4] L. Huang, J. M. Rondinelli, Reliable electrochemical phase diagrams of magnetic transition metals and related compounds from high-throughput ab initio calculations, npj Mater. Degrad. 3 (1) (2019) 26. doi:10.1038/s41529-019-0088-z.

[5] C. Kittel, Introduction to Solid State Physics, 8th Edition, John Wiley & Sons, Inc., 2005.

[6] J. Malcolm W. Chase, JANAF thermochemical tables. [Temperature dependence], New York : American Institute of Physics for the National Institute of Standards and Technology, 1998. doi:10.18434/T42S31.

[7] H. Halbach, N. D. Chatterjee, An empirical Redlich-Kwong-type equation of state for water to 1,000°C and 200 kbar, Contrib. Mineral. Petrol. 79 (3) (1982) 337–345. doi:10.1007/bf00371526.

[8] D. D. Wagman, W. H. Evans, V. B. Parker, R. H. Schumm, I. B. Halow, M. Sylvia, K. L. Churney, R. L. Nuttal, The NBS tables of chemical thermodynamic properties. selected values for inorganic and C_1 and C_2 organic substances in SI units, J. Phys. Chem. Ref. Data 11 (1982) 2–119.
URL https://srd.nist.gov/JPCRD/jpcrdS2Vol11.pdf

[9] J. Speight, Lange's Handbook of Chemistry, Sixteenth Edition, McGraw-Hill Education, New York, 2005.
URL https://www.accessengineeringlibrary.com/content/book/9780071432207/toc-chapter/chapter1/section/section1

[10] M. R. Schock, Response of lead solubility to dissolved carbonate in drinking water, J. Am. Water Works Assoc. 72 (12) (1980) 695–704. doi:10.1002/j.1551-8833.1980.tb04616.x.

[11] P. Vieillard, Y. Tardy, Thermochemical properties of phosphates, in: Photosphate Minerals, Springer Berlin Heidelberg, Berlin, Heidelberg, 1984, pp. 171–198. doi:10.1007/978-3-642-61736-2_4.

[12] M. A. Mercy, P. A. Rock, W. H. Casey, M. M. Mokarram, Gibbs energies of formation for hydrocerussite $[Pb(OH)_2{\cdot}(PbCO3)_{2(s)}]$ and hydrozincite $[Zn(OH)_2]_3{\cdot}(ZnCO_3)_{2(s)}]$ at 298 K and 1 bar from electrochemical cell measurements, Am. Min. 83 (7-8) (1998) 739–745. doi:10.2138/am-1998-7-806.

[13] J. O. Nriagu, Lead orthophosphates. i. solubility and hydrolysis of secondary lead orthophosphate, Inorg. Chem. 11 (10) (1972) 2499–2503. doi:10.1021/ic50116a041.

[14] Y. Zhu, Z. Zhu, X. Zhao, Y. Liang, Y. Huang, Characterization, dissolution, and solubility of lead hydroxypyromorphite [$Pb_5(PO_4)_3OH$] at 25–45°C, J. Chem. 2015 (2015) 1–10. doi:10.1155/2015/269387.

[15] J. M. Cowley, Electron-diffraction study of the structure of basic lead carbonate, $2PbCO_3{\cdot}Pb(OH)_2$, Acta Crystallogr. 9 (4) (1956) 391–396. doi:10.1107/s0365110x56001133.

[16] P. Martinetto, M. Anne, E. Dooryhée, P. Walter, G. Tsoucaris, Synthetic hydrocerussite, $2PbCO_3{\cdot}Pb(OH)_2$, by x-ray powder diffraction, Acta Crystallogr. C 58 (6) (2002) i82–i84. doi:10.1107/s0108270102006844.

[17] R. J. Thibeau, C. W. Brown, A. Z. Goldfarb, R. H. Heidersbach, Infrared and raman spectroscopy of aqueous corrosion films on lead, J. Electrochem. Soc. 127 (1) (1980) 37.

[18] K. J. Pieper, R. Martin, M. Tang, L. Walters, J. Parks, S. Roy, C. Devine, M. A. Edwards, Evaluating water lead levels during the Flint water crisis, Environ. Sci. Technol. 52 (15) (2018) 8124–8132. doi:10.1021/acs.est.8b00791.

[19] L. Dutcher, W. Moyle, Tables for reducing bicarbonate to compute sum of determined constituents and for calculating hardness of a natural ground water (1960). doi:10.3133/ofr6042.

[20] C. Zhang, J. He, R. McClain, H. Xie, S. Cai, L. N. Walters, J. Shen, F. Ding, X. Zhou, C. D. Malliakas, J. M. Rondinelli, M. G. Kanatzidis, C. Wolverton, V. P. Dravid, K. R. Poeppelmeier, Low thermal conductivity in heteroanionic materials with layers of homoleptic polyhedra, J. Am. Chem. Soc. 144 (6) (2022) 2569–2579. doi:10.1021/jacs.1c10284.

[21] L.-F. Huang, H. M. Ha, K. Lutton Cwalina, J. R. Scully, J. M. Rondinelli, Understanding electrochemical stabilities of ni-based nanofilms from a comparative theory–experiment approach, J. Phys. Chem. C 123 (47) (2019) 28925–28940. doi:10.1021/acs.jpcc.9b05773.

[22] J. E. Saal, S. Kirklin, M. Aykol, B. Meredig, C. Wolverton, Materials design and discovery with high-throughput density functional theory: The open quantum materials database (OQMD), JOM 65 (11) (2013) 1501–1509. doi:10.1007/s11837-013-0755-4.

[23] S. Kirklin, J. E. Saal, B. Meredig, A. Thompson, J. W. Doak, M. Aykol, S. Rühl, C. Wolverton, The open quantum materials database (OQMD): assessing the accuracy of DFT formation energies, npj Comput. Mater. 1 (1) (2015). doi:10.1038/npjcompumats.2015.10.

[24] A. Jain, G. Hautier, C. J. Moore, S. Ping Ong, C. C. Fischer, T. Mueller, K. A. Persson, G. Ceder, A high-throughput infrastructure for density functional theory calculations, Comput. Mater. Sci. 50 (8) (2011) 2295–2310. doi:10.1016/j.commatsci.2011.02.023.

[25] A. Jain, S. P. Ong, G. Hautier, W. Chen, W. D. Richards, S. Dacek, S. Cholia, D. Gunter, D. Skinner, G. Ceder, K. A. Persson, Commentary: The Materials Project: A materials genome approach to accelerating materials innovation, APL Mater. 1 (1) (2013) 011002. doi:10.1063/1.4812323.

[26] L. N. Walters, L.-F. Huang, J. M. Rondinelli, First-principles-based prediction of electrochemical oxidation and corrosion of copper under multiple environmental factors, J. Phys. Chem. C 125 (25) (2021) 14027—-14038. doi:10.1021/acs.jpcc.1c02505.

[27] L. Huang, J. M. Rondinelli, Electrochemical phase diagrams of Ni from ab initio simulations: role of exchange interactions on accuracy, J. Condens. Matter Phys. 29 (47) (2017) 475501. doi:10.1088/1361-648x/aa9140.

[28] K. A. Persson, B. Waldwick, P. Lazic, G. Ceder, Prediction of solid-aqueous equilibria: Scheme to combine first-principles calculations of solids with experimental aqueous states, Phys. Rev. B 85 (2012) 235438. doi:10.1103/PhysRevB.85.235438.

[29] E. L. Shock, D. C. Sassani, M. Willis, D. A. Sverjensky, Inorganic species in geologic fluids: Correlations among standard molal thermodynamic properties of aqueous ions and hydroxide complexes, Geochim. Cosmochim. Acta 61 (5) (1997) 907–950. doi:10.1016/s0016-7037(96)00339-0.

[30] A. Belsky, M. Hellenbrandt, V. L. Karen, P. Luksch, New developments in the inorganic crystal structure database (ICSD): accessibility in support of materials research and design, Acta Cryst. B 58 (3 Part 1) (2002) 364–369. doi:10.1107/S0108768102006948.

[31] J. Gamon, D. Giaume, G. Wallez, J.-B. Labégorre, O. I. Lebedev, R. Al Rahal Al Orabi, S. Haller, T. Le Mercier, E. Guilmeau, A. Maignan, P. Barboux, Substituting copper with silver in the BiMOCh layered compounds (M = Cu or Ag; Ch = S, Se, or Te): Crystal, electronic structure, and optoelectronic properties, Chem. Mater. 30 (2) (2018) 549–558. doi:10.1021/acs.chemmater.7b04962.

[32] A. BaQais, A. Curutchet, A. Ziani, H. Ait Ahsaine, P. Sautet, K. Takanabe, T. Le Bahers, Bismuth silver oxysulfide for photoconversion applications: Structural and optoelectronic properties, Chem. Mater. 29 (20) (2017) 8679–8689. doi:10.1021/acs.chemmater.7b02664.

[33] J. W. Gibbs, On the equilibrium of heterogeneous substances (1876).

[34] C. Wolverton, G. Ceder, D. Fontaine, H. Dressyé, Ground state searches in fcc intermetallics, lBNL Report #: LBL-31831 (1991).
URL https://escholarship.org/uc/item/34m336nz

[35] D. D. Lee, J. H. Choy, J. K. Lee, Computer generation of binary and ternary phase diagrams via a convex hull method, J. Phase Equilibria Diffus. 13 (4) (1992) 365–372. doi:10.1007/bf02674981.

[36] A. Jain, S. P. Ong, G. Hautier, W. Chen, W. D. Richards, S. Dacek, S. Cholia, D. Gunter, D. Skinner, G. Ceder, K. A. Persson, Commentary: The materials project: A materials genome approach to accelerating materials innovation, APL Mater. 1 (1) (2013) 011002. doi:10.1063/1.4812323.

[37] J.-M. R. Génin, C. Ruby, A. Gehin, P. Refait, Synthesis of green rusts by oxidation of $Fe(OH)_2$, their products of oxidation and reduction of ferric oxyhydroxides; eh-ph pourbaix diagrams, CR Geosci. 338 (6) (2006) 433–446. doi:10.1016/j.crte.2006.04.004.

[38] R. M. Nyffenegger, B. Craft, M. Shaaban, S. Gorer, G. Erley, R. M. Penner, A hybrid electrochemical/-chemical synthesis of zinc oxide nanoparticles and optically intrinsic thin films, Chem. Mater. 10 (4) (1998) 1120–1129. doi:10.1021/cm970718m.

[39] W. Sun, D. A. Kitchaev, D. Kramer, G. Ceder, Non-equilibrium crystallization pathways of manganese oxides in aqueous solution, Nat. Commun. 10 (1) (2019). doi:10.1038/s41467-019-08494-6.

[40] L. Liu, Y. Ou, D. Gao, L. Yang, H. Dong, P. Xiao, Y. Zhang, Surface engineering by a novel electrochemical activation method for the synthesis of Co^{3+} enriched $Co(OH)_2$/CoOOH heterostructure for water oxidation, J. Power Sources 396 (2018) 395–403. doi:10.1016/j.jpowsour.2018.06.030.

[41] L. Tang, B. Han, K. Persson, C. Friesen, T. He, K. Sieradzki, G. Ceder, Electrochemical stability of nanometer-scale Pt particles in acidic environments, J. Am. Chem. Soc. 132 (2) (2009) 596–600. doi:10.1021/ja9071496.

[42] V. Sumaria, D. Krishnamurthy, V. Viswanathan, Quantifying confidence in DFT predicted surface Pourbaix diagrams and associated reaction pathways for chlorine evolution, ACS Catal. 8 (10) (2018) 9034–9042. doi:10.1021/acscatal.8b01432.

[43] K. S. Williams, J. P. Labukas, V. Rodriguez-Santiago, J. W. Andzelm, First principles modeling of water dissociation on Mg(0001) and development of a Mg surface Pourbaix diagram, CORROSION 71 (2) (2015) 209–223. doi:10.5006/1322.

[44] L. Huang, J. M. Rondinelli, Electrochemical phase diagrams for Ti oxides from density functional calculations, Phys. Rev. B 92 (2015) 245126. doi:10.1103/PhysRevB.92.245126.

[45] B.-R. Chen, W. Sun, D. A. Kitchaev, J. S. Mangum, V. Thampy, L. M. Garten, D. S. Ginley, B. P. Gorman, K. H. Stone, G. Ceder, M. F. Toney, L. T. Schelhas, Understanding crystallization pathways leading to manganese oxide polymorph formation, Nat. Commun. 9 (1) (2018). doi:10.1038/s41467-018-04917-y.

[46] W.-S. Cho, M. Yoshimura, Hydrothermal, hydrothermal-electrochemical and electrochemical synthesis of highly crystallized barium tungstate films, Jpn. J. Appl. Phys. 36 (Part 1, No. 3A) (1997) 1216–1222. doi:10.1143/jjap.36.1216.

[47] A. Rabenau, The role of hydrothermal synthesis in preparative chemistry, Angew. Chem. 24 (12) (1985) 1026–1040. doi:10.1002/anie.198510261.

[48] R. Piticescu, C. Monty, D. Millers, Hydrothermal synthesis of nanostructured zirconia materials: Present state and future prospects, Sens. Actuator B-Chem. 109 (1) (2005) 102–106. doi:10.1016/j.snb.2005.03.092.

[49] M. Yu, T. I. Draskovic, Y. Wu, Understanding the crystallization mechanism of delafossite $CuGaO_2$ for controlled hydrothermal synthesis of nanoparticles and nanoplates, Inorg. Chem. 53 (11) (2014) 5845–5851. doi:10.1021/ic500747x.

[50] J. Chen, A. Selloni, First principles study of cobalt (hydr)oxides under electrochemical conditions, J. Phys. Chem. C 117 (39) (2013) 20002–20006. doi:10.1021/jp406331h.

[51] A. Lee, J. E. S. Suchismita Sarker, L. Ward, C. Borg, A. Mehta, C. Wolverton, Machine learned synthesizability predictions aided by density functional theory, Commun. Mater. 3 (73) (2022) 1–11. doi:10.1038/s43246-022-00295-7.

[52] M. Aykol, S. S. Dwaraknath, W. Sun, K. A. Persson, Thermodynamic limit for synthesis of metastable inorganic materials, Sci. Adv. 4 (4) (2018) 1–7. doi:10.1126/sciadv.aaq0148.

[53] W. T. Thompson, M. H. Kaye, C. W. Bale, A. D. Pelton, Pourbaix diagrams for multielement systems, John Wiley & Sons, Ltd, 2011, Ch. 8, pp. 103–109. doi:10.1002/9780470872864.ch8.

[54] A. Dias, Theoretical calculations and hydrothermal processing of $BaWO_4$ materials under environmentally friendly conditions, J. Solution Chem. 40 (6) (2011) 1126–1139. doi:10.1007/s10953-011-9706-2.

[55] N. K. V. Nadimpalli, R. Bandyopadhyaya, V. Runkana, Thermodynamic analysis of hydrothermal synthesis of nanoparticles, Fluid Ph. Equilibria 456 (2018) 33–45. doi:10.1016/j.fluid.2017.10.002.

[56] A. Anderko, S. J. Sanders, R. D. Young, Real-solution stability diagrams: A thermodynamic tool for modeling corrosion in wide temperature and concentration ranges, Corrosion 53 (01) (1997) 43–53. doi:10.5006/1.3280432.

[57] C. Technologies, Corrosion cost and preventive strategies in the united states [summary] (March 2002). URL https://rosap.ntl.bts.gov/view/dot/39217#tabs-2

[58] J. K. Harada, N. Charles, K. R. Poeppelmeier, J. M. Rondinelli, Heteroanionic materials by design: Progress toward targeted properties, Adv. Mater. 31 (19) (2019) 1805295. doi:10.1002/adma.201805295.

[59] A. Fuertes, Synthetic approaches in oxynitride chemistry, J. Solid State Chem. 51 (2018) 63–70. doi:10.1016/j.progsolidstchem.2017.11.001.

[60] H. Kageyama, K. Hayashi, K. Maeda, J. P. Attfield, Z. Hiroi, J. M. Rondinelli, K. R. Poeppelmeier, Expanding frontiers in materials chemistry and physics with multiple anions, Nat. Commun. 9 (2018) 772. doi:10.1038/s41467-018-02838-4.

[61] K. Kovnir, Predictive synthesis, Chem. Mater. 33 (13) (2021) 4835–4841. doi:10.1021/acs.chemmater.1c01484.

[62] M. Bianchini, J. Wang, R. J. Clément, B. Ouyang, P. Xiao, T. S. Daniil Kitchaev, Y. Zhang, Y. Wang, H. Kim, M. Zhang, J. Bai, F. Wang, W. Sun, G. Ceder, The interplay between thermodynamics and kinetics in the solid-state synthesis of layered oxides, Nat. Mater. 19 (2020) 1088—1095. doi:10.1038/s41563-020-0688-6.

[63] L. N. Walters, C. Zhang, V. P. Dravid, K. R. Poeppelmeier, J. M. Rondinelli, First-principles hydrothermal synthesis design to optimize conditions and increase the yield of quaternary heteroanionic oxychalcogenides, Chem. Mater. 33 (8) (2021) 2726–2741. doi:10.1021/acs.chemmater.0c02682.

[64] D. P. Shoemaker, Y.-J. Hu, D. Y. Chung, G. J. Halder, P. J. Chupas, L. Soderholm, J. F. Mitchell, M. G. Kanatzidis, In situ studies of a platform for metastable inorganic crystal growth and materials discovery, Proc. Natl. Acad. Sci. U.S.A. 111 (30) (2014) 10922–10927. doi:10.1073/pnas.1406211111.

[65] A. S. Haynes, C. C. Stoumpos, H. Chen, D. Chica, M. G. Kanatzidis, Panoramic synthesis as an effective materials discovery tool: The system Cs/Sn/P/Se as a test case, J. Am. Chem. Soc. 139 (31) (2017) 10814–10821. doi:10.1021/jacs.7b05423.

[66] V. Gvozdetskyi, B. Owens-Baird, S. Hong, T. Cox, G. Bhaskar, C. Harmer, Y. Sun, F. Zhang, C.-Z. Wang, K.-M. Ho, J. V. Zaikina, From $NaZn_4Sb_3$ to HT-$Na_{1-x}Zn_{4-y}Sb_3$: Panoramic hydride

synthesis, structural diversity, and thermoelectric properties, Chem. Mater. 31 (21) (2019) 8695–8707. doi:10.1021/acs.chemmater.9b02239.

[67] M. M. Łencka, R. E. Riman, Thermodynamic modeling of hydrothermal synthesis of ceramic powders, Chem. Mater. 5 (1) (1993) 61–70. doi:10.1021/cm00025a014.

[68] M. M. Lencka, E. Nielsen, A. Anderko, R. E. Riman, Hydrothermal synthesis of carbonate-free strontium zirconate: Thermodynamic modeling and experimental verification, Chem. Mater. 9 (5) (1997) 1116–1125. doi:10.1021/cm960444n.

[69] R. E. Riman, W. L. Suchanek, M. M. Lencka, Hydrothermal crystallization of ceramics, Ann. Chim. Sci. Mat. 27 (6) (2002) 15–36. doi:10.1016/S0151-9107(02)90012-7.

[70] A. Dias, Thermodynamic studies as predictive tools of the behavior of electroceramics under different hydrothermal environments, J. Solution Chem. 38 (7) (2009) 843–856. doi:10.1007/s10953-009-9413-4.

[71] A. Dias, V. S. Ciminelli, Thermodynamic calculations and modeling of the hydrothermal synthesis of nickel tungstates, J. Eur. Ceram. Soc. 21 (10) (2001) 2061–2065. doi:10.1016/S0955-2219(01)00172-8.

[72] W. Sun, M. J. Powell-Palm, Generalized Gibbs' phase rule (2021). doi:10.48550/ARXIV.2105.01337.

[73] M. W. Chase, NIST-JANAF Thermochemical Tables, 4th Edition, American Institute of Physics, New York, 1998.

[74] J. M. Dick, Diagrams with multiple metals in chnosz, Appl. Comput. Geosci 10 (2021) 100059. doi:10.1016/j.acags.2021.100059.

[75] Y. Wang, J. Lv, Q. Li, H. Wang, Y. Ma, Calypso method for structure prediction and its applications to materials discovery (2018). doi:10.1007/978-3-319-50257-1_70-1.

[76] A. Walle, G. Ceder, Automating first-principles phase diagram calculations, J. Phase Equilibria Diffus. 23 (4) (2002) 348–359. doi:10.1361/105497102770331596.

[77] A. van de Walle, M. Asta, Self-driven lattice-model Monte Carlo simulations of alloy thermodynamic properties and phase diagrams, Model. Simul. Mater. Sci. Eng. 10 (5) (2002) 521–538. doi:10.1088/0965-0393/10/5/304.

[78] A. van de Walle, M. Asta, G. Ceder, The alloy theoretic automated toolkit: A user guide, Calphad 26 (4) (2002) 539–553. doi:10.1016/s0364-5916(02)80006-2.

[79] A. van de Walle, Multicomponent multisublattice alloys, nonconfigurational entropy and other additions to the alloy theoretic automated toolkit, Calphad 33 (2) (2009) 266–278. doi:10.1016/j.calphad.2008.12.005.

[80] G. L. W. Hart, R. W. Forcade, Algorithm for generating derivative structures, Phys. Rev. B 77 (2008) 224115. doi:10.1103/PhysRevB.77.224115.

[81] A. van de Walle, P. Tiwary, M. de Jong, D. Olmsted, M. Asta, A. Dick, D. Shin, Y. Wang, L.-Q. Chen, Z.-K. Liu, Efficient stochastic generation of special quasirandom structures, Calphad 42 (2013) 13–18. doi:10.1016/j.calphad.2013.06.006.

[82] M. Ångqvist, W. A. Muñoz, J. M. Rahm, E. Fransson, C. Durniak, P. Rozyczko, T. H. Rod, P. Erhart, ICET – a python library for constructing and sampling alloy cluster expansions, Adv. Theory Simul. 2 (7) (2019) 1900015. doi:10.1002/adts.201900015.

[83] G. L. W. Hart, R. W. Forcade, Algorithm for generating derivative structures, Phys. Rev. B 77 (22) (2008). doi:10.1103/physrevb.77.224115.

[84] G. L. W. Hart, R. W. Forcade, Generating derivative structures from multilattices: Algorithm and application to hcp alloys, Phys. Rev. B 80 (1) (2009). doi:10.1103/physrevb.80.014120.

[85] A. Zunger, S.-H. Wei, L. G. Ferreira, J. E. Bernard, Special quasirandom structures, Phys. Rev. Lett. 65 (3) (1990) 353–356. doi:10.1103/physrevlett.65.353.

[86] A. van de Walle, P. Tiwary, M. de Jong, D. Olmsted, M. Asta, A. Dick, D. Shin, Y. Wang, L.-Q. Chen, Z.-K. Liu, Efficient stochastic generation of special quasirandom structures, Calphad 42 (2013) 13–18. doi:10.1016/j.calphad.2013.06.006.

[87] P. Hohenberg, W. Kohn, Inhomogeneous electron gas, Phys. Rev. 136 (1964) B864–B871. doi:10.1103/PhysRev.136.B864.

[88] W. Kohn, L. J. Sham, Self-consistent equations including exchange and correlation effects, Phys. Rev. 140 (1965) A1133–A1138. doi:10.1103/PhysRev.140.A1133.

[89] L.-F. Huang, M. J. Hutchison, R. J. Santucci, J. R. Scully, J. M. Rondinelli, Improved electrochemical phase diagrams from theory and experiment: The Ni-water system and its complex compounds, J. Phys. Chem. C 121 (18) (2017) 9782–9789. doi:10.1021/acs.jpcc.7b02771.

[90] A. Benisek, E. Dachs, The accuracy of standard enthalpies and entropies for phases of petrological interest derived from density-functional calculations, Contrib. Mineral. Petrol. 173 (11) (2018). doi:10.1007/s00410-018-1514-x.

[91] A. V. Krukau, O. A. Vydrov, A. F. Izmaylov, G. E. Scuseria, Influence of the exchange screening parameter on the performance of screened hybrid functionals, J. Chem. Phys. 125 (22) (2006) 224106. doi:10.1063/1.2404663.

[92] P. E. Blöchl, Projector augmented-wave method, Phys. Rev. B 50 (1994) 17953–17979. doi:10.1103/PhysRevB.50.17953.

[93] G. Kresse, D. Joubert, From ultrasoft pseudopotentials to the projector augmented-wave method, Phys. Rev. B 59 (1999) 1758–1775. doi:10.1103/PhysRevB.59.1758.

[94] K. A. Baseden, J. W. Tye, Introduction to density functional theory: Calculations by hand on the helium atom, J. Chem. Educ. 91 (12) (2014) 2116–2123. doi:10.1021/ed5004788.

[95] M.-C. Kim, E. Sim, K. Burke, Understanding and reducing errors in density functional calculations, Phys. Rev. Lett. 111 (2013) 073003. doi:10.1103/PhysRevLett.111.073003.

[96] G. Kresse, J. Hafner, Ab initio molecular dynamics for liquid metals, Phys. Rev. B 47 (1) (1993) 558. doi:10.1103/PhysRevB.47.558.

[97] G. Kresse, J. Hafner, Ab initio molecular-dynamics simulation of the liquid-metal–amorphous-semiconductor transition in germanium, Phys. Rev. B 49 (20) (1994) 14251. doi:10.1103/PhysRevB.49.14251.

[98] G. Kresse, J. Furthmüller, Efficiency of ab-initio total energy calculations for metals and semiconductors using a plane-wave basis set, Comput. Mater. Sci. 6 (1) (1996) 15–50. doi:10.1016/0927-0256(96)00008-0.

[99] G. Kresse, J. Furthmüller, Efficient iterative schemes for ab initio total-energy calculations using a plane-wave basis set, Phys. Rev. B 54 (16) (1996) 11169–11186. doi:10.1103/PhysRevB.54.11169.

[100] J. P. Perdew, A. Ruzsinszky, G. I. Csonka, O. A. Vydrov, G. E. Scuseria, L. A. Constantin, X. Zhou, K. Burke, Restoring the density-gradient expansion for exchange in solids and surfaces, Phys. Rev. Lett. 100 (2008) 136406. doi:10.1103/PhysRevLett.100.136406.

[101] G. I. Csonka, J. P. Perdew, A. Ruzsinszky, P. H. T. Philipsen, S. Lebégue, J. Paier, O. A. Vydrov, J. G. Ángyán, Assessing the performance of recent density functionals for bulk solids, Phys. Rev. B 79 (2009) 155107. doi:10.1103/PhysRevB.79.155107.

[102] J. Sun, A. Ruzsinszky, J. P. Perdew, Strongly constrained and appropriately normed semilocal density functional, Phys. Rev. Lett. 115 (2015) 036402. doi:10.1103/PhysRevLett.115.036402.

[103] J. P. Perdew, K. Burke, M. Ernzerhof, Generalized gradient approximation made simple, Phys. Rev. Lett. 77 (1996) 3865–3868. doi:10.1103/PhysRevLett.77.3865.

[104] J. P. Perdew, K. Burke, M. Ernzerhof, Generalized gradient approximation made simple, Phys. Rev. Lett. 78 (1997) 1396–1396. doi:10.1103/PhysRevLett.78.1396.

[105] J. P. Perdew, A. Zunger, Self-interaction correction to density-functional approximations for many-electron systems, Phys. Rev. B 23 (1981) 5048–5079. doi:10.1103/PhysRevB.23.5048.

[106] J. B. Forsyth, P. J. Brown, B. M. Wanklyn, Journal of physics C: Solid state physics magnetism in cupric oxide, J. Phys. C: Solid State Phys. 21 (15) (1988) 2917. doi:10.1088/0022-3719/21/15/023.

[107] W. T. Borden, R. Hoffmann, T. Stuyver, B. Chen, Dioxygen: What makes this triplet diradical kinetically persistent?, J. Am. Chem. Soc. 139 (26) (2017) 9010–9018. doi:10.1021/jacs.7b04232.

[108] A. Tkatchenko, M. Scheffler, Accurate molecular van der waals interactions from ground-state electron density and free-atom reference data, Phys. Rev. Lett. 102 (2009) 073005. doi:10.1103/PhysRevLett.102.073005.

[109] R. Sabatini, T. Gorni, S. de Gironcoli, Nonlocal van der Waals density functional made simple and efficient, Phys. Rev. B 87 (2013) 041108. doi:10.1103/PhysRevB.87.041108.

[110] S. Grimme, J. Antony, S. Ehrlich, H. Krieg, A consistent and accurate ab initio parametrization of density functional dispersion correction (DFT-D) for the 94 elements H-Pu, J. Chem. Phys. 132 (15) (2010) 154104. doi:10.1063/1.3382344.

[111] A. Togo, I. Tanaka, First principles phonon calculations in materials science, Scr. Mater. 108 (2015) 1–5.

[112] B. Fultz, Vibrational thermodynamics of materials, Prog. Mater. Sci. 55 (2010) 247. doi:10.1016/j.pmatsci.2009.05.002.

[113] H. C. Helgeson, Prediction of the thermodynamic properties of electrolytes at high pressures and temperatures, Phys. Chem. Earth 13-14 (1981) 133–177. doi:10.1016/0079-1946(81)90009-4.

[114] E. L. Shock, H. C. Helgeson, Calculation of the thermodynamic and transport properties of aqueous species at high pressures and temperatures: Correlation algorithms for ionic species and equation of state predictions to 5 kb and 1000 °C, Geochim. Cosmochim. Acta 52 (8) (1988) 2009–2036. doi:10.1016/0016-7037(88)90181-0.

[115] E. L. Shock, H. C. Helgeson, D. A. Sverjensky, Calculation of the thermodynamic and transport properties of aqueous species at high pressures and temperatures: Standard partial molal properties of inorganic neutral species, Geochim. Cosmochim. Acta 53 (9) (1989) 2157–2183. doi:10.1016/0016-7037(89)90341-4.

[116] H. C. Helgeson, Thermodynamics of complex dissociation in aqueous solution at elevated temperatures, J. Phys. Chem. 71 (10) (1967) 3121–3136. doi:10.1021/j100869a002.

[117] H. C. Helgeson, D. H. Kirkham, G. C. Flowers, Theoretical prediction of the thermodynamic behavior of aqueous electrolytes by high pressures and temperatures; IV, calculation of activity coefficients, osmotic coefficients, and apparent molal and standard and relative partial molal properties to 600 °C and 5kb, Am. J. Sci. 281 (1981) 1249. doi:10.2475/ajs.281.10.1249.

[118] J. C. Tanger, H. C. Helgeson, Calculation of the thermodynamic and transport properties of aqueous species at high pressures and temperatures; revised equations of state for the standard partial molal properties of ions and electrolytes, Am. J. Sci. 288 (1) (1988) 19–98. doi:10.2475/ajs.288.1.19.

[119] P. Dalla-Betta, M. Schulte, Calculation of the aqueous thermodynamic properties of citric acid cycle intermediates and precursors and the estimation of high temperature and pressure equation of state parameters, Int. J. Mol. Sci. 10 (6) (2009) 2809–2837. doi:10.3390/ijms10062809.

[120] B. Beverskog, I. Puigdomenech, Revised pourbaix diagrams for iron at 25-300 °C, Corros. Sci. 38 (12) (1996) 2121–2135. doi:10.1016/S0010-938X(96)00067-4.

[121] B. Beverskog, I. Puigdomenech, Revised Pourbaix diagrams for copper at 25 to 300 °C, J. Electrochem. Soc. 144 (10) (1997) 3476–3483. doi:10.1149/1.1838036.

[122] C. C. Binter, Implementation of the Helgeson-Kirkham-Flowers model to study reservoir temperature evolution during CO_2 injection, Master's thesis, San Diego State University (2012).

[123] E. L. Shock, E. H. Oelkers, J. W. Johnson, D. A. Sverjensky, H. C. Helgeson, Calculation of the thermodynamic properties of aqueous species at high pressures and temperatures. Effective electrostatic radii, dissociation constants and standard partial molal properties to 1000°C and 5 kbar, J. Chem. Soc., Faraday Trans. 88 (1992) 803–826. doi:10.1039/FT9928800803.

[124] J. W. Johnson, D. Norton, Critical phenomena in hydrothermal systems; state, thermodynamic, electrostatic, and transport properties of H_2O in the critical region, Am. J. Sci. 291 (6) (1991) 541–648. doi:10.2475/ajs.291.6.541.

[125] A. Patel, J. K. Nørskov, K. A. Persson, J. H. Montoya, Efficient pourbaix diagrams of many-element compounds (2019). arXiv:1909.00035.

[126] K. Wang, J. Han, A. Y. Gerard, J. R. Scully, B.-C. Zhou, Potential-pH diagrams considering complex oxide solution phases for understanding aqueous corrosion of multi-principal element alloys, npj Mater. Degrad. 4 (1) (2020). doi:10.1038/s41529-020-00141-6.

[127] R. H. Stokes, R. A. Robinson, Ionic hydration and activity in electrolyte solutions, J. Am. Chem. Soc. 70 (5) (1948) 1870–1878. doi:10.1021/ja01185a065.

[128] L. A. Bromley, Thermodynamic properties of strong electrolytes in aqueous solutions, AIChE J. 19 (2) (1973) 313–320. doi:10.1002/aic.690190216.

[129] L. A. Bromley, D. Singh, P. Ray, S. Sridhar, S. M. Read, Thermodynamic properties of sea salt solutions, AIChE J. 20 (2) (1974) 326–335. doi:10.1002/aic.690200218.

[130] J. F. Zemaitis, Predicting vapor-liquid-solid equilibria in multicomponent aqueous solutions of electrolytes, in: Thermodynamics of Aqueous Systems with Industrial Applications, AMERICAN CHEMICAL SOCIETY, 1980, pp. 227–246. doi:10.1021/bk-1980-0133.ch010.
URL https://doi.org/10.1021/bk-1980-0133.ch010

[131] A. M. Patel, J. K. Nørskov, K. A. Persson, J. H. Montoya, Efficient Pourbaix diagrams of many-element compounds, Phys. Chem. Chem. Phys. 21 (2019) 25323–25327. doi:10.1039/C9CP04799A.

[132] P. K. Todd, M. J. McDermott, C. L. Rom, A. A. Corrao, J. J. Denney, S. S. Dwaraknath, P. G. Khalifah, K. A. Persson, J. R. Neilson, Selectivity in yttrium manganese oxide synthesis via local chemical potentials in hyperdimensional phase space, J. Am. Chem. Soc. 143 (37) (2021) 15185–15194. doi:10.1021/jacs.1c06229.

[133] K. A. Persson, B. Waldwick, P. Lazic, G. Ceder, Prediction of solid-aqueous equilibria: Scheme to combine first-principles calculations of solids with experimental aqueous states, Phys. Rev. B 85 (23) (2012). doi:10.1103/physrevb.85.235438.

[134] A. K. Singh, L. Zhou, A. Shinde, S. K. Suram, J. H. Montoya, D. Winston, J. M. Gregoire, K. A. Persson, Electrochemical stability of metastable materials, Chem. Mater. 29 (23) (2017) 10159–10167. doi:10.1021/acs.chemmater.7b03980.

[135] E. S. Wiedner, M. B. Chambers, C. L. Pitman, R. M. Bullock, A. J. M. Miller, A. M. Appel, Thermodynamic hydricity of transition metal hydrides, Chem. Rev. 116 (15) (2016) 8655–8692. doi:10.1021/acs.chemrev.6b00168.

[136] L. N. Walters, E. L. Wang, J. M. Rondinelli, Thermodynamic descriptors to predict oxide formation in aqueous solutions, J. Phys.Chem. Lett. 13 (26) (2022) 6236–6243. doi:10.1021/acs.jpclett.2c01173.

[137] D. W. Oxtoby, Nucleation of first-order phase transitions, Acc. Chem. Res. 31 (2) (1998) 91–97. doi:10.1021/ar9702278.

[138] S. P. Ong, L. Wang, B. Kang, G. Ceder, Li-Fe-P-O_2 phase diagram from first principles calculations, Chem. Mater. 20 (5) (2008) 1798–1807. doi:10.1021/cm702327g.

[139] P. Delahay, M. Pourbaix, P. V. Rysselberghe, Potential-pH diagram of lead and its applications to the study of lead corrosion and to the lead storage battery, J. Electrochem. Soc. 98 (1951) 57–64. doi:10.1149/1.2778106.

[140] J. Bao, G. K. Tranmer, The utilization of copper flow reactors in organic synthesis, Chem. Commun. 51 (2015) 3037. doi:10.1039/C4CC09221J.

[141] V. Maurice, P. Marcus, Progress in corrosion science at atomic and nanometric scales, Prog. Mater. Sci. 95 (2018) 132–171. doi:10.1016/j.pmatsci.2018.03.001.

[142] B. Beverskog, I. Puigdomenech, Revised Pourbaix diagrams for nickel at 25-300 °C, Corros. Sci. 39 (5) (1997) 969–980. doi:10.1016/S0010-938X(97)00002-4.

[143] R. Revie, Uhlig's corrosion handbook, The ECS Series of Texts and Monographs, Wiley, 2011.

[144] W. G. Cook, R. P. Olive, Pourbaix diagrams for chromium, aluminum and titanium extended to high-subcritical and low-supercritical conditions, Corros. Sci. 58 (2012) 291–298. doi:10.1016/j.corsci.2012.02.002.

[145] A. J. Bard, Standard potentials in aqueous solution, 1st Edition, Marcel Dekker, 1985. doi:10.1201/9780203738764.

[146] J. Burgess, Metal ions in solution, Ellis Horwood, 1978.

[147] N. Saito, Y. Tsuchiya, S. Yamamoto, Y. Akai, T. Yotsuyanagi, M. Domae, Y. Katsumura, Chemical thermodynamics consideration on corrosion products in supercritical-water-cooled reactor coolant, Nucl. Technol. 155 (1) (2006) 105–113. doi:10.13182/NT06-A3749.

[148] G. Grass, C. Rensing, M. Solioz, Metallic copper as an antimicrobial surface, Appl. Environ. Microbiol. 77 (5) (2011) 1541–1547. doi:10.1128/AEM.02766-10.

[149] J. Scully, Editorial - THE COVID-19 PANDEMIC, Part 1: Can antimicrobial copper-based alloys help suppress infectious transmission of viruses originating from human contact with high-touch surfaces?, Corrosion 76 (6) (2020) 523–527. doi:10.5006/3568.

[150] R. F. Eife, M. P. Weiss, V. de Oliveira Barros, B. Sigmund, U. Goriup, D. Komb, W. Wolf, J. H. Kittel, P. Schramel, K. D. I. Reiter, Chronic poisoning by copper in tap water: I. copper intoxications with predominantly gastointestinal symptoms., Eur. J. Med. Res. 4 (1999) 219–223.

[151] K. C. Spitalny, J. Brondum, R. L. Vogt, H. E. Sargent, S. Kappel, Drinking-water-induced copper intoxication in a vermont family, Pediatrics 74 (6) (1984) 1103–1106.

[152] J. Walker-Smith, J. Blomfield, Wilson's disease or chronic copper poisoning?, Arch. Dis. Child. 48 (6) (1973) 476–479. doi:10.1136/adc.48.6.476.

[153] M. J. Lehtola, I. T. Miettinen, M. M. Keinänen, T. K. Kekki, O. Laine, A. Hirvonen, T. Vartiainen, P. J. Martikainen, Microbiology, chemistry and biofilm development in a pilot drinking water distribution system with copper and plastic pipes, Water Res. 38 (17) (2004) 3769–3779. doi:10.1016/j.watres.2004.06.024.

[154] E. Mattsson, Counteraction of pitting in copper water pipes by bicarbonate dosing, Mater. Corros. 39 (11) (1988) 499–503. doi:10.1002/maco.19880391104.

[155] B. Wenn, M. Conradi, A. D. Carreiras, D. M. Haddleton, T. Junkers, Photo-induced copper-mediated polymerization of methyl acrylate in continuous flow reactors, Polym. Chem. 5 (8) (2014) 3053–3060. doi:10.1039/c3py01762a.

[156] F. Bergner, A. Ulbricht, H.-W. Viehrig, Acceleration of irradiation hardening of low-copper reactor pressure vessel steel observed by means of SANS and tensile testing, Philos. Mag. Lett. 89 (12) (2009) 795–805. doi:10.1080/09500830903304117.

[157] W. C. Stewart, F. L. LaQue, Corrosion resisting characteristics of iron modified 90:10 cupro nickel alloy, Corrosion 8 (8) (1952) 259–277. doi:10.5006/0010-9312-8.8.259.

[158] K. D. Efird, The synergistic effect of Ni and Fe on the sea water corrosion of copper alloys, Corrosion 33 (10) (1977) 347–350. doi:10.5006/0010-9312-33.10.347.

[159] Y.-J. Oh, G.-S. Park, C.-H. Chung, Planarization of copper layer for damascene interconnection by electrochemical polishing in alkali-based solution, J. Electrochem. Soc. 153 (2006) G617–G621. doi:10.1149/1.2200288.

[160] T. Nakagawa, Etching solution for copper or copper alloy (1997).

[161] N. J. Nelson, Copper etching process and solution (1986).

[162] A. P. Sudarsan, V. M. Ugaz, Printed circuit technology for fabrication of plastic-based microfluidic devices, Anal. Chem. 76 (11) (2004) 3229–3235. doi:10.1021/ac035411n.

[163] D. O. Okanigbe, A. P. I. Popoola, A. A. Adeleke, Hydrometallurgical processing of copper smelter dust for copper recovery as nano-particles: A review, in: L. Zhang, J. W. Drelich, N. R. Neelameggham, D. P. Guillen, N. Haque, J. Zhu, Z. Sun, T. Wang, J. A. Howarter, F. Tesfaye, S. Ikhmayies, E. Olivetti, M. W. Kennedy (Eds.), Energy Technology 2017, Springer International Publishing, Cham, 2017, pp. 205–226.

[164] P. Gonzalez-Montero, N. Iglesias-Gonzalez, R. Romero, A. Mazuelos, F. Carranza, Recovery of zinc and copper from copper smelter flue dust. optimisation of sulphuric acid leaching, Environ. Technol. 0 (0) (2018) 1–8. doi:10.1080/09593330.2018.1521473.

[165] T. Standish, J. Chen, R. Jacklin, P. Jakupi, S. Ramamurthy, D. Zagidulin, P. Keech, D. Shoesmith, Corrosion of copper-coated steel high level nuclear waste containers under permanent disposal conditions, Electrochim. Acta 211 (2016) 331–342. doi:10.1016/j.electacta.2016.05.135.

[166] D. S. Hall, P. G. Keech, An overview of the canadian corrosion program for the long-term management of nuclear waste, Corros. Eng. Sci. Technol. 52 (sup1) (2017) 2–5. doi:10.1080/1478422x.2016.1275419.

[167] Z. Qin, R. Daljeet, M. Ai, N. Farhangi, J. J. Noël, S. Ramamurthy, D. Shoesmith, F. King, P. Keech, The active/passive conditions for copper corrosion under nuclear waste repository environment, Corros. Eng. Sci. Technol. 52 (sup1) (2017) 45–49. doi:10.1080/1478422x.2016.1274088.

[168] T. Martino, R. Partovi-Nia, J. Chen, Z. Qin, D. W. Shoesmith, Mechanisms of film growth on copper in aqueous solutions containing sulphide and chloride under voltammetric conditions, Electrochim. Acta 127 (2014) 439–447. doi:10.1016/j.electacta.2014.02.050.

[169] N. E. Agency, Regulation and guidance for the geoglogical disposal of radioactive waste (2010).

[170] D. P. Crisman, G. K. Jacobs, Native copper deposits of the Portage Lake volcanics, Michigan: their implications with respect to canister stability for nuclear waste isolation in the Columbia River basalts beneath the Hanford Site, Washington, report (1982).

[171] P. A. Korzhavyi, I. L. Soroka, E. I. Isaev, C. Lilja, B. Johansson, Exploring monovalent copper compounds with oxygen and hydrogen, Proc. Natl. Acad. Sci. U.S.A. 109 (3) (2012) 686–689. doi:10.1073/pnas.1115834109.

[172] J. Kunze, V. Maurice, L. H. Klein, H.-H. Strehblow, P. Marcus, In situ scanning tunneling microscopy study of the anodic oxidation of Cu(111) in 0.1 M NaOH, J. Phys. Chem. B 105 (19) (2001) 4263–4269. doi:10.1021/jp004012i.

[173] H.-H. Strehblow, V. Maurice, P. Marcus, Initial and later stages of anodic oxide formation on cu, chemical aspects, structure and electronic properties, Electrochim. Acta 46 (24) (2001) 3755–3766. doi:10.1016/S0013-4686(01)00657-0.

[174] V. Maurice, H.-H. Strehblow, P. Marcus, In situ stm study of the initial stages of oxidation of Cu(111) in aqueous solution, Surf. Sci. 458 (1) (2000) 185–194. doi:10.1016/S0039-6028(00)00442-8.

[175] I. L. Soroka, A. Shchukarev, M. Jonsson, N. V. Tarakina, P. A. Korzhavyi, Cuprous hydroxide in a solid form: does it exist?, Dalton Trans. 42 (2013) 9585–9594. doi:10.1039/C3DT50351H.

[176] L. Var'yash, Equilibria in the $Cu - Cu_2O - H_2O$ system at 150–450 °C, Geochem. Int. 26 (10) (1989) 80.

[177] J. W. Larson, P. Cerutti, H. K. Garber, L. G. Hepler, Electrode potentials and thermodynamic data for aqueous ions. Copper, zinc, cadmium, iron, cobalt, and nickel, J. Phys. Chem. 72 (8) (1968) 2902–2907. doi:10.1021/j100854a037.

[178] N. V. Plyasunova, M. Wang, Y. Zhang, M. Muhammed, Critical evaluation of thermodynamics of complex formation of metal ions in aqueous solutions II. hydrolysis and hydroxo-complexes of Cu^{2+} at 298.15 K, Hydrometallurgy 45 (1) (1997) 37–51. doi:10.1016/S0304-386X(96)00073-4.

[179] S. E. Ziemniak, M. E. Jones, K. E. S. Combs, Copper(II) oxide solubility behavior in aqueous sodium phosphate solutions at elevated temperatures, J. Solution Chem. 21 (2) (1992) 179–200. doi:10.1007/BF00647007.

[180] C. F. Baes, The hydrolysis of cations, Wiley, New York, 1976.

[181] B. X. Yang, T. R. Thurston, J. M. Tranquada, G. Shirane, Magnetic neutron scattering study of single-crystal cupric oxide, Phys. Rev. B 39 (1989) 4343–4349. doi:10.1103/PhysRevB.39.4343.

[182] J. Sun, R. C. Remsing, Y. Zhang, Z. Sun, A. Ruzsinszky, H. Peng, Z. Yang, A. Paul, U. Waghmare, X. Wu, M. L. Klein, J. P. Perdew, Accurate first-principles structures and energies of diversely bonded systems from an efficient density functional, Nat. Chem. 8 (2016) 831–836. doi:10.1038/nchem.2535.

[183] L. Wang, T. Maxisch, G. Ceder, Oxidation energies of transition metal oxides within the gga+u framework, Phys. Rev. B 73 (2006) 195107. doi:10.1103/PhysRevB.73.195107.

[184] A. A. Adllan, A. D. Corso, Ultrasoft pseudopotentials and projector augmented-wave data sets: application to diatomic molecules, J. Condens. Matter Phys. 23 (42) (2011) 425501. doi:10.1088/0953-8984/23/42/425501.

[185] L. A. Curtiss, K. Raghavachari, G. W. Trucks, J. A. Pople, Gaussian-2 theory for molecular energies of first- and second-row compounds, J. Chem. Phys. 94 (11) (1991) 7221–7230. doi:10.1063/1.460205.

[186] A. D. Becke, Density-functional thermochemistry. II. the effect of the Perdew–Wang generalized-gradient correlation correction, J. Chem. Phys. 97 (12) (1992) 9173–9177. doi:10.1063/1.463343.

[187] J. A. Pople, M. Head-Gordon, D. J. Fox, K. Raghavachari, L. A. Curtiss, Gaussian-1 theory: A general procedure for prediction of molecular energies, J. Chem. Phys. 90 (10) (1989) 5622–5629. doi:10.1063/1.456415.

[188] E. L. Shock, D. C. Sassani, M. Willis, D. A. Sverjensky, Inorganic species in geologic fluids: Correlations among standard molal thermodynamic properties of aqueous ions and hydroxide complexes, Geochim. Cosmochim. Acta 61 (5) (1997) 907–950. doi:10.1016/S0016-7037(96)00339-0.

[189] R. Car, Fixing Jacob's ladder, Nat. Chem. 8 (2016) 820–821. doi:10.1038/nchem.2605.

[190] J. W. Hodby, T. E. Jenkins, C. Schwab, H. Tamura, D. Trivich, Cyclotron resonance of electrons and of holes in cuprous oxide, Cu_2O, J. Phys. C: Solid State Phys. 9 (8) (1976) 1429–1439. doi:10.1088/0022-3719/9/8/014.

[191] B. K. Meyer, A. Polity, D. Reppin, M. Becker, P. Hering, P. J. Klar, T. Sander, C. Reindl, J. Benz, M. Eickhoff, C. Heiliger, M. Heinemann, J. Bläsing, A. Krost, S. Shokovets, C. Müller, C. Ronning, Binary copper oxide semiconductors: From materials towards devices, Phys. Status Solidi B 249 (8) (2012) 1487–1509. doi:10.1002/pssb.201248128.

[192] G. L. Draper, Conductive inks and films via intense pulsed light., Master's thesis, University of Louisville (2016).

[193] Z. Zhai, Y. You, L. Ma, D. Jiang, F. Li, H. Yuan, M. Zheng, W. Shen, One-step in situ self-assembly of cypress leaf-like $CuOH_2$ nanostructure/graphene nanosheets composite with excellent cycling stability for supercapacitors, Nanoscale Res. Lett. 14 (1) (2019) 167. doi:10.1186/s11671-019-3000-4.

[194] X. Wang, X. Yin, X.-Y. Lai, Y.-T. Liu, Magnetism, stability and electronic properties of a novel one-dimensional infinite monatomic copper wire: a density functional study, New J. Chem. 43 (2019) 5065–5069. doi:10.1039/C8NJ04975K.

[195] P. Umek, A. Zorko, P. Cevc, M. Škarabot, Z. Jagličič, J. W. Seo, L. Forró, H. van Tool, L. C. C. Brunel, D. Arčon, The impact of ageing on the magnetic properties of $Cu(OH)_2$ nanoribbons, Nanotechnology 16 (9) (2005) 1623–1629. doi:10.1088/0957-4484/16/9/037.

[196] F. Marabelli, G. B. Parravicini, F. Salghetti-Drioli, Optical gap of CuO, Phys. Rev. B 52 (1995) 1433–1436. doi:10.1103/PhysRevB.52.1433.

[197] F. P. Koffyberg, F. A. Benko, A photoelectrochemical determination of the position of the conduction and valence band edges of p-type CuO, J. Appl. Phys. 53 (2) (1982) 1173–1177. doi:10.1063/1.330567.

[198] E. B. Isaacs, C. Wolverton, Performance of the strongly constrained and appropriately normed density functional for solid-state materials, Phys. Rev. Mater. 2 (2018) 063801. doi:10.1103/PhysRevMaterials.2.063801.

[199] D. A. Palmer, The solubility of crystalline cupric oxide in aqueous solution from 25°C to 400°C, J. Chem. Thermodyn. 114 (2017) 122–134, special issue on Thermodynamics of Nuclear Materials. doi:10.1016/j.jct.2017.03.012.

[200] L. Hidmi, M. Edwards, Role of temperature and pH in $CuOH_2$ solubility, Environ. Sci. Technol. 33 (15) (1999) 2607–2610. doi:10.1021/es981121q.

[201] M. Edwards, K. Powers, L. Hidmi, M. Schock, The role of pipe ageing in copper corrosion by-product release, Water Supply 1 (3) (2001) 25–32. doi:10.2166/ws.2001.0050.

[202] C. K. Nguyen, K. A. Powers, M. A. Raetz, J. L. Parks, M. A. Edwards, Rapid free chlorine decay in the presence of $CuOH_2$: Chemistry and practical implications, Water Res. 45 (16) (2011) 5302–5312. doi:10.1016/j.watres.2011.07.039.

[203] X. Wang, X. Yin, X.-Y. Lai, Y.-T. Liu, Magnetism, stability and electronic properties of a novel one-dimensional infinite monatomic copper wire: a density functional study, New J. Chem. 43 (2019) 5065–5069. doi:10.1039/C8NJ04975K.

[204] S. Refaey, F. Taha, A. A. El-Malak, Inhibition of stainless steel pitting corrosion in acidic medium by 2-mercaptobenzoxazole, Appl. Surf. Sci. 236 (1) (2004) 175–185. doi:10.1016/j.apsusc.2004.04.016.

[205] J. M. Kolotyrkin, Pitting corrosion of metals, Corrosion 19 (8) (1963) 261t–268t. doi:10.5006/0010-9312-19.8.261.

[206] I. Puigdomenech, C. Taxen, Thermodynamic data for copper implications for the corrosion of copper under repository conditions (skb-tr–00-13), report (2000).

[207] T. I. Barry, The computation of pourbaix diagrams, ACS Symp. Ser. Am. Chem. Soc. 35 (1980) 681–699. doi:10.1021/bk-1980-0133.ch035.

[208] R. Biernat, R. Robins, High temperature potential/ph diagrams for the sulphur-water system, Electrochim. Acta 14 (9) (1969) 809–820. doi:10.1016/0013-4686(69)87003-9.

[209] D. Kong, A. Xu, C. Dong, F. Mao, K. Xiao, X. Li, D. D. Macdonald, Electrochemical investigation and ab initio computation of passive film properties on copper in anaerobic sulphide solutions, Corros. Sci. 116 (2017) 34–43. doi:10.1016/j.corsci.2016.12.010.

[210] F. Mao, C. Dong, S. Sharifi-Asl, P. Lu, D. D. Macdonald, Passivity breakdown on copper: Influence of chloride ion, Electrochim. Acta 144 (2014) 391–399. doi:10.1016/j.electacta.2014.07.160.

[211] T. Martino, R. Partovi-Nia, J. Chen, Z. Qin, D. W. Shoesmith, Mechanisms of film growth on copper in aqueous solutions containing sulphide and chloride under voltammetric conditions, Electrochim. Acta 127 (2014) 439–447. doi:10.1016/j.electacta.2014.02.050.

[212] T. Martino, J. Chen, M. Guo, S. Ramamurthy, D. W. Shoesmith, J. J. Noël, Comments on E. Huttunen-Saarivirta et al., "Kinetic properties of the passive film on copper in the presence of sulfate-reducing bacteria" [*J. Electrochem. Soc.*, 165, c450 (2018)], J. Electrochem. Soc. 166 (10) (2019) Y13–Y16. doi:10.1149/2.0761910jes.

[213] L. N. Walters, A. T. Tai, R. J. Santucci, J. R. Scully, J. M. Rondinelli, Density functional theory-based thermodynamic model for stable scale formation in lead-water systems, J. Phys. Chem. C 126 (39) (2022) 16841–16850. doi:10.1021/acs.jpcc.2c04836.

[214] J. M. Gibson, M. Fisher, A. Clonch, J. M. MacDonald, P. J. Cook, Children drinking private well water have higher blood lead than those with city water, Proc. Natl. Acad. Sci. U.S.A. 117 (29) (2020) 16898–16907. doi:10.1073/pnas.2002729117.

[215] F. W. A. T. Force, Flint water advisory task force: Final report (2016).

[216] R. J. Santucci, J. R. Scully, The pervasive threat of lead (Pb) in drinking water: Unmasking and pursuing scientific factors that govern lead release, Proc. Natl. Acad. Sci. U.S.A. 117 (38) (2020) 23211–23218. doi:10.1073/pnas.1913749117.

[217] S. Roy, M. A. Edwards, Preventing another lead (Pb) in drinking water crisis: Lessons from the Washington D.C. and Flint MI contamination events, Curr. Opin. Environ. Sci. Health 7 (2019) 34–44. doi:10.1016/j.coesh.2018.10.002.

[218] A. E. Nigra, Environmental racism and the need for private well protections, Proc. Natl. Acad. Sci. U.S.A. 117 (30) (2020) 17476–17478. doi:10.1073/pnas.2011547117.

[219] National primary drinking water regulations: Lead and copper rule revisions (Jan 2020). URL https://www.federalregister.gov/documents/2021/01/15/2020-28691/national-primary-drinking-water-regulations-lead-and-copper-rule-revisions

[220] L. Nalley, V. Rafla, R. Santucci, J. Scully, Method to rapidly characterize reduced lead corrosion in phosphate inhibited drinking water, Corrosion 75 (2) (2019) 147–151. doi:10.5006/3031.

[221] L. S. McNeill, M. Edwards, Importance of pb and cu particulate species for corrosion control, J. Environ. Eng. 130 (2) (2004) 136–144. doi:10.1061/(ASCE)0733-9372(2004)130:2(136).

[222] J. Zhao, D. E. Giammar, J. D. Pasteris, C. Dai, Y. Bae, Y. Hu, Formation and aggregation of lead phosphate particles: Implications for lead immobilization in water supply systems, Environ. Sci. Technol. 52 (21) (2018) 12612–12623. doi:10.1021/acs.est.8b02788.

[223] R. Renner, Reaction to the solution: Lead exposure following partial service line replacement, Environmental Health Perspectives 118 (5) (2010). doi:10.1289/ehp.118-a202.

[224] M. R. Schock, A. F. Cantor, S. Triantafyllidou, M. K. Desantis, K. G. Scheckel, Importance of pipe deposits to lead and copper rule compliance, J. Am. Water Works Assoc. 106 (7) (2014) E336–E349.

[225] J. Tully, M. K. DeSantis, M. R. Schock, Water quality–pipe deposit relationships in midwestern lead pipes, AWWA Wat. Sci. 1 (2) (2019) e1127. doi:10.1002/aws2.1127.

[226] F. A. Vasquez, R. Heaviside, Z. J. Tang, J. S. Taylor, Effect of free chlorine and chloramines on lead release in a distribution system, J. Am. Water Works Ass. 98 (2) (2006) 144–154. doi:10.1002/j.1551-8833.2006.tb07596.x.

[227] P. Delahay, M. Pourbaix, P. V. Rysselberghe, Potential-pH diagram of lead and its applications to the study of lead corrosion and to the lead storage battery, J. Electrochem. Soc. 98 (2) (1951) 57. doi:10.1149/1.2778106.

[228] P. A. Nikolaychuk, The revised potential – pH diagram for Pb–H_2O system, Ovidius Univ. Ann. Chem. 29 (2) (2018) 55–67. doi:10.2478/auoc-2018-0008.

[229] A. A. Abokifa, P. Biswas, Modeling soluble and particulate lead release into drinking water from full and partially replaced lead service lines, Environ. Sci. Technol. 51 (6) (2017) 3318–3326. doi:10.1021/acs.est.6b04994.

[230] D. G. Wahman, M. D. Pinelli, M. R. Schock, D. A. Lytle, Theoretical equilibrium lead(ii) solubility revisited: Open source code and practical relationships, AWWA Wat. Sci. 3 (5) (2021) e1250. doi:10.1002/aws2.1250.

[231] J. D. Hopwood, G. R. Derrick, D. R. Brown, C. D. Newman, J. Haley, R. Kershaw, M. Collinge, The identification and synthesis of lead apatite minerals formed in lead water pipes, J. Chem. 2016 (2016).

[232] X. Li, B. Azimzadeh, C. E. Martinez, M. B. McBride, Pb mineral precipitation in solutions of sulfate, carbonate and phosphate: Measured and modeled Pb solubility and Pb^{2+} activity, Minerals 11 (6) (2021) 620. doi:10.3390/min11060620.

[233] U. S. E. P. Agency, Optimal corrosion control treatment evaluation technical recommendations for primacy agencies and public water system (2016).

[234] Y. Bae, J. D. Pasteris, D. E. Giammar, The ability of phosphate to prevent lead release from pipe scale when switching from free chlorine to monochloramine, Environ. Sci. Technol. 54 (2) (2020) 879–888. doi:10.1021/acs.est.9b06019.

[235] H. Ke, C. D. Taylor, Density functional theory: an essential partner in the integrated computational materials engineering approach to corrosion, Corrosion 75 (7) (2019) 708–726.

[236] L.-F. Huang, J. R. Scully, J. M. Rondinelli, Modeling corrosion with first-principles electrochemical phase diagrams, Annu. Rev. Mater. Res. 49 (1) (2019) 53–77. doi:10.1146/annurev-matsci-070218-010105.

[237] R. Ahuja, A. Blomqvist, P. Larsson, P. Pyykkö, P. Zaleski-Ejgierd, Relativity and the lead-acid battery, Phys. Rev. Lett. 106 (2011) 018301. doi:10.1103/PhysRevLett.106.018301.

[238] R. T. Grimes, J. A. Leginze, R. Zochowski, J. W. Bennett, Surface transformations of lead oxides and carbonates using first-principles and thermodynamics calculations, Inorg. Chem. 60 (2) (2021) 1228–1240. doi:10.1021/acs.inorgchem.0c03398.

[239] A. Voronova, B. Vainshtein, An electron-diffraction study of the crystal structure of $PbCO_3PbO(H_2O)_2$, Kristallografiya 9 (1964) 197–203.

[240] A. Slepko, A. A. Demkov, First-principles study of the biomineral hydroxyapatite, Phys. Rev. B 84 (13) (2011). doi:10.1103/physrevb.84.134108.

[241] O. Miyawaki, A. Saito, T. Matsuo, K. Nakamura, Activity and activity coefficient of water in aqueous solutions and their relationships with solution structure parameters, Biosci. Biotechnol. Biochem. 61 (3) (1997) 466–469. doi:10.1271/bbb.61.466.

[242] I. Persson, K. Lyczko, D. Lundberg, L. Eriksson, A. Płaczek, Coordination chemistry study of hydrated and solvated lead(II) ions in solution and solid state, Inorg. Chem. 50 (3) (2011) 1058–1072. doi:10.1021/ic1017714.

[243] M. C. F. Wander, A. E. Clark, Hydration properties of aqueous Pb(II) ion, Inorg. Chem. 47 (18) (2008) 8233–8241. doi:10.1021/ic800750g.

[244] H. Feilchenfeld, J. Fuchs, Hydration numbers of some acids and salts, Isr. J. Chem. 12 (5) (1974) 899–904. doi:10.1002/ijch.197400081.

[245] Y. yan Wang, L. yuan Chai, H. Chang, X. yu Peng, Y. de Shu, Equilibrium of hydroxyl complex ions in Pb^{2+}-H_2O system, Trans. Nonferrous Met. Soc. China 19 (2) (2009) 458–462. doi:10.1016/S1003-6326(08)60295-2.

[246] P. L. Brown, C. Ekberg (Eds.), Hydrolysis of metal ions, Wiley-VCH Verlag GmbH & Co. KGaA, 2016. doi:10.1002/9783527656189.

[247] C. F. Baes, R. S. Mesmer, The Hydrolysis of cations, John Wiley & Sons, 1976.

[248] J. D. Noel, Y. Wang, D. E. Giammar, Effect of water chemistry on the dissolution rate of the lead corrosion product hydrocerussite, Water Res. 54 (2014) 237–246. doi:10.1016/j.watres.2014.02.004.

[249] Y. Takeuchi, T. Suzuki, H. Arai, A study of equilibrium and mass transfer in processes for removal of heavy-metal ions by hydroxyapatite., J. Chem. Eng. Japan 21 (1) (1988) 98–100. doi:10.1252/jcej.21.98.

[250] Q. Y. Ma, S. J. Traina, T. J. Logan, J. A. Ryan, In situ lead immobilization by apatite, Environ. Sci. Technol. 27 (9) (1993) 1803–1810. doi:10.1021/es00046a007.

[251] Y. Zhu, B. Huang, Z. Zhu, H. Liu, Y. Huang, X. Zhao, M. Liang, Characterization, dissolution and solubility of the hydroxypyromorphite–hydroxyapatite solid solution $[(Pb_xCa_{1-x})_5(PO_4)_3OH]$ at 25 °C and pH 2–9, Geochem. Trans. 17 (1) (2016). doi:10.1186/s12932-016-0034-8.

[252] J. D. Pasteris, Y. Bae, D. E. Giammar, S. N. Dybing, C. H. Yoder, J. Zhao, Y. Hu, Worth a closer look: Raman spectra of lead-pipe scale, Minerals 11 (10) (2021) 1047. doi:10.3390/min11101047.

[253] S. Vesecky, J. Liu, R. Friedman, F. Pacholec, J. Lechner, Comparison of film formation using phosphate inhibitors in systems with comparable water qualities, J. N. Engl. Water Works Assoc. 111 (3) (1997) 258–267.

[254] G. P. Lobo, A. J. Gadgil, Preventing leaching from lead water pipes with electrochemistry: an exploratory study, Environ. Sci. Water Res. Technol. 7 (2021) 1267–1278. doi:10.1039/d1ew00160d.

[255] B. P. Boffardi, A. M. Sherbondy, Control of lead corrosion by chemical treatment, Corrosion 47 (12) (1991) 966–975. doi:10.5006/1.3585211.

[256] Y. Bae, J. D. Pasteris, D. E. Giammar, Impact of orthophosphate on lead release from pipe scale in high ph, low alkalinity water, Water Res. 177 (2020) 115764. doi:10.1016/j.watres.2020.115764.

[257] M. K. DeSantis, M. R. Schock, Ground truthing the 'conventional wisdom' of lead corrosion control using mineralogical analysis, in: Proc. AWWA 2014 Water Quality Technology Conference, New Orleans, 2014.

[258] L. W. Wasserstrom, S. A. Miller, S. Triantafyllidou, M. K. Desantis, M. R. Schock, Scale formation under blended phosphate treatment for a utility with lead pipes, J. Am. Water Work. Assoc. 109 (2017) E464–E478. doi:10.5942/jawwa.2017.109.0121.

[259] X. Zhang, Galvanic corrosion, Uhlig's corrosion handbook 10 (2011) 123–143.

[260] V. V. Goncharuk, V. A. Bagrii, L. A. Mel'nik, R. D. Chebotareva, S. Y. Bashtan, The use of redox potential in water treatment processes, J. Water Chem. Technol. 32 (1) (2010) 1–9. doi:10.3103/s1063455x10010017.

[261] S. Masters, G. J. Welter, M. Edwards, Seasonal variations in lead release to potable water, Environ. Sci. Technol. 50 (10) (2016) 5269–5277. doi:10.1021/acs.est.5b05060.

[262] J. Sima, X. Cao, L. Zhao, Q. Luo, Toxicity characteristic leaching procedure over- or under-estimates leachability of lead in phosphate-amended contaminated soils, Chemosphere 138 (2015) 744–750. doi:10.1016/j.chemosphere.2015.07.028.

[263] C. Nguyen, B. Clark, K. Stone, M. Edwards, Role of chloride, sulfate, and alkalinity on galvanic lead corrosion, Corrosion 67 (6) (2011) 065005–1.

[264] Y. Kobayashi, Y. Tsujimoto, H. Kageyama, Property engineering in perovskites via modification of anion chemistry, Annu. Rev. Mater. Res. 48 (1) (2018) 303–326. doi:10.1146/annurev-matsci-070317-124415.

[265] N. Charles, R. J. Saballos, J. M. Rondinelli, Structural diversity from anion order in heteroanionic materials, Chem. Mater. 30 (10) (2018) 3528–3537. doi:10.1021/acs.chemmater.8b01336.

[266] J. K. Harada, K. R. Poeppelmeier, J. M. Rondinelli, Predicting the structure stability of layered heteroanionic materials exhibiting anion order, Inorg. Chem. 58 (19) (2019) 13229–13240. doi:10.1021/acs.inorgchem.9b02077.

[267] H. Kabbour, E. Janod, B. Corraze, M. Danot, C. Lee, M.-H. Whangbo, L. Cario, Structure and magnetic properties of oxychalcogenides $A_2F_2Fe_2OQ_2$ (A = Sr, Ba; Q = S, Se) with Fe_2O square planar layers representing an antiferromagnetic checkerboard spin lattice, J. Am. Chem. Soc. 130 (26) (2008) 8261–8270. doi:10.1021/ja711139g.

[268] Q. D. Gibson, T. D. Manning, M. Zanella, T. Zhao, P. A. E. Murgatroyd, C. M. Robertson, L. A. H. Jones, F. McBride, R. Raval, F. Cora, B. Slater, J. B. Claridge, V. R. Dhanak, M. S. Dyer, J. Alaria, M. J. Rosseinsky, Modular design via multiple anion chemistry of the high mobility van der waals semiconductor $Bi_4O_4SeCl_2$, J. Am. Chem. Soc. 142 (2) (2019) 847–856. doi:10.1021/jacs.9b09411.

[269] N. J. Szymanski, L. N. Walters, D. Puggioni, J. M. Rondinelli, Design of heteroanionic MoON exhibiting a peierls metal-insulator transition, Phys. Rev. Lett. 123 (2019) 236402. doi:10.1103/PhysRevLett.123.236402.

[270] G. Gou, M. Zhao, J. Shi, J. K. Harada, J. M. Rondinelli, Anion ordered and ferroelectric ruddlesden-popper oxynitride $Ca_3Nb_2N_2O_5$ for visible-light-active photocatalysis, Chem. Mater. 32 (7) (2020) 2815–2823. doi:10.1021/acs.chemmater.9b04429.

[271] H. Fu, S. Zhang, L. Zhang, Y. Zhu, Visible-light-driven $\mathrm{natao}_{3-x}\mathrm{n}_x$ catalyst prepared by a hydrothermal process, Mater. Res. Bull. 43 (4) (2008) 864–872. doi:10.1016/j.materresbull.2007.05.013.

[272] W. C. Sheets, E. S. Stampler, H. Kabbour, M. I. Bertoni, L. Cario, T. O. Mason, T. J. Marks, K. R. Poeppelmeier, Facile synthesis of BiCuOS by hydrothermal methods, Inorg. Chem. 46 (25) (2007) 10741–10748. doi:10.1021/ic7014622.

[273] E. S. Stampler, W. C. Sheets, M. I. Bertoni, W. Prellier, T. O. Mason, K. R. Poeppelmeier, Temperature driven reactant solubilization synthesis of BiCuOSe, Inorg. Chem. 47 (21) (2008) 10009–10016. doi:10.1021/ic801267m.

[274] M. Yoshimura, Importance of soft solution processing for advanced inorganic materials, J. Mater. Res. Technol. 13 (4) (1998) 796–802. doi:10.1557/JMR.1998.0101.

[275] J. Gopalakrishnan, Chimie douce approaches to the synthesis of metastable oxide materials, Chem. Mater. 7 (7) (1995) 1265–1275. doi:10.1021/cm00055a001.

[276] S.-H. YU, Hydrothermal/solvothermal processing of advanced ceramic materials, J. Ceram. Soc. Jpn 109 (1269) (2001) S65–S75. doi:10.2109/jcersj.109.1269_S65.

[277] A. Dias, V. S. T. Ciminelli, Electroceramic materials of tailored phase and morphology by hydrothermal technology, Chem. Mater. 15 (6) (2003) 1344–1352. doi:10.1021/cm0210187.

[278] G. R. Fox, J. H. Adair, R. E. Newnham, Effects of pH and H_2O_2 upon coprecipitated $PbTiO_3$ powders part I properties of as-precipitated powders, J. Mater. Sci. 25 (8) (1990) 3634–3640. doi:10.1007/BF00575398.

[279] G. Canu, V. Buscaglia, Hydrothermal synthesis of strontium titanate: Thermodynamic considerations, morphology control and crystallisation mechanisms, Cryst. Eng. Comm. 19 (28) (2017) 3867–3891. doi:10.1039/c7ce00834a.

[280] L.-D. Zhao, J. He, D. Berardan, Y. Lin, J.-F. Li, C.-W. Nan, N. Dragoe, BiCuSeO oxyselenides: new promising thermoelectric materials, Energy Environ. Sci. 7 (2014) 2900–2924. doi:10.1039/C4EE00997E.

[281] J.-B. Labégorre, R. Al Rahal Al Orabi, A. Virfeu, J. Gamon, P. Barboux, L. Pautrot-d'Alençon, T. Le Mercier, D. Berthebaud, A. Maignan, E. Guilmeau, Electronic band structure engineering and enhanced thermoelectric transport properties in pb-doped bicuos oxysulfide, Chem. Mater. 30 (3) (2018) 1085–1094. doi:10.1021/acs.chemmater.7b04989.

[282] J. Li, C. Zhang, Y. Yan, J. Yang, B. Shi, Y. Wang, Z. Cheng, Predicting excellent anisotropic thermoelectric performance of the layered oxychalcogenides BiAgOCh (Ch=S, Se, and Te), Computational Materials Science 171 (2020) 109273. doi:10.1016/j.commatsci.2019.109273.

[283] Y.-L. Pei, J. He, J.-F. Li, F. Li, Q. Liu, W. Pan, C. Barreteau, D. Berardan, N. Dragoe, L.-D. Zhao, High thermoelectric performance of oxyselenides: Intrinsically low thermal conductivity of ca-doped bicuseo, NPG Asia Mater. 5 (5) (2013) e47–e47. doi:10.1038/am.2013.15.

[284] J. Li, J. Sui, Y. Pei, C. Barreteau, D. Berardan, N. Dragoe, W. Cai, J. He, L.-D. Zhao, A high thermoelectric figure of merit ZT > 1 in Ba heavily doped BiCuSeO oxyselenides, Energy Environ. Sci. 5 (2012) 8543–8547. doi:10.1039/C2EE22622G.

[285] A. L. Pacquette, H. Hagiwara, T. Ishihara, A. A. Gewirth, Fabrication of an oxysulfide of bismuth Bi_2O_2S and its photocatalytic activity in a Bi_2O_2S/In_2O_3 composite, J. Photochem. Photobiol. 277 (2014) 27–36. doi:10.1016/j.jphotochem.2013.12.007.

[286] X. Tian, H. Luo, R. Wei, C. Zhu, Q. Guo, D. Yang, F. Wang, J. Li, J. Qiu, An ultrabroadband mid-infrared pulsed optical switch employing solution-processed bismuth oxyselenide, Adv. Mater. 30 (31) (2018) 1801021. doi:10.1002/adma.201801021.

[287] S. D. Luu, P. Vaqueiro, Synthesis, characterisation and thermoelectric properties of the oxytelluride Bi_2O_2Te, J. Solid State Chem. 226 (2015) 219–223. doi:10.1016/j.jssc.2015.02.026.

[288] H. Hiramatsu, H. Yanagi, T. Kamiya, K. Ueda, M. Hirano, H. Hosono, Crystal structures, optoelectronic properties, and electronic structures of layered oxychalcogenides MCuOCh (M = Bi, La; Ch = S, Se, Te): Effects of electronic configurations of M^{3+} ions, Chem. Mater. 20 (1) (2008) 326–334. doi:10.1021/cm702303r.

[289] A. Richard, J. Russell, A. Zakutayev, L. Zakharov, D. Keszler, J. Tate, Synthesis, structure, and optical properties of BiCuOCh (Ch=S, Se, and Te), J. Solid State Chem. 187 (2012) 15–19. doi:10.1016/j.jssc.2011.11.013.

[290] P. Berdonosov, A. Kusainova, L. Kholodkovskaya, V. Dolgikh, L. Akselrud, B. Popovkin, Powder X-Ray and IR studies of the new oxyselenides MOCuSe (M = Bi, Gd, Dy), J. Solid State Chem. 118 (1) (1995) 74–77. doi:10.1006/jssc.1995.1312.

[291] A. K. Singh, L. Zhou, A. Shinde, S. K. Suram, J. H. Montoya, D. Winston, J. M. Gregoire, K. A. Persson, Electrochemical stability of metastable materials, Chem. Mater. 29 (23) (2017) 10159–10167. doi:10.1021/acs.chemmater.7b03980.

[292] J. A. Mavrogenes, A. J. Berry, M. Newville, S. R. Sutton, Copper speciation in vapor-phase fluid inclusions from the mole granite, Australia, Am. Mineral. 87 (10) (2002) 1360–1364. doi:10.2138/am-2002-1011.

[293] G. J. F. MacDonald, Gibbs free energy of water at elevated temperatures and pressures with applications to the brucite-periclase equilibrium, J. Geol. 63 (3) (1955) 244–252. doi:10.1086/626253.

[294] T. Seward, Metal complex formation in aqueous solutions at elevated temperatures and pressures, Phys. Chem. Earth 13-14 (1981) 113–132. doi:10.1016/0079-1946(81)90008-2.

[295] Y. Xie, D. M. Artymowicz, P. P. Lopes, A. Aiello, D. Wang, J. L. Hart, E. Anber, M. L. Taheri, H. Zhuang, R. C. Newman, K. Sieradzki, A percolation theory for designing corrosion-resistant alloys, Nat. Mater. 20 (6) (2021) 789–793. doi:10.1038/s41563-021-00920-9.

[296] L. Sziráki, Á. Cziráki, I. Geröcs, Z. Vértesy, L. Kiss, A kinetic model of the spontaneous passivation and corrosion of zinc in near neutral Na_2SO_4 solutions, Electrochim. Acta 43 (1-2) (1998) 175–186. doi:10.1016/s0013-4686(97)00223-5.

[297] N. Sinha, K. R. Hebert, Kinetic Model for Oxide Film Passivation in Aluminum Etch Tunnels, J. Electrochem. Soc. 147 (11) (2000) 4111. doi:10.1149/1.1394027.

[298] P. Yu, S. A. Hayes, T. J. O'Keefe, M. J. O'Keefe, J. O. Stoffer, The phase stability of cerium species in aqueous systems, J. Electrochem. Soc. 153 (1) (2006) C74. doi:10.1149/1.2130572.

[299] Y. Zhao, J. Xie, G. Zeng, T. Zhang, D. Xu, F. Wang, Pourbaix diagram for HP-13Cr stainless steel in the aggressive oilfield environment characterized by high temperature, high CO_2 partial pressure and high salinity, Electrochim. Acta 293 (2019) 116–127. doi:10.1016/j.electacta.2018.08.156.

[300] H. Inaba, M. Kimura, H. Yokokawa, An analysis of the corrosion resistance of low chromium-steel in a wet CO_2 environment by the use of an electrochemical potential diagram, Corros. Sci. 38 (9) (1996) 1449–1461. doi:10.1016/0010-938x(96)00032-7.

[301] C. Duhamel, S. Venkataraman, S. Scudino, J. Eckert, Diffusionless Transformations, World Scientific, 2008, Ch. 5, pp. 119–145. doi:10.1142/9789812790590_0006.

[302] T. Holm, J. Ågren, II.15 - The carbon potential during the heat treatment of steel, in: K. Hack (Ed.), The SGTE Casebook (Second Edition), second edition Edition, Woodhead Publishing Series in Metals and Surface Engineering, Woodhead Publishing, 2008, pp. 212–223. doi:10.1533/9781845693954.2.212.

[303] M. J. McDermott, S. S. Dwaraknath, K. A. Persson, A graph-based network for predicting chemical reaction pathways in solid-state materials synthesis, Nat. Commun. 12 (1) (2021). doi:10.1038/s41467-021-23339-x.

[304] B. Ash, V. S. Nalajala, A. K. Popuri, T. Subbaiah, M. Minakshi, Perspectives on nickel hydroxide electrodes suitable for rechargeable batteries: Electrolytic vs. chemical synthesis routes, Nanomaterials 10 (9) (2020) 1878. doi:10.3390/nano10091878.

[305] M. G. Ortiz, A. Visintin, S. G. Real, Synthesis and electrochemical properties of nickel oxide as anodes for lithium-ion batteries, J. Electroanal. Chem. 883 (2021) 114875. doi:10.1016/j.jelechem.2020.114875.

[306] C. Wolverton, K. C. Hass, Phase stability and structure of spinel-based transition aluminas, Phys. Rev. B 63 (2000) 024102. doi:10.1103/PhysRevB.63.024102.

[307] V. E. Gromov, S. V. Konovalov, Y. A. Rubannikova, A. P. Semin, Ways of increasing mechanical properties of cantor high entropy alloy, in: PROCEEDINGS OF THE INTERNATIONAL CONFERENCE "PHYSICAL MESOMECHANICS. MATERIALS WITH MULTILEVEL HIERARCHICAL STRUCTURE AND INTELLIGENT MANUFACTURING TECHNOLOGY", AIP Publishing, 2022. doi:10.1063/5.0084580.

[308] B. Cantor, I. Chang, P. Knight, A. Vincent, Microstructural development in equiatomic multicomponent alloys, Mater. Sci. Eng. A 375-377 (2004) 213–218. doi:10.1016/j.msea.2003.10.257.

[309] K. Okhotnikov, T. Charpentier, S. Cadars, Supercell program: a combinatorial structure-generation approach for the local-level modeling of atomic substitutions and partial occupancies in crystals, J. Cheminform. 8 (1) (2016). doi:10.1186/s13321-016-0129-3.

[310] Y. Qiu, M. A. Gibson, H. L. Fraser, N. Birbilis, Corrosion characteristics of high entropy alloys, Mater. Sci. Technol. 31 (10) (2015) 1235–1243. doi:10.1179/1743284715y.0000000026.

[311] P. Lu, J. E. Saal, G. B. Olson, T. Li, S. Sahu, O. J. Swanson, G. Frankel, A. Y. Gerard, J. R. Scully, Computational design and initial corrosion assessment of a series of non-equimolar high entropy alloys, Scr. Mater. 172 (2019) 12–16. doi:10.1016/j.scriptamat.2019.07.003.

[312] C. R. Clayton, Y. C. Lu, A bipolar model of the passivity of stainless steel: The role of mo addition, J. Electrochem. Soc. 133 (12) (1986) 2465–2473. doi:10.1149/1.2108451.

[313] F. Presuel-Moreno, M. Jakab, N. Tailleart, M. Goldman, J. Scully, Corrosion-resistant metallic coatings, Mater. Today 11 (10) (2008) 14–23. doi:10.1016/s1369-7021(08)70203-7.

[314] C. Tsuyuki, A. Yamanaka, Y. Ogimoto, Phase-field modeling for pH-dependent general and pitting corrosion of iron, Scientific Reports 8 (1) (2018) 12777. doi:10.1038/s41598-018-31145-7.

[315] A. Imanian, M. Amiri, Phase field modeling of galvanic corrosion, ArXiv: 1804.08517 (2018). doi:10.48550/ARXIV.1804.08517.
URL https://arxiv.org/abs/1804.08517

[316] Q. C. Sherman, P. W. Voorhees, Phase-field model of oxidation: Equilibrium, Phys. Rev. E 95 (2017) 032801. doi:10.1103/PhysRevE.95.032801.

[317] A. P. Bhati, S. Wan, D. W. Wright, P. V. Coveney, Rapid, accurate, precise, and reliable relative free energy prediction using ensemble based thermodynamic integration, J. Chem. Theory Comput. 13 (1) (2016) 210–222. doi:10.1021/acs.jctc.6b00979.

[318] M. T. C. Martins-Costa, M. F. Ruiz-López, Highly accurate computation of free energies in complex systems through horsetail QM/MM molecular dynamics combined with free-energy perturbation theory, Theor. Chem. Acc. 136 (4) (2017). doi:10.1007/s00214-017-2078-y.

[319] K. D. Wispelaere, P. N. Plessow, F. Studt, Toward computing accurate free energies in heterogeneous catalysis: a case study for adsorbed isobutene in H-ZSM-5, ACS Phys. Chem Au 2 (5) (2022) 399–406. doi:10.1021/acsphyschemau.2c00020.

[320] R. A. Robie, B. S. Hemingway, J. R. Fisher, Thermodynamic properties of minerals and related substances at 298.15 K and 1 bar (105 Pascals) pressure and at higher temperatures, Tech. rep. (1978). doi:10.3133/b1452.

[321] O. Åke, O. N. E. Agency, Chemical Thermodynamics of Selenium, 6th Edition, Elsevier, Amsterdam; Boston, 2005.

[322] S. P. Ong, W. D. Richards, A. Jain, G. Hautier, M. Kocher, S. Cholia, D. Gunter, V. L. Chevrier, K. A. Persson, G. Ceder, Python Materials Genomics (pymatgen): A robust, open-source python library for materials analysis, Comput. Mater. Sci. 68 (2013) 314–319. doi:10.1016/j.commatsci.2012.10.028.

Appendix A: Additional Tables Supplementing Results Chapters

8.4. Results Chapter 5 Crystallographic and Phase Information

Table 8.1. Crystallographic parameters for the lead oxides calculated utilizing DFT-PBEsol with spin-orbit coupling and Van der Waals forces implemented. Z is the number of formula units (f.u.) per unit cell.

Pb (metal), $Fm\bar{3}m$ symmetry, Z = 4				
a = 4.8527 Å,				
Atom	Wyckoff Orbit	x	y	z
Pb(1)	4a	0.0000	0.0000	0.0000
Pb_2O (insulator), $Pn\bar{3}m$ symmetry, Z = 2				
a = 5.3620 Å				
Pb(1)	4b	0.0000	0.0000	0.0000
O(1)	2a	0.2500	0.2500	0.2500
PbO (insulator), $Pbcm$ symmetry, Z = 4				
a = 5.7594, b = 5.4821, c = 4.7014 Å				
Pb(1)	4d	0.2378	0.4901	0.2500
O(1)	4d	0.8610	0.5913	0.2500

Pb_3O_4 (metal), $P4_2/mbc$ symmetry, Z = 4				
a = 8.7169, c = 6.6204 Å				
Pb(1)	4*d*	0.0000	0.5000	0.2500
Pb(2)	8*h*	0.8402	0.8591	0.0000
O(1)	8*g*	0.8261	0.3261	0.2500
O(2)	8*h*	0.3598	-0.0926	0.0000

Pb (metal), $Fm\bar{3}m$ symmetry, Z = 4				
a = 4.8527 Å,				
Pb_2O_3 (metal), $P2_1/c$ symmetry, Z = 4				
a = 7.4987, b = 5.6377, c = 7.7649 Å, β = 112.92 °				
Pb(1)	4*e*	-0.0911	0.7458	0.8823
Pb(2)	4*e*	0.6110	0.2390	0.1410
O(1)	4*e*	0.6267	0.8738	0.7287
O(2)	4*e*	0.1927	0.5927	0.0497
O(3)	4*e*	0.0715	0.0644	0.8615

PbO_2 (metal), $P4_2/mnm$ symmetry, Z = 2				
a = 4.9704, c = 3.4012 Å				
Pb(1)	2*b*	0.0000	0.0000	0.5000
O(1)	4*g*	0.8073	0.1927	0.0000

Table 8.2. Crystallographic parameters for the lead carbonates derived from relaxation calculations utilizing DFT-PBEsol with spin-orbit coupling. Z is the number of formula units (f.u.) per unit cell.

$PbCO_3$ (insulator), $Pnma$ symmetry, Z = 4

a = 5.9864, b = 5.1369, c = 8.4524 Å

Atom	Wyckoff Orbit	x	y	z
Pb(1)	4c	0.7550	0.2500	0.4167
C(1)	4c	-0.0899	0.2500	0.7603
O(1)	4c	-0.0997	0.2500	-0.0866
O(2)	8d	-0.0926	0.4684	0.6832

Pb_2OCO_3 (insulator), $P222$ symmetry, Z = 4

a = 5.0669, b = 8.8179, c = 9.2129 Å

Atom	Wyckoff Orbit	x	y	z
Pb(1)	4a	0.5115	0.0608	0.0848
Pb(2)	4a	0.4726	0.7431	0.8440
C(1)	4a	0.4918	-0.0098	0.3996
O(1)	4a	0.7150	-0.0088	0.3335
O(2)	4a	0.2269	-0.0010	0.8281
O(3)	4a	0.5159	0.4768	-0.0408
O(4)	4a	0.5390	0.8144	0.0739

$Pb(CO_3)Pb_2(OH)_2$ (insulator)*, $P31m$ symmetry, $Z = 3$

$a = 15.32491$, $c = 14.00625$ Å, $\gamma = 120.00°$

Atom	Wyckoff Orbit	x	y	z
Pb(1)	1a	0.0000	0.0000	-0.0902
Pb(2)	2b	0.3333	0.6667	-0.0502
Pb(3)	3c	0.3537	0.0000	0.5276
Pb(4)	3c	0.6702	0.0000	0.1237
C(1)	1a	0.0000	0.0000	0.2068
C(2)	2b	0.3333	0.6667	0.2142
C(3)	3c	0.6668	0.0000	0.7787
O(1)	3c	0.0831	0.0000	0.2057
O(2)	6d	0.5750	0.2624	0.2133
O(3)	3c	0.5852	0.0000	0.7618
O(4)	6d	0.3367	0.2526	0.7887
O(5)	1a	0.0000	0.0000	0.5523
O(6)	2b	0.3333	0.6667	0.5063
O(7)	3c	0.6690	0.0000	0.4796
H(1)	1a	0.0000	0.0000	0.4829
H(2)	3c	0.6073	0.0000	0.4971
H(3)	2b	0.3333	0.6667	0.4364

Table 8.3. Crystallographic parameters for the lead phosphates derived from relaxation calculations utilizing DFT-PBEsol with spin-orbit coupling. Z is the number of formula units (f.u.) per unit cell.

$Pb_3(PO_4)_2$ (metal)*, $C2/c$ symmetry, $Z = 4$

$a = 13.7198$, $b = 5.8244$, $c = 9.3333$ Å, $\beta = 101.92°$

Atom	Wyckoff Orbit	x	y	z
Pb(1)	$4e$	0.0000	0.6942	0.2500
Pb(2)	$8f$	0.3171	0.3250	0.8483
P(1)	$8f$	0.3995	0.2506	0.5555
O(1)	$8f$	0.3533	0.0389	0.6173
O(2)	$8f$	0.3698	0.4719	0.6318
O(3)	$8f$	0.1421	0.2209	0.6127
O(4)	$8f$	0.5136	0.2206	0.5817

$Pb_4O(PO_4)_2$ (metal), $P2_1/c$ symmetry, $Z = 4$

a9.1981, b = 6.9573, c = 13.9556 Å, β = 104.43 °

Atom	Wyckoff Orbit	x	y	z
Pb(1)	4e	-0.0301	0.3155	0.6421
Pb(2)	4e	0.3365	0.2687	0.8369
Pb(3)	4e	0.3232	0.5055	0.5793
Pb(4)	4e	0.2947	0.0086	0.6117
P(1)	4e	0.0311	0.2915	-0.0974
P(1)	4e	0.3677	0.7276	0.8237
O(1)	4e	-0.0331	0.4971	0.8915
O(2)	4e	0.1865	0.2793	-0.0220
O(3)	4e	0.2406	0.2922	0.6730
O(4)	4e	0.2463	0.5941	0.8471
O(5)	4e	0.4972	0.7539	-0.0819
O(6)	4e	-0.0823	0.1596	-0.0662
O(7)	4e	0.0655	0.2170	0.8053
O(8)	4e	0.2923	-0.0785	0.7859
O(9)	4e	0.4367	0.6298	0.7445

$Pb_8O(PO_4)_2$ (metal), $C2/m$ symmetry, $Z = 4$

$a = 10.4833$, $b = 9.9571$, $c = 14.0192$ Å, $\beta = 98.79°$

Atom	Wyckoff Orbit	x	y	z
Pb(1)	4i	-0.0681	0.0000	0.2956
Pb(2)	4i	0.3483	0.0000	0.8866
Pb(3)	4i	0.7524	0.0000	0.4912
Pb(4)	4i	0.4318	0.0000	0.2974
Pb(5)	8j	0.0963	0.2506	-0.0865
Pb(6)	8j	0.1907	0.2533	0.2974
P(1)	4i	0.1561	0.0000	0.0961
P(2)	4h	0.0000	0.2567	0.5000
O(1)	8j	0.3057	0.3542	0.1910
O(2)	8j	0.0749	0.3462	0.4366
O(3)	4i	0.7289	0.0000	0.3346
O(4)	8j	0.0272	0.3571	0.2106
O(5)	4i	0.1415	0.0000	-0.0153
O(6)	8j	0.0956	0.1281	0.1343
O(7)	4i	0.3025	0.0000	0.1372
O(4)	8j	0.4031	0.3313	0.4329

$Pb_5(PO_4)_3OH$ (metal), $P2_1$ symmetry, $Z = 2$

$a = 9.8158$, $b = 7.3274$, $c = 9.8158$ Å, $\beta = 120.00°$

Atom	Wyckoff Orbit	x	y	z
Pb(1)	2a	0.3333	-0.0020	0.6667
Pb(2)	2a	0.6667	0.0032	0.3333
Pb(3)	2a	0.0045	0.7609	0.2527
Pb(4)	2a	0.7473	0.7609	0.7518
Pb(5)	2a	0.2482	0.7609	-0.0045
P(1)	2a	0.6327	0.7524	0.0346
P(2)	2a	-0.0346	0.7524	0.5980
P(3)	2a	0.4020	0.7524	0.3673
O(1)	2a	0.5187	0.7563	0.8554
O(2)	2a	0.1446	0.7563	0.6633
O(3)	2a	0.3367	0.7563	0.4813
O(4)	2a	0.5372	0.7474	0.1231
O(5)	2a	0.8769	0.7474	0.4141
O(6)	2a	0.5859	0.7474	0.4628
O(7)	2a	0.7415	-0.0775	0.0950
O(8)	2a	-0.0950	-0.0775	0.6465
O(9)	2a	0.3535	-0.0775	0.2585
O(10)	2a	0.2582	0.0819	-0.0846
O(11)	2a	0.0846	0.0819	0.3428
O(12)	2a	0.6572	0.0819	0.7418
O(13)	2a	0.0000	0.3284	0.0000
H(1)	2a	0.0000	0.4623	0.0000

Table 8.4. Phases considered in the simulated phase diagrams. Note that experimental $\Delta_f G$ values are listed for aqueous ions along with the reference study [1, 8, 29]. Solid $\Delta_f G$ values are listed at the PBEsol+SOC level from our DFT calculations and are used throughout. Multi-element lead carbon and phosphorous species were considered if they contained the carbonate or phosphate groups.

Material	Considered?	Lead State	Oxidation	$\Delta_f G$ (eV/f.u.)
$PbOH^+$	yes	II		-2.2647, Ref. [29]
Pb^{2+}	yes	II		-0.2485, Ref. [1]
$HPbO_2^-$	yes	II		-3.5120, Ref. [1]
PbO_2^{2-}	yes	II		-3.5075, Ref. [8]
$Pb(OH)_3^-$	yes	II		-5.9657, Ref. [8]
$Pb(OH)_2$	yes	II		-4.1623, Ref. [246]
Pb^{3+}	no	III		-
Pb^{4+}	yes	IV		3.1352, Ref. [1]
PbO_3^{2-}	yes	IV		-2.8768, Ref. [1]
PbO_4^{4-}	yes	IV		-2.9236, Ref. [1]
Pb^{5+}	no	V		-
$Pb_2O_{(s)}$	yes	I		-0.6390
$PbO_{(s)}$	yes	II		-1.9758
$Pb_2O_{3(s)}$	yes	III		-4.4715
$Pb_3O_{4(s)}$	yes	II/IV		-6.3159
$PbO_{2(s)}$	yes	IV		-2.3119
$PbCO_{3(s)}$	yes	II		-6.5530
$Pb_2O(CO_3)_{(s)}$	yes	II		-8.6476
$Pb_3(CO_3)_2(OH)_{2(s)}$ *	yes	II		-16.9861
$Pb_3(PO_4)_{2(s)}$	yes	II		-23.4763
$Pb_4O(PO_4)_{2(s)}$	yes	II		-25.9576
$Pb_8O_5(PO_4)_{2(s)}$	yes	II		-23.4054
$Pb_5(PO_4)_3(OH)_{(s)}$	yes	II		-38.4626

8.5. Results Chapter 6 Crystallographic and Phase Information

Table 8.5. Crystallographic information for the bismuth oxychalcogenide target phases. Parameters are given for experimentally synthesized products [30-32], and for the computationally optimized crystal structure relaxed with the PBEsol functional. All target phases exhibit $P4/nmm$ symmetry with $Z = 2$. We also give z_1 and z_2 positions for bismuth and selenium, where z corresponds to free parameter in the $2c$ Wyckoff position $(1/4, 1/4, z)$.

Experimental Structures				
Compound	a (Å)	c (Å)	z_1 $2c$(Bi)	z_2 $2c$(Se)
BiCuOS	3.8713	8.5678	0.6482	0.1710
BiAgOS	3.9188	9.2149	0.6990	0.1370
BiCuOSe	3.9303	8.9319	0.6402	0.1756
BiAgOSe	3.9962	9.4321	0.6309	0.2026
DFT Optimized Structures				
Compound	a (Å)	c (Å)	z_1 $2c$(Bi)	z_2 $2c$(Se)
BiCuOS	3.8425	8.4957	0.6512	0.1650
BiAgOS	4.1076	8.8253	0.6394	0.1969
BiCuOSe	3.9059	8.9062	0.8581	0.3270
BiAgOSe	3.9704	9.3933	0.6321	0.2010

Table 8.6. Single element solids considered in our thermodynamic diagrams. Crystal structure information, sources, and the Gibbs free energy of formation ($\Delta_f G$) from computational (this study) and experimental sources are provided.

Compound	**Source**	**Crystal System**	**Computational $\Delta_f G$ (eV)**	**Experimental $\Delta_f G$ (eV)**
Cu	ICSD	Cubic	0.0 (*Ref*)	0.0 (*Ref*)
Cu_2O	ICSD	Cubic	-1.1199	-1.5327 [1, 6, 121]
CuO	ICSD	Monoclinic	-1.1369	-1.3297 [1, 6, 121]
$Cu(OH)_2$	ICSD	Orthorhombic	-3.4363	-3.8623 [1, 6, 121]
Ag	ICSD	Cubic	0.0 (*Ref*)	0.0 (*Ref*)
Ag_2O	ICSD	Cubic	-0.3052	-0.1121 [1, 9, 53]
AgO	ICSD	Monoclinic	-0.3654	0.1127 [1, 9, 53]
Ag_2O_3	ICSD	Cubic	0.5446	1.2582 [1, 9, 53]

Bi	ICSD	Trigonal	0.0 (*Ref*)	0.0 (*Ref*)
Bi_2O_3	MP	Trigonal	-7.2904	-5.1473 [1]
Bi_4O_7	MP	Triclinic	-15.4064	-10.0930 [1]
Bi_2O_4	ICSD	Monoclinic	-7.6153	-4.7267 [1]
Bi_2O_5	MP	Orthorhombic	-5.9491	-3.9709 [1]
S	ICSD	Orthorhombic	0.0 (*Ref*))	0.0 (*Ref*)
Se	ICSD	Monoclinic	0.0 (*Ref*)	0.0 (*Ref*)

Table 8.7. Binary element solids considered in our thermodynamic diagrams. Crystal structure information, sources, and the Gibbs free energy of formation ($\Delta_f G$) from computational (this study) and experimental sources are provided, when possible.

Compound	**Source**	**Crystal System**	$\Delta_f G$ **(eV)**	**Experimental** $\Delta_f G$ **(eV)**
CuS	MP	Orthorhombic	-0.4588	-0.5087 [320]
Cu_2S	ICSD	Hexagonal	-0.4334	-0.9003 [320]
CuS_2	MP	Orthorhombic	-0.5183	
Cu_7S_4	MP	Orthorhombic	-2.1411	
$Cu_2(SO_4)_3$	MP	Trigonal	-18.0188	
CuSe	MP	Orthorhombic	-0.2824	-0.3814 [321]
$CuSe_2$	MP	Orthorhombic	-0.4316	-0.4270 [321]
Cu_3Se_2	MP	Tetragonal	-0.7916	
$Cu_2O(SeO_3)$	ICSD	Cubic	-4.9188	
CuO_3Se	ICSD	Orthorhombic	-3.6289	
CuO_4Se	MP	Orthorhombic	-3.7876	
CuO_5Se_2	MP	Monoclinic	-6.2280	
Ag_2S	MP	Monoclinic	-0.0930	-0.4214 [9]
Ag_8S	ICSD	Orthorhombic	1.6062	

AgSe	ICSD	Cubic	0.1779	
Ag_2Se	MP	Orthorhombic	-0.2508	-0.4861 [9, 321]
Ag_2SeO_3	MP	Monoclinic	-3.1914	-3.0927 [9, 321]
Ag_2SeO_4	MP	Orthorhombic	-3.5008	-3.4217645 [9, 321]
BiCu	ICSD	Orthorhombic	-0.7669	
$Cu(BiO_2)_2$	MP	Tetragonal	-8.9425	
$BiAg_5O_4$	MP	Monoclinic	-4.7101	
$BiAg_2O_3$	MP	Orthorhombic	-4.3401	
$BiAgO_3$	ICSD	Trigonal	-3.8081	
BiS_2	MP	Monoclinic	-1.4952	
Bi_2S_3	MP	Orthorhombic	-3.0501	
Bi_2OS_2	MP	Tetragonal	-4.6905	
$Bi_2(SO_4)_3$	MP	Trigonal	-25.9265	
Bi_2O_2S	ICSD	Orthorhombic	-6.2557	
Bi_3Se_4	ICSD	Trigonal	-4.7166	
Bi_4Se_3	ICSD	Trigonal	-5.2953	
Bi_2Se_2	ICSD	Trigonal	-2.8929	-0.9701 [321]
$BiSe_2$	ICSD	Monoclinic	-1.6438	
Bi_2Se_3	David	Trigonal	-3.3801	-1.5194 [321]
Bi_2O_2Se	David	Tetragonal	-6.4567	
Bi_2O_5Se	David	Orthorhombic	-10.9477	
$Bi_2(SeO_3)_3$	MP	Monoclinic	-16.5421	

Table 8.8. Ternary element solids considered in our thermodynamic diagrams. Crystal structure information, sources, and the Gibbs free energy of formation ($\Delta_f G$) from computational (this study) and experimental sources are provided, when possible.

Compound	**Source**	**Crystal System**	$\Delta_f G$ **(eV)**	**Experimental** $\Delta_f G$ **(eV)**
BiCuOS	ICSD	Tetragonal	-3.3806	
$BiCu_3S_3$	ICSD	Orthrombic	-2.0831	
$Bi_4Cu_4S_9$	MP	Orthrombic	-6.7229	
$Cu_4(BiS_2)_5$	MP	Monoclinic	-7.8584	
$BiCuS_2$	ICSD	Orthrombic	-1.6201	
BiAgOS	This work	Tetragonal	-3.0226	
$BiAgS_2$	ICSD	Cubic	-1.6455	
Bi_3AgS_5	MP	Monoclinic	-4.8242	
Bi_6AgS_9	ICSD	Monoclinic	-8.9945	
BiCuOSe	ICSD	Tetragonal	-3.5053	
$BiCuSe_2$	ICSD	Orthrombic	-1.8157	
$BiCu_6Se_6$	ICSD	Orthrombic	-3.1504	
$Bi_2Cu(SeO_3)_4$	ICSD	Monoclinic	-19.1080	
BiAgOSe	J. Gabon *et al.* [31]	Tetragonal	-3.1707	
$BiAgSe_2$	MP	Trigonal	-1.5769	

Appendix B: Density Functional Theory Settings

8.6. Results Chapter 4 DFT Settings

Density functional theory calculations were performed with the Vienna Ab initio Simulation Package (VASP) [96-99]. Density functionals at different approximation levels were utilized to optimize solid structures and obtain the ground state formation energy for each composition: the local density approximation (LDA), the generalized gradient approximation (GGA) by Perdew-Burke-Ernzerhof (PBE), the Perdew-Burke-Ernzerhof generalized gradient approximation revised for solids (PBEsol), the strongly constrained and appropriately normed semilocal density functional metaGGA (SCAN), and the hybrid exchange-correlation functional (HSE06) [91, 100-105]. Plane wave calculations with PBEsol were used for all lattice dynamics calculations [92, 93, 100, 101]. Sampling of the Brillouin zone was done by converging to at least 4,000 k-points per reciprocal atom (KPPRA), and was implemented with a Γ centered k-mesh. Gaussian smearing was used with a small smearing width of 0.1 eV to accurately obtain any electronic band gaps. The oxygen molecular and hydrogen molecular bonds were relaxed within a simulation cell with $15 \times 15 \times 15$ Å^3 vacuum. A triplet state ferromagnetic moment was preserved in the end of the $O_{2(g)}$ relaxations for all functionals. The initial antiferromagentic moment for copper (II) oxide was chosen based on experiment [106, 181], and single-point-energy calculations showed the experimental magnetic moment was consistent with the DFT ground state. The total energy was converged to 10^{-7} eV and forces were converged to less than 10^{-3} meV Å^{-1} during relaxations. An energy cutoff of 700 eV was used for all calculations. Nonspherical gradient corrections within the PAW spheres were included. Van der Waals forces were considered for all solids implemented using the Tkatchenko-Scheffler method with iterative Hirshfeld partitioning for the LDA and GGA functionals in VASP. Van der Waals corrections for SCAN were implemented with the revised Vydrov and Van Voorhis nonlocal functional (rVV10) [109] and with the DFT-D3 dispersion correction for HSE06 [110]. The hydrated solid $Cu(OH)_{2(s)}$ was found to exhibit the largest van der Waals corrections to the energy.

Lattice dynamics calculations were performed with VASP and the Phonopy software [111]. We generated small displacements (displacement amplitude = 0.01 Å) within supercells for the frozen phonon method using the harmonic approximation [112]. All solid-state phases were found to be dynamically stable. We calculated thermodynamic data using statistical thermodynamics expressions implemented in Phonopy.

8.7. Results Chapter 5 DFT Settings

DFT calculations were performed with the Vienna Ab initio Simulation Package (VASP) [96-99] using the projector augmented-wave method [92, 93]. We utilized a 520 eV energy cutoff for all materials and projector-augmented wave (PAW) pseudopotentials [92, 93] to treat the separation between the core and valence electrons. We examined the effect of electronic exchange through comparing different DFT functionals, including the local density approximation (LDA), the generalized gradient approximation (GGA) by Perdew-Burke-Ernzerhof (PBE), the Perdew-Burke-Ernzerhof generalized gradient approximation revised for solids (PBEsol), the strongly constrained and appropriately normed semilocal density functional metaGGA (SCAN) [100-105]. We included spin-orbit coupling (SOC) in all static simulations of Pb-containing materials; SOC was not included in the lattice dynamics calculations. SOC leads to significant changes in $\Delta_f G$ for lead containing compounds, as has been previously reported [237] and described in the Supporting Information (SI). Final calculations with PBEsol were performed with van der Waals forces for all solids implemented using the Tkatchenko-Scheffler method with iterative Hirshfeld partitioning in VASP.

Initial solid state crystal structures were sourced from the International Crystal Structures Database (ICSD) [30]. Structures were optimized such that total energies were converged to 10^{-7} eV and forces were converged to less than 1 meV Å^{-1}. The Brillouin zones of all structures were sampled with a minimum of 3,000 k-points per reciprocal atom (KPRRA) and used a Γ-centered mesh. Lattice dynamical calculations used the PBEsol functional to obtain the vibrational energies (F_{vib}).

8.8. Results Chapter 6 DFT Settings

First principles density functional theory (DFT) calculations were performed using the Vienna Ab initio Simulation Package (VASP) [96-99] with the Perdew-Burke-Ernzerhof (PBE) generalized gradient approximation revised for solids (PBEsol) functional [92, 93, 100, 101]. We used a 550 eV energy cutoff for

all materials and projector-augmented wave (PAW) pseudopotentials [92, 93] to treat the separation between the core and valence electrons. The Brillouin zones of all structures were sampled with a minimum of 3,000 k-points per reciprocal atom (KPRRA) and used a Γ-centered mesh. Total energies were converged to 10^{-7} eV and forces were converged to less than $1\,\mathrm{meV\,atom^{-1}}$ within an ionic relaxation loop. For magnetically ordered compounds, we initialized the spin order to the experimentally observed configuration and allowed the magnitude of the collinear spins to relax. Spin-orbit coupling (SOC) was used in all simulations of materials comprising bismuth. Lattice dynamical calculations were performed using the small displacement method ($\approx 0.01 - 0.03\,\mathrm{Å}$) implemented in the Phonopy software [111]. Vibrational energies (F_{vib}) were calculated using the quasi-harmonic approximation [112] at $T = 298.15\,\mathrm{K}$ for standard state simulations.

Appendix C: Code Usage

Code central to creating predominance diagrams in the respective chapters is listed below. All code are Python scripts. Therefore, within an Python integrated development environment (IDE), code can simply be executed as a script with no build or compile necessary. Some programs contain dependencies for other free and open source libraries, such pymatgen [322]. For chapters which utilize multiple programs, any running order dependency will be listed within the relevant section. Most code contained may also be found in Github repositories (see Section 3.3).

8.9. Results Chapter 4 Code and Use

```
#!/usr/bin/env python3
# -*- coding: utf-8 -*-
import numpy as np
import matplotlib.pyplot as plt

#Created by Lauren Walters, 2017-2018
#Contributions by Liang Feng Huang
#For reactions in aqueous conditions

#Thermo data: http://www.conradnaleway.net/ThermoData.PDF, Pourbaix Book


#find out how much detail you want in your graph
#n=int;
#n=input("Enter the grid detail you want (0-100): ")
n=50;

#Constants
R=8.31447;          #J/(mol*K)
T=298.15;           #K
#T=473.15
F= 9.648533*10**4; #J/(V*mol)
P=1;                #bar, 10^5*Pa
```

```
eta=6
nI=10**-eta;          #Activity Concentration

#pH Constants
lowpH = 2;
highpH = 12;
pHrange = int;
pHrange = highpH-lowpH;
pHcount = pHrange/n; #used to iterate through pH range

#U Constants
Ulow = -1.0;          #V
Uhigh = 1.0;          #V
Urange  = Uhigh-Ulow; #V
Ucount = Urange/n;    #used to iterate through U (energy) range

#PBE
#Ee_Cu=-3.727442565;            #eV/atom #set as 0 value
#Ee_CuO=-9.870476045;          #eV/atom
#Ee_Cu2O=-13.64922363;         #eV/atom
#Ee_O2=-9.89611509;           #eV/O2
#Ee_H2=-6.7746011
#Ee_CuOH2_s=-24.55448475

#PBEsol
#Ee_Cu=-4.3083660025;            #eV/atom #set as 0 value
#Ee_CuO=-10.7432559675;          #eV/atom
#Ee_Cu2O=-14.988153475;         #eV/atom
#Ee_O2=-10.28833536;
#Ee_H2=-6.515187
#Ee_CuOH2_s=-25.606095;

#PBEsol +SOC
#Ee_Cu=-4.3152965;             #eV/atom #set as 0 value
#Ee_CuO=-10.7488868;          #eV/atom
#Ee_Cu2O=-14.99698;          #eV/atom
#Ee_CuOH2_s=-25.1916025;
#Ee_O2=-10.281123
#Ee_H2=-6.5141508

#Scan
#Ee_Cu=-15.135967;             #eV/atom #set as 0 value
#Ee_CuO=-22.9833752;          #eV/atom
```

```
#Ee_Cu2O=-37.995761;          #eV/atomm
#Ee_O2=-12.322421;              #eV/O2
#Ee_H2=-6.9120129
#Ee_CuOH2_s=-38.68172;
#Ee_CuOH2_s=-36.8449925;

#HSE06
Ee_Cu=-3.65597325;             #eV/atom #set as 0 value #From HSE06
Ee_CuO=-48.49823829/4;          #eV/atom
Ee_Cu2O=-31.734654/2;         #eV/atom
Ee_O2=-14.12028857; #Liang
Ee_H2=-7.8316838
#Ee_CuOH2_s=-30.08723;

#LDA
#Ee_Cu=-4.707347975;             #eV/atom
#Ee_CuO=-46.49804486/4;          #eV/atom
#Ee_Cu2O=-16.304663885;         #eV/atom
#Ee_O2=-10.48946456;              #eV/O2
#Ee_H2=-6.7005255;
#Ee_CuOH2_s=-27.457315

#Vibrational and Translational Energies (Phonopy)
#Fvib, Frot, Ftrans, take from the F value in the DFT output
#Found with mesh.conf and the command TROP=.true.
#eV/stoichiometric unit
Fvib_O2=-0.272;                       #eV/O2
F_rot_trans_O2=0.099;               #eV/O2
Ftot_O2=Fvib_O2+F_rot_trans_O2;  #eV/O2
F_H = .202; #eV/H

##############################################################################
############################Vibrational Energies##############################
##############################################################################
#Room Temperature
#Solid Copper species, found from Phonopy PBEsol WHERE IS THIS FROM
Fvib_CuO=0.01295;                   #eV/atom #Phonopy
Fvib_Cu2O=-0.202775;                #eV/atom #Phonopy
Fvib_Cu=-0.04189825;                #eV/atom #Phonopy
Fvib_CuOH2_s=0.643953328858

#30 C
#Fvib_Cu=-0.01562229435825
```

```
#Fvib_CuO=0.03238025334 # PBEsol
#Fvib_Cu2O=-0.0209987707197
#50 C
#Fvib_CuO=0.0221406759264
#Fvib_Cu2O=-0.04181165458 82
#Fvib_Cu=-0.02231218494087
#100 C
#Fvib_CuO=-0.00584618492307
#Fvib_Cu2O=-0.0973199131906
#Fvib_Cu=-0.0403414887809
#200 C
#Fvib_CuO=-0.0708965108501
#Fvib_Cu2O=-0.22159084325
#Fvib_Cu=-0.0812560725897
################################################################################
################################################################################

#Calculations of the deltaGf delta G of Formation
#Ftot=deltaGf=Ef+deltaF
                                    #eV/atom
dGf_CuO= (Ee_CuO+Fvib_CuO) - (Ee_Cu+Fvib_Cu) - 0.5*(Ee_O2+Ftot_O2); #eV/atom
dGf_Cu2O=(Ee_Cu2O+Fvib_Cu2O) - (2*(Ee_Cu+Fvib_Cu)) - 0.5*(Ee_O2+Ftot_O2);#Might need to be not *2*Fvib_Cu
dGf_CuOH2_s= (Ee_CuOH2_s+Fvib_CuOH2_s)-(Ee_Cu+Fvib_Cu)-(Ee_O2+Ftot_O2)-(Ee_H2+F_H);  #eV/atom
dGf_H2O=-2.458;
dGf_Cu= 0.00;

#print(dGf_CuO)                                  #eV/atom
#print(dGf_Cu2O)
#print(dGf_CuOH2_s)
#Experimental Values,from online database
dGf_Cu2O=-1.5168    #eV/atom
dGf_CuO=-1.328      #eV/atom
#dGf_Cu1= 0.518018;                                  #eV/atom
#dGf_Cu2= 0.678772;                                  #eV/atom

################################################################################
####################ENERGY CORRECTIONS##########################################
################################################################################


#print(dGf_Cu2O/3)
print(dGf_CuOH2_s)
```

```
#dGf_Cu2O_Exp=-1.5328759
#Ecorr=(dGf_Cu2O-dGf_Cu2O_Exp)/2
#print(dGf_Cu2O)
#print(Ecorr)

#dGf_CuO_Exp=-1.3296325
#Ecorr=dGf_CuO-dGf_CuO_Exp
#print(dGf_CuO)
#print(Ecorr)

#HSE06_CuO=-1.26709378;
#Ecorr=dGf_CuO-HSE06_CuO;


Ecorr=0.0
################################################################################
################################################################################

#Values from the paper by Puigdomench
dGf_Cu=    0.0;                #kJ/mol
#dGf_CuO=   -1.3296325;         #kJ/mol
#dGf_Cu2O=  -1.5328759;         #kJ/mol
#dGf_CuOH2_s=-3.86234972 ## Janaf Tables
dGf_CuOH2_s=100#-3.7303089; #Pugiomench paper
dGf_Cu1=   0.506502+Ecorr;          #kJ/mol
dGf_Cu2=   0.674092+Ecorr;          #kJ/mol
dGf_CuOH4_2= -6.8143018+Ecorr;      #kJ/mol
dGf_CuOH2= -3.2666113+Ecorr;        #kJ/mol
dGf_CuOH2_minus= -3.4518209+Ecorr;  #kJ/mol
dGf_CuOH3= -5.1197432+Ecorr;        #kJ/mol
dGf_CuOH_Plus= -1.3127387+Ecorr; #kJ/mol
dGf_CuOH = -1.2677578+Ecorr;
dGf_Cu2OH2_2plus=-2.9424173+3*Ecorr;
dGf_Cu3OH4_2plus=-6.567839+3*Ecorr;

#print(dGf_Cu1)
#Convert from eV/atom to kJ/mol
dGf_Cu=    dGf_Cu*F#+0.03315*T;             #kJ/mol
dGf_CuO=   dGf_CuO*F#+0.0426*T;             #kJ/mol
dGf_Cu2O=  dGf_Cu2O*F#+0.09236*T;           #kJ/mol
dGf_CuOH2_s=dGf_CuOH2_s*F;
dGf_Cu1=   dGf_Cu1*F#+0.0406*T;             #kJ/mol
```

```
dGf_Cu2=   dGf_Cu2*F#-0.098*T;                #kJ/mol
dGf_H2O=   dGf_H2O*F;                        #kJ/mol
dGf_CuOH4_2= dGf_CuOH4_2*F#-0.175*T;         #kJ/mol
dGf_CuOH2= dGf_CuOH2*F#+0.026*T;             #kJ/mol
dGf_CuOH3= dGf_CuOH3*F#-0.014*T;             #kJ/mol
dGf_CuOH_Plus= dGf_CuOH_Plus*F#-0.061*T; #kJ/mol
dGf_CuOH = dGf_CuOH*F;
dGf_Cu2OH2_2plus=dGf_Cu2OH2_2plus*F;
dGf_Cu3OH4_2plus=dGf_Cu3OH4_2plus*F;
dGf_CuOH2_minus=dGf_CuOH2_minus*F;

#ax.plot(pH[:], muH[:])

#create a grid of zeros to graph the chemical potential
grid = np.zeros((n+1,n+1))
m=int;

#should be as long as there are specicies considered
#populate with smaller values that will be calculated.
muValues=np.array([10,10,10,10,10,10,10,10,10,10,10,10,10,10])

#fill in the grid. Calculate
for i in range(0, (n+1)):
    #calculate the energies for each species number
    pH=lowpH+i*pHcount;
    for j in range(0,(n+1)):

        U=Ulow+(Ucount*j);

        #Check concentrations of ions for Cu1+ and Cu2+
        #Solubility of Copper Oxides in Water and Steam
        muValues[0]=(dGf_Cu2+R*T*np.log(nI))-2*F*U;   # Cu2 #kJ/mol
        muValues[1]=(dGf_Cu1+R*T*np.log(nI))-F*U;   # Cu1 #kJ/mol
        muValues[2]=0.00;   # Cu #kJ/mol
        muValues[3]=dGf_CuO-2*R*T*np.log(10.0)*pH-2*F*U-(dGf_Cu+dGf_H2O);   #CuO #kJ/mol
        muValues[4]=(dGf_Cu2O-2*R*T*np.log(10.0)*pH-2*F*U-(2*dGf_Cu+dGf_H2O))/2;   #Cu2O #kJ/mol
        muValues[5]=dGf_CuOH4_2+R*T*np.log(nI)-2.0*F*U-4.0*R*T*np.log(10.0)*pH-4.0*dGf_H2O;
        muValues[6]=   dGf_CuOH2+R*T*np.log(nI)-2.0*F*U-2.0*R*T*np.log(10.0)*pH-2.0*dGf_H2O; #Cu(OH)2 minus
        muValues[7]=   dGf_CuOH3+R*T*np.log(nI)-2.0*F*U-3.0*R*T*np.log(10.0)*pH-3.0*dGf_H2O; #Cu(OH)3 minus
        muValues[8]= dGf_CuOH_Plus+R*T*np.log(nI)-2.0*F*U-R*T*np.log(10.0)*pH-dGf_H2O;#Cu(OH)+
        muValues[9]= dGf_CuOH+R*T*np.log(nI)-1.0*F*U-1.0*R*T*np.log(10.0)*pH-dGf_H2O;
        muValues[10]= (dGf_Cu2OH2_2plus +R*T*np.log(nI)-4.0*F*U-2.0*R*T*np.log(10.0)*pH-2*dGf_H2O)/2;
        muValues[11]= (dGf_Cu3OH4_2plus +R*T*np.log(nI)-6.0*F*U-4.0*R*T*np.log(10.0)*pH-4*dGf_H2O)/3;
```

```
        muValues[12]=dGf_CuOH2_s-2.0*F*U-2.0*R*T*np.log(10.0)*pH-2.0*dGf_H2O;
        muValues[13]=dGf_CuOH2_minus+R*T*np.log(nI)-1.0*F*U-2.0*R*T*np.log(10.0)*pH-2.0*dGf_H2O;



        m=np.argmin(muValues);

        grid[i,j] = m;

        #update values in array to ensure numbers are calculated properly
        muValues=np.array([10,10,10,10,10,10,10,10,10,10,10,10,10,10]);



#Create the line for the dotted lines
#These are found from the O2 and H+ stabilities***
muH=np.zeros((pHrange));
muH2O=np.zeros((pHrange));
pHArray=np.zeros((pHrange));
for i in range(0, pHrange):
    pHArray[i] =lowpH+i;
    muH[i]=-0.059*pHArray[i];
    muH2O[i]=1.23-0.059*pHArray[i];

fig =plt.figure()
ax=plt.subplot(111)
flag=np.zeros((14));

#For loops to iterate through plotting
#Implements if statments to plot grid of points
#plt.plot((pH, muH))
for i in range(0, (n+1)):
    pH=lowpH+i*pHcount;
    for j in range(0,(n+1)):
        U=Ulow+(Ucount*j);
        if grid[i,j] == 0:
            if flag[0]==0:
                ax.plot(pH,U, 'r.',label='$Cu^{2+}$')
                flag[0]=1;
            else:
                ax.plot(pH,U, 'r.')
        elif grid[i,j] == 1:
            if flag[1]==0:
```

```
            ax.plot(pH,U, 'y.',label='$Cu^{1+}$')
            flag[1]=1;
        else:
            ax.plot(pH,U, 'y.')
    elif grid[i,j] == 2:
        if flag[2]==0:
            ax.plot(pH,U, color = 'lightpink', marker = '.', label='$Cu$')
            flag[2]=1;
        else:
            ax.plot(pH,U, color = 'lightpink', marker = '.')
    elif grid[i,j] == 3:
        if flag[3]==0:
            ax.plot(pH,U, 'b.',label='$CuO$')
            flag[3]=1;
        else:
            ax.plot(pH,U, 'b.')
    elif grid[i,j] == 4:
        if flag[4]==0:
            ax.plot(pH,U, 'm.',label='$Cu_2O$')
            flag[4]=1;
        else:
            ax.plot(pH,U, 'm.')
    elif grid[i,j] == 5:
        if flag[5]==0:
            ax.plot(pH,U, 'c.',label='$Cu(OH)_4^{2-}$')
            flag[5]=1;
        else:
            ax.plot(pH,U, 'c.')
    elif grid[i,j] == 6:
        if flag[6]==0:
            ax.plot(pH,U, 'k.',label='$Cu(OH)_2$')
            flag[6]=1;
        else:
            ax.plot(pH,U, 'k.')
    elif grid[i,j] == 7:
        if flag[7]==0:
            ax.plot(pH,U, color = 'goldenrod', marker = '.',label='$Cu(OH)_3^-$')
            flag[7]=1;
        else:
            ax.plot(pH,U, color = 'goldenrod', marker = '.')
    elif grid[i,j] == 8:
        if flag[8]==0:
            ax.plot(pH,U, color = 'lightgreen', marker = '.',label='$CuOH^+$')
```

```
                flag[8]=1;
            else:
                ax.plot(pH,U, color = 'lightgreen', marker = '.')
        elif grid[i,j] == 9:
            if flag[9]==0:
                ax.plot(pH,U, color = 'azure', marker = '.',label='$CuOH$')
                flag[9]=1;
            else:
                ax.plot(pH,U, color = 'azure', marker = '.')
        elif grid[i,j] == 10:
            if flag[10]==0:
                ax.plot(pH,U, color = 'lightblue', marker = '.',label='$Cu_2(OH)_2^{2+}$')
                flag[10]=1;
            else:
                ax.plot(pH,U, color = 'lightblue', marker = '.')
        elif grid[i,j] == 11:
            if flag[11]==0:
                ax.plot(pH,U, color = 'maroon', marker = '.',label='$Cu_3(OH)_4^{2+}$')
                flag[11]=1;
            else:
                ax.plot(pH,U, color = 'maroon', marker = '.')
        elif grid[i,j] == 12:
            if flag[12]==0:
                ax.plot(pH,U, color = 'maroon', marker = '.',label='$Cu(OH)_{2(s)}$')
                flag[12]=1;
            else:
                ax.plot(pH,U, color = 'maroon', marker = '.')
        else:
            if flag[13]==0:
                ax.plot(pH,U, color = 'lemonchiffon', marker = '.',label='$Cu(OH)_{2}^-$')
                flag[13]=1;
            else:
                ax.plot(pH,U, color = 'lemonchiffon', marker = '.')


ax.plot(pHArray[:], muH[:],'c',label='$H_2$',linewidth=3)
ax.plot(pHArray[:], muH2O[:],'k',label='$H_2O$', linewidth=3)

plt.ylabel('Electric Potential, E(V)')
plt.xlabel('pH')
plt.title('Copper Pourbaix Diagram, Experimental Data, $\eta=10^{-'+str(eta)+'}$')
chartBox=ax.get_position()
ax.set_position([chartBox.x0, chartBox.y0, chartBox.width*.9, chartBox.height])
```

```
ax.legend(loc='upper_center', bbox_to_anchor=(1.45, 0.8), ncol=1)
plt.show()
plt.savefig('PourbaixDiagram_CopperOxide.png')
#plt.legend((plt_Cu2, plt_Cu1, plt_Cu, plt_CuO, plt_Cu2O),('Cu2-','Cu1-', 'Cu', 'CuO', 'CuO'))


def graphlines():
    ###################Plot Materials#####################

    #find out how much detail you want in your graph: Recommended 30-100
    n=400;
    pHcount = pHrange/n; #used to iterate through pH range
    Ucount = Urange/n;     #used to iterate through U (energy) range

    #create a grid of zeros to graph the chemical potential
    grid = np.zeros((n+1,n+1))
    #Declare Constant
    m=int;

    #Matrix to store calculated mu values at each iteration of the loop.
    #populate with smaller values that will be calculated.
    muValues=np.array([10,10,10,10,10,10,10,10,10,10,10,10,10])

    ######################Begin Chemical Potential Loop############################
    #fill in the grid. Calculate chemical potential
    #Iterate over all the pH and voltage range for the detail specified.
    for i in range(0, n+1):
        #calculate the energies for each species number
        pH=lowpH+i*pHcount;
        for j in range(0,n+1):

            U=Ulow+(Ucount*j);

            #Check concentrations of ions for Cu1+ and Cu2+
            #Solubility of Copper Oxides in Water and Steam
            muValues[0]=(dGf_Cu2+R*T*np.log(nI))-2*F*U;   # Cu2 #kJ/mol
            muValues[1]=(dGf_Cu1+R*T*np.log(nI))-F*U;   # Cu1 #kJ/mol
            muValues[2]=0.00;   # Cu #kJ/mol
            muValues[3]=dGf_CuO-2*R*T*np.log(10.0)*pH-2*F*U-(dGf_Cu+dGf_H2O);   #CuO #kJ/mol
            muValues[4]=(dGf_Cu2O-2*R*T*np.log(10.0)*pH-2*F*U-(2*dGf_Cu+dGf_H2O))/2;   #Cu2O #kJ/mol
            muValues[5]=dGf_CuOH4_2+R*T*np.log(nI)-2.0*F*U-4.0*R*T*np.log(10.0)*pH-4.0*dGf_H2O;
            muValues[6]=   dGf_CuOH2+R*T*np.log(nI)-1.0*F*U-2.0*R*T*np.log(10.0)*pH-2.0*dGf_H2O; #Cu(OH)2 minus
            muValues[7]=   dGf_CuOH3+R*T*np.log(nI)-2.0*F*U-3.0*R*T*np.log(10.0)*pH-3.0*dGf_H2O; #Cu(OH)3 minus
```

```
        muValues[8]= dGf_CuOH_Plus+R*T*np.log(nI)-2.0*F*U-R*T*np.log(10.0)*pH-dGf_H2O;#Cu(OH)+
        muValues[9]= dGf_CuOH+R*T*np.log(nI)-1.0*F*U-1.0*R*T*np.log(10.0)*pH-dGf_H2O;
        muValues[10]= (dGf_Cu2OH2_2plus +R*T*np.log(nI)-4.0*F*U-2.0*R*T*np.log(10.0)*pH-2*dGf_H2O)/2;
        muValues[11]= (dGf_Cu3OH4_2plus +R*T*np.log(nI)-6.0*F*U-4.0*R*T*np.log(10.0)*pH-4*dGf_H2O)/3;
        muValues[12]=dGf_CuOH2_s-2.0*F*U-2.0*R*T*np.log(10.0)*pH-2.0*dGf_H2O;
        muValues[13]=dGf_CuOH2_minus+R*T*np.log(nI)-1.0*F*U-2.0*R*T*np.log(10.0)*pH-2.0*dGf_H2O;

        #Find minimum chemical potential
        m=np.argmin(muValues);


        #Assign the correct species to that point on the grid
        grid[i,j] = m;

        #update values in array to ensure numbers are calculated properly
        muValues=np.array([10,10,10,10,10,10,10,10,10,10,10,10,10]);



########################END LOOP#####################################################



ax=plt.subplot(111)
axes = plt.gca()
axes.set_xlim([lowpH,highpH])
axes.set_ylim([Ulow,Uhigh])


#lines = np.zeros((2*n,2*n))
for i in range(1, (n-1)):
    pH=lowpH+i*pHcount;
    for j in range(1,(n-1)):
        U=Ulow+(Ucount*j);
        if grid[i,j] != grid[i-1, j]:
            #lines[2*n-1, 2*n]=1
            ax.plot(pH,U,'k.',markersize=0.4)
        if grid[i,j] != grid[i, j-1]:
            #lines[2*n, 2*n-1]=1
            ax.plot(pH,U, 'k.',markersize=0.4)

#########################################################
```

```
    #####Plot H2O and H2 lines##################################
    muH=np.zeros((pHrange+1));
    muH2O=np.zeros((pHrange+1));
    pHArray=np.zeros((pHrange+1));
    for i in range(0, pHrange):
        pHArray[i] =lowpH+i;
        muH[i]=-0.059*pHArray[i];
        muH2O[i]=1.23-0.059*pHArray[i];

    pHArray[pHrange] =lowpH+(pHrange);
    muH[pHrange]=-0.059*pHArray[pHrange];
    muH2O[pHrange]=1.23-0.059*pHArray[pHrange];
    ax.plot(pHArray[:], muH[:],'c--',label='$H_2$',linewidth=1)
    ax.plot(pHArray[:], muH2O[:],'b--',label='$H_2O$', linewidth=1)
    ############################################################3

    plt.ylabel('Electric Potential, E(V)',fontsize=15)
    plt.xlabel('pH',fontsize=15)
    plt.title('Scan Copper, $\eta=10^{-'+str(eta)+'}$',fontsize=18)
    chartBox=ax.get_position()
    ax.set_position([chartBox.x0, chartBox.y0, chartBox.width*1.1, chartBox.height*1.3])
    #ax.legend(loc='upper center', bbox_to_anchor=(1.45, 0.8), ncol=1)
    plt.show()


graphlines()



print('End of Script')
```

8.10. Results Chapter 5 Code and Use

All programs given below should be imported into the same folder. Then, Pourbaix diagrams can be created by running the top file listed (__init__.py), and then the second file listed (run.py).

```
from .generate_mesh import generate
from .makeplot import makeplot



from generate_mesh import generate
from makeplot import makeplot
```

```
import numpy as np

pH_, V_, mesh = generate(conc = 1.5e-3, carbon = None, phosphate = 1e-3)
print(mesh)
makeplot(pH_, V_, mesh, 'plot', exp = True)


import matplotlib.pyplot as plt
import numpy as np
import pandas as pd

colordict = {
    "Pb": "#85807b",
    "Pb++": "#db653d",
    "PbO": "#e04a16",
    "PbO2": "#3ec760",
    "Pb3O4": "#2a8744",
    "Pb++++": "#c92840",
    "HPbO2-": "#db7d42",
    "PbO3--": "#bf3939",
    "Hc": "#191cf7",
    "PbCO3": "#007BA7",
    "Pb3(PO4)2": "#d142f5"
    }

pHexp = [7,    7,    7,    7,    7,    7,    7,    7,    7,    7,    7,    10,    10,
... 10, 10,    10,    10,    10,    10,    10,    10,    10,    10,    10,    10]
Vexp = [-0.62, -0.62, -0.16, -0.12, 0.06, 0.48, 0.58, 0.67, 0.74, 1.08, 1.08, -0.8,  -0.42,
... -0.28,     -0.26, -0.03, 0.02,  0.24, 0.34, 0.46, 0.75, 0.75, 0.84, 0.94, 0.94, 1.24]

def makeplot(pH_, V_, mesh, title, exp = False):

    print("making plot")

    #identify unique species, turn grid into numbers and make colormap
    nmesh = np.empty(np.shape(mesh), dtype=float)
    present = pd.unique(mesh.flatten())
    print("Species Present: ", present)
    colors_ = []
    for i in range(len(present)):
        nmesh[mesh == present[i]] = i
        colors_.append(colordict[present[i]])
    print(nmesh)
    print(colors_)
```

```
    levels = np.arange(len(present)+1)
    levels = levels - .5
    print(levels)

    fig, ax = plt.subplots()

    #fill regions
    CS = ax.contourf(pH_, V_, nmesh, levels, colors = colors_)
    ax.contour(pH_, V_, nmesh, colors= 'k', linewidths=0.25, antialiased=True)

    #experimental data
    if exp:
        for i in list(range(3)) + list(range(11,12)):
            plt.plot(pHexp[i], Vexp[i], 'o', color = 'k')
        for i in list(range(3,11))+list(range(13,26)):
            plt.plot(pHexp[i], Vexp[i], '^', color = 'red', markeredgewidth=0.5, markeredgecolor='k')

    #water stability lines
    a = 1.299-0.0592*pH_[0]
    b = -0.059*pH_[0]
    plt.plot(pH_[0], a, '--', color='b')
    plt.plot(pH_[0], b, '--', color='b')
    plt.text(0,1.1,'Water_Oxidation', fontsize=11, rotation=-7, color='b')
    plt.text(0,-0.2,'Water_Reduction', fontsize=11, rotation=-7, color='b')

    #axes
    plt.xticks(np.arange(-2,17,2))
    plt.yticks(np.arange(-2,4.5,1))
    plt.xlabel('pH')
    plt.ylabel('$\mathrm{V_{SHE}}$')

    plt.savefig(title, dpi = 300)


import numpy as np
import math

#constants
R=.008314 #kJ/mol-K
T=298.15 #K
F=96.485 #kJ/V-g

#Gibbs Free Energy from PBEsol, kJ/mol
GPb = 0
```

```
GPbO = -182.179911180077
GPbO2 = -225.05892068112
GPb2O3 = -409.660823950954
GPb3O4 = -606.321927722997
PbCO3 = -636.8927823795264
hc = -1680.6559541150234
pbphos = -2265.1179660491134

#experimental Gibbs Free Energy values for ions, kJ/mol
GPb4 = 302.50074
GPb2 = -23.9743
GHPbO2 = -338.904
GPbO3 = -277.56656
GPbO4 = -282.08946
GPbH2 = 290.788
OH = -157.33514
CO3 = -527.97896
H2CO3 = -623.2068
HCO3 = -586.93152

#set up pH range (consider doing this in input)
pHstart = -2
pHend = 16
dpH = 0.045
pHvec = np.arange(pHstart, pHend, dpH)

#set up potential range(consider doing this in input)
Vstart = 4
Vend = -2
dV = -0.045
Vvec = np.arange(Vstart, Vend, dV)

#set up grid
pH_, V_ = np.meshgrid(pHvec, Vvec)
Z = np.empty(np.shape(pH_), dtype = object)

def generate(conc = 1.5e-8, carbon = False, phosphate = False):
    print("calculating stable species")
    print("Pb concentration: ", conc)
    i = 0
    j = 0
    for pH in pHvec:
        i = 0
```

```
for V in Vvec:
    lowpot = 10000000
    stable = "check"
    ue = -F * V
    uH = -R*T*math.log(10)*pH
    uPb = GPb
    uH2O = -237.18

    #Pb
    lowpot = uPb
    stable = "Pb"

    #Pb2+
    pot = GPb2 + R*T*math.log(conc)
    urxn = pot + 2*ue - uPb
    #print("Pb2+: ", urxn)
    #pb2plus[j] == urxn
    if (urxn <= lowpot) :
        lowpot = urxn
        stable = "Pb++"

    #PbO
    urxn = GPbO + 2*ue + 2*uH - uPb - uH2O
    #print("PbO: ", urxn)
    if (urxn <= lowpot) :
        lowpot = urxn
        stable = "PbO"

    #PbO2
    urxn = GPbO2 + 4*ue + 4*uH - uPb - 2*uH2O
    if (urxn <= lowpot) :
        lowpot = urxn
        stable = "PbO2"

    #Pb3O4
    urxn = (GPb3O4 + 8*ue + 8*uH - 3*uPb -4*uH2O)/3
    if (urxn <= lowpot) :
        lowpot = urxn
        stable = "Pb3O4"

    #Pb4+
    pot = GPb4 + R*T*math.log(conc)
    urxn = pot + 4*ue - uPb
```

```
if (urxn <= lowpot) :
    lowpot = urxn
    stable = "Pb++++"

#HPbO2
pot = GHPbO2 + R*T*math.log(conc)
urxn = pot + 3*uH + 2*ue - 2*uH2O - uPb
#print("HPbO2: ", urxn)
if (urxn <= lowpot) :
    lowpot = urxn
    stable = "HPbO2-"

#PbO3--
pot = GPbO3 + R*T*math.log(conc)
urxn = pot + 6*uH + 4*ue - 3*uH2O - uPb
#print("PbO3: ", urxn)
if (urxn <= lowpot) :
    lowpot = urxn
    stable = "PbO3--"

if (carbon):
    #Hc
    urxn = (hc + 2*uH + 6*ue - 2*uH2O - 2*(CO3 + R*T*math.log(carbon)))/3
    #print(urxn)
    if (urxn <= lowpot):
        lowpot = urxn
        stable = "Hc"

    #PbCO3

    border1 = 6.35
    border2 = 10.33
    if pH < border1:
        urxn = PbCO3 + 2*ue + 2*uH - (H2CO3 + R*T*math.log(carbon))
    elif pH < border2:
        urxn = PbCO3 + 2*ue + uH - (HCO3 + R*T*math.log(carbon))
    else:
        urxn = PbCO3 + 2*ue - (CO3 + R*T*math.log(carbon))
    #print("PbCO3: ",urxn )
    if (urxn <= lowpot) :
        lowpot = urxn
        stable = "PbCO3"
```

```
            if (phosphate):
                #ortho

                h3po4 = -1147.2 + R*T*math.log(phosphate)
                h2po4 = -1135.119 + R*T*math.log(phosphate)
                hpo4 = -1094.116 + R*T*math.log(phosphate)
                po4 = -1025.498 + R*T*math.log(phosphate)

                border1 = 2.03
                border2 = 7.19
                border3 = 12.03

                if (pH<border1):
                    urxn = (pbphos + 6*uH + 6*ue - 2*h3po4)/3
                elif (pH<border2):
                    urxn = (pbphos + 4*uH + 6*ue - 2*h2po4)/3
                elif (pH<border3):
                    urxn = (pbphos + 2*uH + 6*ue - 2*hpo4)/3
                else:
                    urxn = (pbphos + 6*ue - 2*po4)/3

                if (urxn <= lowpot):
                    lowpot = urxn
                    stable = "Pb3(PO4)2"

            Z[i,j] = stable
            i+=1
        j+=1
    return pH_, V_, Z


# -*- coding: utf-8 -*-
"""
Created on Wed Jul 22 11:45:30 2020
@author: alex
"""

import matplotlib.pyplot as plt

x = [0, 0.33333, 0.43, 0.5, 1]

PBESolnospin = [0,-1.198046802365,-1.28165956625446,-1.2980779290629,0]

PBESolspin = [0,-0.781454585698333,-0.902264773397317,-0.9488537040629,0]
```

```
PBE = [0,-0.689102119031667,-0.861826944825888,-0.9212704790629,0]

LDA = [0,-1.059241252365,-1.12240284482589,-1.1483685790629,0]

Exp = [0, -0.75106433333, -0.890143, -0.9737235, 0]

MP = [0, -1.31, -1.456, -1.477, 0]

SCAN = [0,-0.773937335698331,-0.915539451968747,-0.978315204062902,0]

HSE = [0, -0.704489645698334, -0.855641074825888, -0.9231525615629, 0]


# print('difference btwn PBESolspin and Exp')

# print("PbO2 ", (PBESolspin[1]-Exp[1]), "eV", (PBESolspin[1]-Exp[1])/Exp[1]*100, "%")
# print("Pb3O4", (PBESolspin[2]-Exp[2]), "eV", (PBESolspin[2]-Exp[2])/Exp[2]*100, "%")
# print("PbO  ", (PBESolspin[3]-Exp[3]), " eV", (PBESolspin[3]-Exp[3])/Exp[3]*100, "%")



fig, ax = plt.subplots()
ax.plot(x, SCAN, label='SCAN, SOC', marker = "D", color='darkorange')
ax.plot(x, PBE, label = 'PBE, SOC', marker = "o")
ax.plot(x, HSE, label = 'HSE, no SOC', marker = "^", color='purple')
ax.plot(x, PBESolspin, label = 'PBEsol, SOC', marker = ">", color='limegreen')

for i in range(5):
    ax.plot(x[i], Exp[i], 'x', color='k', markersize=10)

ax.plot(x, LDA, label = 'LDA, SOC', marker = "<", color='r')
ax.plot(x,PBESolnospin, label = 'PBEsol, no SOC', marker = "s",linestyle='dashed', color='darkgreen')

#ax.plot(x, MP, label = "Materials Project", marker = ".")

ax.legend()
ax.set(xlim=(0, 1), ylim=(-1.5, 0))
plt.xlabel('Pb$_{1-x}$O$_{x}$ Composition', fontsize=13)
plt.ylabel('eV atom$^{-1}$', fontsize=13)
plt.savefig('Energies', dpi=300)
```

8.11. Results Chapter 6 Code and Use

Code given below is to create Bi-Cu-Se Diagrams. For brevity please find programs for other targeted bismuth oxychalcogenide systems in Github repositories (see Section 3.3).

```
#!/usr/bin/env python3
# -*- coding: utf-8 -*-
"""
Created on Mon Jul 23 13:17:41 2018
@author: laurenwalters
"""

import numpy as np
import matplotlib.pyplot as plt
import random
#For saving/importing data
from numpy import asarray
from numpy import save
from numpy import load

#Created by Lauren Walters, 2018-2020
#Contributions by Liang Feng Huang
#For reactions in aqueous conditions



#find out how much detail you want in your graph
#n=input("Enter the mesh grid detail you want, suggested (30-140): ")
n=30;

#Constants
R=8.31447;          #kJ/(mol*K)
T=298.15;           #K
F= 9.648533*10**4; #kJ/(V*mol)
P=1;                #bar, 10^5*Pa
eta=6
nI=10**-eta;          #Activity Concentration

#Array showing the composition of Cu:Bi:Se
composition=np.array([1,1,1])

#pH Range and Constants
lowpH = -2;
highpH = 16;
pHrange = int;
pHrange = highpH-lowpH;
```

```
pHcount = pHrange/n; #used to iterate through pH range

#Applied Potential Range and Constants
Ulow = -1.5;            #V
Uhigh = 1.5;            #V
Urange  = Uhigh-Ulow; #V
Ucount = Urange/n;      #used to iterate through U (energy) range

##############################################################################
######################### DFT CALCULATIONS ###################################
##############################################################################
#Electronic Energies in eV/f.u.
#PBEsol with SOC
Ee_Bi= -5.114928333;
Ee_Bi2O3= -31.163316;
Ee_Bi2O5= -40.1344765;
Ee_Bi2O4=-36.7221975;
Ee_Bi4O7=-68.40888;
#PBEsol
Ee_Cu=-4.3152965;
Ee_CuO=-10.7488868
Ee_Cu2O=-14.99698;
Ee_CuOH2_s=-25.1916025;
#PBEsol
Ee_H2=-6.5141508
Ee_Se=-3.82509;
Ee_O2=-10.281123
##############################################################################
########### MULTICOMPONENT SPECIES ###########################################
#Calculated with PBEsol
Ee_CuSe=-8.423751;
Ee_CuSe2=-12.4053445;
Ee_Cu3Se2=-21.3757505;
Ee_CuSeO3=-27.14741;
Ee_CuSeO4=-32.428945;
Ee_CuSe2O5=-43.830852;
Ee_Cu2OSeO3= -37.8371125;

Ee_BiCu=-9.31218;
Ee_CuBiO2_2=-42.245475;

Ee_Bi3Se4=-32.7784733;
Ee_Bi4Se3=-33.8044333;
```

```
Ee_Bi2Se2=-19.06480267;
Ee_BiSe2=-13.56499625;
Ee_Bi2Se3=-23.401805;
Ee_Bi2SeO2=-29.049585;
Ee_Bi2SeO5=-48.87748;
Ee_Bi2SeO3_3=-82.53894;

Ee_BiCuSeO=-20.997467;
Ee_CuBiSe2=-18.03100075;
Ee_Cu6BiSe6=-56.2063125;
Ee_CuBi2SeO3_4=-108.6834
##########################################################################################
###### Vibrational Energy ################################################################
##########################################################################################
#EVibrational Energies in eV/f.u.
#From PBEsol Phonon Calculations
Fvib_O2=-0.272;
F_rot_trans_O2=0.099;
Ftot_O2=Fvib_O2+F_rot_trans_O2;
F_H = .202;

Fvib_Se=-0.045190058131115

Fvib_CuO=0.062498987735
Fvib_Cu2O=0.00507624852
Fvib_Cu=-0.007167374680
Fvib_CuOH2_s=0.66653026525

Fvib_Bi=-0.0761976993239
Fvib_Bi2O3=-0.057653546889
Fvib_Bi2O5=0.14677315404
Fvib_Bi2O4=0.12231438709
Fvib_Bi4O7=0.08741679245

Fvib_CuSe=-0.05134468202
Fvib_CuSe2=-0.08927955844
Fvib_Cu3Se2=-0.1237964858
Fvib_CuSeO3=0.163533442904
Fvib_CuSeO4=0.23234661816
Fvib_CuSe2O5=0.26947710925
Fvib_Cu2OSeO3=0.18689283016

Fvib_BiCu=-0.11006963132
```

```
Fvib_CuBiO2_2=0.09853363658

Fvib_Bi3Se4=-0.417899867987
Fvib_Bi4Se3=-0.43313969435
Fvib_Bi2Se2=-0.2343788142756
Fvib_BiSe2=-0.1523250019192
Fvib_Bi2Se3=-0.25487956184
Fvib_Bi2SeO2=-0.05124595680
Fvib_Bi2SeO5=0.12343256096
Fvib_Bi2SeO3_3=0.2336827957

Fvib_BiCuSeO=-0.087566901314
Fvib_CuBiSe2=-0.18058569383
Fvib_Cu6BiSe6=-0.4334411850770
Fvib_CuBi2SeO3_4=0.45729680915
##############################################################################
###   Compounds-Calculate the formation energies   #############################
##############################################################################
#Free Energies of Formation in eV/f.u.
dGf_CuSe=(Ee_CuSe+Fvib_CuSe)              -(Ee_Cu+Fvib_Cu)-(Ee_Se+Fvib_Se);
dGf_CuSe2=(Ee_CuSe2+Fvib_CuSe2)           -(Ee_Cu+Fvib_Cu)-2*(Ee_Se+Fvib_Se);
dGf_Cu3Se2=(Ee_Cu3Se2+Fvib_Cu3Se2)        -3*(Ee_Cu+Fvib_Cu)-2*(Ee_Se+Fvib_Se);
dGf_CuSeO3=(Ee_CuSeO3+Fvib_CuSeO3)        -(Ee_Cu+Fvib_Cu)-(Ee_Se+Fvib_Se)-1.5*((Ee_O2)-Ftot_O2);
dGf_CuSeO4=(Ee_CuSeO4+Fvib_CuSeO4)        -(Ee_Cu+Fvib_Cu)-(Ee_Se+Fvib_Se)-2.0*((Ee_O2)-Ftot_O2);
dGf_CuSe2O5=(Ee_CuSe2O5+Fvib_CuSe2O5)     -(Ee_Cu+Fvib_Cu)-2*(Ee_Se+Fvib_Se)-2.5*((Ee_O2)-Ftot_O2);
dGf_Cu2OSeO3=(Ee_Cu2OSeO3+Fvib_Cu2OSeO3)-2*(Ee_Cu+Fvib_Cu)-(Ee_Se+Fvib_Se)-2.0*((Ee_O2)-Ftot_O2);

dGf_BiCu=(Ee_BiCu+Fvib_BiCu)                -(Ee_Cu+Fvib_Cu)-(Ee_Bi+Fvib_Bi);
dGf_CuBiO2_2=(Ee_CuBiO2_2+Fvib_CuBiO2_2)   -(Ee_Cu+Fvib_Cu)-2*(Ee_Bi+Fvib_Bi)-2.0*((Ee_O2)-Ftot_O2);

dGf_Bi3Se4=(Ee_Bi3Se4+Fvib_Bi3Se4)          -4*(Ee_Se+Fvib_Se)-3*(Ee_Bi+Fvib_Bi);
dGf_Bi4Se3=(Ee_Bi4Se3+Fvib_Bi4Se3)          -3*(Ee_Se+Fvib_Se)-4*(Ee_Bi+Fvib_Bi);
dGf_Bi2Se2=(Ee_Bi2Se2+Fvib_Bi2Se2)          -2*(Ee_Se+Fvib_Se)-2*(Ee_Bi+Fvib_Bi);
dGf_BiSe2=(Ee_BiSe2+Fvib_BiSe2)             -2*(Ee_Se+Fvib_Se)-(Ee_Bi+Fvib_Bi);
dGf_Bi2Se3=(Ee_Bi2Se3+Fvib_Bi2Se3)          -3*(Ee_Se+Fvib_Se)-2*(Ee_Bi+Fvib_Bi);
dGf_Bi2SeO2=(Ee_Bi2SeO2+Fvib_Bi2SeO2)       -(Ee_Se+Fvib_Se)-2*(Ee_Bi+Fvib_Bi)-1.0*((Ee_O2)-Ftot_O2);
dGf_Bi2SeO5=(Ee_Bi2SeO5+Fvib_Bi2SeO5)       -(Ee_Se+Fvib_Se)-2*(Ee_Bi+Fvib_Bi)-2.5*((Ee_O2)-Ftot_O2);
dGf_Bi2SeO3_3=(Ee_Bi2SeO3_3+Fvib_Bi2SeO3_3) -3*(Ee_Se+Fvib_Se)-2*(Ee_Bi+Fvib_Bi)-4.5*((Ee_O2)-Ftot_O2);

dGf_BiCuSeO=(Ee_BiCuSeO+Fvib_BiCuSeO)          -(Ee_Cu+Fvib_Cu)-(Ee_Bi+Fvib_Bi)-(Ee_Se+Fvib_Se)-
... 0.5*((Ee_O2)-Ftot_O2);
dGf_CuBiSe2=(Ee_CuBiSe2+Fvib_CuBiSe2)          -(Ee_Cu+Fvib_Cu)-(Ee_Bi+Fvib_Bi)-2*(Ee_Se+Fvib_Se);
dGf_Cu6BiSe6=(Ee_Cu6BiSe6+Fvib_Cu6BiSe6)       -6*(Ee_Cu+Fvib_Cu)-(Ee_Bi+Fvib_Bi)-6*(Ee_Se+Fvib_Se);
```

```
dGf_CuBi2SeO3_4=(Ee_CuBi2SeO3_4+Fvib_CuBi2SeO3_4)-(Ee_Cu+Fvib_Cu)-2*(Ee_Bi+Fvib_Bi)-4*(Ee_Se+Fvib_Se)-
... 6*((Ee_O2)-Ftot_O2);

dGf_CuO= (Ee_CuO+Fvib_CuO)                -(Ee_Cu+Fvib_Cu) - 0.5*(Ee_O2+Ftot_O2);
dGf_Cu2O=(Ee_Cu2O+Fvib_Cu2O)              -2.0*(Ee_Cu+Fvib_Cu) - 0.5*(Ee_O2+Ftot_O2);
dGf_CuOH2_s= (Ee_CuOH2_s+Fvib_CuOH2_s) -(Ee_Cu+Fvib_Cu)-(Ee_O2+Ftot_O2)-(Ee_H2+F_H);

dGf_Bi2O3= ((Ee_Bi2O3)+Fvib_Bi2O3) -2.0*(Ee_Bi+Fvib_Bi)-1.5*(Ee_O2-Ftot_O2);
dGf_Bi2O5= ((Ee_Bi2O5)+Fvib_Bi2O5) -2.0*(Ee_Bi+Fvib_Bi)-2.5*(Ee_O2-Ftot_O2);
dGf_Bi2O4= ((Ee_Bi2O4)+Fvib_Bi2O4) -2.0*(Ee_Bi+Fvib_Bi)-2.0*(Ee_O2-Ftot_O2);
dGf_Bi4O7= ((Ee_Bi4O7)+Fvib_Bi4O7) -4.0*(Ee_Bi+Fvib_Bi)-3.5*(Ee_O2-Ftot_O2);

#Set the reference values
dGf_Cu=0.0;
dGf_Bi=0.0;
dGf_Se=0.0;
################################################################################
################################################################################
################################################################################

################################################################################
############## Aqueous Ion Free Energies of Formation ##########################
#Free Energies of Formation in eV/f.u.
##Elemental Bismuth Species
dGf_Bi_3Plus= 0.6430898
dGf_BiOH_2Plus=  -1.6968378
dGf_BiO_Plus=  -1.4977965

##Elemental Copper Species
dGf_Cu1=  0.506502
dGf_Cu2=  0.674092
dGf_CuOH2_minus= -3.4518209
dGf_CuOH3= -5.1197432
dGf_CuOH_Plus= -1.3127387
dGf_CuOH4_2=-6.814302
dGf_CuOH2= -3.2666113
dGf_CuOH = -1.2677578
dGf_Cu2OH2_2plus=-2.942417
dGf_Cu3OH4_2plus=-6.567839

#Elemental Selenium Species
dGf_H2Se= 0.7978997
dGf_HSe_Minus=1.01906
```

```
dGf_Se_2Minus= 1.8473
dGf_H2SeO3=-4.4144669
dGf_HSeO3_Minus= -4.26269
dGf_SeO3_2Minus=-3.8737164
dGf_H2SeO4=-4.571445
dGf_HSeO4_Minus=-4.692
dGf_SeO4_2Minus=-4.5757814

dGf_H2O=-2.458;
##############################################################################
##############################################################################
##############################################################################


##############################################################################
#############   CONVERT from eV to kJ/mol   ###################################
##############################################################################
dGf_Cu=    dGf_Cu*F;
dGf_CuO=   dGf_CuO*F;
dGf_Cu2O=  dGf_Cu2O*F;
dGf_Cu1=   dGf_Cu1*F;
dGf_Cu2=   dGf_Cu2*F;
dGf_CuOH4_2= dGf_CuOH4_2*F;
dGf_CuOH2_minus= dGf_CuOH2_minus*F;
dGf_CuOH3= dGf_CuOH3*F;
dGf_CuOH_Plus= dGf_CuOH_Plus*F;
dGf_CuOH2= dGf_CuOH2*F;
dGf_CuOH = dGf_CuOH*F;
dGf_Cu2OH2_2plus=dGf_Cu2OH2_2plus*F;
dGf_Cu3OH4_2plus=dGf_Cu3OH4_2plus*F;
dGf_CuOH2_s=dGf_CuOH2_s*F

dGf_Bi=    dGf_Bi*F;
dGf_Bi2O3=   dGf_Bi2O3*F;
dGf_Bi2O5= dGf_Bi2O5*F;
dGf_Bi2O4=dGf_Bi2O4*F;
dGf_Bi4O7=dGf_Bi4O7*F;
dGf_Bi_3Plus= dGf_Bi_3Plus*F;
dGf_BiOH_2Plus=   dGf_BiOH_2Plus*F;
dGf_BiO_Plus=   dGf_BiO_Plus*F;

dGf_Se=    dGf_Se*F;
dGf_H2Se= dGf_H2Se*F;
```

```
dGf_HSe_Minus=dGf_HSe_Minus*F;
dGf_Se_2Minus= dGf_Se_2Minus*F;
dGf_H2SeO3= dGf_H2SeO3*F;
dGf_HSeO3_Minus= dGf_HSeO3_Minus*F;
dGf_SeO3_2Minus= dGf_SeO3_2Minus*F;
dGf_H2SeO4= dGf_H2SeO4*F;
dGf_HSeO4_Minus= dGf_HSeO4_Minus*F;
dGf_SeO4_2Minus= dGf_SeO4_2Minus*F;

dGf_CuSe=dGf_CuSe*F;
dGf_CuSe2=dGf_CuSe2*F;
dGf_Cu3Se2=dGf_Cu3Se2*F;
dGf_CuSeO3=dGf_CuSeO3*F;
dGf_CuSeO4=dGf_CuSeO4*F;
dGf_CuSe2O5=dGf_CuSe2O5*F;
dGf_Cu2OSeO3=dGf_Cu2OSeO3*F;

dGf_BiCu=dGf_BiCu*F;
dGf_CuBiO2_2=dGf_CuBiO2_2*F;

dGf_Bi3Se4=dGf_Bi3Se4*F;
dGf_Bi4Se3=dGf_Bi4Se3*F;
dGf_Bi2Se2=dGf_Bi2Se2*F;
dGf_BiSe2=dGf_BiSe2*F;
dGf_Bi2Se3=dGf_Bi2Se3*F;
dGf_Bi2SeO2=dGf_Bi2SeO2*F;
dGf_Bi2SeO5=dGf_Bi2SeO5*F;
dGf_Bi2SeO3_3=dGf_Bi2SeO3_3*F;

dGf_BiCuSeO=dGf_BiCuSeO*F;
dGf_CuBiSe2=dGf_CuBiSe2*F;
dGf_Cu6BiSe6=dGf_Cu6BiSe6*F;
dGf_CuBi2SeO3_4=dGf_CuBi2SeO3_4*F;

dGf_H2O=  dGf_H2O*F;
################################################################################
################################################################################
################################################################################

################################################################################
###############   Populate the species matrix   ################################
################################################################################
species=np.zeros((52,8))
```

```
######## Formation Energies ##################################################
species[0,0]=0.00;
species[1,0]=dGf_CuO
species[2,0]=dGf_Cu2O
species[3,0]=dGf_Cu1
species[4,0]=dGf_Cu2
species[5,0]=dGf_CuOH4_2
species[6,0]=dGf_CuOH2_minus
species[7,0]=dGf_CuOH3
species[8,0]=dGf_CuOH_Plus
species[9,0]=dGf_CuOH2
species[10,0]=dGf_CuOH
species[11,0]=dGf_Cu2OH2_2plus
species[12,0]=dGf_Cu3OH4_2plus

species[13,0]=dGf_Bi
species[14,0]=dGf_Bi2O3
species[15,0]=dGf_Bi2O5
species[16,0]=dGf_Bi2O4
species[17,0]=dGf_Bi4O7
species[18,0]=dGf_Bi_3Plus
species[19,0]=dGf_BiOH_2Plus
species[20,0]=dGf_BiO_Plus

species[21,0]=dGf_Se
species[22,0]=dGf_H2Se
species[23,0]=dGf_HSe_Minus
species[24,0]=dGf_Se_2Minus
species[25,0]=dGf_H2SeO3
species[26,0]=dGf_HSeO3_Minus
species[27,0]=dGf_SeO3_2Minus
species[28,0]=dGf_H2SeO4
species[29,0]=dGf_HSeO4_Minus
species[30,0]=dGf_SeO4_2Minus

species[31,0]=dGf_CuSe
species[32,0]=dGf_CuSe2
species[33,0]=dGf_Cu3Se2
species[34,0]=dGf_CuSeO3
species[35,0]=dGf_CuSeO4
species[36,0]=dGf_CuSe2O5
species[37,0]=dGf_Cu2OSeO3
```

```
species[38,0]=dGf_BiCuSeO
species[39,0]=dGf_CuBiSe2
species[40,0]=dGf_Cu6BiSe6
species[41,0]=dGf_CuBi2SeO3_4

species[42,0]=dGf_BiCu
species[43,0]=dGf_CuBiO2_2

species[44,0]=dGf_Bi3Se4
species[45,0]=dGf_Bi4Se3
species[46,0]=dGf_Bi2Se2
species[47,0]=dGf_BiSe2
species[48,0]=dGf_Bi2Se3
species[49,0]=dGf_Bi2SeO2
species[50,0]=dGf_Bi2SeO5
species[51,0]=dGf_Bi2SeO3_3

######## Electron Count ####################################################
#Cu
species[0,1]=0.00;
species[1,1]=2
species[2,1]=2
species[3,1]=1
species[4,1]=2
species[5,1]=2
species[6,1]=1
species[7,1]=2
species[8,1]=2
species[9,1]=2
species[10,1]=1
species[11,1]=4
species[12,1]=6
#Bi
species[13,1]=0
species[14,1]=6
species[15,1]=10
species[16,1]=8
species[17,1]=14
species[18,1]=3
species[19,1]=3
species[20,1]=3
#Selenium
```

```
species[21,1]=0
species[22,1]=-2
species[23,1]=-2
species[24,1]=-2
species[25,1]=4
species[26,1]=4
species[27,1]=4
species[28,1]=6
species[29,1]=6
species[30,1]=6
#CuSeBiO
species[31,1]=0
species[32,1]=0
species[33,1]=0
species[34,1]=6
species[35,1]=8
species[36,1]=10
species[37,1]=8
species[38,1]=2
species[39,1]=0
species[40,1]=0
species[41,1]=24
species[42,1]=0
species[43,1]=8

#BiSeO
species[44,1]=0
species[45,1]=0
species[46,1]=0
species[47,1]=0
species[48,1]=0
species[49,1]=4
species[50,1]=10
species[51,1]=18

######## Hydrogen H+ Count ####################################################
#Cu
species[0,2]=0
species[1,2]=2
species[2,2]=2
species[3,2]=0
species[4,2]=0
species[5,2]=4
```

```
species[6,2]=2
species[7,2]=3
species[8,2]=1
species[9,2]=2
species[10,2]=1
species[11,2]=2
species[12,2]=4
#Bi
species[13,2]=0
species[14,2]=6
species[15,2]=10
species[16,2]=8
species[17,2]=14
species[18,2]=0
species[19,2]=1
species[20,2]=2
#Selenium
species[21,2]=0
species[22,2]=-2
species[23,2]=-1
species[24,2]=0
species[25,2]=4
species[26,2]=5
species[27,2]=6
species[28,2]=6
species[29,2]=7
species[30,2]=8
#BiCuSeO
species[31,2]=0
species[32,2]=0
species[33,2]=0
species[34,2]=6
species[35,2]=8
species[36,2]=10
species[37,2]=8
species[38,2]=2
species[39,2]=0
species[40,2]=0
species[41,2]=24
species[42,2]=0
species[43,2]=8
#BiSeO
species[44,2]=0
```

```
species[45,2]=0
species[46,2]=0
species[47,2]=0
species[48,2]=0
species[49,2]=4
species[50,2]=10
species[51,2]=18

########## Number of Coppers Cu ##############################################
#Copper
species[0,3]=1
species[1,3]=1
species[2,3]=2
species[3,3]=1
species[4,3]=1
species[5,3]=1
species[6,3]=1
species[7,3]=1
species[8,3]=1
species[9,3]=1
species[10,3]=1
species[11,3]=2
species[12,3]=3
#Bismuth
species[13,3]=0
species[14,3]=0
species[15,3]=0
species[16,3]=0
species[17,3]=0
species[18,3]=0
species[19,3]=0
species[20,3]=0
#Selenium
species[21,3]=0
species[22,3]=0
species[23,3]=0
species[24,3]=0
species[25,3]=0
species[26,3]=0
species[27,3]=0
species[28,3]=0
species[29,3]=0
species[30,3]=0
```

```
#BiCuSeO
species[31,3]=1
species[32,3]=1
species[33,3]=3
species[34,3]=1
species[35,3]=1
species[36,3]=1
species[37,3]=2
species[38,3]=1
species[39,3]=1
species[40,3]=6
species[41,3]=1
species[42,3]=1
species[43,3]=1
#BiSeO
species[44,3]=0
species[45,3]=0
species[46,3]=0
species[47,3]=0
species[48,3]=0
species[49,3]=0
species[50,3]=0
species[51,3]=0

########## Number of Bismuths Bi ##############################################
#Copper
species[0,4]=0
species[1,4]=0
species[2,4]=0
species[3,4]=0
species[4,4]=0
species[5,4]=0
species[6,4]=0
species[7,4]=0
species[8,4]=0
species[9,4]=0
species[10,4]=0
species[11,4]=0
species[12,4]=0
#Bismuth
species[13,4]=1
species[14,4]=2
species[15,4]=2
```

```
species[16,4]=2
species[17,4]=4
species[18,4]=1
species[19,4]=1
species[20,4]=1
#Selenium
species[21,4]=0
species[22,4]=0
species[23,4]=0
species[24,4]=0
species[25,4]=0
species[26,4]=0
species[27,4]=0
species[28,4]=0
species[29,4]=0
species[30,4]=0
#BiCuSeO
species[31,4]=0
species[32,4]=0
species[33,4]=0
species[34,4]=0
species[35,4]=0
species[36,4]=0
species[37,4]=0
species[38,4]=1
species[39,4]=1
species[40,4]=1
species[41,4]=2
species[42,4]=1
species[43,4]=2
#BiSeO
species[44,4]=3
species[45,4]=4
species[46,4]=2
species[47,4]=1
species[48,4]=2
species[49,4]=2
species[50,4]=2
species[51,4]=2

########## Number of Selenium Se  ##############################################
#Copper
species[0,5]=0
```

```
species[1,5]=0
species[2,5]=0
species[3,5]=0
species[4,5]=0
species[5,5]=0
species[6,5]=0
species[7,5]=0
species[8,5]=0
species[9,5]=0
species[10,5]=0
species[11,5]=0
species[12,5]=0
#Bismuth
species[13,5]=0
species[14,5]=0
species[15,5]=0
species[16,5]=0
species[17,5]=0
species[18,5]=0
species[19,5]=0
species[20,5]=0
#Selenium
species[21,5]=1
species[22,5]=1
species[23,5]=1
species[24,5]=1
species[25,5]=1
species[26,5]=1
species[27,5]=1
species[28,5]=1
species[29,5]=1
species[30,5]=1
#BiCuSeO
species[31,5]=1
species[32,5]=2
species[33,5]=2
species[34,5]=1
species[35,5]=1
species[36,5]=2
species[37,5]=1
species[38,5]=1
species[39,5]=2
species[40,5]=6
```

```
species[41,5]=4
species[42,5]=0
species[43,5]=0
#BiSeO
species[44,5]=4
species[45,5]=3
species[46,5]=2
species[47,5]=2
species[48,5]=3
species[49,5]=1
species[50,5]=1
species[51,5]=3

######### Number of H2O's ####################################################
#Copper
species[0,6]=0
species[1,6]=1
species[2,6]=1
species[3,6]=0
species[4,6]=0
species[5,6]=4
species[6,6]=2
species[7,6]=3
species[8,6]=1
species[9,6]=2
species[10,6]=1
species[11,6]=2
species[12,6]=4
#Bi
species[13,6]=0
species[14,6]=3
species[15,6]=5
species[16,6]=4
species[17,6]=7
species[18,6]=0
species[19,6]=1
species[20,6]=1
#Selenium
species[21,6]=0
species[22,6]=0
species[23,6]=0
species[24,6]=0
species[25,6]=3
```

```
species[26,6]=3
species[27,6]=3
species[28,6]=4
species[29,6]=4
species[30,6]=4
#CuSeBiO
species[31,6]=0
species[32,6]=0
species[33,6]=0
species[34,6]=3
species[35,6]=4
species[36,6]=5
species[37,6]=4
species[38,6]=1
species[39,6]=0
species[40,6]=0
species[41,6]=12
species[42,6]=0
species[43,6]=4
#BiSeO
species[44,6]=0
species[45,6]=0
species[46,6]=0
species[47,6]=0
species[48,6]=0
species[49,6]=2
species[50,6]=5
species[51,6]=9

########## Aqueous Ions?????? ##################################################
#Copper
species[0,7]=0
species[1,7]=0
species[2,7]=0
species[3,7]=1
species[4,7]=1
species[5,7]=1
species[6,7]=1
species[7,7]=1
species[8,7]=1
species[9,7]=1
species[10,7]=1
species[11,7]=1
```

```
species[12,7]=1
#Bismuth
species[13,7]=0
species[14,7]=0
species[15,7]=0
species[16,7]=0
species[17,7]=0
species[18,7]=1
species[19,7]=1
species[20,7]=1
#Selenium
species[21,7]=0
species[22,7]=1
species[23,7]=1
species[24,7]=1
species[25,7]=1
species[26,7]=1
species[27,7]=1
species[28,7]=1
species[29,7]=1
species[30,7]=1
#CuSeBiO
species[31,7]=0
species[32,7]=0
species[33,7]=0
species[34,7]=0
species[35,7]=0
species[36,7]=0
species[37,7]=0
species[38,7]=0
species[39,7]=0
species[40,7]=0
species[41,7]=0
species[42,7]=0
species[43,7]=0
#SeBiO
species[44,7]=0
species[45,7]=0
species[46,7]=0
species[47,7]=0
species[48,7]=0
species[49,7]=0
species[50,7]=0
```

```
species[51,7]=0


#Function to determine species combinations
try:
    combos=load('BiCuOSe-speciesCombo.npy')
    num=load('BiCuOSe-numberSpecies.npy')
    combo_num=int(num[0])
except OSError:
    print('Cannot Open File')
    ###############################################################################
    #### Determine which species are able to combine at the composition ##########
    ###############################################################################
    t=1
    flag=1
    f_total=int;
    f=np.zeros((3))
    combos=np.zeros((25000,9,3))
    combo_num=0
    combos[combo_num, 0, 0]=-1
    combos[combo_num, 0, 1]=-1
    combos[combo_num, 0, 2]=-1
    for k in range(0, len(species)):
        for m in range(0, len(species)):
            for p in range(0, len(species)):
                #Check to make sure each element is in this combination of species
                if((species[k, 3]>0 or species[m, 3] >0 or species[p, 3]) \
                   and (species[k, 4]>0 or species[m, 4] >0 or species[p, 4]) \
                   and (species[k, 5]>0 or species[m, 5] >0 or species[p, 5])):
                    #save species in array
                    t=1
                    a = np.array([[species[k, 3],species[m, 3], species[p,3]], \
                                  [species[k, 4],species[m, 4], species[p,4]], \
                                  [species[k, 5],species[m, 5], species[p,5]]])

                    #check to see if each species contains a single element. This is a really long call.
                    flag=1
                    if((species[k, 3]==0 and species[m, 3] ==0) or \
                       (species[m, 3]==0 and species[p, 3] ==0) or \
                       (species[k, 3]==0 and species[p, 3] ==0)):
                        if((species[k, 4]==0 and species[m, 4] ==0) or \
                           (species[m, 4]==0 and species[p, 4] ==0) or \
                           (species[k, 4]==0 and species[p, 4] ==0)):
                            if((species[k, 5]==0 and species[m, 5] ==0) or \
```

```
                                (species[m, 5]==0 and species[p, 5] ==0) or \
                                (species[k, 5]==0 and species[p, 5] ==0)):

                                 flag=0
                                 #if so, find the composition though linear algebra.
                                 try:
                                     f=np.linalg.solve(a, composition)
                                 except:
                                     #print('Error: Species '+str(k)+', Species2: '+str(m)+',
                            Species3: '+str(p)+'\n')
____________________________________t=1
__________________________________t=0


__________________#If there is at least one multi-element species in this combination
____________________if(flag==1):
________________________#test each linear combination
____________________________for h in range(1, 20):
______________________________for i in range(1, 20):
________________________________for j in range(1, 20):
____________________________________#Is there a linear combination of the elements that will allow
____________________________________#For the
____________________________________if(((h*a[0,0]+i*a[0,1]+j*a[0,2])/(h*a[1,0]+i*a[1,1]+j*a[1,2]))==
____________________________________...composition[0]/composition[1] and \
________________________________________((h*a[1,0]+i*a[1,1]+j*a[1,2])/(h*a[2,0]+i*a[2,1]+j*a[2,2]))==
________________________________________...composition[1]/composition[2] and \
____________________________________((h*a[0,0]+i*a[0,1]+j*a[0,2])/(h*a[2,0]+i*a[2,1]+j*a[2,2]))==
____________________________________...composition[0]/composition[2]):
________________________________________#save the composition
________________________________________f[0]=h
________________________________________f[1]=i
________________________________________f[2]=j
________________________________________#Ending parameters, break loops
________________________________________t=0;
________________________________________h=40;
________________________________________i=40;
________________________________________j=40;


__________________________________#If there is a linear combination, save the species in the combos array.


____________________if(t==0):
________________________#print(str(combo_num)+': Species1: '+str(k)+', Species2: '+str(m)+'\n')
________________________#Species Number
```

```
                        combos[combo_num, 0, 0]=k
                        combos[combo_num, 0, 1]=m
                        combos[combo_num, 0, 2]=p
                        #Energy
                        combos[combo_num, 1, 0]=species[k,0]
                        combos[combo_num, 1, 1]=species[m,0]
                        combos[combo_num, 1, 2]=species[p,0]
                        #Electrons
                        combos[combo_num, 2, 0]=species[k,1]
                        combos[combo_num, 2, 1]=species[m,1]
                        combos[combo_num, 2, 2]=species[p,1]
                        #H+
                        combos[combo_num, 3, 0]=species[k,2]
                        combos[combo_num, 3, 1]=species[m,2]
                        combos[combo_num, 3, 2]=species[p,2]
                        #Number Silvers
                        combos[combo_num, 4, 0]=species[k,3]
                        combos[combo_num, 4, 1]=species[m,3]
                        combos[combo_num, 4, 2]=species[p,3]
                        #Number Bismuth
                        combos[combo_num, 5, 0]=species[k,4]
                        combos[combo_num, 5, 1]=species[m,4]
                        combos[combo_num, 5, 2]=species[p,4]
                        #Number H2O
                        combos[combo_num, 6, 0]=species[k,5]
                        combos[combo_num, 6, 1]=species[m,5]
                        combos[combo_num, 6, 2]=species[p,5]
                        #Aqueous Ions
                        combos[combo_num, 7, 0]=species[k,6]
                        combos[combo_num, 7, 1]=species[m,6]
                        combos[combo_num, 7, 2]=species[p,6]
                        #Percent of each in species in final combo
                        f_total=f[0]+f[1]+f[2];
                        combos[combo_num, 8, 0]=f[0]/f_total
                        combos[combo_num, 8, 1]=f[1]/f_total
                        combos[combo_num, 8, 2]=f[2]/f_total

                        combo_num=combo_num+1;
                        t=1
                        #print('entered')
                    else:
                        #Catch and switch the value of t back to no
                        t=1
```

```
    save('BiCuOSe-speciesCombo.npy', combos)
    save('BiCuOSe-numberSpecies.npy', asarray([[combo_num]]))
    print('The number of species combinations is '+str(combo_num)+'.\n')
##############################################################################
##############################################################################
##############################################################################


##############################################################################
##########  Chemical Potential Mesh Calculations  ############################
##############################################################################
#should be as long as there are specicies considered
#populate with smaller values that will be calculated.
muValues=np.zeros((n+1,n+1,4))
current_mu=int
current_ele=int
current_H=int
current_H2O=int
current_aquI=int
current_NumEle=int
sort=np.zeros((3,1))

#fill in the grid. Calculate
for i in range(0, n+1):
    #calculate the energies for each species number
    pH=lowpH+(i*pHcount);
    for j in range(0,n+1):
        U=Ulow+(j*Ucount);
        muValues[i,j,0]=-1
        muValues[i,j,1]=-1
        muValues[i,j,2]=-1
        muValues[i,j,3]=100000000
        #Go through all species, commpare all pairs
        for k in range(0, combo_num):
            p=int(combos[k,0,0]);
            m=int(combos[k,0,1]);
            s=int(combos[k,0,2]);
            f1=combos[k,8,0];
            f2=combos[k,8,1];
            f3=combos[k,8,2];

            #The first species's contribution to the mu
```

```
current_eng=species[p,0]
current_ele=F*U*(species[p,1])
current_H=R*T*np.log(10.0)*pH*(species[p,2])
current_H2O=dGf_H2O*(species[p,6])
current_aquI=R*T*np.log(nI)*(species[p,7])
current_NumEle=1
for t in range(3,6):
    if(species[p,t]>1):
        current_NumEle=current_NumEle*species[p,t];
current_mu=f1*((current_eng+current_aquI-current_ele-current_H-current_H2O)/current_NumEle);

#The second species' contribution to the mu
current_eng=species[m,0];
current_ele=F*U*(species[m,1])
current_H=R*T*np.log(10.0)*pH*(species[m,2])
current_H2O=dGf_H2O*(species[m,6])
current_aquI=R*T*np.log(nI)*(species[m,7])
current_NumEle=1
for t in range(3,6):
    if(species[m,t]>1):
        current_NumEle=current_NumEle*species[m,t];
current_mu=current_mu+f2*((current_eng+current_aquI-current_ele-current_H-current_H2O)
.../current_NumEle);

#The second species' contribution to the mu
current_eng=species[s,0];
current_ele=F*U*(species[s,1])
current_H=R*T*np.log(10.0)*pH*(species[s,2])
current_H2O=dGf_H2O*(species[s,6])
current_aquI=R*T*np.log(nI)*(species[s,7])
current_NumEle=1
for t in range(3,6):
    if(species[s,t]>1):
        current_NumEle=current_NumEle*species[s,t];
current_mu=current_mu+f3*((current_eng+current_aquI-current_ele-current_H-current_H2O)
.../current_NumEle);
if(current_mu<muValues[i,j,3]):
    sort[0,0]=p
    sort[1,0]=m
    sort[2,0]=s
    a=np.sort(sort[:,0])
    muValues[i,j,0]=a[0]
    muValues[i,j,1]=a[1]
```

```
                muValues[i,j,2]=a[2]
                muValues[i,j,3]=current_mu
                if(a[0]==37 and (a[1]==37 or a[1]==43) and a[2]==43 and pH>8 and U>0.2 and U<0.5):
                    print(k)


###############################################################################
###############################################################################
###############################################################################


###############################################################################
##################  Plot Pourbaix Diagram  ####################################
###############################################################################
flag = np.zeros((50,6)) # The first 4 indexes are the materials stored, the next three are the colors
index=0;
fig =plt.figure()
ax=plt.subplot(111)
ax = plt.gca()
ax.set_xlim([lowpH,highpH])
ax.set_ylim([Ulow,Uhigh])
l=0;
index=0;
for i in range(0, n+1):
    pH=lowpH+i*pHcount;
    for j in range(0,n+1):
        U=Ulow+(Ucount*j);
        l=0
        for k in range(0, len(flag)):
            if(flag[k,0]==muValues[i,j,0] and flag[k,1]==muValues[i,j,1] and flag[k,2]==muValues[i,j,2]):
                ax.plot(pH,U,'.', color = [flag[k,3],flag[k,4],flag[k,5]],markersize=4)
                #break loop, the color is found
                k=len(flag)+1
                l=1
            elif(flag[k,0]==muValues[i,j,1] and flag[k,1]==muValues[i,j,2]and flag[k,2]==muValues[i,j,0]):
                ax.plot(pH,U,'.', color = [flag[k,3],flag[k,4],flag[k,5]],markersize=4)
                #break loop, the color is found
                k=len(flag)+1
                l=1
            elif(flag[k,0]==muValues[i,j,2] and flag[k,1]==muValues[i,j,0]and flag[k,2]==muValues[i,j,1]):
                ax.plot(pH,U,'.', color = [flag[k,3],flag[k,4],flag[k,5]],markersize=4)
                #break loop, the color is found
                k=len(flag)+1
```

```
                l=1
        if(l==0):
            label='M1: '+str(muValues[i,j,0])+', M2: '+str(muValues[i,j,1])+' M3: '+str(muValues[i,j,2])
            flag[index,0] = muValues[i,j,0]
            flag[index,1] = muValues[i,j,1]
            flag[index,2] = muValues[i,j,2]
            flag[index,3] = random.random();
            flag[index,4] = random.random();
            flag[index,5] = random.random();
            ax.plot(pH,U,'.', color = [flag[index,3],flag[index,4],flag[index,5]],markersize=4,
            ...label=label)
            index=index+1;


#####Plot H2O and H2 lines###################################
muH=np.zeros((pHrange+1));
muH2O=np.zeros((pHrange+1));
pHArray=np.zeros((pHrange+1));
for i in range(0, pHrange):
    pHArray[i] =lowpH+i;
    muH[i]=-0.059*pHArray[i];
    muH2O[i]=1.23-0.059*pHArray[i];

pHArray[pHrange] =lowpH+(pHrange);
muH[pHrange]=-0.059*pHArray[pHrange];
muH2O[pHrange]=1.23-0.059*pHArray[pHrange];
############################################################


ax.plot(pHArray[:], muH[:],'c--',label='$H_2$',linewidth=1)
ax.plot(pHArray[:], muH2O[:],'b--',label='$H_2O$', linewidth=1)
ax.legend(loc='upper center', bbox_to_anchor=(1.3, 0.9), ncol=1)
plt.ylabel('Electric Potential, E(V)')
plt.xlabel('pH')
plt.title('Bi-Cu-Se Pourbaix Diagram, $\eta_{Bi,Cu,Se}=10^{-'+str(eta)+'}$, '+str(composition[0])+...
'Cu:' +str(composition[1])+'Bi:'+str(composition[2])+'Se')


#############################################################################
##############    Plot with Lines    ########################################
#############################################################################
flag = np.zeros((50,6)) # The first 4 indexes are the materials stored, the next three are the colors
index=0;
fig =plt.figure()
```

```
ax=plt.subplot(111)
ax = plt.gca()
ax.set_xlim([lowpH,highpH])
ax.set_ylim([Ulow,Uhigh])

#If drawing lines for metastable phases
for i in range(1, n):
    #calculate the energies for each species number
    pH=lowpH+(i*pHcount);
    for j in range(1,n):
        U=Ulow+(j*Ucount);
        #If drawing lines for metastable phases

        if((muValues[i,j,0]!=muValues[i-1,j,0])):
            ax.plot(pH,U,'.', color = [0.0,0.0,0.0],markersize=2)
        elif(muValues[i,j,1]!=muValues[i-1,j,1]):
            ax.plot(pH,U,'.', color = [0.0,0.0,0.0],markersize=2)
        elif((muValues[i,j,0]!=muValues[i,j-1,0]) or (muValues[i,j,1]!=muValues[i,j-1,1])):
            ax.plot(pH,U,'.', color = [0.0,0.0,0.0],markersize=2)
        elif((muValues[i,j,2]!=muValues[i,j-1,2]) or (muValues[i,j,2]!=muValues[i-1,j,2])):
            ax.plot(pH,U,'.', color = [0.0,0.0,0.0],markersize=2)

ax.plot(pHArray[:], muH[:],'c—',label='$H_2$',linewidth=1)
ax.plot(pHArray[:], muH2O[:],'b—',label='$H_2O$', linewidth=1)

plt.ylabel('Electric Potential, E(V)')
plt.xlabel('pH')
plt.title('Bi–Cu–Se Pourbaix Diagram, $\eta_{Bi,Cu,Se}=10^{-'+str(eta)+'}$, '+str(composition[0])+...
'Cu:' +str(composition[1])+'Bi:'+str(composition[2])+'Se')
chartBox=ax.get_position()
ax.set_position([chartBox.x0, chartBox.y0, chartBox.width*1.5, chartBox.height*1.5])
ax.legend(loc='upper center', bbox_to_anchor=(1.3, 0.9), ncol=1)
plt.show()



print('End of Script')
```

8.12. Results Chapter 7 Code and Use

Code given below is to calculate single element MDFs and multiple element MDFs. For brevity please find programs and the packaged files necessary to execute these programs in relevant Github repositories (see Section 3.3).

```
# other than using experimental data rather than MP data and being only single-element
```

```
# this version also gives MDFs for each passivation product with a DF < 0 in the pH-potential window
# rather than a single MDF for all passivation products
from Packaged.MDFwithexperimental import *


# example for single element
CONCEN = 1e-6
precision = 0.01
RANGE_PH = ([2.5, 12.5], precision)
RANGE_POTENTIAL = ([-0.5, 0.75], precision)
METAL = "Nb"
if check_metals([METAL]):
    SPECIES = construct_s_from_oxides(ox_names_by_metal[METAL])
    intermediates = driving_force_2D_helper(SPECIES, METAL, RANGE_PH, RANGE_POTENTIAL, CONCEN)
    if intermediates:
        max_dr = driving_force_2D(intermediates, [METAL], RANGE_PH, RANGE_POTENTIAL)
        print_dr_dict(max_dr)



# example of periodic trend from Sc to Zn (multiple MDFs)
CONCENTRATION = 10**-6
# start metal num, end metal num, [pH range], [potential range], precision, concentration
# so in this case, 21 = Scandium, 30 = Zinc, then ...
plotted_metals, oxs1, drs1, oxs2, drs2, all_dicts = periodic_trend(21, 30, [2.5, 12.5], [-0.5, 0.75],
... 0.01, CONCENTRATION)



from Packaged.MDFwithpymatgen import *
from pymatgen.ext.matproj import MPRester
mpr = MPRester("NGpMC4M2qzg2ZpPEX")

# example for a single element system with MP's filter:
METALS = ["Fe"]
# adjustment for multi-element:
# METALS = ["Al", "Cr"]
# ADJUSTED_RATIO = [0.9, 0.1]
# METAL_RATIOS = {i: j for i, j in zip(METALS, ADJUSTED_RATIO)}
CONCEN = 1e-6
precision = 0.01
RANGE_PH = ([2.5, 12.5], precision)
RANGE_POTENTIAL = ([-0.5, 0.75], precision)
if check_metals(METALS):
```

```
    entries = mpr.get_pourbaix_entries(METALS)
    pbx = PourbaixDiagram(entries, conc_dict={met: CONCEN for met in METALS})
    # multi-element: pbx = PourbaixDiagram(entries, comp_dict = METAL_RATIOS, conc_dict={met: CONCEN for met
    #in METALS})
    using_entries = pbx.all_entries
    if using_entries is not None:
        intermediates = driving_force_2D_helper(using_entries, RANGE_PH, RANGE_POTENTIAL, single = True, ...
        ox_req = False)
    if intermediates is not None:
        # does not zoom for single element since it usually doesn't have other participating products that
        # are invisible on the existing plots
        max_dr = driving_force_2D(intermediates, METALS, RANGE_PH, RANGE_POTENTIAL, plot = True, zoom = 1)
        print_dr_dict(max_dr)

# example for multi-element system with our filter
METALS = ["Fe", "Sc"]
CONCEN = 1e-6
# ratio of elements, must sum to 1
ADJUSTED_RATIO = [0.9, 0.1]
METAL_RATIOS = {i: j for i, j in zip(METALS, ADJUSTED_RATIO)}
precision = 0.01
RANGE_PH = ([2.5, 12.5], precision)
RANGE_POTENTIAL = ([-0.5, 0.75], precision)
# options for class_of_pourbaix: PourbaixDiagram, PourbaixDiagramMP, PourbaixDiagramAllPC,
#PourbaixDiagramBrute
class_of_pourbaix = PourbaixDiagram
if check_metals(METALS):
    using_entries = get_entries_with_my_filter(mpr, class_of_pourbaix, METALS, METAL_RATIOS,
    ... {i: CONCEN for i in METALS})
    if using_entries is not None:
        intermediates = driving_force_2D_helper(using_entries, RANGE_PH, RANGE_POTENTIAL, ox_req = False)
    if intermediates is not None:
        max_dr = driving_force_2D(intermediates, METALS, RANGE_PH, RANGE_POTENTIAL, plot = False,
        ... zoom = 1)
        print_dr_dict(max_dr)

# using the intermediates from cell above to see the plots
max_dr = driving_force_2D(intermediates, METALS, RANGE_PH, RANGE_POTENTIAL, zoom = 1)
print_dr_dict(max_dr)

# example for multi-element system with our filter
METALS = ["Al", "Si", "Cu"]
CONCEN = 1e-6
```

```
# ratio of elements, must sum to 1
ADJUSTED_RATIO = [(1/3), (1/3), (1/3)]
METAL_RATIOS = {i: j for i, j in zip(METALS, ADJUSTED_RATIO)}
precision = 0.01
RANGE_PH = ([2.5, 12.5], precision)
RANGE_POTENTIAL = ([-0.5, 0.75], precision)
# RANGE_PH = ([-2, 16], precision)
# RANGE_POTENTIAL = ([-2, 2], precision)
# options for class_of_pourbaix: PourbaixDiagram, PourbaixDiagramMP, PourbaixDiagramAllPC,
# PourbaixDiagramBrute
class_of_pourbaix = PourbaixDiagram
if check_metals(METALS):
    using_entries = get_entries_with_my_filter(mpr, class_of_pourbaix, METALS, METAL_RATIOS,
    ... {i: CONCEN for i in METALS})
    if using_entries is not None:
        intermediates = driving_force_2D_helper(using_entries, RANGE_PH, RANGE_POTENTIAL, ox_req = False)
    if intermediates is not None:
        max_dr = driving_force_2D(intermediates, METALS, RANGE_PH, RANGE_POTENTIAL, plot = False,
        ... zoom = 1)
        print_dr_dict(max_dr)



# MDF trends across periodic table example
# start metal num, end metal num, [pH range], [potential range], precision, concentration
# "myfilter" means using our filter
# if an element is not possible, it will be skipped + a message will be displayed for why
periodic_trend(mpr, 39, 55, [2.5, 12.5], [-0.5, 0.75], 0.01, 10**-6, myfilter = True)
```

Appendix D: Full Synopsis of the Revised Helgeson-Kirkham-Flowers Method

The Helgeson-Kirkham-Flowers (HKF) method encompasses a collection of works published from the 1970s through the 1990s, including the select works highlighted herein [113-119]. Several studies use the revised HKF method to account for different thermodynamic behavior of solutions at nonstandard state, including to construct Pourbaix Diagrams [120, 121]. The method is founded on the basis that the change in behavior of a solution can be derived from the sum of its solvated and nonsolvated contributions, and approximates the size of the ion radius and its subsequent Born coefficient through experimental observations and fitted data. Further dependence of solution structure based upon changes to the dielectric constant and effective volume are documented with temperature and pressure changes. Several parameters and functions, including the g-function and the dielectric constant of water, have been well documented. The entropy, enthalpy, heat capactiy, and therefore formation energies of solutions can be calculated at nonstandard state. We utilized the following equations, similar to those those used by Puigdomenech and Binter [120, 122], to find the entropy and heat capacity at elevated temperatures.

We start with the equation for the molal formation energy of a species at nonstandard state:

$$\Delta\bar{G}^{\circ} = \Delta\bar{G}^{\circ}_{f} + (\bar{G}^{\circ}_{P,T} - \bar{G}^{\circ}_{P_r,T_r}) \tag{8.1}$$

where the difference $(\bar{G}^{\circ}_{P,T} - \bar{G}^{\circ}_{P_r,T_r})$ is related to our definition of the Gibbs formation energy, which is dependent on the entropy, heat capacity, volume, and pressure:

$$\bar{G}^{\circ}_{P,T} - \bar{G}^{\circ}_{P_r,T_r} = -\bar{S}^{\circ}_{P_r,T_r}(T - T_r) + \int_{T_r}^{T} \bar{C}^{\circ}_{P_r} dT - T\int_{T_r}^{T} \bar{C}^{\circ}_{P_r} d\ln(T) + \int_{Pr}^{P} \bar{V}^{\circ}_{T} dP\,. \tag{8.2}$$

In this study we assumed the $\int_{Pr}^{P} \bar{V}_T^{\circ} dP$ term, describing the change in volume in the system at different pressure, is negligible. We therefore need the nonstandard state heat capacity in order to calculate the change in formation energy. We also assume that the integrated heat capacity can be approximated by the average temperature of the heat capacity at the given temperature range. The equation for partial molal heat capacity, $\bar{C}_P^0$, is shown below as a sum of its solvated and nonsolvated contributions.

$$\bar{C}_P^0 = \Delta\bar{C}_{P,n}^0 + \Delta\bar{C}_{P,s}^0 \tag{8.3}$$

This ultimately gives us the final equation for the standard partial molal heat capacity as:

$$\begin{aligned} \bar{C}_P^0 = \quad & c_1 + \frac{c_2}{(T-\Theta)^2} - \left(\frac{2T}{(T-\Theta)^3}\right) \times \left(a_3(P-P_r) + a_4 \ln\left(\frac{\Psi+P}{\Psi+P_r}\right)\right) \\ & + \omega T X + 2TY\left(\frac{\partial \omega}{\partial T}\right)_P - T\left(\frac{1}{\epsilon} - 1\right)\left(\frac{\partial^2 \omega}{\partial T^2}\right)_P , \end{aligned} \tag{8.4}$$

where $\bar{C}_P^0$ is given as a function of temperature and pressure. It accounts for changes in temperature and pressure through the inclusion of the dielectric constant and its dependent terms, the Born coefficient, and the coefficients of equations of state. The nonstandard state temperature and pressure are given by T and P respectively. Θ and Ψ are solvent parameters equal to 228 K and 2800 bar. Implementation of these equations yields the standard molal heat capacity at elevated temperatures and pressures.

We show the $\Delta\bar{C}_P^0$ is dependent upon parameters c_1, c_2, a_3, a_4, Z, and ω. Additional equations-of-state coefficients a_1 and a_2 are used for the approximation of other properties like nonstandard state entropy, but are not needed for this study. The values for the equations-of-state coefficients are derived from experiment, and are given in a variety of works [**114**, **115**, **123**]. In the case where parameters were not given, the coefficients were approximated by the coefficients provided for structurally and electronically similar ions found in works by Shock and Helgeson, particalularly when modeling anionic copper complexes [**114**,**115**,**118**]. We point out that the cuprite and cuprous hydrolysis series found to be stable in largely basic conditions, such as $Cu(OH)_3^-$ and $Cu(OH)_4^{2-}$, can also be written as the $HCuO_2^-$ and CuO_2^{2-}.

The series of the conventional Born coefficient ω_j and its partial derivatives with respect to temperature are given below, which exhibit a dependence on the g-function (within the radii terms, $r_{e,j}$):

$$\omega_j = \omega_j^{\text{abs}} - Z_j \omega_{H^+}^{\text{abs}} \tag{8.5}$$

$$\omega_j^{\text{abs}} = \frac{N^0 e^2 Z_j^2}{2 r_{e,j}} = \frac{\eta_j^2 Z_j^2}{r_{e,j}} \tag{8.6}$$

$$\omega_j^{\text{abs}} = \frac{\eta Z_{e,j}^2}{r_{e,j}} \tag{8.7}$$

where Z is the formal charge on the ion, N^0 is Avagadro's number, e is the absolute electronic charge equal to 4.80298×10^{-10} esu, and $\eta = 1.66027 \times 10^5$ Åcal/mol. An important point to note is that neutral ions are often found to still behave as a charged ion in solution, but the revised HKF method for neutral atoms does not define a formal charge for these species. Values in the original works were found from experimental extrapolation exclusively. In this work, we define $Z = 0$ for electronically neutral ions, and extrapolate reported values for structurally similar ions to our own species. The value $\omega_{H^+}^{\text{abs}}$ is the Born coefficient of the H^+ ion, equal to approximately $5.387{\times}10^4$ cal/mol (225.4 kJ/mol) at standard state [115]. The effective radii of the j^{th} ion, $r_{e,j}$ is defined as

$$r_{e,j} = r_{x,j} + |Z_j|(k_z + g) \tag{8.8}$$

where $r_{x,j}$ is the crystallographic radius of the ion, k_z is a charge dependent constant defined as 0.94 for cations and 0.0 for anions [114], and g is the g function characterized in J.C. Tanger and H.C. Helgeson (1988) [118]. The values of the g function are reported in E.L. Shock *et al.* (1992) and further in this section [123].

To calculate the $\bar{C}_P^0$ value, we find the partial derivatives of the Born coefficient with respect to temperature. These are defined below, where each partial derivative similarly relies on the g-function and its partial derivatives.

$$\left(\frac{\partial \omega}{\partial T}\right)_P = -\eta \left[\frac{\text{abs}(Z^3)}{r_e^2} - \left(\frac{Z}{(3.082 + g)^2}\right)\right]\left(\frac{\partial g}{\partial T}\right)_P \tag{8.9}$$

$$\left(\frac{\partial^2 \omega}{\partial T^2}\right)_P = 2\eta \left[\frac{Z^4}{r_e^3} - \left(\frac{Z}{(3.082 + g)^3}\right)\right]\left(\frac{\partial g}{\partial T}\right)_P^2 - \eta \left[\frac{\text{abs}(Z^3)}{r_e^2} - \left(\frac{Z}{(3.082 + g)^2}\right)\right]\left(\frac{\partial^2 g}{\partial T^2}\right)_P \tag{8.10}$$

We highlight that the g-function, while defined elsewhere, was defined and then fit with a power series in J.C. Tanger and H.C. Helgeson (1988) [118], and later E. L. Shock *et al.* [123]. As discussed in E. L. Shock *et al.* (1992) [123], the g-function is a solvent function that describes the effective electrostatic radii of pressure and temperature dependence of the solvent, in this case water [118]. We define it below.

$$g = a_g(1-\hat{\rho})^{b_g} \tag{8.11}$$

$$a_g = a_g^{'} + a_g^{''}T + a_g^{'''}T^2 \tag{8.12}$$

$$b_g = b_g^{'} + b_g^{''}T + b_g^{'''}T^2 \tag{8.13}$$

Here, a_i and b_j are parameters given in a variety of texts, T is temperature, and $\hat{\rho}$ is the density of water divided by 1 $\frac{g}{cm^3}$ [122]. Qualitative trends and descriptions of the g-function can be found in E.L. Shock *et al.* [123].

The partial derivatives of the g-function with respect to temperature, at constant pressure, are necessary to find the final temperature-dependence of the Born coefficient as shown below. Explicit values of the partial derivatives at different pressures and temperatures are found in E.L. Shock *et al.* [123]

$$\left(\frac{\partial g}{\partial T}\right)_P = g\left[\frac{\hat{\rho}\alpha b_g}{1-\hat{\rho}} + (b_g^{''} + 2b_g^{'''}T)\ln(1-\hat{\rho}) + \frac{a_g^{''} + a_g^{'''}T}{a_g}\right] \tag{8.14}$$

$$\begin{aligned}\left(\frac{\partial^2 g}{\partial T^2}\right)_P &= g\left[\frac{\hat{\rho}\alpha b_g}{1-\hat{\rho}}\left[\frac{2(b_g^{''} + 2b_g^{'''}T)}{b_g} + \frac{1}{\alpha}\left(\frac{\partial \alpha}{\partial T}\right)_P - \alpha - \frac{\hat{\rho}\alpha}{(1-\hat{\rho})}\right]\right. \\ &+ \left. 2b_g^{'''}\ln(1-\hat{\rho}) + \frac{2a_g a_g^{'''} - (a_g^{''} + 2a_g^{'''}T)^2}{a_g^2}\right] + \frac{1}{g}\left(\frac{\partial g}{\partial T}\right)_P^2\end{aligned} \tag{8.15}$$

where α is the coefficient of thermal expansion for water.

Also necessary for the calculation of $\bar{C}_p^0$ are X, Y, and Z, which allow for the changes in the dielectric behavior of water, including its ability to stabilize solvents with temperature and pressure. We note that the Z in this case is dependent upon the dielectic constant of water, and is not the ion's formal charge. The definitions of X, Y, and Z are below, where ϵ is the dielectric constant of water:

$$Z = -\frac{1}{\epsilon} \tag{8.16}$$

$$Y = \left(\frac{\partial Z}{\partial T}\right)_P = \left(\frac{1}{\epsilon^2}\right)\left(\frac{\partial \epsilon}{\partial T}\right)_P \tag{8.17}$$

$$X = \left(\frac{\partial Y}{\partial T}\right)_P = \left(\frac{1}{\epsilon^2}\right)\left[\left(\frac{\partial^2 \epsilon}{\partial T^2}\right)_P - \frac{2}{\epsilon}\left(\frac{\partial \epsilon}{\partial T}\right)_P^2\right] \tag{8.18}$$

The values of X, Y, and Z at a range of pressures and temperatures are documented in E.L. Shock *et al.* [123] The variation of the dielectric constant of water is based on temperature, pressure and density has been well documented [122, 124].

$$\epsilon = \sum_{i=0}^{4} k_i(\tau)\hat{\rho}^i \tag{8.19}$$

where $k_i(\tau)$ are fitting parameters for the density of water, given as $\hat{\rho}$ divided by $1\,\mathrm{g\ cm^{-3}}$. Therefore, the first and second partial derivatives with respect to temperature of Z used to calculate the Y and X functions are:

$$\left(\frac{\partial \epsilon}{\partial T}\right)_P = \sum_{i=0}^{4} \hat{\rho}\left[\left(\frac{\partial k_i(\tau)}{\partial T}\right)_P - i\alpha k_i(\tau)\right] \tag{8.20}$$

$$\left(\frac{\partial^2 \epsilon}{\partial T^2}\right)_P = \sum_{i=0}^{4} \hat{\rho}^i\left[\left(\frac{\partial^2 k_i(\tau)}{\partial T^2}\right)_P - i\left(\alpha\left(\frac{\partial k_i(\tau)}{\partial T}\right)_P + k_i(\tau)\left(\frac{\partial \alpha}{\partial T}\right)_P\right) - i\alpha\left(\left(\frac{\partial k_i(\tau)}{\partial T}\right)_P - i\alpha k_i(\tau)\right)\right] \tag{8.21}$$

These equations are founded on established changes in the dielectric constant of water with respect to temperature and pressure. To implement these equations we require the coefficient of thermal expansion, α, and its respective derivatives, which can be found in a variety of sources [113, 114, 117].

In summary, the follow general steps are necessary to calculate the Gibbs free energy of formation for aqueous ions at elevated temperatures with the revised HKF model:

(1) Enumerate ion independent parameters in the methodology, such as Ψ and Θ.

(2) Establish known and desired thermodynamic data and properties for the given ion. This includes the desired nonstandard state pressure and temperature, charge, and standard state values of $\Delta_f G$, S and C.

(3) Find temperature and pressure independent parameters for the ion including c_1, c_2, a_1, a_2, etc. These should be experimentally given or approximated.

(4) Calculate or find from the literature the volume and volume derivatives of water, its dielectric coefficient and its derivatives, and the g-function and its derivatives.

(5) Calculate or find from literature the born functions of water, such as Z, Y, X.

(6) Enumerate the ionic radii and effective ionic radii of the ion.

(7) Calculate the Born coefficient and its derivatives.

(8) Calculate the heat capacity and entropy of the ion. Utilize use the (non-)standard state thermodynamic properties to approximate the extrapolated $\Delta_f G$ at nonstandard state.

The thermodynamic behavior found in this study should be viewed as correctly capturing the trends for the aqueous ions considered, and is not claimed to give exact values of the formation energies of these species at higher temperatures. Future experimental work could focus on identifying the nonstandard state thermodynamic properties of copper aqueous ions. To that end, we find agreement between our calculated entropies and heat capacities to those calculated by Puigdomenech [**121**]. Furthermore, these approximations for the temperature and pressure dependence of the formation energies have been used successfully before [**119**].